UNCERTAINTY IN LATTICE REACTOR PHYSICS CALCULATIONS

UNCERTAINTY IN LATTICE REACTOR PHYSICS CALCULATIONS

By MATTHEW RYAN BALL, M.A.Sc., B.A.Sc.

A Thesis Submitted to the School of Graduate Studies in Partial Fulfilment
of the Requirements for the Degree of Doctor of Philosophy

McMaster University DOCTOR OF PHILOSOPHY (2011) Hamilton, Ontario (Engineering Physics)

TITLE: Uncertainty in Lattice Reactor Physics Calculations AUTHOR: Matthew Ryan Ball, M.A.Sc., B.A.Sc.(McMaster University) SUPERVISORS: Professor D. R. Novog and Professor J. C. Luxat NUMBER OF PAGES: xv, 207

Abstract

Comprehensive sensitivity and uncertainty analysis has been performed for light-water reactor and heavy-water reactor lattices using three techniques; adjoint-based sensitivity analysis, Monte Carlo sampling, and direct numerical perturbation. The adjoint analysis was performed using a widely accepted, commercially available code, whereas the Monte Carlo sampling and direct numerical perturbation were performed using new codes that were developed as part of this work.

Uncertainties associated with fundamental nuclear data accompany evaluated nuclear data libraries in the form of covariance matrices. As nuclear data are important parameters in reactor physics calculations, any associated uncertainty causes a loss of confidence in the calculation results. The quantification of output uncertainties is necessary to adequately establish safety margins of nuclear facilities.

In this work, the propagation of uncertainties associated with both physics parameters (e.g. microscopic cross-sections) and lattice model parameters (e.g. material temperature) have been investigated, and the uncertainty of all relevant lattice calculation outputs, including the neutron multiplication constant and few-group, homogenized cross-sections have been quantified. Sensitivity and uncertainty effects arising from the resonance self-shielding of microscopic cross-sections were addressed using a novel set of resonance integral corrections that are derived from perturbations in their infinite-dilution counterparts.

It was found that the covariance of the U^{238} radiative capture cross-section was the dominant contributor to the uncertainties of lattice properties. Also, the uncertainty associated with the prediction of isotope concentrations during burnup is significant, even when uncertainties of fission yields and decay rates were neglected. Such burnup related uncertainties result solely due to the uncertainty of fission and radiative capture rates that arises from physics parameter covariance.

The quantified uncertainties of lattice calculation outputs that are described in this work are suitable for use as input uncertainties to subsequent reactor physics calculations, including reactor core analysis employing neutron diffusion theory.

Acknowledgements

I am grateful to my supervisors, Dr. David Novog and Dr. John Luxat from whom I have learned an immense amount. Without their support and assistance, the completion of this work would have been impossible. Likewise, my gratitude must be expressed to Dr. Ben Rouben and Dr. Bartosz Protas whose advice and recommendations greatly contributed to my understanding as well as to the completion of this work.

Also, my sincere thanks to Dr. Carlo Parisi, Dr. Alessandro Petruzzi, and Dr. Francesco D'Auria for the opportunity to study at GRNSPG, University of Pisa, and benefit from their distinguished expertise.

My heartfelt thanks must be expressed to my parents, for their continual support and encouragement.

Contents

List of Figures

List of Tables

List of Abbreviations

Abbreviations

AOO	anticipated operational occurence
BoC	beginning of cycle
DBA	design basis accident
ENDF	Evaluated Nuclear Data Files
ENDL	evaluated nuclear data library
EoC	end of cycle
GPT	generalized perturbation theory
GRS	Gesellschaft für Anlagen- und Reaktorsicherheit
HFP	hot full-power
HWR	heavy-water reactor
HZP	hot zero-power
IAEA	International Atomic Energy Agency
IST	industry standard tool
JEFF	Joint Evaluated Fission and Fusion File
JENDL	Japanese Evaluated Neutron Data Library
LFP	lumped fission product
LWR	light-water reactor
MT	ENDF section (e.g. cross-section) identifier
NEA	Nuclear Energy Agency
NR	narrow resonance
OECD	Organization for Economic Co-operation and Development
ORNL	Oak Ridge National Laboratory
PDF	probability density function
UAM	Uncertainty Analysis in Best-Estimate Modeling
WLUP	WIMS library update project

Units

barn	10^{-24} cm^2
eV	electron-Volt
W	Watt

Variables

$\bar{\nu}$	mean number of neutrons emitted per fission
$\bar{\sigma}$	resonance self-shielded microscopic cross-section

χ	energy distribution of fission neutrons
μ	neutron lethargy
ϕ	neutron flux
Σ	macroscopic cross-section
σ	infinite-dilution microscopic cross-section
σ_o	Bondarenko background cross-section
k_∞	infinite lattice neutron multiplication constant
E	neutron energy
T	temperature

Chapter 1

Introduction

The determination of neutron energy and trajectory within a nuclear reactor core is of primary concern in many operational and safety assessments. Such calculations involve the combination of theory, approximations, numerical methods and empirical approaches based on experimental evidence. The assessment of uncertainties related to nuclear reactor analysis predictions is an arduous task, and involves many physics and engineering disciplines ranging from reactor physics and thermal-hydraulics to thermodynamics and fuel performance. Errors in predicted quantities can be introduced through experimental uncertainties, imprecise empirical correlations, the use of physics models as substitutes for measured data or more rigorous theoretical formulations, and calculation approximations intended to reduce the computational effort of an analysis. A fundamental objective of this thesis is to develop, implement and analyze methods capable of performing uncertainty analysis.

Reactor analysis has traditionally been organized as a series of calculations, arranged in a mostly feed-forward sequence in which the outputs at each step are used as inputs at the subsequent step[1]. Depending on the analysis, the calculation sequence may span multiple dimensionalities (1D to 3D), multiple scales (from fuel pins to bundles to the whole reactor core), and multiple physics (e.g. reactor physics and thermal-hydraulics). The propagation of uncertainties traces that of the underlying calculation sequence, with uncertainties moving from stage to stage, clinging to the inputs and outputs through the sequence and modified by each calculation.

In the case of steady-state reactor physics calculations, the sequence begins with the preparation of nuclear data using a generic estimation of a neutron flux spectrum. This *cross-section processing* step takes fundamental nuclear data as input that is continuously-varying in the energy domain, and performs flux-weighted averaging to produce a set of discrete *multi-group* nuclear data that are discretized in energy and computationally manageable for use in deterministic solutions of problem geometries. The multi-group constants, or "group constants" for short, are fairly problem-independent, with general applicability to broad classes of systems, such as thermal, light water moderated reactors. Neutron flux is selected as the appropriate

weighting function for group averaging in order to preserve the prediction of nuclear reaction rates.

The source of continuous-energy data is one of several evaluated nuclear data libraries (ENDL) such as ENDF/B[2], JEFF[3], JENDLE[4], and others. The term "continuous-energy" may be more accurately referred to as "pointwise", since the data is stored on a very fine energy grid, albeit often with accompanying interpolation rules to find data values between grid points[2]. Data found in an ENDL is drawn from experimental measurements, such as those stored in the EXFOR[5] database and in the *Atlas of Neutron Resonances*[6], and from a collection of nuclear physics models that supplement experimental findings[1]. Experimental uncertainties as well as those associated with the selection of physics model parameters and interpolation schemes cause related uncertainty on the pointwise cross-section in the ENDL, which is discussed in section 1.4. Since these uncertainties are present in the initial data, they permeate all subsequent predictions.

1.1 Cross-section processing

Cross-section processing is a preliminary calculation performed without regard to any specific nuclear geometry or composition, thus the generic neutron flux weighting-function is estimated based on reasonable approximations of the flux spectrum that occur in the broad class of nuclear systems to which the multi-group data will be applied. Generally, the estimate of the flux is derived from first principles of reactor theory, or alternatively, a continuous energy flux solver, such as MCNP[7], can be used to calculate the spectrum for a simple system representative of the multi-group target class of problems. For systems that are fully moderated by H^1 (i.e. light water), a common strategy is to assemble the generic weighting function in three parts, each reflecting the predominant behaviour of neutron flux in a particular range of energy. Several pre-defined weighting functions included in the NJOY[8] cross-section processing code are constructed in this manner.

In the fast energy region – above one MeV or so – neutrons are born from fission events with a characteristic energy distribution that depends strongly on the fissioning nuclides (typically U^{235} for uranium-fueled reactors), and weakly on the energy of the fission-inducing incident neutron[9]; sufficiently weak that the dependency on incident neutron energy is generally neglected. Therefore, generic weighting functions in the MeV range can be reasonably approximated by the fission energy spectrum of the primary fission material evaluated at a typical incident neutron energy.

Once neutrons are born from fission events, if they do not wander out of the reactor core, they will either be absorbed at high energy, which has low probability, or will progressively lose their energy after suffering collisions with nuclei. A neutron with energy E being scattered by a nucleus with scattering cross-section $\sigma(E)$ will

be left with some lesser[1] energy E'. The differential scattering cross-section, from incident energy E to resultant energy E' is characterized by equation (1.1.1) in the case of entirely elastic, isotropic scattering.

$$\sigma_s(E' \rightarrow E) = \begin{cases} \dfrac{\sigma_s(E')}{(1-\alpha)E'} & \text{for } E < E' < \dfrac{E}{\alpha} \\ 0 & \text{otherwise} \end{cases} \tag{1.1.1}$$

where,

$$\alpha = \left(\frac{A-1}{A+1}\right)^2 \tag{1.1.2}$$

and A is the mass of the scattering nucleus in neutron mass units. A neutron slowing-down equation for an infinite, homogeneous medium can be defined[10] as,

$$[\Sigma_a(E) + \Sigma_s(E)]\phi(E) = \int_E^\infty dE' \Sigma_s(E' \rightarrow E)\phi(E') + S(E) \tag{1.1.3}$$

Maintaining the assumed prohibition against inelastic or anisotropic scattering, the microscopic differential scattering cross-section in equation (1.1.1) can be substituted and incorporated into its macroscopic counterpart in equation (1.1.3). Moreover, for systems without neutron absorption occurring at intermediate energies, which are moderated solely by H^1 – whose mass is approximately equal to that of a neutron – the slowing-down equation can be reformulated as,

$$\Sigma_s(E)\phi(E) = \int_E^\infty dE' \frac{\Sigma_s(E')\phi(E')}{E'} + S(E) \tag{1.1.4}$$

The solution to equation (1.1.4) at energies below that of the neutron source takes the form $\phi(E) \propto 1/E$ if the scattering cross-section Σ_s can be approximated as being constant with respect to energy, which is not unrealistic. Thus, the generic weighting function for slowing-down energies in the approximate range of 1 eV to 1 MeV for light water moderated systems takes the form of $1/E$.

For thermal reactors, neutrons will slow down until reaching thermal equilibrium with the moderating atoms, and thus take on a Maxwell-Boltzmann energy distribution that corresponds to the moderator temperature. It is this neutron energy distribution which is often used as a generic weighting function for the thermal energy range.

The piecewise, generic weighting function described above is applied to continuous-energy cross-sections that have been subjected to Doppler-broadening[1] to effectively account for the component of relative speed between neutrons and nuclei due to the nuclei's thermal motion. Recall that cross-section processing is performed with intended applicability to many systems, and thus several temperatures are often

[1] Up-scattering can be neglected at energies higher than a couple electron-Volts.

used to generate a table of multi-group constants, indexed by energy and temperature, which can subsequently be interpolated to specific problem temperatures.

Cross-section processing produces a reasonable working set of multi-group nuclear constants for use in reactor analysis, without depending on intimate geometric or material details of the reactor to be analyzed. This is especially true because the weighting function need not accurately describe the neutron flux profile *between* energy group intervals. Only the intra-group weighting function is important when collapsing the continuously-varying cross-section into discrete groups. Once collapsed to multiple energy groups – usually numbering from a few dozen to a few hundred – the data is written to multi-group nuclear data libraries, and often packaged with lattice physics codes, whose task is to determine relative flux between energy groups using problem-specific materials and geometries. The cross-section averaging in each group g, using an estimated weighting function, $W(E)$, is shown in equation (1.1.5).

$$\sigma^g = \frac{\int_g \sigma(E)W(E)dE}{\int_g W(E)dE} \tag{1.1.5}$$

1.2 Lattice physics

Naturally, as the name suggests, the purpose of reactor analysis is to predict the properties and behaviours of reactors, which are large, finite, heterogeneous, three-dimensional objects. Lattice physics calculations estimate the problem-specific flux by solving the *neutron transport equation* (see section 1.3) applied to a small, infinitely repeating unit of geometry that will alone constitute a suitable analogue, from a neutron kinetics perspective, to produce a flux distribution representative of that which is encountered in the finite reactor. The repeating unit, called the *lattice cell*, is generally taken to be a fuel pin or assembly, which are arranged in a large rectangular or hexagonal grid, or lattice, when viewed in an axial cross-section of a three-dimensional reactor core. Fuel pins and assemblies are sufficiently long in most reactor applications that the boundary effects encountered at each end do not significantly impact the axially-averaged reaction rates over their full length, allowing them to be modelled in just two dimensions. In other words, the three-dimensional finite reactor core, with all its complexity, is modelled as a two-dimensional infinite grid of simple units. The resulting flux, which varies in both energy and space, is used as a weighting function to collapse the multi-group constants into a fewer number of groups – typically two – averaged over the entire lattice volume.

Lattice physics is the first component of reactor physics analysis that involves problem-specific materials and geometries. Just as cross-section processing estimates a generic flux for the collapsing of cross-sections from continuous-energy to multi-group form, a goal of lattice physics is to estimate a problem-specific flux to conduct

a further collapse from a multi-group structure to only a few groups – typically a single thermal group and single fast group. This is done to facilitate large scale, steady-state and transient reactor core calcultaions in subsequent steps. In contrast to cross-section processing, lattice calculations not only collapse cross-sections in the energy domain, but also homogenize cross-sections in space, producing a set of macroscopic cross-sections that correspond to the materials of the lattice cell being somewhat smeared together. As with energy, the spatial homogenization is done in such a way as to preserve the total reaction rates of the entire homogenized volume.

Few-group, spatially homogenized cross-sections produced by lattice physics calculations are ultimately used in the analysis of three-dimensional, finite reactors using neutron diffusion theory. Each lattice cell in the finite reactor, such as each fuel assembly, is replaced by something of a smeared material, lacking any detailed structure, and characterized by that cell's homogenized, few-group macroscopic cross-sections. The diffusion calculation is performed with the spatially homogenized, few-group cross-sections so that the three-dimensional steady-state and transient calculations are computationally tractable.

1.2.1 Resonance self-shielding

Despite the effort involved with cross-section processing to create applicable multi-group constants for lattice analysis, in some cases they cannot be directly used in lattice calculations without first being modified to some degree using problem-specific material information. The thermal distribution weighting function used to generate low-energy multi-group constants is a quite reasonable approximation, as is the fission spectrum for neutron flux at high energies. However, the $1/E$ approximation for slowing-down energies is *not necessarily* reasonable for all nuclides, at all energies. Recall that the derivation of the $1/E$ form of the slowing-down flux assumed there is no substantial absorption taking place at those energies. In practice, neutrons at intermediate energies are likely be absorbed by some materials in narrow intervals of energy that correspond to sharp peaks in absorption cross-section called resonances. The complex cross-section structure of many closely packed resonances can be observed between the energies of 1 eV and 10 keV of the radiative capture cross-section of U^{238}, shown in figure 1.1. The presence of absorption peaks perturbs the smooth $1/E$ form of the flux in the neighbourhood of the resonance, producing a flux depression. The magnitude of the depression is a function of the *dilution* of the nuclide within a material mixture, that is to say, the fractional contribution to the total macroscopic cross-section of the mixture caused by the nuclide. The less dilute the nuclide, the larger its contribution to total cross-section and the larger the flux depression that results. A nuclide admixed at infinite dilution causes no perturbation and the flux remains smoothly varying as $1/E$. Therefore, multi-group constants at resonance energies that were weighted by a $1/E$ function are equivalently those of an infinitely dilute mixture.

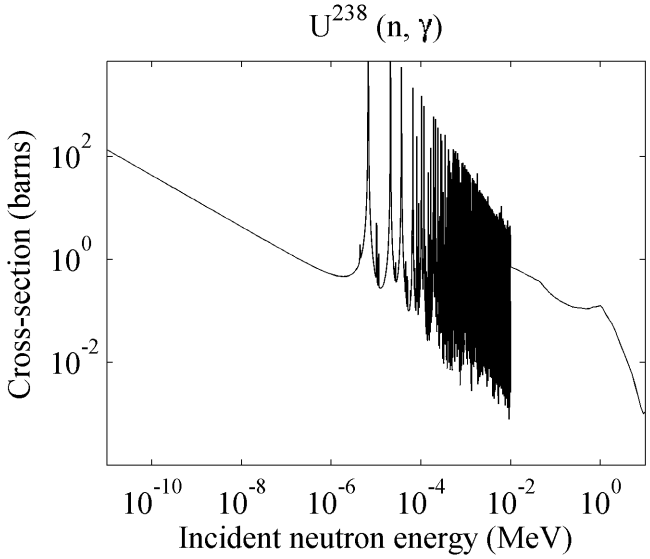

Figure 1.1: U^{238} (n, γ) cross-section resonances

Depressions in flux cause the group constants that contain resonances to take on smaller values, since the flux, acting as an averaging weighting function, exhibits a local minimum that corresponds to the cross-section peak energy. This effect is called *resonance self-shielding*[2], on account of the flux being effectively prevented by the resonance from attaining a smoothly varying form when at low dilution. The flux will be reduced (or shielded) as compared to that observed at high dilution. Figure 1.2 shows a flux depression that has formed in the presence of a strong cross-section resonance.

The process of correcting the multi-group cross-sections to new values that reflect the flux depressions at the problem dilution is an initial step of any lattice calculation. Multi-group libraries, such as the WIMS-D4 or AMPX master libraries, are designed to allow for self-shielding calculations, and include resonance paramaters specifically to accommodate that task. The quantity and style of resonance parameters are tailored to particular resonance self-shielding methods. A common and straightforward strategy is Bondarenko's method[11].

If one invokes a narrow resonance (NR) approximation, then it is assumed that resonances are sufficiently sharp and widely spaced that neutrons entering resonance energies were scattered from higher energies at which the flux assumes a $1/E$ shape. In other words, the neutron source term within each resonance is unrelated to the shape of the resonance itself. The Bondarenko method observes that given the NR approximation, the flux in the neighborhood of the resonance behaves as the product of two components: an underlying smooth $1/E$ component, and a component

[2]A distinct effect, known as spatial self-shielding, also exists. In this text, however, the term "self-shielding" refers solely to the resonance rather than spatial variety of self-shielding.

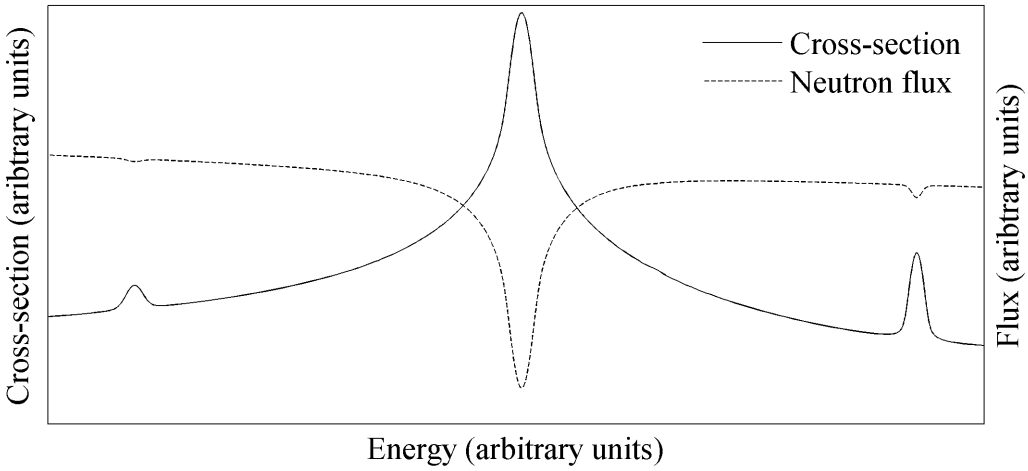

Figure 1.2: Example of a resonance flux depression

that varies as $1/\Sigma_T$,

$$\phi(E) = \frac{1/E}{\Sigma_T(E)} \tag{1.2.1}$$

which, for a mixture of n nuclides, can be re-written as,

$$\phi(E) = \frac{1/E}{\sum_j^n N^j \sigma_t^j(E)} \tag{1.2.2}$$

For the purposes of resonance self-shielding an absorber nuclide i, its contribution to Σ_T can be explicitly isolated from all other contributions.

$$\begin{aligned} \phi(E) &= \frac{1/E}{N^i\Big(\sigma_t^i(E) + \sum_{j\neq i}^n \frac{N^j}{N^i}\sigma_t^j(E)\Big)} \\ \phi(E) &= \frac{1/E}{N^i\big(\sigma_t^i(E) + \sigma_o(E)\big)} \end{aligned} \tag{1.2.3}$$

where N^i is the atom density of nuclide i, and σ_o is referred to as nuclide i's background cross-section, which is the total microscopic cross-section, in per-absorber atom units, caused by all other nuclides in the same mixture. Substituting the formulation of $\phi(E)$ in equation (1.2.3) into the cross-section averaging in equation (1.1.5), gives the Bondarenko formula of a self-shielded cross-section $\bar{\sigma}^g$,

$$\bar{\sigma}^g = \frac{\int_g \frac{\sigma(E)1/E}{\sigma_t(E)+\sigma_o} dE}{\int_g \frac{1/E}{\sigma_t(E)+\sigma_o} dE} \tag{1.2.4}$$

where σ_o is assumed to be constant over the group energy interval. Note that the shielded cross-section at infinite dilution reduces to the unshielded group value weighted by $1/E$,

$$\begin{aligned}\lim_{\sigma_o \to \infty} \bar{\sigma}^g \equiv \sigma^\infty &= \lim_{\sigma_o \to \infty} \frac{\frac{1}{\sigma_o}\int_g \frac{\sigma(E)}{E} dE}{\frac{1}{\sigma_o}\int_g \frac{1}{E} dE} \\ &= \frac{\int_g \frac{\sigma(E)}{E} dE}{\int_g \frac{1}{E} dE}\end{aligned}$$

Figure 1.3 shows a magnified portion of the U^{238} capture cross-section including three large resonance peaks, and the corresponding flux depressions at multiple dilutions as determined using the Bondarenko method. Self-shielded group cross-sections, corrected for the resonance flux depressions are shown in figure 1.4.

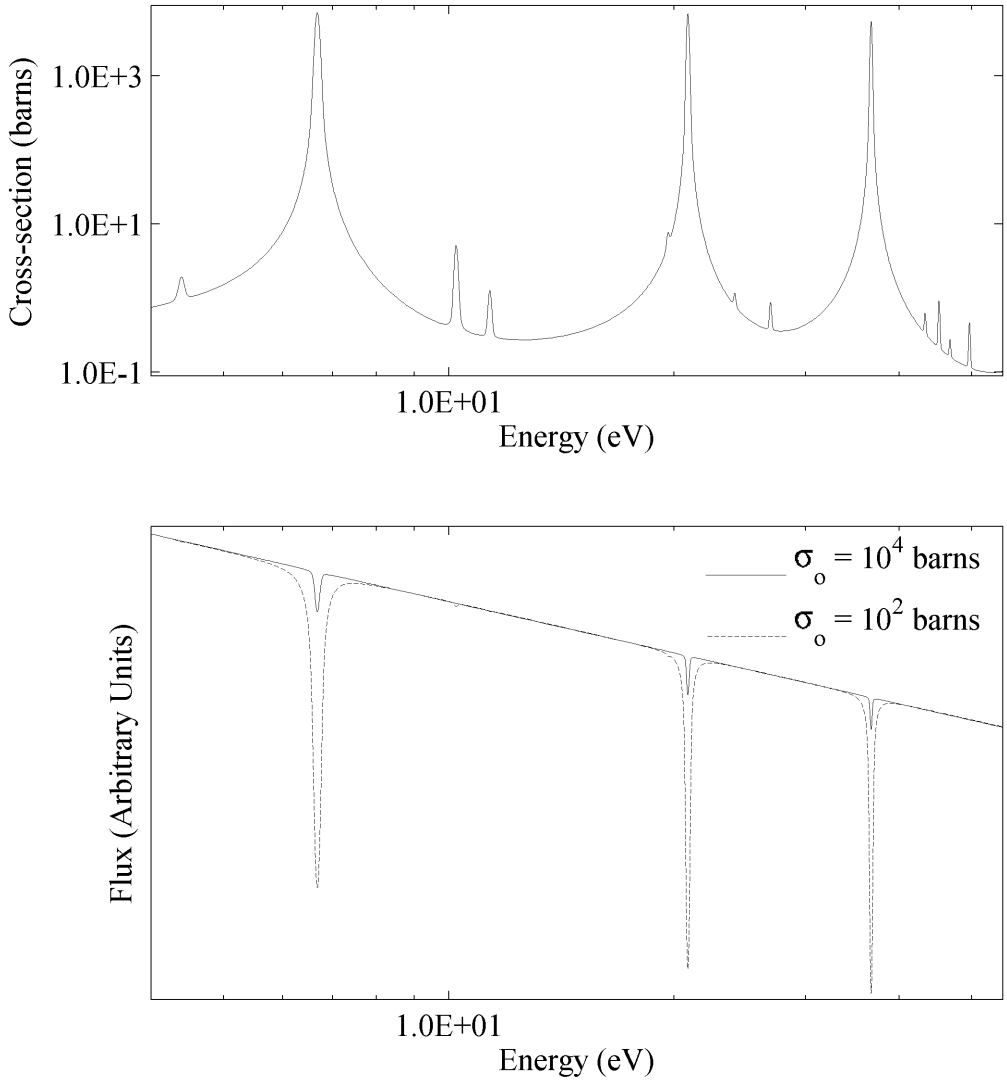

Figure 1.3: U^{238} (n, γ) resonances and flux depressions

If a cross-section processing code evaluates resonant energy group constants at several dilutions, and writes each value to a multi-group library indexed by σ_o, the lattice code needs merely interpolate between the tabled constants to calculate the appropriate shielded cross-section for the problem dilution.

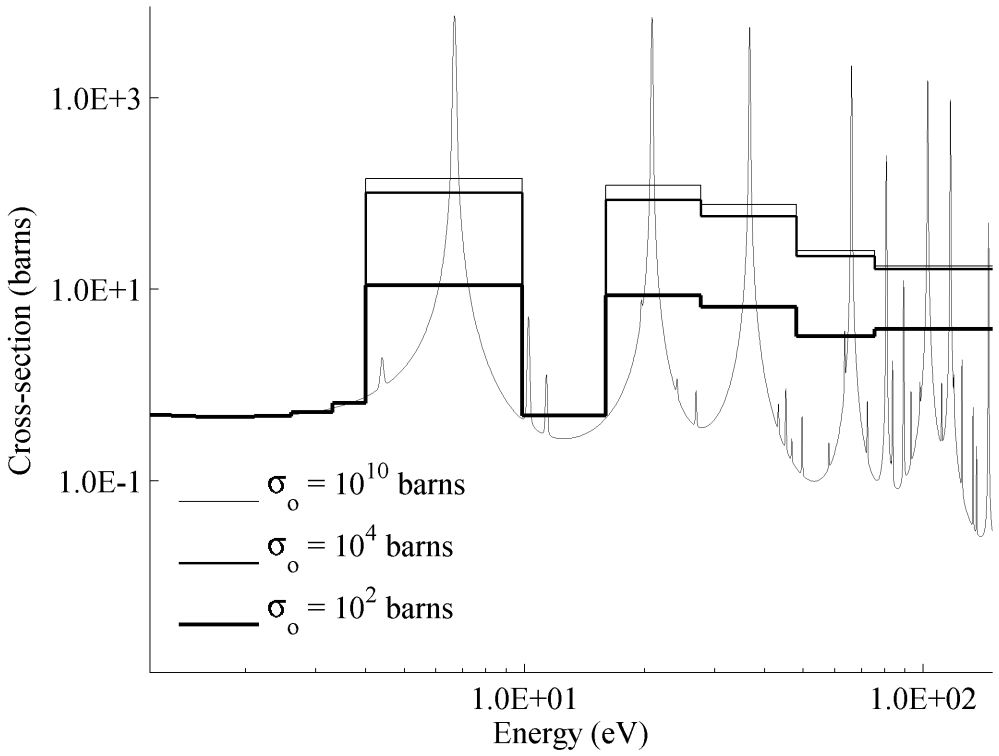

Figure 1.4: Resonance self-shielded U^{238} (n, γ) group constants

1.3 Neutron transport

Lattice flux can be predicted by solving the neutron transport equation – a rigorous accounting of all possible neutron gain and removal mechanisms. The transport equation, also referred to as the Boltzmann transport equation due to its similarity to an equation of the same name developed in the 19th century for rarefied gas dynamics[12], has the following continuously-varying, steady-state form,

$$\begin{aligned}\vec{\Omega}\cdot\nabla\vec{\phi}(r,E,\vec{\Omega})+\Sigma_T(r,E)\phi(r,E,\vec{\Omega})&\\ =\int_{4\pi}d\vec{\Omega}'\int_0^\infty\Sigma_S(r,E'\rightarrow E,\vec{\Omega}'\rightarrow\vec{\Omega})\vec{\phi}(r,E',\vec{\Omega}')dE'&\\ +\frac{\chi(E)}{4\pi k}\int_{4\pi}d\vec{\Omega}'\int_0^\infty\bar{\nu}(r,E')\Sigma_F(r,E')\phi(r,E',\vec{\Omega}')dE'&\quad(1.3.1)\end{aligned}$$

where,

$\vec{\phi}(r, E, \vec{\Omega})$	is angular neutron flux density
$\Sigma_T(r, E)$	is the macroscopic total neutron interaction cross-section at energy E and location r
$\Sigma_S(r, E' \to E, \vec{\Omega}' \to \vec{\Omega})$	is the macroscopic scattering cross-section from energy E' to E and angle $\vec{\Omega}'$ to $\vec{\Omega}$ at location r
$\Sigma_F(r, E')$	is the macroscopic fission cross-section at energy E' and location r
$\chi(E)$	is the energy probability distribution of fission neutron energies
and,	
$\bar{\nu}(r, E')$	is the average number of fission neutrons emitted from fission induced by a neutron of energy E' at location r

Each term in equation (1.3.1) represents a rate of change of neutron density in E, $\vec{\Omega}$ and $\Re^3$ space. The solution, $\vec{\phi}(r, E, \vec{\Omega})$, is an angular flux density, having units $\left[\frac{\text{flux}}{\text{eV} \cdot \text{sr}}\right]$, or equivalently, $\left[\frac{\text{neutrons}}{\text{sec} \cdot \text{eV} \cdot \text{sr} \cdot \text{cm}^2}\right]$, and describes the flux of neutrons at point r, along direction $\vec{\Omega}$ with energy E, which are the criteria of interest for flux in the neutron balance equation. Hence, neutrons of interest are located in a small volume dV about r, with trajectory in solid angle $d\vec{\Omega}$ about $\vec{\Omega}$, whose energies lie in a small interval dE about E. The first term on the left side of the equation tallies the rate of net leakage of neutrons at the region of interest due to their drifting motion. The second term on the same side accounts for the reaction rate of the neutrons of interest – scattering reactions will alter the direction or energy of the neutrons so they are no longer of interest, and absorption reactions will delete the neutron entirely from consideration. Conversely, the first term on the right side of the equation represents the neutrons already present at r, who are scattered into the energy and trajectory of interest. The final term of the equation accounts for neutrons that are born from fission reactions within the criteria of interest, assuming an isotropic distribution of fission neutron trajectories at birth.

Naturally, the loss and gain mechanisms are equal when at steady-state, however, this is unlikely to be the case in a real reactor application given only its static material geometries and compositions, or, in other words, in the absence of a reactivity control system or other controlling effects including feedback mechanisms. The steady-state equation can still be applied, however, through the introduction of a system eigenvalue, $1/k$. Called the multiplication constant, k modifies the magnitude of the fission source term by whatever multiplicative factor is necessary to achieve steady-state flux. Therefore, the presence of k in equation (1.3.1) is a mathematical convenience that causes time-dependent terms to vanish for all systems, even those

not in steady-state. Consequently, value of k larger than one corresponds to positive reactivity, in which the system has more neutron production than loss. Likewise, a value of k less than one indicates a subcritical system characterized by more neutron loss than production. In the case of an infinite lattice calculation with no neutron leakage out of the system, it is referred to as an infinite multiplication constant, k_∞.

The continuous transport equation is not solved analytically by lattice physics codes. Indeed, an analytical solution is not possible, except for very simplified problems. Rather, the terms in equation (1.3.1) are discretized in energy, space and solid angle, allowing for a numerical solution by any of several techniques. The discretization in energy is the focus of previously described cross-section processing and resonance self-shielding efforts – the methods of discretizing the remaining parameters is outside the scope of this dissertation.

The flux solution of the transport equation permits the calculation of lattice properties that are collapsed in energy structure to fewer groups, and homogenized in space, using a combination of flux and volume weighted averaging. Spatially homogenized, few-group macroscopic cross-sections are the ultimate end-products of lattice physics calculations.

1.4 Nuclear data uncertainties

Nuclear data contained within an ENDL, including continuous-energy cross-sections and resonance parameters, are not precisely known. Measurement uncertainties as well as the use of physics models diminish our confidence that the values in an ENDL are exactly correct. The library format of ENDF/B-VI, which has been internationally adopted and updated to ENDF/B-VII, contains fields in which uncertainties associated with the nuclear data is recorded[2]. The characterization of those uncertainties is by the statistical measure of covariance, in the form of a covariance matrix. Covariance describes the mutual variation of one or more random variables. The covariance of random variables x and y is defined as,

$$cov(x,y) \equiv E\big[\big(x - E(x)\big)\big(y - E(y)\big)\big] \tag{1.4.1}$$

where $E(x)$ is the expected value of x. The covariance of a random variable with itself reduces to its variance. In this context, the random variables are, for example, neutron interaction cross-sections at each energy point. The description of the uncertainties of n random variables, $x_1 \ldots x_n$, is by an $n \times n$ covariance matrix, in which covariance, $cov(x_i, x_j)$, is entered in the ith row and jth column of the matrix. Covariance is closely related to Pearson's correlation coefficient, defined as,

$$\rho(x,y) = \frac{cov(x,y)}{\sigma_x \sigma_y} \tag{1.4.2}$$

where σ_x is the standard deviation of x. The correlation coefficient is bounded in the closed interval $[-1, 1]$. A correlation of one indicates the two variables vary together

in an entirely linear way, related by a positive proportionality constant. A correlation of negative one means the same, but with a proportionality constant that is negative. A zero correlation implied that the variations of the two variables are entirely independent.

The interdependency between variables prohibits their variances alone from completely describing the constraints imposed on the collective variation of their values. Some interdependencies are straightforward to identify. In most cases, a cross-section follows a $1/\sqrt{E}$ contour at small ($\lesssim$ 100 meV) neutron energies[13], therefore an interdependency exists between its thermal values; the relative values at various energies cannot take on permutations that are contrary to $1/\sqrt{E}$. Consequently, strong correlations, and hence significant covariance, tend to exist in a cross-section's thermal range. Similarly, the physics of neutron/nucleus interaction dictates covariances in other energy regions. Dependencies also exist as a mathematical necessity between some cross-sections. Naturally, the variation of the total cross-section is related to the variation of a constituent cross-section that contributes part of the total, such as the absorption cross-section. Other dependencies are not so *a priori* known, such as those between cross-sections of different nuclides, which result from experimental data collection and the inability to wholly isolate nuclides during measurement.

The covariance matrix contained in the ENDL is constructed by a group of experts during an evaluation process, and therefore depends to some degree on expert judgment. A collection of procedures and computer tools are selected and employed by the evaluation group during covariance estimation, at great computational cost[14]. Cross-section processing codes such as NJOY or AMPX[15][16] feature routines that collapse ENDL covariances to a multi-group energy structure that is consistent with, and applicable to, the multi-group constants described in section 1.1.

The tools, therefore, for propagating uncertainties through cross-section processing to produce multi-group covariance matrices are widely available. Uncertainty propagation through lattice calculations are another matter. One has everything one might need to perform such a propagation – a set of multi-group constants and its associated covariance matrix – except for a complete set of tools to do so. The availability and capability of computer codes to conduct lattice uncertainty analysis is the focus of chapter 2.

1.5 The purpose of lattice physics uncertainty analysis

The purpose of conducting uncertainty analysis on a reactor calculation is identical to that of performing the reactor calculation itself. That purpose, of course, is to predict the properties and behaviour of the reactor under a variety of conditions, from normal operation to accident scenarios. Uncertainty analysis is required merely from the admission that there is more than one solution to the flux and multiplication that

can be reasonably expected. Rather than there being a single outcome that is certain, there is a *range* of possible outcomes that emerges given the range of possible input values that exists due to our foggy view of their true measure and the simplifications (i.e. discretization of energy) in the solution method.

Some operational reactor properties can be measured with acceptable confidence on a day-to-day basis. For such properties, the impact of uncertainty on their predicted values is diminished (but still present), because their predicted values can be replaced or supplemented by measured quantities. There are a great number of properties, however, that cannot be adequately measured in-core, either due impracticality of instrumentation placement, or unacceptably large instrumentation uncertainty. An example is the spatial power distribution on the level of fuel pins, for which the knowledge of the neutron flux is required with a high spatial resolution. In the area of reactor physics specifically, the uncertainty in neutron flux drives the uncertainty associated with many calculation end-products, including macroscopic cross-sections, local reaction rates and isotopic concentrations during burnup. During fast-acting transients like those corresponding to some reactor accidents, calculated predictions of reactor behaviour are even more important.

Traditionally, reactor safety analysis has been performed with the use of conservative assumptions and large safety margins to account for unknown and unquantified uncertainties associated with calculation solutions. Sufficiently large safety margins combined with sufficiently pessimistic and conservative assumptions can guard against calculation uncertainties; a value that is worse than predicted may still be better than that which was pessimistically presumed. However, it prompts the question of what exactly constitutes a "sufficient" margin in the face of an unquantified uncertainty! Another drawback of that approach is the use of conservatisms, which may even be non-physical, e.g. assuming a variable has a large value in one calculation and simultaneously a low value in another calculation, depending on which is more conservative in each context. Conservative assumptions do not lead to any realistic prediction of actual system behaviour, but merely a dipiction of a probably unrealistic and plausibly impossible scenario.

Comprehensive uncertainty analysis alleviates the need for conservative assumptions and provides a realistic and justifiable range of solutions from which safety margins can be properly established. A best-estimate solution can be determined, which lacks any conservative contrivances and is based solely on realistic assumptions and models. When evaluated with consideration to its quantified uncertainty, the best-estimate solution provides valuable information that is unavailable through a conservative approach.

Lattice physics, being the first calculation step at which problem-dependent specifications are involved, is the first opportunity at which uncertainties of nuclear physics quantities can be propagated in the context of a realizable, designed system. Uncertainties associated with lattice calculation outputs will propagate through all subsequent calculations that depend on those outputs. Therefore, lattice uncertainty

analysis forms the foundation of reactor physics uncertainty analysis in general, as well as the capability to establish realistic and comprehensively justifiable reactor safety margins that include the effects of fundamental nuclear data.

1.6 OECD/NEA uncertainty analysis in modeling benchmark

The Nuclear Energy Agency (NEA) of the Organization for Economic Co-operation and Development (OECD) in 2006 began work to establish an Uncertainty Analysis in Best-Estimate Modeling (UAM) benchmark[17], through which international participants would develop and share acquired experience in the field of uncertainty analysis for multi-scale, multi-physics nuclear reactor analysis. The motivation of the benchmark was based on the recognition by the NEA of the growing interest in unertainty analysis methods applied to reactor safety, "In recent years there has been an increasing demand from nuclear research, industry, safety and regulation for best estimate predictions to be provided with their confidence bounds"[17, p. 3].

The benchmark is organized into a sequence of nine steps, referred to as exercises, that collectively span a typical light-water reactor (LWR) safety analysis. The first exercises involve the calculation of covariance matrices appicable to multi-group cross-sections, followed by covariance propagation through resonance self-shielding and lattice physics calculations. Uncertainties are then to be methodically propagated to larger scale analyses that incorporate additional physics, including nuclear fuel performance and thermal-hydraulics, and additional sources of uncertainty including those associated with geometry (manufacturing), isotopic enrichment and material temperature. The final exercises involve full-core multi-physics (coupled reactor physics/thermal-hydraulics). Summarily, the objective of the benchmark exercises is to establish a set of best-practices and procedures for performing comprehensive uncertainty analysis, to disseminate insight gained by participants during the evolution of their uncertainty assessment strategies, and to foster the development of computer tools that facilitate uncertainty and sensitivity analysis.

As a result in part due to the UAM benchmark, tools and procedures for uncertainty analysis in lattice physics have been rapidly emerging from a number of academic and research institutions. It is in the context of the OECD/NEA UAM benchmark that a great deal of this dissertation was developed.

Chapter 2

Review of practices and literature

Uncertainty propagation of fundamental nuclear data through reactor physics calculations is an emerging field, and thus at the time of this writing most available toolsets are essentially still in their infancy. The approaches of currently available tools for performing lattice uncertainty propagation broadly fall into two categories: 1) sensitivity-based approaches, and 2) statistical approaches. After a brief overview of the two approaches, this chapter will discuss four particular lattice uncertainty tools in additional detail.

Sensitivity-Based Approaches

Tools of the first group estimate the uncertainty of a scalar response function (i.e. a calculation output functional such as k_∞) that results from an input parameter uncertainty through use of the sensitivity of the response to the input[18] according to perturbation theory. The response, as a function of the input parameter, can be precisely represented by a Taylor series expansion of infinite order. However, lattice physics uncertainty tools predominantly, if not exclusively, employ a first-order approximation in which second and higher-order terms are neglected, thereby estimating a linear relationship that is characterized by the partial derivative of the response with respect to the parameter. The oft-used "sandwich rule"[18], which is described in more detailed in section 3.2, is used to calculate the uncertainty of the response given the estimated sensitivity from a Taylor series expansion, and the uncertainty of a parameter[18]. This approach has elsewhere been summarized thusly:

> The probability distribution of the objective function is approximated by the probability distribution of its low-order approximation, which can be directly calculated from the probability distribution of the source uncertainties. [19, p. 10]

The most widely adopted technique for determining lattice physics response sensitivities is that of adjoint analysis[20][21][22][23][24]. By solving for the "adjoint-flux", ϕ^+, which is the solution to the adjoint formulation of the neutron transport

equation, estimates of the sensitivities of lattice responses to input parameters can be analytically formulated. Adjoint-based sensitivity and uncertainty analysis is an efficient technique when the number of responses is small and the number of input parameters is large, because the computational effort associated with this technique is related to the determination of the forward and adjoint of the function taken by each response, and not to the size of the input parameter population. Sensitivities to every input parameter are simultaneously determined with the computational effort equivalent to just a few best-estimate lattice calculations[25]. In the context of lattice physics, adjoint analysis is particularly well-suited to the estimation of k_∞ sensitivities with respect to self-shielded, multi-group cross-sections. Recall, however, that multi-group nuclear data covariance (produced by NJOY, for example), apply to unshielded, infinite-dilution cross-sections. Therefore, uncertainty propagation requires the sensitivity of k_∞ to unshielded data, which can be assembled using the chain rule of calculus, if the sensitivities of the shielded cross-sections to unshielded cross-sections are also known.

The determination of the shielded-to-unshielded data sensitivity is problematic with adjoint analysis, and has motivated the use of other methods specifically targeting that particular sensitivity in the context of adjoint-based tools. Another difficulty encountered with adjoint sensitivity analysis applied to lattice physics is the propagation of geometry uncertainties, for which a smooth change in the geometry input parameter causes a discontinuous change in cross-sections as a function of space.

Other methods for calculating sensitivities include automatic differentiation[27] and direct numerical perturbation[28] [29] (also known as direct differentiation and numerical sensitivity analysis, respectively). In recent lattice physics uncertainty research – in particular the work by UAM participants – automatic differentiation and direct numerical perturbation have received less attention than adjoint-based methods. Automatic differentiation is a source code transformation procedure that involves the insertion of extra lines of code into calculation software, the purpose of which is to compute partial derivatives between variables, determined according to the mathematical operations performed on the variables in the base code. Several automatic differentiation post-processing packages are commercially available, that scan pre-existing software source code and add sensitivity-related instructions where it is deemed appropriate. Verification that the automated sensitivity post-processing properly captures the sensitivities between all variables of interest demands evaluation by an individual with thorough familiarity – at the source code level – of the base software. Software subjected to automatic differentiation may also be prone to substantial increases in execution time and memory usage[25].

Direct numerical perturbation is a straightforward numerical alternative to the adjoint method, by which partial derivatives of the response are estimated by making small changes to the input parameter of interest and evaluating the response with each change, according to, for example, a method of finite difference. In comparison to adjoint methods, direct numerical perturbation can be more efficient when

the number of responses is large, and the number of inputs is small. In terms of computational effort, numerical perturbation is essentially the inverse of adjoint analysis, in that the number of required lattice calculations is equal to the number of perturbed input parameters, but independent of the number of responses; the sensitivity of all responses with respect to a single parameter are simultaneously available after each calculation. Numerical sensitivity analysis offers additional flexibility over adjoint analysis – all input parameters, including temperatures and geometries, can be perturbed in a straightforward manner without relying on *a priori* knowledge of how they are mathematically related to the responses.

For the case of a nonlinear functions, a first-order finite differencing scheme better approximates the true partial derivative when the perturbation size is small, as this reduces the contributions from the higher-order terms. However, when implemented on a computational machine, tiny perturbations can be subjected to a host of numerical issues that can cause significant error in the estimate of the partial derivative. Such limitations stem from finite bit-length floating point representation, numerical convergence criteria, and rounding errors. Therefore, the perturbation size must be small to reduce the effect of the trunction of higher-order terms, but must also be large to reduce the effect of numerical errors. This has been referred to as a "step-size dilemma"[26]. The "complex-step derivative approximation" has been proposed as a strategy for greatly reducing the effects of numerical error[26]. Direct numerical perturbation is discussed in more detail in section 3.2, as is a rationale behind the selection of perturbation sizes when applied to lattice physics calculations.

Statistical Approaches

The second group of approaches involves a Monte Carlo[1] sampling of input parameters across their probability distributions. Lattice simulations conducted for each sample of input parameters produce a corresponding probability distribution of each response. The computational effort related to statistical uncertainty analysis is independent of both the number of responses and the number of parameters, and depends only on the desired confidence associated with the statistical measures of the response distributions. This class of methods is also trivially parallelizable, as the simulation applied to each input sample can be executed on its own CPU independent of every other simulation.

The flexibility of this approach is equally good as that of direct numerical perturbation; all input parameters can easily be subjected to Monte Carlo sampling, and the statistics of all responses can be easily compiled. Also, unlike the first-order approximations employed by sensitivity-based approaches, statistical sampling is not constrained to some finite order truncation of power series that relate responses to parameters; all high-order terms are implicitly treated.

[1]Monte Carlo sampling of input parameters should not be confused with Monte Carlo solution methods of the transport equation.

Statistical methods are gaining popularity for lattice uncertainty analysis as a result of their flexibility concerning a variety of input parameters, competitive computational requirements when faced with many responses, and easily parallelizable nature. Statistical sampling is discussed in additional detail in section 3.1.

2.1 Currently available tools

This section describes selected tools for performing lattice uncertainty propagation that are currently available to analysts, as well as those that are in the development stage as reported in literature. The tools described in the remainder of the chapter are selected to span several common methodologies for performing analysis of lattice uncertainty.

2.1.1 TSUNAMI-1D/3D

The Tools for Sensitivity and Uncertainty Analysis Methodology Implementation (TSUNAMI)[30][31] is the leading, state-of-the-art sensitivity and uncertainty toolset that is incorporated into the SCALE[32] code system developed by Oak Ridge National Laboratory (ORNL). TSUNAMI is the natural benchmark against which the capabilities of competing tools must be measured.

TSUNAMI is an adjoint-based sensitivity tool employing generalized perturbation theory (GPT). Forward and adjoint flux calculations are performed for one-dimensional geometries using the XSDRNPM[33] deterministic transport solver in a sequence controlled by TSUNAMI-1D[30], and for three-dimensional geometries by the KENO V.a[34] Monte Carlo[2] solver in a sequence controlled by TSUNAMI-3D. TSUNAMI codes were first introduced in July 2004 as part of release version 5 of SCALE[35]. Original and subsequent versions of the TSUNAMI codes, including those released with SCALE 5.1 and SCALE 6, suffered from several limitations that hindered their usefulness in comprehensive lattice physics uncertainty analysis – primarily, the inability to calculate covariance of the homogenized, few-group cross-sections that are the primary output of lattice calculations. This shortcoming was addressed by ORNL with the development of SCALE 6.1, that overlapped with the work of this dissertation, and was recently released in the summer of 2011[36]. SCALE 6.1 includes a TSUNAMI-2D sequence, that uses the deterministic transport code NEWT[37] to calculate forward and adjoint flux for two-dimensional systems. TSUNAMI-1D and TSUNAMI-2D of SCALE 6.1 include the capability to calculate covariance of few-group, homogenized lattice cross-sections, although this feature is still absent from TSUNAMI-3D in the SCALE 6.1 release.

[2] A Monte Carlo solution of the transport equation should not be confused with Monte Carlo sampling of input parameters.

Another limitation in even the most recent versions of the TSUNAMI family of codes is their sole focus of propagating nuclear data uncertainties. While uncertainties of this type certainty account for a large portion of the uncertainty associated with lattice responses (as will be shown in chapters 5 and 6), other source uncertainties, such as those associated with material temperature, are still of moderate importance and should be included in an analysis for the sake of completeness. For the same reason, so should geometric and material composition uncertainties. Concerning output uncertainties, TSUNAMI lacks the capability to calculate uncertainties associated with burnup effects, including the uncertainties associated with k_∞, few-group homogenized cross-sections, and isotopic concentrations, all as a function of power history.

Method Overview

The TSUNAMI family of codes traces the sensitivity of k_∞ with respect to a self-shielded cross-section along a multi-step path that is stitched together using derivative chain rules. A thorough description can be found in the documentation of SAMS[38] – the code of the TSUNAMI sequence that is tasked with calculating sensitivities – but is summarized in this section with deliberate brevity.

The first step in a SAMS sensitivity trace is the calculation of $S_{k,\Sigma}$, the sensitivity of k_∞ with respect to a particular macroscopic cross-section, Σ at some region of discretized space. The formulation of the sensitivities to macroscopic cross-sections are derived by first principles from the transport equation. An important simplification is introduced in the SAMS calculation of $S_{k,\Sigma}$, namely, that perturbations of the neutron flux caused by perturbations of cross-sections is insignificant and can be neglected[38, pp. F22.2.2]. Sensitivities must subsequently be computed that relate macroscopic cross-sections to each other as well as to the number densities (total cross-section) of nuclides, as they constitute an implicit influence through the dilution dependency of resonance self-shielding effects. A third link in the chain of sensitivities are those of macroscopic total cross-section with respect to the component microscopic cross-sections of each nuclide.

Sensitivities calculated by SAMS can be labeled as either "explicit" or "implicit". Explicit effects are those perturbations of k_∞ that are due to cross-sections directly perturbing the loss and gain operators of the transport equation. For example, the expression for the explicit sensitivity of k_∞ to a particular fission cross-section, $\Sigma^i_{f,g,z}$ of isotope i, at energy group g, and spatial region z, is formulated as,

$$S^i_{f,g,z} = \frac{1}{D}\Bigg[\left(\frac{1}{k}\bar{\nu}^i_{g,z}\Sigma^i_{f,g,z}\chi^i_{g,z} - \Sigma^i_{f,g,z}\right)P^0_{g,g,z} + \sum_{g'\neq g}^{G}\frac{1}{k}\bar{\nu}^i_{g,z}\Sigma^i_{fg,z}\chi^i_{g',z}P^0_{g,g',z} - \Sigma^i_{f,g,z}\sum_{l=1}^{L}(2l+1)P^l_{g,g,z}\Bigg]$$

$$D = \frac{1}{k}\sum_{i=1}^{I}\sum_{z=1}^{R} V_z \sum_{g=1}^{G}\left(\bar{\nu}^i_{g,z}\Sigma^i_{f,g,z}\phi_{g,z}\right)\sum_{g=1}^{G}(\chi^i_{g',z}\phi^+_{g',z})$$

$$P^l_{g,g',z} = V_z \sum_j \phi^{+j}_{g',z}\phi^j_{g,z}$$

where,

$\phi_{g,z}$	is neutron flux of group g in region z,
$\phi^j_{g,z}$	is the j^{th} component flux moment of group g in region z,
$\phi^+_{g,z}$	is the neutron flux adjoint of group g in region z,
$\phi^{+j}_{g,z}$	is the j^{th} component adjoint flux moment of group g in region z,
l	is the Lengendre order corresponding to the j^{th} flux moment,
L	is the highest Legendre order of scattering,
I	is the total number of isotopes present,
G	is the total number of energy groups,
R	is the total number of spatial regions,

and,

V_z	is the volume of spatial region z

As shown above, explicit sensitivities are evaluated numerically as a function of forward/adjoint flux and nuclear data, but formulated from first principles. Implicit effects involve the perturbations that cross-sections have on one another through resonance self-shielding, and are computed through automatic differentiation. SCALE self-shielding modules were processed with the GRESS[27] automatic differentiation code which produced sensitivity versions of the self-shielding executables[39][40]. When called by the TSUNAMI sequence, the GRESS-enhanced self-shielding modules not only perform resonance shielding calculations on cross-sections but also record sensitivities of those shielded cross-sections with respect to its input parameters. Sensitivity versions of all the self-shielding modules were present in SCALE 5.1, but the most rigorous of the modules, CENTRMST[41] has subsequently been removed as of SCALE 6.0. The removal of CENTRMST from the TSUNAMI sequence was motivated by its unreasonably long execution time and computational resource consumption, as well as due to limitations in the automatic differentiation tool that produced CENTRMST from its non-sensitivity version[42].

2.1.2 SUSD3D

The code SUSD3D[43] is a sensitivity and uncertainty calculator that takes forward and adjoint flux solutions and produces the uncertainties of responses that arise from cross-section covariance. The flux solutions are supplied by one of several compatible deterministic transport codes including ANISN[44], DOT-3.5[45],

DANTSYS[46], DORT, and TORT[47]. Coupling between SUSD3D and the transport code DRAGON[48] is currently under development[24].

As with TSUNAMI, explicit sensitivities are formulated by first principles from the transport equation, and solved numerically as a function of flux and nuclear data. The explicit sensitivity formulation is described elsewhere[43, pp. 61-63], but a noteworthy characteristic of SUSD3D is that the nuclear data used to solve the explicit sensitivities is not necessarily the same nuclear data that was used by the coupled transport codes to compute the forward/adjoint flux. Rather than the coupled transport codes passing their microscopic cross-sections(which may not provide sufficient information to calculate explicit sensitivities) to SUSD3D, only the flux solutions are passed. SUSD3D then looks up cross-section data from an ENDL, using NJOY to create cross-sections of the same energy structure employed by the transport solver. This method will result in cross-sections that are identical to those used by the transport code only if the ENDL selection and NJOY parameters (e.g. weighting function, temperature, etc.) are consistent with those employed to create the transport code's multi-group library.

The SUSD3D package is capable of only calculating explicit sensitivities, and cannot account for implicit sensitivity components that arise through resonance self-shielding effects. ORNL has observed that the implicit sensitivity component can contribute up to 40% of the total k_∞ sensitivity[49].

2.1.3 XSUSA

The XSUSA[50] code is a statistical sampling code developed by Gesellschaft für Anlagen- und Reaktorsicherheit (GRS) and implemented with the SCALE code system. XSUSA samples self-shielded cross-sections and performs a single SCALE simulation for each sample, generating a collection of responses whose distribution can be subsequently measured. Because XSUSA samples cross-sections that are already self-shielded, implicit effects cannot be captured in the uncertainty propagation procedure. The number of samples taken, and hence the number of SCALE simulations executed is determined by the user's desired confidence level associated with the response uncertainties. XSUSA benefits from all the qualities of a statistical approach: the number of calculations is independent of the number of parameters and responses; all high-order perturbation effects are inherently captured in the analysis; and the uncertainty and covariances of all responses are trivially easy to calculate subsequent to performing the simulations. XSUSA facilitates uncertainty propagation for 1D, 2D and 3D models by invoking the appropriate SCALE transport solver that corresponds to each dimensionality.

GRS has reported good agreement between XSUSA and TSUNAMI in the context of pin cell simulations, and has also applied XSUSA beyond lattice physics, to core diffusion calculations. Uncertainties associated with homogenized, few-group cross-sections, diffusion coefficients and power distribution have all been calculated

for uranium and MOX test cases that have been reported in literature[51].

2.1.4 CASMO-5/DP

The Paul Scherrer Institute has developed a version of the CASMO-5 transport code[52] that implements a direct numerical perturbation strategy for sensitivity and uncertainty analysis. Without access to the proprietary CASMO-5 library format, multi-group constants could not be perturbed directly, thus PSI added routines to CASMO-5 that perform the perturbation after the multi-group constants are read from the library. The CASMO-5 library records multi-group constants for neutron total absorption and total scattering, but not partial cross-section components thereof such as capture $\left(\sigma_{\gamma}\right)$, alpha emission $\left(\sigma_{\alpha}\right)$, nor elastic or inelastic scattering $\left(\sigma_{n_o}\right.$ and $\left.\sigma_{\gamma n'}\right.$, respectively$\left.\right)$. The numerical perturbation routines of CASMO-5 therefore consult an ENDL, through NJOY, to estimate the proportions of partial cross-sections in order to establish their individual sensitivity contributions. Like XSUSA and SUSD3D, CASMO-5 direct numerical perturbation routines cannot account for implicit, self-shielding effects on the response sensitivities.

2.2 Themes in lattice sensitivity and uncertainty analysis

Themes emerge from current literature regarding the propagation of lattice uncertainties. These themes are not so much a result of the objectives of lattice uncertainty analysis, but more a product of the limitations of the analysis methods commonly employed for the task. This section brings attention to several trends of currently available lattice uncertainty toolsets.

Physics parameters are the only sources of uncertainty.

Lattice sensitivity and uncertainty tools are currently focused on propagating covariance of physics parameters (e.g. cross-sections, χ, $\bar{\nu}$) and neglect uncertainty associated with other model parameters including enrichment, material compositions, material temperatures, and geometry dimensions. The implicit assumption that physics parameters dominate the uncertainty in lattice outputs may indeed prove to be reasonable. However, without a comprehensive study of uncertainty contributions from all sources, it is impossible to conclusively demonstrate the validity of neglecting non-physics uncertainties.

Adjoint-based sensitivity and uncertainty analysis is particularly ill-suited to the propagation of geometry uncertainties, due to the complicated relationship between geometry and macroscopic cross-sections. Not only is the relationship non-linear, but also discontinuous. That is to say, smooth changes in a geometric parameter (e.g. the diameter of a fuel pin) do not result in a smooth change in macroscop cross-section, but rather a stepwise change.

While XSUSA and CASMO-5/DP employ uncertainty propagation methodologies that are fundamentally suitable to the propagation of all types of parameter uncertainties, it is not clear from published literature whether the treatment of modelling uncertainties are currently implemented in those codes. In general, analysis of the sensitivities and uncertainty contributions arising from modelling parameters compared to those of physics parameters is a subject not yet adequately addressed in the field of lattice physics.

Infinite-dilution covariances are applied directly to self-shielded cross-sections.

With the notable exception of TSUNAMI, implicit uncertainty contributions related to resonance self-shielding effects are ignored by lattice uncertainty tools. Equivalently, problem-independent covariance matrices that correspond to infinite-dilution cross-sections are applied to self-shielded cross-sections, without commensurate modification to the covariance. Addressing self-shielding effects on cross-section covariance is problematic for adjoint methods (hence TSUNAMI's use of automatic differentiation for that step), and also problematic even for statistical sampling and direct numerical perturbation methods depending on the resonance parameters that are used by the lattice code (as will be shown in chapter 3).

The evolution of lattice uncertainties with burnup is not commonly studied.

A comprehensive reactor uncertainty analysis must necessarily involve the variation of fuel properties with burnup. During burnup, the isotopic composition of reactor materials change as fission products, decay products and activation products are created, and as isotopes are subjected to fission and neutron capture. The change in material composition not only affects the fuel properties, but also the uncertainties associated with those properties, given that different isotopes do not share the same cross-section covariance matrix. Therefore, the consideration of burnup effects on lattice uncertainties is an essential component to any practical reactor uncertainty analysis.

It should be noted that burnup will cause variation in both explicit and implicit components of lattice output uncertainties. As isotopic concentrations change due to irradiation, a related change of their dilution occurs, and thus so does the degree to which their cross-sections are self-shielded.

Uncertainty associated with k_∞ has received the most attention.

Lattice uncertainty tools have historically focused on quantifying the uncertainty associated with the lattice multiplication constant, k_∞. However, k_∞ is not an especially important output of lattice physics calculations. The outputs of primary concern, and those that are used in ensuing reactor analysis (such as 3D core diffusion) are homogenized, few-group lattice cross-sections. In other words, quantifying the uncertainty of k_∞ is not particularly useful in facilitating subsequent uncertainty analysis of reactor core properties including: the core multiplication constant, k_{eff}; or three-dimensional

power distribution. The starting point to full-core uncertainty analysis must be the quantification of all lattice output uncertainties, especially homogenized, few-group cross-section covariance.

The capability to calculate these uncertainties of interest has only recently been added to the TSUNAMI-1D and TSUNAMI-2D sequences (as of SCALE 6.1). Few-group cross-section covariance calculation has been performed using XSUSA and reported in literature[51], and CASMO-5/DP was designed with this capability in mind. Therefore, in recent years the topic of few-group, homogenized cross-section covariance has had increasing attention, although currently the only toolset with the capability to quantify that covariance in three dimensions is XSUSA, coupled with the 3D Monte Carlo transport solver in SCALE.

Multi-group cross-section libraries are often ill-suited to lattice uncertainty analysis.

An equivalent statement can be that evaluated covariance matrices are often ill-suited to particular multi-group cross-section libraries. To propagate nuclear data uncertainties, the parameters for which there is a covariance matrix must exist on the multi-group library. In other words, the cross-section library and covariance library should involve a common set of parameters. However, partial cross-sections (such as (n, γ), (n, α), etc.) are often not stored on multi-group libraries because they are not individually necessary to solve the transport equation. Rather, it may be only aggregate cross-sections, such as (n, absorption) = (n, γ)+(n, α)+ . . . , that are stored there. If only aggregate cross-section parameters exist on the libraries, and if only partial cross-section parameters have covariance matrices, then information required to propagate uncertainties is missing – namely, the proportions by which the partial cross-section covariances should be applied to the aggregate cross-sections. It is due to this common occurrence that uncertainty tools such as SUSD3D and CASMO-5/DP consult ENDLs in addition to those used by their respective transport solvers; ENDLs contain the information that the multi-group libraries lack.

Choices for three-dimensional lattice uncertainty analysis are limited.

As most of the nuclear industry is concerned with LWR-type reactors that can be reasonably modelled by a two-dimensional geometry, uncertainty analysis tools have developed a similar focus. For example, TSUNAMI-3D, unlike its one and two-dimensional counterparts, lacks the capability to calculate covariance associated with homogenized, few-group cross-sections. Similarly, all uncertainty tools designed to be coupled to two-dimensional lattice solvers (e.g. CASMO-5), are limited to the same dimensionality.

For application to LWRs, the limitation of analysis tools to one or two dimensions is not a hindrance to the propagation of uncertainties. In the case of CANDU® reactors, however, three-dimensional modelling is a necessary component to lattice analysis[54][53], and, therefore, propagation of uncertainties for three-dimensional models is a necessary component to lattice uncertainty analysis.

2.3 Problem statement

The objectives of the work described in this dissertation were to develop a comprehensive lattice physics uncertainty and sensitivity analysis tool that is applicable to LWR and CANDU® reactors. The tool must: propagate all input parameter uncertainties; thoroughly treat implicit uncertainty effects of resonance self-shielding; calculate covariance of all lattice calculation outputs, including k_∞ and few-group, homogenized cross-sections; quantify the evolution of lattice uncertainties during burnup; and be applicable to two and three-dimensional nuclear systems.

Some currently existing tools can do some combinations of the lattice uncertainty analysis requirements listed above: TSUNAMI-3D can quantify k_∞ uncertainty and implicit effects, but not homogenized, few-group uncertainties; XSUSA can calculate homogenized, few-group uncertainties, but not account for implicit effects; etc. Similarly, no currently available tool has demonstrated the capability for treating modelling parameter uncertainties, nor the effects related to burnup, as detailed in the previous section.

This dissertation aims to achieve comprehensive lattice sensitivity and uncertainty analysis by accounting for all relevant effects in all relevant dimensionalities, coupled to DRAGON, a Canadian Industry Standard Tool (IST) best-estimate lattice solver proven for conducting safety analysis for CANDU® reactors.

Chapter 3

Methodology

Three methodologies have been adopted to perform the lattice physics uncertainty propagation described in this dissertation – statistical sampling, direct numerical perturbation, and adjoint sensitivity analysis. Uncertainty analysis by the first two methods was achieved by developing a set of new tools which add to the unique contribution of this dissertation. A primary focus in the development of the original tools of this dissertation was to capture all problem-dependent, implicit uncertainty effects that arise through resonance self-shielding. Recall from chapter 2 that difficulties related to quantifying self-shielding effects in lattice uncertainty propagation leads to these effects being neglected by most currently available tools. This chapter presents a detailed overview of the implementations of the statistical sampling and direct numerical perturbation tools developed in this work, include a comprehensive description of their capabilities and any simplifying assumptions that were employed. Adjoint-based sensitivity and uncertainty analysis was performed using the TSUNAMI code to provide a benchmark of the quantified output uncertainties.

The basis of the implemented statistical sampling method is to treat all uncertain values as dependent random variables by sampling them according to a multi-variate probability density function (PDF). For each randomly sampled set of inputs, there exists a corresponding set of outputs which are the solution to the lattice physics equations acting on the the input sample. Inputs can be randomly sampled either one at a time, in groups, or all at once.

The implementation of the direct numerical perturbation method involves calculating partial derivatives of outputs with respect to each input of concern one at a time, and uncertainty propagation is performed using the *sandwich rule*. The direct perturbation method offers is more computationally demanding than the statistical sampling method, but offers additional information of value, namely sensitivity coefficients and rank of importance corresponding to each input parameter.

Computer codes have been developed in this work to propagate lattice physics uncertainties in conjunction with two best-estimate lattice physics solvers. SCALE-Statistical Sampling (SCALE-SS) was a preliminary implementation of the

statistical sampling methodology with the lattice physics solvers of the SCALE Code System[32] developed by Oak Ridge National Laboratory (ORNL). The purpose of developing SCALE-SS was to have a vehicle for propagating uncertainties of both one and two-dimensional system that could be directly compared to TSUNAMI[30], which is the native nuclear data uncertainty analysis module of SCALE that is based on an adjoint-based sensitivity approach. The SCALE-SS code developed in this work calculates uncertainties associated with k_∞ and determines the contribution to that uncertainty resulting from each uncertain input. The code has a limited number of features and capabilities and served primarily as a feasibility exercise in propagating uncertainties using a stochastic method comparable against a validated and widely accepted adjoint tool.

DRAGON Implementations of Numerical Or Statistical Analysis of Uncertainties in Reactors (DINOSAUR) was developed in this work to propagate uncertainties of both nuclear data and problem-dependent model data through lattice calculations performed by the solver DRAGON[48]. Uncertainties are propagated through all stages of the calculation including resonance self-shielding, multi-group neutron transport solution, and flux- or volume-weighted homogenization. Both statistical sampling and direct numerical perturbation methods for performing uncertainty analysis can be performed using DINOSAUR. The code generates uncertainties associated with predictions of k_∞, spatially-varying multi-group neutron flux, and few-group homogenized neutron flux and cross-sections. The relative contributions to output uncertainties arising from each uncertain input can be established, in addition to first-order partial derivatives and sensitivity coefficients of output variables with respect to various inputs.

3.1 Statistical sampling

When statistically sampling lattice physics inputs such as neutron interaction cross-sections, each input is treated as a dependent random variable. Random implies that the variables can take on different values according to a PDF, while their dependency requires that values of some variables cannot be generated without regard to those of other variables. The first two statistical moments (mean and variance/co-variance) of the variable PDFs must be known to perform the statistical sampling uncertainty propagation; higher-order moments can be assumed when not given. For simple lattice systems consisting of a single fuel pin and moderator, the number of nuclear data inputs is large. The value of each cross-section (e.g. (n, g), (n, 2n)) or reaction parameter (e.g. $\bar{\nu}$, χ) in every energy group for every nuclide is treated as a random variable. For pin cells consisting of a modest number of nuclides, each with several multi-group reaction properties of interest, the random variables used in the lattice calculation can number in the tens of thousands. That number further increases for larger systems such as fuel bundles or assemblies, which contain additional nuclides. The *input vector* of length n, which is defined in this text as a vector consisting of

all the input variables for a particular system, has a corresponding $n \times n$ variance-covariance matrix that describes the uncertainty associated with each element of the input vector, as well as the correlations that exists between elements. By definition, the covariance matrix consists of the second statistical moment of the random variables, and the first moment is taken to be the *reference* input vector, which is stored on the unperturbed nuclear data library used as an input when calculating the best-estimate lattice solution.

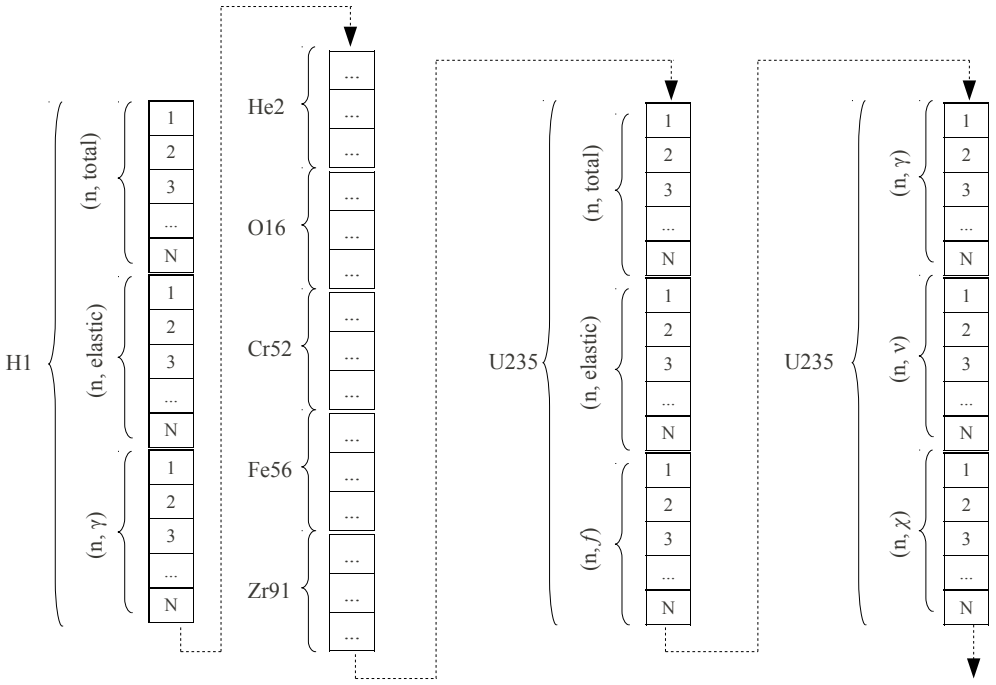

Figure 3.1: A partial input vector, with N enegy groups

Figure 3.1 shows part of a lattice physics input vector, similar to those which are commonly encountered in LWR and CANDU lattice cells. While figure 3.1 shows neutron cross-sections discretized into N energy groups, input vectors typically include additional nuclear data which is not shown, such as resonance parameters and tables describing group-to-group scattering, as well as the listing of certain data several times corresponding to various temperatures. Because multi-group nuclear data libraries are designed to be problem-independent with a wide range of applicability, they generally contain far more data than is needed for any one particular lattice calculation. Problem-dependent inputs to lattice calculations are supplied by the user in a file known as an *input deck* that generally consists of non-nuclear properties, such as mixture compositions, geometry and temperature of materials.

Although the covariance matrix for the input vector is large, many of its elements are zero. Variables in the input vector associated with the zero values of

the covariance matrix needn't be included in the sampling procedure, since even an infinite number of samples of such a variable would produce no value other than the reference value. For the variables that remain – those with non-zero covariance – rather than generating new vectors directly from their PDFs, the approach of this work was to statistically compute vectors of *perturbation factors*, that when multiplied by the reference input vector will produce a population of vectors whose mean is equal to the reference and whose elements have dependencies as given by the covariance matrix.

When generating values of several dependent random variables according to a covariance matrix, their mutual dependencies demand that they be generated simultaneously in vector form rather than one at a time. A procedure for generating vectors of dependent random variables consistent with a given covariance matrix involves performing a spectral (eigenvalue) decomposition of the matrix.

$$\mathbf{\Sigma} = \mathbf{V} \times \mathbf{D} \times \mathbf{V}^T \tag{3.1.1}$$

The matrix of absolute covariance, $\mathbf{\Sigma}$, in equation (3.1.1) is decomposed into the product of three matrices, where $\mathbf{V}$ is a matrix whose columns are eigenvectors of $\mathbf{\Sigma}$, and $\mathbf{D}$ is a diagonal matrix of eigenvalues that correspond to the eigenvectors in $\mathbf{V}$. The $\mathbf{\Sigma}^{1/2}$ matrix is defined as:

$$\mathbf{\Sigma}^{1/2} = \mathbf{V} \times \mathbf{D}^{1/2} \times \mathbf{V}^T \tag{3.1.2}$$

where $\mathbf{D}^{1/2}$ is a diagonal matrix whose elements are the roots of the elements in $\mathbf{D}$. Generating a vector, $\mathbf{G}$, of n normally distributed dependent random variables, $\mathbf{G} = [x_1, x_2, \ldots, x_n]^T$, with means $\boldsymbol{\mu} = [\mu_1, \mu_2, \ldots, \mu_n]^T$ and covariance defined by $\mathbf{\Sigma}$ can be achieved as shown below.

$$\mathbf{G}(\boldsymbol{\mu}, \mathbf{\Sigma}) = \mathbf{\Sigma}^{1/2}\mathbf{G}(0, 1) + \boldsymbol{\mu} \tag{3.1.3}$$

$\mathbf{G}(0, 1)$ is a vector of n independent, normally-distributed random variables, each with a mean of zero and standard deviation of one. Note that the above formulation of equations (3.1.1) through (3.1.3) involves $\mathbf{\Sigma}$, an absolute covariance matrix, rather than the typical evaluation of nuclear data uncertainties which is by relative covariance. Therefore, directly generating random vectors of nuclear data would first involve the calculation of absolute covariance by the multiplication of an evaluated relative covariance matrix with a set of means, or reference values, of the nuclear data. This method leads to several practical inconveniences. Firstly, the matrix decomposition procedure would be intimately tied to the reference values of the inputs to be randomly sampled; if one wished to re-evaluate lattice physics uncertainties based on new reference values (i.e. ENDF vs. JEFF vs. JENDL), the covariance decomposition would need to be performed again. In other words, the calculated $\mathbf{\Sigma}^{1/2}$ matrix is not cross-compatible between different nuclear libraries by virtue of their potentially inconsistent reference data. Secondly, even when concerned with a

single nuclear library, some data have more than one reference value. An example is a neutron cross-section whose reference value is temperature-dependent, which is generally the case. For such data, the matrix decomposition in equation (3.1.1) must be performed once for each set of reference data (e.g. for each temperature), resulting in a list of $\mathbf{\Sigma}^{1/2}$ matrices that must be applied selectively against the different reference values of the data.

The method of generating vectors of perturbation factors rather than generating new input vectors directly alleviates the practical issues described above. The procedure for generating perturbation factors is as follows. Equations (3.1.1) and (3.1.2) are calculated similarly, but with the substitution of a relative covariance matrix, $\mathbf{\Sigma}_r$ in the place of the absolute covariance $\mathbf{\Sigma}$, ultimately resulting in a matrix $\mathbf{\Sigma}_r^{1/2}$. The $\mathbf{\Sigma}_r^{1/2}$ matrix is identical to the matrix $\mathbf{\Sigma}^{1/2}$ if and only if all of the variable reference values are equal to unity. Next, a vector of perturbation factors $\mathbf{P} = [p_1, p_1, \ldots, p_n]^T$ can be found.

$$\mathbf{P} = \mathbf{\Sigma}^{1/2}\mathbf{G}(0,1) + [1.0, 1.0, \ldots, 1.0]^T \tag{3.1.4}$$

Once again, $\mathbf{G}(0,1)$ is a vector of n independent, normally-distributed random variables, each with a mean of zero and standard deviation of one. Therefore, $\mathbf{P} \equiv \mathbf{G}(1, \mathbf{\Sigma})$. The calculation of perturbation factors is entirely independent of the reference values of the random data, and can be computed and stored even if the reference data is unknown. Therefore, the decomposition of covariance is de-coupled from the underlying nuclear library of reference values. The nuclear data can be subsequently randomly sampled by using the precomputed perturbation factors in combination with a particular set of reference values, $\boldsymbol{\mu} = [\mu_1, \mu_2, \ldots, \mu_n]^T$.

$$\mathbf{G}(\boldsymbol{\mu}, \mathbf{\Sigma}) = \mathbf{P}^T\boldsymbol{\mu} \tag{3.1.5}$$

The method for generating input vectors using perturbation factors is essentially identical to using equations (3.1.1) through (3.1.3) to generate input vectors on data with assumed reference values of unity, and later scaling those vectors by the data's true reference values, $\boldsymbol{\mu}$. Once a new input vector has been randomly generated using either equation (3.1.5) or equation (3.1.3), its values must over-write and replace the reference values of the multi-group nuclear data library accessed by the lattice solver. In the case of SCALE, the multi-group library used in this work is the *AMPX*-format *"44GROUPNDF5"* library in 44 energy groups, and in the case of DRAGON the 69-group library is of a *WIMS-D* format. When the reference values of the multi-group reference library have been replaced with their randomly generated counterparts, the lattice physics equations will be solved using the perturbed data as inputs, resulting in a set of outputs that correspond to the new input data set. The uncertainty of an output response is then quantified from first-principles by the calculation of the variance of its sample set. Covariance between output responses can be calculated from first-principles using equation (1.4.1).

Therefore, the method of propagating uncertainties described in this dissertation is as independent as possible from the internal behaviour of the lattice physics codes, and only requires information regarding the format of the lattice code's multi-group nuclear library. The generating of perturbed *WIMS-D* format libraries can just as easily be used to propagate uncertainties with other lattice codes as it can with DRAGON, granting that the other lattice codes are themselves compatible with the *WIMS-D* library format. Likewise, SCALE-SS was used to propagate input uncertainties using two lattice solvers that were each compatible with the *AMPX*-format *44GROUPNDF5* library - XSDRNPM[33] and NEWT[37]. They both are lattice solvers in the SCALE Code System; XSDRNPM solves the neutron transport equation in one dimension and NEWT solves it in two. The same set of perturbed *44GROUPNDF5* libraries were used to propagate uncertainties through both codes' lattice calculations with no additional modifications or extensions required. In other words, the uncertainty analysis tools are library-dependent, but independent of the lattice solver.

As an example, consider the 69-group radiative capture cross-section, (n γ), of Pu^{239}, whose reference values are shown in figure 3.2a. A set of 256 perturbation factors, each of 69 groups, were generated using equation (3.1.4). Those factors were then used in combination with the Pu^{239} (n, γ) covariance matrix shown in figure 3.3 to calculate samples of the cross-section according to equation (3.1.5), which are shown in figure 3.2b.

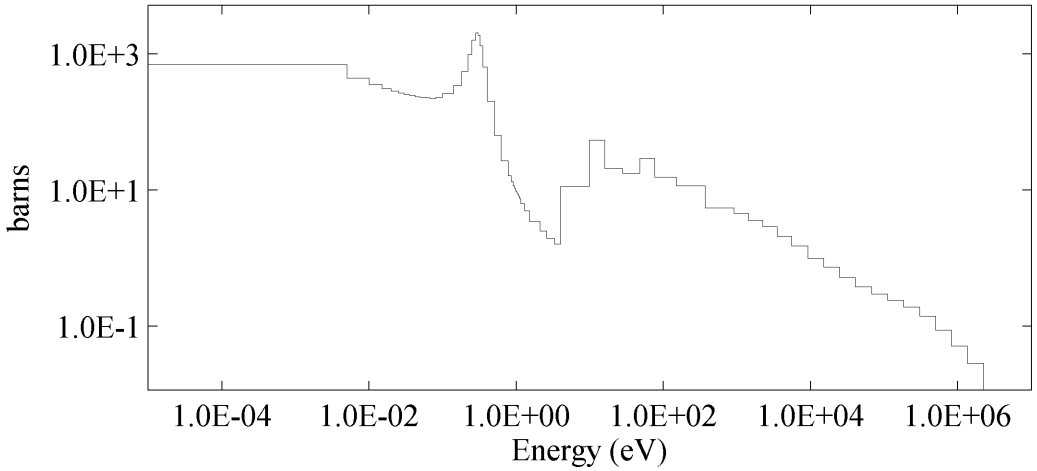

(a) reference

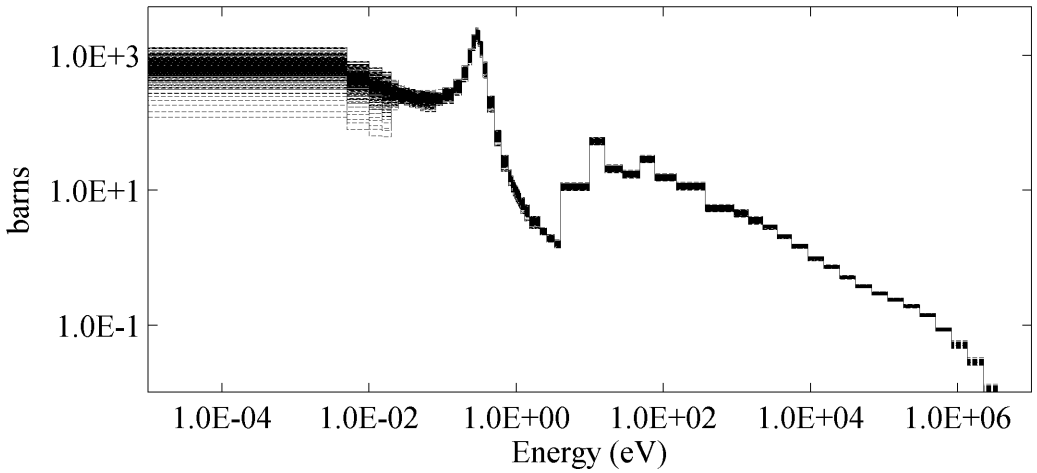

(b) 256 statistical samples

Figure 3.2: Pu^{239} (n, γ) cross-section

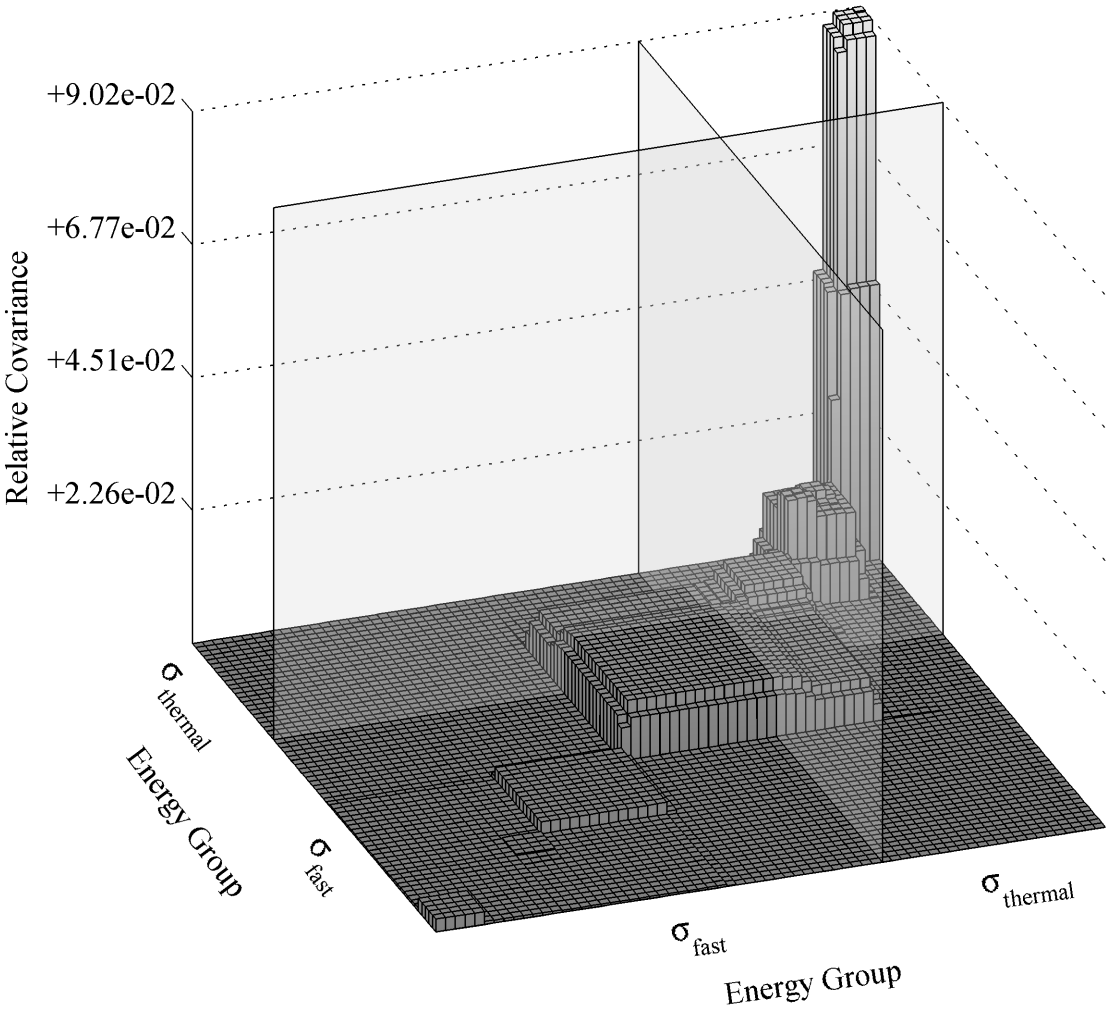

Figure 3.3: Pu^{239} (n, γ) 69-group relative covariance matrix

3.1.1 Covariance decomposition

The random generation of input vectors having a given covariance invariably involves an eigenvalue decomposition of the covariance matrix. Since the decomposition forms the basis for randomly generating all input vectors, precise determination of the matrix's eigenvectors and eigenvalues is of critical importance. The algorithm used in this work to decompose covariance matrices is based on the Jacobi Rotation method, working to machine precision (iterations cease when all double-precision, off-diagonal elements underflow to zero). The Jacobi Rotation method is applicable to any symmetric matrix, and the motivation for its use in this work is subsequently described in this section.

Note that when generating real-valued input vectors or perturbation factors, equation (3.1.2) requires that the eigenvalues of the covariance matrix be non-negative. Since, by definition, a covariance matrix must be both symmetric and positive-semidefinite[55], its eigenvalues must always be positive or zero. However, in practice, a covariance matrix may fail the positive-semidefinite test and negative eigenvalues can arise through two mechanisms. Firstly, covariance matrices may lose their positive semi-definite characteristic during linear interpolation to a new energy group structure, a process which can also cause them to become non-symmetric. Secondly, numerical eigenvalue decomposition algorithms may produce negative eigenvalues even when working on positive semi-definite matrices, as a result of numerical precision limitations. In both cases, what should be small, non-negative eigenvalues may be incorrectly identified as small (in absolute value), negative eigenvalues. Similarly, zero-valued eigenvalues may be calculated as being small, positive eigenvalues. The potential calculation of negative eigenvalues of a matrix that, by definition, should be positive semi-definite demands one or more of the following actions: pre-process the covariance matrix thereby forcing it to be positive-semidefinite and symmetric; or post-process the decomposition of the covariance by substituting negative eigenvalues with zeros. The latter strategy is essentially equivalent to *retroactively* forcing positive semidefiniteness on the covariance matrix by adjusting its spectral components rather the covariance matrix directly.

A matrix can be pre-processed to guarantee positive semidefiniteness by scaling the elements of the matrix in a reasonable way until the negative eigenvalues vanish. For example, a *diagonally dominant* symmetric matrix with non-negative diagonal elements is necessarily positive semidefinite[56]. Diagonal dominance requires that in any row, the diagonal element is not less than the sum of the absolute values of all other elements in the row. This property equally applies to the columns of a covariance matrix as a result of its symmetry.

$$\text{For a diagonally-dominant matrix, } \mathbf{A}\text{: } A_{i,i} >= \sum_{j \neq i} A_{i,j} \quad \forall \quad i \tag{3.1.6}$$

A matrix can be adjusted to guarantee positive semidefiniteness by utilizing the property of diagonal dominance and appropriately scaling diagonal or off-diagonal

elements so that equation (3.1.6) is satisfied. For nuclear data, typically the variance of variables (diagonal entries) carries more significant uncertainty information than the co-variance (off-diagonal entries). Therefore, down-scaling off-diagonal elements of the covariance to satisfy equation (3.1.6) is preferable to up-scaling the diagonal elements. Once a matrix has been processed in this way and is necessarily positive-semidefinite, a more specialized eigenvalue algorithm, such as the Cholesky decomposition, can be performed. In the work presented in this thesis, covariance matrices pre-processed for symmetry (as shown in figure 3.4), and post-processed for positive-semidefiniteness. The rational behind this approach is that even when pre-processed for positive-semidefiniteness, negative eigenvalues can still sometimes appear due to the numerical precision of decomposition algorithms, and therefore a rejection of tiny, negative eigenvalues could still be necessary despite the pre-processing.

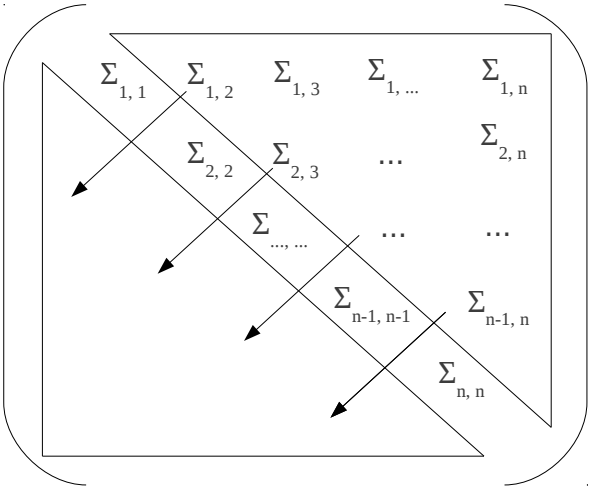

Figure 3.4: Forcing the symmetry of a covariance matrix

Because this work does not pre-process covariance matrices to ensure a positive-semidefinite condition, a more general eigenvalue decomposition algorithm than Cholesky was adopted. The Jacobi Rotation algorithm requires only that the target matrix be symmetric, and will solve for negative eigenvalues if they exist. A simple post-processing operation is subsequently performed that sets all negative eigenvalues to zero, to avoid imaginary components from appearing in $\mathbf{\Sigma}_r^{1/2}$.

Table 3.1 shows the Jacobi-calculated eigenvalues of the U^{238} (n, γ) covariance matrix in 69 energy groups. Of the 69 eigenvalues, 24 are negative, but small in magnitude; the largest (absolute value) negative eigenvalue is six orders of magnitude smaller than the dominant (largest magnitude) eigenvalue. In this case, the covariance decomposition post-processing routines of DINOSAUR would replace the 24 negative eigenvalues with zeros.

1.90E-01	1.38E-05	8.46E-10	3.54E-20	-2.18E-10
9.98E-02	4.94E-06	6.26E-10	2.67E-20	-5.25E-10
3.94E-02	1.41E-07	3.75E-10	4.38E-22	-5.94E-10
2.65E-02	6.86E-08	2.87E-10	-9.40E-22	-1.61E-09
1.26E-02	3.64E-08	1.97E-10	-9.16E-21	-2.83E-09
5.37E-03	2.53E-08	6.52E-11	-1.35E-20	-4.57E-09
5.01E-03	2.07E-08	5.94E-12	-2.30E-20	-8.12E-09
2.20E-03	1.46E-08	1.40E-19	-3.15E-20	-9.83E-09
1.42E-03	1.18E-08	1.14E-19	-8.16E-20	-1.19E-08
5.92E-04	1.02E-08	1.04E-19	-1.51E-19	-1.90E-08
3.83E-04	6.97E-09	6.57E-20	-1.69E-19	-3.16E-08
2.31E-04	4.83E-09	4.99E-20	-7.79E-12	-3.65E-08
1.43E-04	3.50E-09	4.95E-20	-1.25E-10	-1.12E-07
6.71E-05	1.34E-09	4.91E-20	-1.59E-10	

Table 3.1: U^{238} (n, γ) covariance matrix eigenvalues

3.2 Direct numerical perturbation

Direct numerical perturbation of an input value is used to calculate a first-order estimate of the partial derivatives of output variables with respect to the perturbed input. When the partial derivatives of an output with respect to its inputs are known, the covariance propagation can be performed by the sandwich rule. Implemented in DINOSAUR, the direct numerical perturbation method produces information otherwise unavailable by conducting a statistical sampling, such the partial derivative and sensitivity coefficient of k_∞ with respect to a particular cross-section in a particular energy group. The compilation of sensitivity coefficients against all inputs facilitates a more thorough analysis of the propagation of their uncertainties. The basis of the direct numerical perturbation used in this work is the first-order estimation of partial derivatives as shown below,

$$f'(x) \approx \frac{f(x + \Delta x) - f(x)}{\Delta x} \tag{3.2.1}$$

A small perturbation is made by DINOSAUR on a variable, for example the g_{th} energy group of a cross-section σ belonging to some nuclide, denoted as σ_g, by multiplying it by a scaling factor $1 + \delta$, where ideally $\delta \ll 1$. The output of interest, k_∞, is a function of the variable, and hence can be written as $k(\sigma_g)$. When acting on the perturbed $\sigma_g + \delta\sigma_g$, the function output will also be perturbed from $k(\sigma_g)$ to $k(\sigma_g(1 + \delta))$. Therefore, the first-order estimate of the partial derivative of k_∞ with respect to σ_g is:

$$\frac{\partial k(\sigma_g)}{\partial \sigma_g} = \frac{k(\sigma_g(1 + \delta)) - k(\sigma_g)}{\delta\sigma_g} \tag{3.2.2}$$

While the first-order estimate of the partial derivative grows more accurate with a smaller perturbation, δ, there is a practical constraint imposed on the size of the

perturbation by the numerical reality of the lattice solver DRAGON. The response, k_∞, is calculated by DRAGON to a (default) precision of six decimal places, which consequently demands a minimum perturbation on σ_g such that the perturbed value of k_∞ is distinguishable from the unperturbed value by at least two decimal places so that the difference can be reasonably quantified. Equivalently, a nuclear datum should be perturbed to a degree no less than what is required to produce a change in reactivity of at least 0.01 mk for the lattice model under investigation. Applied to input variables with especially low sensitivity as it relates to k_∞, the perturbation demanded by numerical considerations may be so large as to no longer result in a suitable estimation of the partial derivative about the unperturbed value.

If a covariance matrix is supplied, DINOSAUR calculates the uncertainty associated with k_∞ using the sandwich rule shown in equation (3.2.3).

$$\Delta^2 k = S \times COV \times S^T \tag{3.2.3}$$

where S is a row vector of partial derivates of k_∞ with respect to each input, and COV is a covariance matrix associated with the inputs in S.

In addition to calculating the partial derivatives of k_∞ with respect to input cross-sections (and parameters $\bar{\nu}$ and χ) and associated uncertainties, DINOSAUR routines also compute dimensionless sensitivity coefficients, which indicate the ratio of relative change in output to the relative change in input. Given that different input cross-sections can vary by six or more orders of magnitude, an absolute perturbation of 1 barn may be a significant change for some inputs but be trivial for others. The dimensionless sensitivity coefficient, as defined in equation (3.2.4), is a more reasonable metric for comparing sensitivities with respect to inputs whose reference values show such a dissimilarity in magnitude.

$$S_{x_g} = \frac{\partial k/k}{\partial \sigma_{x_g}/\sigma_{x_g}} \tag{3.2.4}$$

Discrete energy groups are not, in general, of equal width. For example, the first (highest energy) group of the *WIMS-D*-format *IAEA* library spans an interval from 10 MeV to 6 MeV, whereas the last (lowest energy) group has a width that is nearly one-billion times smaller, ranging from 5 meV to 10 μeV. It is reasonable to conclude that cross-sections of some energy groups have greater influence on k_∞ than others, thereby producing higher sensitivities, merely as a result of the relative widths of the groups in which they reside, and their occupying vastly different fractions of the available energy spectrum. A modified sensitivity parameter, sensitivity per unit lethargy, S_L, removes biases in sensitivity coefficients and discontinuities in energy-dependent sensitivity profiles that arise solely due to energy group widths.

$$S_{L,x_g} = \frac{S_{x_g}}{\mu_g^- - \mu_g^+} = \frac{S_{x_g}}{log(E_g^+/E_g^-)} \tag{3.2.5}$$

where lethargy, μ that corresponds to energy, E, is,

$$\mu(E) = log\left(\frac{E_o}{E}\right) \tag{3.2.6}$$

where E_o is the largest neutron energy of interest in the system, usually taken to be 20 MeV. In equation (3.2.5), μ_g^-, μ_g^+, E_g^- and E_g^+ are the lower and upper lethargy and energy boundaries of group g, respectively.

Unlike the statistical sampling method, by which multiple inputs can be sampled simultaneously, the calculation of partial derivatives and sensitivity coefficients must be performed on one input variable at a time. This implies solving the lattice physics equations N times for each cross-section, where N is the number of energy groups. For light water reactor fuel cells, there are twenty or more cross-sections of primary importance, which, when discretized into sixty-nine energy groups, requires nearly fourteen-hundred solutions of the lattice equations, each working on a set of inputs that includes a single perturbed variable. DINOSAUR co-ordinates the perturbation of each variable with an associated solution of the lattice equations by DRAGON, and subsequently determines partial derivatives and sensitivity coefficients by scanning the appropriate DRAGON output files for the resultant change in k_∞.

A useful benefit of the numerical perturbation method is that virtually all of the computation effort involved is in the calculation of partial derivatives, and very little effort is needed in propagating covariance using the sandwich rule. Therefore, recalculating output covariance based on new input covariances is a trivial task; one must merely resolve the sandwich equation using the same partial derivatives. This is in contrast to the statistical sampling approach, which is strongly tied to the input covariance from the very beginning of the analysis.

3.3 Generating nuclear data libraries

Through either statistical sampling or numerical perturbation, the uncertainty analysis performed in this dissertation requires the creation of nuclear data libraries, which are copies of a reference library with the exception of some values which have been strategically changed. When some data in a library is modified, additional steps must be taken to ensure that the new library is physically appropriate and its data, when taken as a whole, is self-consistent. Some variables are subject to inherent limitations on their possible ranges of variation, either individually or as a group. As examples, neutron interaction cross-sections cannot in reality be negative, and nor can the integrated spectrum of fission neutron energies vary from unity. However, considerations regarding the range of possible values taken by variables is not all that is required to produce a sensible library. A library's collection of variables generally possesses interdependencies and redundant information, such that the change in one variable demands changes in other variables to achieve library self-consistency. A nonphysical or inconsistent library has the potential to cause unpredictable behaviour by the

lattice physics code which is using the library as source of inputs, leading to numerical convergence failure, program crashes, or incorrect solutions. Therefore, lattice physics uncertainty analysis codes must follow a set of consistency rules that regulate the changes made to nuclear data.

3.3.1 Consistency requirements

Total vs. Constituent Data Consistency

Neutron cross-sections can be categorized as being either fundamental[1] cross-sections, which correspond to a particular nuclear reaction, or as aggregate cross-sections, which are the sum of multiple fundamental cross-sections, that generally describe broad mechanisms of neutron loss or production. Fundamental cross-sections include those of the (n, γ) reaction, (n, fission), (n, α), (n, 2n) and others. An example of an aggregate cross-section is (n, total), which describes the total probability of any neutron interaction of any type occurring, or (n, absorb), which is the sum of all reaction cross-sections in which the incident neutron is absorbed by the target nucleus. Naturally, aggregate cross-sections depend on the magnitudes of their constituent components, so if a perturbation is performed on (n, γ), a correction is warranted on both (n, total) and (n, absorb) belonging to the same nuclide.

Scattering Table vs. Scattering Vector Consistency

Nuclear scattering reactions, both elastic and inelastic, are not fully described by multi-group cross-sections alone. Accordingly, libraries also commonly store the energy and angular characteristics of the scattered neutrons in tables of values that are distinct from the multi-group scattering cross-section. While the group cross-section represents the likelihood of such scattering reaction taking place, the tables, referred to as *scattering tables*, describe in more detail the properties of the scattered neutron. Therefore, when making changes to a scattering group cross-section, its associated data tables require adjustment for the sake of consistency.

Table 3.2 shows a representation of a generic group-to-group scattering table, with entries $\sigma_{i\to j}$, that describe the probability of a neutron with incident energy, i, being scattered to group j. If the terms in the scattering table are in units of area (i.e. barns), then the sum across a row is equal to the appropriate group cross-section, as in equation (3.3.1).

$$\sigma_i^S = \sum_{j=1}^{N} \sigma_{i\to j} \tag{3.3.1}$$

[1]Despite the term 'partial cross-section' being widely used, the term 'fundamental cross-section' is chosen for this text to avoid confusion between partial cross-sections and partial derivatives.

	Out-group				
	1	2	3	...	N
In-group					
1	$\sigma_{1\to1}$	$\sigma_{1\to2}$	$\sigma_{1\to3}$	...	$\sigma_{1\to N}$
2	$\sigma_{2\to1}$	$\sigma_{2\to2}$	$\sigma_{2\to3}$	...	$\sigma_{2\to N}$
⋮					
N	$\sigma_{N\to1}$	$\sigma_{N\to2}$	$\sigma_{N\to3}$	...	$\sigma_{N\to N}$

Table 3.2: Group-to-group scattering table

When only multi-group uncertainties are known, an assumption must be made regarding how that uncertainty is allocated between each component of the scattering table. The most reasonable treatment in the absence of more detailed uncertainty information is to assume that the uncertainty is primarily associated with a scattering reaction taking place, and not with the distribution of neutron energy post-scattering. Essentially, this is equivalent to assuming full correlation between the each column of every row of the scattering table. Therefore, given a perturbation to a nuclide's scattering cross-section in group i, the scattering table is subject to the following correction:

$$\begin{aligned} \sigma_i^S &\to (1+\delta)\sigma_i^S \\ \sigma_{i\to j} &\to (1+\delta)\sigma_{i\to j} \quad \forall j \end{aligned}$$

Other Consistency Requirements

There are many additional requirements for consistency that depend on the specific collection of data on a library and how that data is represented. Library-specific consistency requirements are described in detail in sections 3.4.3 and 3.5.3.

3.4 SCALE-SS

The set of tools designated as SCALE-SS were developed as part of this dissertation to calculate the uncertainty associated with k_{eff} when solved using the SCALE Code System. SCALE-SS uses a statistical sampling technique to generate a collection of new nuclear data libraries that are identical in structure to a reference library used by SCALE but with modified data. An objective of SCALE-SS was to properly propagate nuclear data uncertainties through all stages of a lattice physics calculation, including resonance self-shielding.

The SCALE Code System contains a collection of routines and modules for performing nuclear analysis, including lattice calculations. A description of SCALE

lattice components and modules is shown in table 3.3, and a program flow diagram of a SCALE lattice calculation sequence in figure 3.5. Other SCALE lattice modules that perform the calculation using alternate techniques, such as CENTRM/PMC/WORKER in place of NITAWL, are not described in this section and were not exploited by SCALE-SS.

Item	Description
44GROUPNDF5	Problem independent, 44-group cross-section library
MIPLIB	SCALE routines for producing problem-dependent library containing only the nuclides of relevance
ft11f001	AMPX master library containing only nuclides of relevance
BONAMI	SCALE self-shielding for unresolved resonances via the Bondarenko method
NITAWL	SCALE self-shielding for resolved resonances via a Nordheim Integral Treatment
ft04f001	AMPX working library containing region-specific, self-shielded cross-sections
XSDRNPM	SCALE 1-D discrete-ordinates transport solver
NEWT	SCALE 2-D discrete-ordinates transport solver

Table 3.3: SCALE lattice sequence component description

The statistical sampling uncertainty tool for SCALE that was developed as part of this work was intended to serve as a basis for comparison with TSUNAMI-1D. Therefore, the functionality of SCALE-SS and TSUNAMI-1D are similar - multi-group nuclear data uncertainties are propagated through resonance self-shielding and neutron transport calculations, resulting in a quantification of uncertainty associated with k_∞. SCALE-SS was also designed, however, to allow a much broader set of problem-dependent uncertainties to be addressed, in many cases for variables not easily adoptable in adjoint methods.

The nuclear data covariance matrix which described input uncertainties was *44GROUPV6REC*, an uncertainty library evaluated by ORNL and adopted by the OECD/NEA as the UAM benchmark covariance matrix at the time of the development of SCALE-SS. It contains uncertainty information for a wide range of nuclear data belonging to over 300 nuclides, in a 44 energy group structure. The 44-group structure of the covariance file is the same as SCALE's 44-group cross-section library,

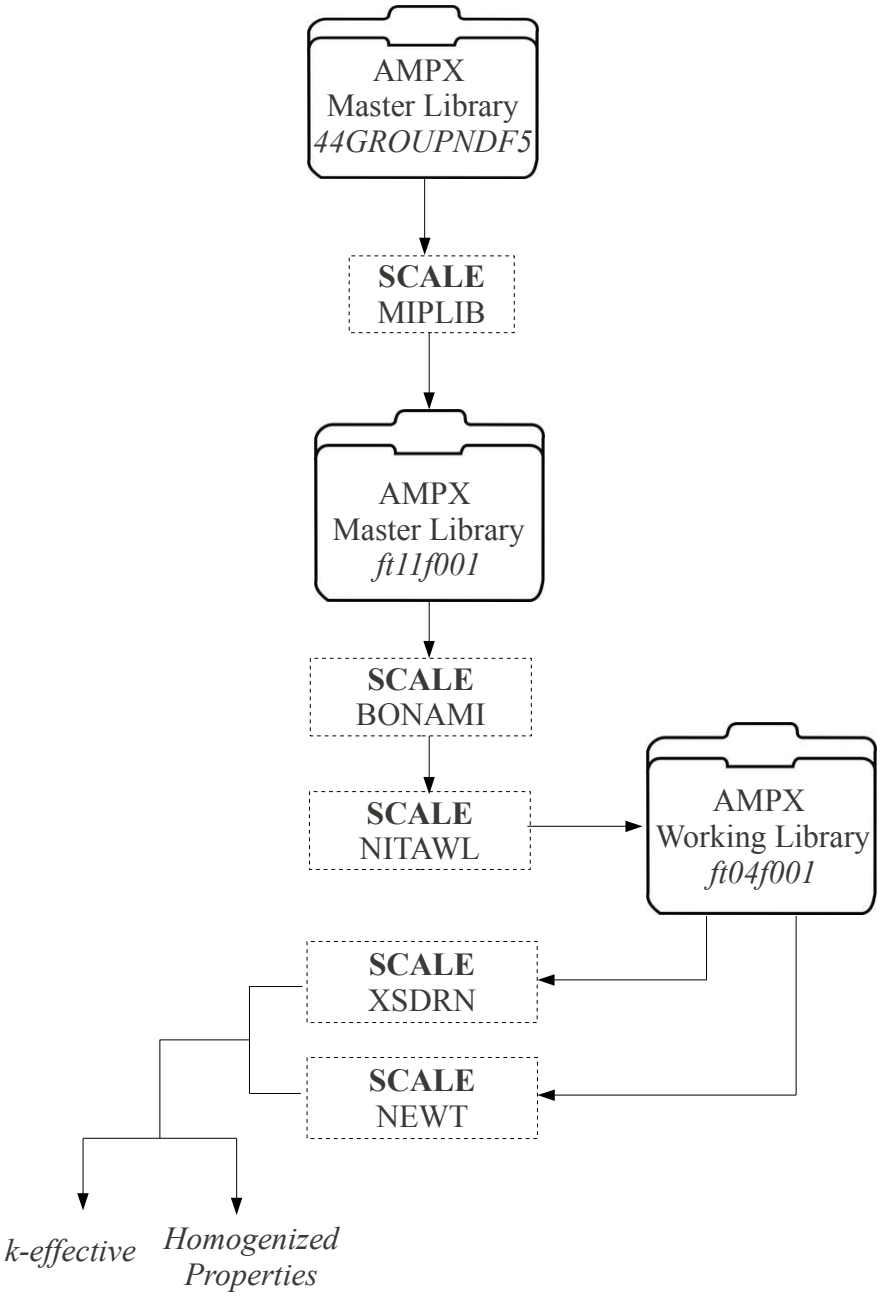

Figure 3.5: SCALE lattice calculation sequence

44GROUPNDF5, which is based on the ENDF/B-V nuclear data evaluation. This multi-group cross-section library was used as the reference values for the statistical sampling of input variables by SCALE-SS.

3.4.1 AMPX-format 44GROUPNDF5 library

The *44GROUPNDF5* library was developed by ORNL and is recommended only for fully-moderated LWR systems. It contains cross-sections and nuclear parameters for all nuclides of the ENDF/B-V[2] data files. Collapsed from a 238-group parent library, *238GROUPNDF5*, it has the same 44 energy group structure (see table 3.4) as the employed covariance library, *44GROUPV6REC*. No interpolations, extensions or modifications of the covariance are necessary for uncertainty propagation using this 44-group library, as each group covariance can be applied on a one-to-one basis to the library cross-sections.

Group	Upper energy limit (eV)	Group	Upper energy limit(eV)
1	2.00E+007	24	1.77E+000
2	8.19E+006	25	1.00E+000
3	6.43E+006	26	6.25E-001
4	4.80E+006	27	4.00E-001
5	3.00E+006	28	3.75E-001
6	2.48E+006	29	3.50E-001
7	2.35E+006	30	3.25E-001
8	1.85E+006	31	2.75E-001
9	1.40E+006	32	2.50E-001
10	9.00E+005	33	2.25E-001
11	4.00E+005	34	2.00E-001
12	1.00E+005	35	1.50E-001
13	2.50E+004	36	1.00E-001
14	1.70E+004	37	7.00E-002
15	3.00E+003	38	5.00E-002
16	5.50E+002	39	4.00E-002
17	1.00E+002	40	3.00E-002
18	3.00E+001	41	2.53E-002
19	1.00E+001	42	1.00E-002
20	8.10E+000	43	7.50E-003
21	6.00E+000	44	3.00E-003
22	4.75E+000		1.00E-005
23	3.00E+000		

Table 3.4: *44GROUPNDF5* energy group boundaries

[2]Except for the default O^{16} data, which is from the ENDF/B-VI evaluation.

Cross-Sections

Neutron cross-sections and reaction parameters are tabled in *44GROUPNDF5* according to ENDF Section (MT)[3] numbers. A list of common MTs stored on *44GROUPNDF5* is shown in table 3.5, which is a partial reproduction of the table found in Appendix B of the ENDF format guide[2].

MT	Reaction/ parameter	Description
1	(n, total)	Total neutron cross-section, sum of MT=2, 4, 5, 11, 16–18, 22–26, 28–37, 41–42, 44–45, 102–117
2	(n, n_o)	Elastic neutron scattering cross-section
4	(n, $n'\gamma$)	Inelastic neutron scatting cross-section
16	(n, 2n)	Production of two neutrons
18	(n, f)	Fission cross-section
27	(n, abs)	Neutron absorption, sum of MT=18, and MT=102 through MT=117
101	(n, disap)	Neutron disappearance, sum of MT=102 through MT=117
102	(n, γ)	Radiative capture
103	(n, p)	Production of a proton
104	(n, d)	Production of a dueterium nucleus
105	(n, t)	Production of a tritium nucleus
106	(n, He^3)	Production of an He^3 nucleus
107	(n, α)	Production of an α-particle
452	$\bar{\nu}$	Average number of fission neutrons (prompt plus delayed) per fission
1018	χ	Spectrum of fission neutron initial energy
3xxx	σ_∞	Infinite dilution cross-sections (i.e. MT=3002 for (n, n_o), MT=3018 for (n, f), MT=3102 for (n, γ), etc.)

Table 3.5: *44GROUPNDF5*
MT numbers of relevance

The uncertainties associated with several fundamental cross-sections were propagated directly using SCALE-SS. Uncertainties related to an aggregate cross-section, such as (n, total), are not propagated directly from its associated covariance matrix, in cases where its covariance matrix exists. Instead, its uncertainty will be manifested by directly sampling its constituent cross-sections, and adjusting the aggregate based on the new totals. This process of varying aggregate cross-sections by directly sampling its component reactions can be referred to as *indirect component*

[3]Except MT=1018, and MT=3xxx, which are not part of the ENDF standard

sampling. Table 3.5 shows all MTs that can be varied by SCALE-SS by both direct (shown in bold) and indirect component sampling.

For each MT listed in table 3.5 there is an array of 44 values, each of which corresponds to one of the available neutron energy groups. Infinite-dilution cross-sections are available for some reactions. In the case of neutron-producing or scattering MTs, or more generally, any that have one or more neutrons in the reaction exit channel, such as MT=2, MT=4 and MT=16, there are additional tables of data that store energy and angular characteristics of post-reaction neutrons. SCALE-SS does not adjust the energy or angular profiles of these neutron tables, but in the case of elastic scattering, will apply an adjustment as described in section 3.3, so that the sum of scattering out-group cross-sections is equivalent to the sampled scattering in-group cross-section.

Resonance Parameters

The *44GROUPDF5* library contains resonance parameters for self-shielding in both the unresolved and resolved resonance energy regions. Self-shielding due to unresolved resonances is performed in SCALE by the BONAMI[57] code using the Bondarenko method. Bondarenko Factors for energy groups containing unresolved resonances are tabled in the library as a function of temperature and background cross-section, σ_o. BONAMI calculates problem-dependent Bondarenko Factors for each resonant nuclide by evaluating the actual background cross-section present in the nuclide's material mixture, and subsequently interpolating between the σ_o values on the table. The Bondarenko Factors used by BONAMI are fractional values that express the ratio of the shielded cross-section at the problem dilution to that at infinite dilution,

$$BF_g(T, \sigma_o) = \frac{\bar{\sigma}_g}{\sigma_{\infty_g}} \tag{3.4.1}$$

where BF_g is the Bondarenko Factor of a cross-section in group g, as a function of temperature, T, and background cross-section, σ_o, and where $\bar{\sigma}_g$ and σ_{∞_g} are the shielded and infinitely dilute cross-sections, respectively.

Resonance self-shielding effects arising due to resolved resonances are computed by the NITAWL[58] module of SCALE. NITAWL has the capability to solve a collision density equation at resonance energies subject to several assumptions. The Nordheim formulation of collision density is shown in equation (3.4.2), with consideration to a maximum of three nuclides: one absorbing nuclide and two moderating nuclides. System heterogeneities are accounted for by the use of a Dancoff factor.

$$\phi(E)\Sigma_T(E) = \sum_{i=1}^{\leq 3} \left[\frac{(1 - P_o^*(E))}{\alpha_i} \int_E^{E/(1-\alpha_i)} \phi(E')\Sigma_{si}(E')\frac{dE'}{E'} + P_o^*\Sigma_{Ti}(E)W(E) \right] \quad (3.4.2)$$

where,

$\phi(E)$	is the energy-dependent neutron flux
$\Sigma_T(E)$	is the energy-dependent total macroscopic cross-section of the absorbing mixture
P_o^*	is the Dancoff-corrected first-flight escape probability out of the absorbing mixture
α_i	is the maximum fraction of energy that can be lost by a neutron during an elastic collusion with nuclide i
Σ_{si}	is the macroscopic, isotropic scattering cross-section of nuclide i
Σ_{Ti}	is the macroscopic, total cross-section of nuclide i
$W(E)$	is the energy-dependent neutron flux in the moderator
i	is an index to the absorbing and moderating nuclides

Equation (3.4.2) is a simple collision density balance equation that describes a necessary consequence of an assumed steady-state condition. Namely, that any neutron/nucleus interactions (collisions) with an energy in dE about E occurring in an absorbing mixture involve neutrons that have have been previously scattered into dE from higher energies within the absorber, or alternately, neutrons already having energy dE about E that have leaked into the absorbing mixture from the adjacent moderator. Several additional assumptions involved in the formulation of equation (3.4.2) are described in NITAWL documents[58].

NITAWL solves equation (3.4.2) on a fine energy mesh across each resolved resonance, which is uniquely characterized by a set of resonance parameters. The fine-mesh resonant cross-section is constructed by NITAWL for use in the equation by using the resonance parameters to define a curve according to the single-level Breit-Wigner formulae, shown in equations (3.4.3) through (3.4.5).

$$\sigma_{n,n}^l(E) = (2l+1)\frac{4\pi}{k^2}\sin^2(\phi_l) + \frac{4\pi}{k^2}g\frac{\Gamma_n^l}{\Gamma}\frac{\sin(2\phi_l)}{2}\chi(X,\xi) + \left(\frac{\Gamma_n^l}{\Gamma} - 2\sin^2(\phi_l)\right)\psi(X,\chi) \quad (3.4.3)$$

Parameter	Description
Γ	total resonance width
AWRI	ratio of the nuclide mass to the mass of a neutron
E'_r	effective resonance energy, related to E_o (see [58])
k	neutron wave number
Γ^l_n	neutron resonance width
Γ^l_γ	capture resonance width
Γ^l_f	fission resonance width
g	a statistical factor
E_o	resonance energy
l	the spin of the resonance
σ_{po}	potential scattering cross-section, used when invoking an NR approximation as well as to determine the energy range of the slowing-down calculation

Table 3.6: *44GROUPND5* resolved resonance parameters

$$\sigma^l_{n,\gamma}(E) = \frac{4\pi}{k^2} g \frac{\Gamma^l_n \Gamma^l_\gamma}{\Gamma} \psi(X,\xi) \tag{3.4.4}$$

$$\sigma^l_{n,f}(E) = \frac{4\pi}{k^2} g \frac{\Gamma^l_n \Gamma^l_f}{\Gamma} \psi(X,\xi) \tag{3.4.5}$$

where, $\psi(X,\xi)$ and $\chi(X,\xi)$ are doppler shape functions,

$$\psi(X,\xi) = \xi/(2\sqrt{\pi}) \int_{-\infty}^{\infty} \exp\Big[-(\frac{\xi}{2})^2 (X-Y)^2\Big](1+Y^2)^{-1} dY \tag{3.4.6}$$

$$\chi(X,\xi) = \xi/(\sqrt{\pi}) \int_{-\infty}^{\infty} \exp\Big[-(\frac{\xi}{2})^2 (X-Y)^2\Big] Y (1+Y^2)^{-1} dY \tag{3.4.7}$$

and,

$$X = 2(E - E'_r)/\Gamma \tag{3.4.8}$$

$$\xi = \Gamma \sqrt{\text{AWRI}/(4E'_r kT)} \tag{3.4.9}$$

where the resonance parameters are listed in table 3.6. The equations listed above can be found in the NITAWL theory manual[58].

3.4.2 44GROUPV6REC covariance library

The covariance library used by both SCALE-SS and TSUNAMI as part of the feasibility study, *44GROUPV6REC*, is one of four covariance libraries that are included with SCALE 5.1. It is a library of relative covariance of multi-group cross-sections and is set

aside from its three peer libraries in SCALE 5.1 as being the one based on more recent data evaluations (ENDF/B-VI for most data, rather than ENDF/B-V) and covering the most isotopes. Although intended for application with ENDF/B-VI cross-section data, it is used in this work with the *44GROUPNDF5* cross-section set for two reasons. Firstly, this covariance was chosen for the sake of consistency with the OECD/NEA UAM benchmark activities, which distributed solely the *44GROUPV6REC* library to the benchmark participants[4]. Secondly, intended as a study of feasibility and comparison to other methods, namely TSUNAMI, the choice of covariance can be arbitrary so long as it is used as a common source of uncertainty by both uncertainty tools.

44GROUPV6REC shares the same SCALE 44-group energy structure as the cross-section library *44GROUPNDF5* (see table 3.4). The covariance library contains uncertainty information for a wide range of nuclides and reactions, making it suitable for broad application to many different lattice problems. Consistent with this broad applicability, the covariances relate to problem-independent, unshielded cross-sections. The library contains covariance only for the multi-group data shown in table 3.7 (see table 3.5 for more details). The full list of over 300 nuclides available in the uncertainty library can be found in SCALE covariance documentation[59].

Covariances exist in *44GROUPV6REC* between energy group values of the same cross-section (i.e. thermal values of U^{235}(n,γ) are correlated), between different cross-section group values belonging to the same nuclide (i.e. U^{235}(n, γ) and U^{235}(n, fission) are correlated), and between group values of cross-sections of different nuclides (i.e. U^{235}(n, γ) and Pu^{239}(n, γ) are correlated).

MT	Reaction
1	(n, total)
2	(n, n_o)
4	(n, n$'\gamma$)
16	(n, 2n)
18	(n, f)
102	(n, γ)
103	(n, p)
104	(n, d)
105	(n, t)
106	(n, ^{3}He)
107	(n, α)

Table 3.7: MTs supported by *44GROUPV6REC*

[4]It has since been replaced in the UAM benchmark by a more recent covariance evaluation, *44GROUPCOV*

3.4.3 Procedures and rules

Recall that SCALE-SS replaces multi-group cross-sections with randomly generated values as described in section 3.1. Because SCALE-SS was intended to propagate uncertainties through all stages of a lattice calculation, the propagation sequence of SCALE-SS, shown in figure 3.6, mirrors that of a standard SCALE lattice calculation sequence (refer to figure 3.5).

Item	Description
44GROUPV6REC	Problem independent, 44-group cross-section uncertainty library
DECOMP	SCALE-SS routines for covariance matrix eigenvalue decomposition; see equations (3.1.1) and (3.1.2)
$\Sigma^{1/2}$	Matrix for generating dependent, random variables; see equations (3.1.1) and (3.1.2)
SCALELIB	SCALE-SS routines for randomly generating new problem-independent cross-sections and writing them to separate AMPX-format master libraries
Master Libraries	Problem-independent cross-section libraries that are populated with random values
Working Libraries	Problem-dependent libraries containing self-shielded cross-sections
KUNCERT	SCALE-SS routines for calculating the variance associated with k_∞

Table 3.8: SCALE-SS uncertainty propagation sequence component description

The cross-sections that are randomly sampled by SCALE-SS are fundamental reactions and are shown in bold in table 3.5, which necessitate the correction of numerous other variables stored on the *44GROUPNDF5* library, such as aggregate cross-sections, scattering matrices, and resonance parameters. If resonance parameters are not adjusted to be in some way consistent with the new cross-sections, uncertainties will not be properly propagated through the self-shielding calculations of the lattice sequence.

Sampling Procedure

All nuclear data that are statistically propagated by SCALE-SS are sampled according to a Gaussian PDF. For each variable, the mean of the PDF is taken to be the variable's reference value on *44GROUPNDF5*, and the covariance is extracted from *44GROUPV6REC*. As previously mentioned in section 3.1.1, the covariance is pre-processed for symmetry and post-processed to guarantee positive-semidefiniteness.

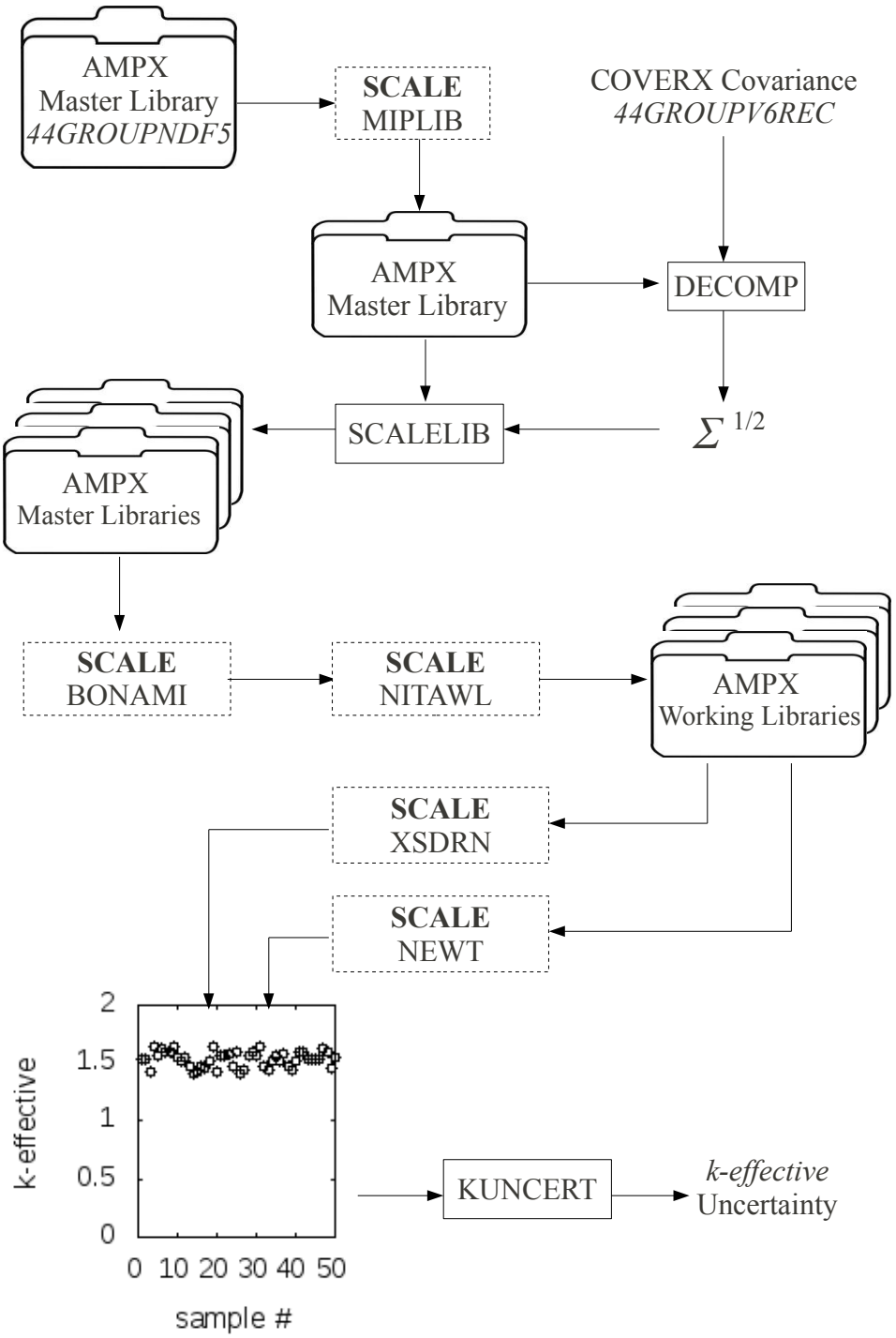

Figure 3.6: SCALE-SS uncertainty propagation sequence

Since the sampling is done according to a Gaussian PDF, negative cross-section values are occasionally generated. Naturally, variables with large relative covariance tend

to produce more negative values than variables with smaller covariance. Negative values are not rejected by SCALE-SS, and they are written as-is to the new multi-group libraries for later use by the lattice solvers of SCALE. It is noteworthy that the reference library, *44GROUPNDF5* contains negative cross-sections from the onset, which makes subsequent discrimination against negative values by SCALE-SS problematic. The existence of a small collection of negative cross-sections ultimately caused no noticeable issues with the solution of the lattice equations or the quantification of output uncertainties, particularly because while some microscopic cross-sections were negative, the macroscopic cross-sections associated with each mixture tended to remain positive. SCALE-SS can sample more than one cross-section at a time. When two or more cross-sections belonging to a particular nuclide are sampled simultaneously, the covariances between cross-sections are included in the sampling procedure. However, for simplicity, SCALE-SS neglects covariances between cross-sections of different isotopes. This was intended as a temporary simplification for preliminary purposes, and isotope-to-isotope covariances may be treated as the code is updated. The effect of cross-isotope covariances is small for the test problems described later in this chapter, as determined with TSUNAMI.

Cross-Section Consistency Rules

When the SCALELIB module of SCALE-SS builds new AMPX master format libraries, many cross-section values that are not randomly sampled must be corrected or recalculated to be consistent with the sampled data. A number of cross-section consistency rules are used by SCALELIB to ensure a self-consistent set of data in each new library.

MT	Description	Rule
1	(n, total)	Sum of MT=2, 4, 5, 11, 16–18, 22–26, 28–37, 41–42, 44–45, 102–117
2	(n, n_o)	Corresponding row of scattering table is scaled uniformly with the 1D scattering cross-section
27	(n, abs)	Sum of MT=18, and MT=102 through MT=117
101	(n, disap)	Sum of MT=102 through MT=117
1018	χ	Sum of all groups normalized to 1.0
3xxx	σ_∞	Scaled uniformly as the weighted cross-section

Table 3.9: SCALE-SS cross-section consistency rules

The rules for MT=1, MT=27 and MT=101 are straightforward and involve the re-totaling of aggregate cross-sections, whose constituent MTs may have been changed by the sampling process. The rule for elastic scattering, MT=2, corrects the group-to-group scattering matrix as described in section 3.3.1, uniformly scaling each row according to the change in the 1D scattering group cross-section. The χ

normalization rule expresses the mathematical necessity that the fission spectrum, χ, is a probability distribution whose sum is unity. Finally, recall that for several cross-sections, *44GROUPNDF5* records multi-group infinite-dilution cross-sections, σ_∞, in addition to the cross-sections weighted by a problem-independent generic flux, σ. Infinite-dilution cross-sections are stored in 44-group vectors, MT=3xxx (e.g. 3018, 3102, etc.), and also in distinct data fields as part of the Bondarenko self-shielding block of the library. Given that both infinite-dilution and weighted cross-section data are a function of the same continuous-energy cross-sections, any uncertainty that affects σ should also affect σ_∞.

Recall that,

$$\sigma_g = \frac{\int_g \sigma(E)W(E)dE}{\int_g W(E)dE} \tag{3.4.10}$$

where,

σ_g	is the weighted cross-section in group g
E_g	is the lower energy limit of group g
$\sigma(E)$	is the continuous-energy cross-section
$W(E)$	is a continuously-varying weighting function (see section 1.1)

If a perturbation, δ, is applied to a weighted cross-section σ_g such that the perturbed cross-section is $\sigma'_g = (1+\delta)\sigma_g$, an assumption can be made relating the change in group value from σ_g to σ'_g to the change in continuous-energy values from $\sigma(E)$ to $\sigma'(E)$ for all values of E within the energy limits of g. If the group cross-section σ_g in equation (3.4.10) is replaced with its perturbed counterpart, σ'_g, we would have,

$$\sigma'_g = (1+\delta)\sigma_g = (1+\delta)\frac{\int_g \sigma(E)W(E)dE}{\int_g W(E)dE} \tag{3.4.11}$$

Since perturbations are step-wise applied to cross-section on a group-by-group basis, it is constant for all energies, E within a particular group, and can therefore be moved inside the integral of equation (3.4.11). Upon making the sensible assumption that small perturbations in $\sigma(E)$ will not cause a related perturbation on the continuous-energy weighting function residing in the same energy group, $W(E)$ can be treated as constant. This is perfectly reasonable since $W(E)$ is a generic weighting function that is independent of the underlying nuclear data at resonant energies. Therefore, a perturbation of σ_g is taken to be solely the result of perturbations of $\sigma(E)$. It is reasonable to introduce an artificial correlation between all

continuous-energy cross-sections within the energy limits of group, g, treating the continuous-energy perturbations as being uniformly applied to all $\sigma(E)$ falling within the limits of that group.

$$\begin{aligned} \sigma'_g &= \frac{\int_g (1+\delta)\sigma(E)W(E)dE}{\int_g W(E)dE} \\ &= \frac{\int_g \sigma'(E)W(E)dE}{\int_g W(E)dE} \end{aligned} \tag{3.4.12}$$

where,

$$\sigma'(E) = (1+\delta)\sigma(E) \tag{3.4.13}$$

The only assumptions employed when arriving at this conclusion are that the group-wise cross-section perturbations are uniformly applied to all continuous-energy data within the group, and that no change in the fine-structure of the weighting function within the group occurs as a result of the uniform perturbation of the cross-section. This correction of the infinite-dilution cross-section arising from the change in flux-weighted group values is important for propagating uncertainties through resonance self-shielding calculations, and is noted as the final rule in table 3.9.

Resonance Parameter Consistency Rules

Bondarenko resonance parameters for unresolved resonance self-shielding include infinite-dilution cross-sections, the treatment of which has been described above, and Bondarenko Factors (see equation (3.4.1)), which relate the self-shielded cross-section at the problem dilution to the infinite-dilution cross-section. Like the infinite-dilution cross-section itself, Bondarenko Factors depend on continuous-energy cross-sections, and should show variation as a result of cross-section perturbations. Recall the shielded cross-section, $\bar{\sigma}$ at a particular problem-dependent dilution (background cross-section), σ_o from equation (1.2.4). In this section it is more convenient to express the self-shielded cross-section in terms of the lethargy variable rather than energy. Recall that,

$$\mu = log\left(\frac{E_o}{E}\right) \quad \text{and hence,} \quad d\mu = -\frac{1}{E}dE \tag{3.4.14}$$

Hence,

$$\bar{\sigma}_g = \frac{\int_g \frac{\sigma(\mu)}{\sigma_t(\mu)+\sigma_o} d\mu}{\int_g \frac{1}{\sigma_t(\mu)+\sigma_o} d\mu} \tag{3.4.15}$$

Where the integrals are taken over an energy group, g, and the background cross-section, σ_o is assumed to not vary within the group for the sake of simplification. Note that this is a simplifying assumption also employed by multi-group lattice physics codes. A uniform perturbation of the continuous-energy cross-section within the group, consistent with equation (3.4.13), will cause a related perturbation on the total cross-section of the same nuclide, $\sigma_t(\mu)$, and on on the shielded cross-section, $\bar{\sigma}_g$.

$$\bar{\sigma}'_g = \frac{\int_g \frac{\sigma'(\mu)}{\sigma'_t(\mu)+\sigma_o} d\mu}{\int_g \frac{1}{\sigma'_t(\mu)+\sigma_o} d\mu} \tag{3.4.16}$$

If only one cross-section is being sampled at a time, then the absolute change in the total cross-section is equal to the absolute change in the sampled cross-section. However, if more than one cross-section is simultaneously sampled, then the change in total cross-section is equal to the net change in all of its constituent cross-section components. To simplify the notation in this text, the former is taken to be the case. Therefore, a perturbation of δ applied to the weighted, and therefore, continuous-energy cross-section, would result in the following expression.

$$\bar{\sigma}'_g = \frac{\int_g \frac{(1+\delta)\sigma(\mu)}{\delta\sigma(\mu)+\sigma_t(\mu)+\sigma_o} d\mu}{\int_g \frac{1}{\delta\sigma(\mu)+\sigma_t(\mu)+\sigma_o} d\mu} \tag{3.4.17}$$

Since the perturbation is constant within the energy group, it can be excluded from the integration, and equation (3.4.17) reduces to,

$$\bar{\sigma}'_g = (1+\delta)\frac{\int_g \frac{\sigma(\mu)}{\sigma_t(\mu)+\sigma'_o} d\mu}{\int_g \frac{1}{\sigma_t(\mu)+\sigma'_o} d\mu} \tag{3.4.18}$$

where,

$\sigma(\mu)$	is the unperturbed continuous-energy cross-section
$\sigma_t(\mu)$	is the unperturbed continuous-energy total cross-section

and,

σ'_o	is the *effective* perturbed background cross-section

$$\sigma'_o = \sigma_o + \delta\sigma_g \tag{3.4.19}$$

Recall the definition of the Bondarenko Factor in equation (3.4.1). Substituting the expression for the perturbed infinite-dilution cross-section from equation (3.4.10),

$$BF'_g(T,\sigma_o) = \frac{(1+\delta)\dfrac{\displaystyle\int_g \frac{\sigma(\mu)}{\sigma_t(\mu)+\sigma'_o}d\mu}{\displaystyle\int_g \frac{1}{\sigma_t(\mu)+\sigma'_o}d\mu}}{(1+\delta)\sigma_{\infty_g}}$$

which is equivalent to,

$$BF'_g(T,\sigma_o) = BF_g(T,\sigma'_o) = BF_g(T,\sigma_o+\delta\sigma_g) \tag{3.4.20}$$

Therefore, unresolved resonance shielding using Bondarenko Factors applied to a perturbed cross-section is equivalent to solving the problem with unperturbed cross-sections at a different background cross-section. This is the most rigorous method to propagate changes in group cross-sections through resonance self-shielding using the Bondarenko method.

If, however, perturbations are sufficiently small such that $\delta\sigma$ is significantly smaller than $\sigma_t(E)+\sigma_o$, then,

$$\sigma_t(E)+\sigma_o+\delta\sigma_g$$

can be approximated by,

$$\sigma_t(E)+\sigma_o$$

According to this approximation, the Bondarenko Factors are left unmodified. This is only a reasonable approximation when $\delta\sigma_g \ll \sigma_t(E)+\sigma_o$. While this applies to many cross-sections of many nuclides, it only becomes questionable in cases of extremely low dilution. However, this approximation is employed by SCALE-SS, with the explicit recommendation that for more rigorous uncertainty propagation through

Bondarenko self-shielding, equation (3.4.20) be implemented in the propagation procedure as part of future work. In summary, the uncertainty propagation through unresolved resonance self-shielding by SCALE-SS has proper consideration for the appropriate adjustments in infinite-dilution cross-sections, and when sampling multiple cross-sections simultaneously, the perturbation of each cross-section will be reflected in adjusted background cross-sections for the others. The change in effective background cross-section resulting from a cross-section's own perturbation, however, is neglected in SCALE-SS.

Consistency adjustments of resolved resonance parameters are more complicated. The reference values in *44GROUPNDF5* of the resolved resonance parameters in table 3.6, that correspond to continuous-energy cross-sections formulated in equations (3.4.3) through (3.4.5) are, by default, physically consistent with the reference flux-weighted and infinite-dilution multi-group cross-sections. The task of developing consistency rules for the resolved resonance self-shielding is to calculate an adjusted or perturbed set of resonance parameters, Γ'_n, Γ'_γ, Γ'_f, E'_o, etc., that are physically consistent with the perturbed multi-group cross-sections, σ', that are generated by the statistical sampling procedure. Making use of a previously employed assumption that a change in multi-group cross-section is uniformly applied to the continuous-energy cross-sections that lay within the energy limits of the group, a perturbation of $\sigma_g^{n,\gamma}$ to ${\sigma'}_g^{n,\gamma} = (1+\delta)\sigma_g^{n,\gamma}$ should manifest a constant scaling of the Breit-Wigner function in equation (3.4.5) by a factor of $(1+\delta)$. Likewise, for $\sigma_g^{n,n}$ and $\sigma_g^{n,f}$. Taking the (n,γ) reaction as an example, recall that corresponding Breit-Wigner formula of equation (3.4.5) for an (n,γ) resonance is,

$$\sigma_{n,\gamma}(E) = \frac{4\pi}{k^2} g \frac{\Gamma_n \Gamma_\gamma}{\Gamma} \psi(X,\chi)$$

where the dependence of the parameters on the resonance spin, l, is implicitly present but not written to simplify the notation of this example. Substituting the expression for $\psi(X,\xi)$ in equations (3.4.6), (3.4.9) and (3.4.8),

$$\sigma_{n,\gamma}(E) = \frac{4\pi}{k^2} g {\Gamma_n}\Gamma_\gamma \frac{\sqrt{\mathrm{AWRI}}}{4\sqrt{\pi E'_r kT}}\, I \tag{3.4.21}$$

where,

$$I = \int_{-\infty}^{\infty} \exp\left[-\frac{\Gamma^2 \mathrm{AWRI}}{16 E'_r kT} \left(\frac{2(E-E'_r)}{\Gamma} - Y \right)^2 \right] (1+Y^2)^{-1} dY \tag{3.4.22}$$

Employing the continuous-energy cross-section correlation assumption, as in equation (3.4.13),

$$\begin{aligned} \sigma'_{n,\gamma}(E) &= (1+\delta)\frac{4\pi}{k^2} g {\Gamma_n}\Gamma_\gamma \frac{\sqrt{\mathrm{AWRI}}}{4\sqrt{\pi E'_r kT}}\, I \\ &= \frac{4\pi}{k^2} g {\Gamma_n}{\Gamma'_\gamma} \frac{\sqrt{\mathrm{AWRI}}}{4\sqrt{\pi E'_r kT}}\, I \end{aligned} \tag{3.4.23}$$

where,

$$\Gamma'_\gamma = (1+\delta)\Gamma_\gamma \tag{3.4.24}$$

similarly,

$$\Gamma'_n = (1+\delta)\Gamma_n \tag{3.4.25}$$

$$\Gamma'_f = (1+\delta)\Gamma_f \tag{3.4.26}$$

Equation (3.4.24) is not an exact resonance parameter correction, however, because the resonance full width, Γ, which is the sum of the partial widths, Γ_n, Γ_γ and Γ_f, appears in the integral, I, as shown in equation (3.4.22). The full width is not stored in *44GROUPNDF5*, but is rather calculated by NITAWL as the sum of the partial widths, which will naturally change when a partial width is corrected as shown in equation (3.4.24). However, if the change in partial width, $\delta\Gamma$ is small compared to the unperturbed total width, Γ, equation (3.4.24) is a reasonable adjustment to the resolved resonance parameter for consistency with a perturbed multi-group cross-section. Naturally, this condition cannot be simultaneously satisfied for each partial width. Also problematic with this formulation of perturbed resonance widths is that the adjustment of one partial width, such as Γ_γ, will change the other two cross-sections, σ_n and σ_f, as well.

Therefore, when a multi-group scattering, radiative capture, or fission cross-section is perturbed due to random sampling by a factor of δ, the corresponding partial width of any resolved resonance whose peak energy, E_o, falls within the group energy limits is scaled uniformly with the multi-group cross-section.

Parameter	Description	Rule
BF	Bondarenko Factors	Remain unchanged
$\Gamma_{n,\gamma,f}$	Resonance partial widths	Scaled with corresponding multi-group cross-section

Table 3.10: SCALE-SS resonance parameter consistency rules

3.4.4 Test cases

Three test cases from the OECD/NEA UAM benchmark[17, pp. 30-32] were used to investigate the effectiveness of SCALE-SS, and the statistical sampling method in general, in propagating lattice physics uncertainties. The test cases are thermal, LWR pin models, which are within the range of applicability of the cross-section library *44GROUPNDF5*. Each pin model corresponds to a unique LWR reactor type, a PWR, BWR, and VVER, that feature varying lattice arrangements, fuel enrichments, lattice geometry, temperature, and material compositions. The fuel cell models are based on the physical core designs of actual nuclear facilities, Peach Bottom unit #2, Three Mile Island unit #1, and Kozloduy unit #6, respectively. Uncertainty analysis

using TSUNAMI-1D and SCALE-SS was performed on each model at hot, zero-power (HZP) state.

The one-dimensional transport solver, XSDRNPM, used by both TSUNAMI-1D and SCALE-SS, demands an axisymmetric input model consisting of a set of concentric circles or tubes to represent fuel pins and their surrounding moderator. Therefore, the fuel pellets, gaps and cladding of the geometries can be used by XSDRNPM without modification (because they are already a set of concentric tubes), but the moderator boundaries, which are either square or hexagonal, must be replaced by a circular boundary of some appropriate diameter. The common Wigner-Seitz approximation[60][61] substitutes a circular boundary in place of the true reflective polygonal boundary such that the diameter of the circle conserves the volume of moderator in the cell. Reflective circular boundaries can be computationally problematic[61], therefore an isotropic return (white) boundary condition is applied to the outer boundary of Wigner-Seitz approximate models. The uncertainty propagation by SCALE-SS was performed on Wigner-Seitz approximate models using XSDRNPM and the true, two-dimensional geometries using NEWT. The BONAMI code was used for resonance self-shielding in the unresolved region, and resolved resonance self-shielding was performed using the NITAWL code, for uncertainty sequences by both SCALE-SS and TSUNAMI-1D.

Parameter	Value
Unit cell pitch [mm]	18.75
Fuel pellet diameter [mm]	12.1158
Fuel pellet material	UO_2
Fuel density [g/cm^3]	10.42
Fuel enrichment, w/o	2.93
Cladding outside diameter [mm]	14.3002
Cladding thickness [mm]	0.9398
Cladding material	Zircaloy-2
Cladding density [g/cm^3]	6.55
Gap material	He
Moderator material	H_2O

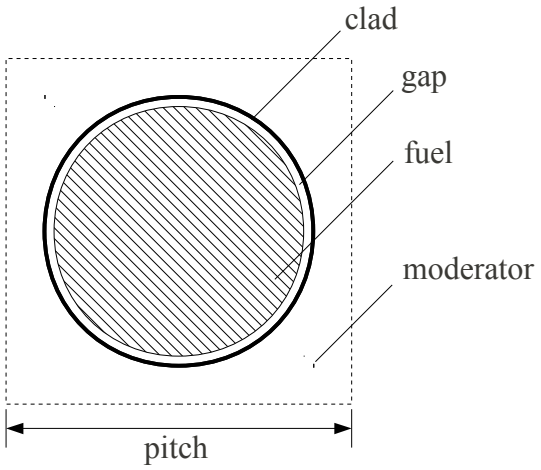

Reactor conditions	HZP	HFP
Fuel temperature [K]	552.833	900.0
Cladding temperature [K]	552.833	600.0
Moderator temperature [K]	552.833	562.0
Moderator density [kg/m^3]	753.978	748.4
Reactor power [kW]	3.293	3293
Void fraction	-	40%

Figure 3.7: Schematic of the Peach Bottom-2 BWR lattice cell

Parameter	Value
Unit cell pitch [mm]	14.427
Fuel pellet diameter [mm]	9.391
Fuel pellet material	UO_2
Fuel density [g/cm^3]	10.283
Fuel enrichment, w/o	4.85
Cladding outside diameter [mm]	10.928
Cladding thickness [mm]	0.673
Cladding material	Zircaloy-4
Cladding density [g/cm^3]	6.55
Gap material	He
Moderator material	H_2O

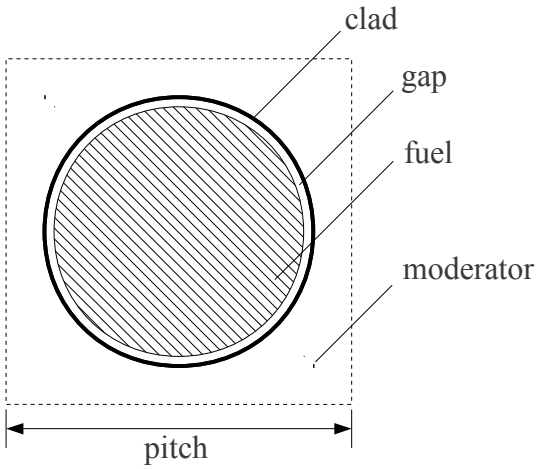

Reactor conditions	HZP	HFP
Fuel temperature [K]	551.0	900.0
Cladding temperature [K]	551.0	600.0
Moderator temperature [K]	551.0	562.0
Moderator density [kg/m^3]	766.0	748.4
Reactor power [kW]	2.772	2772.0

Figure 3.8: Schematic of the Three Mile Island-1 PWR lattice cell

Parameter	Value
Unit cell pitch [mm]	12.75
Fuel pellet diameter [mm]	7.56
Fuel pellet material	UO_2
Fuel density [g/cm^3]	10.4
Fuel enrichment, w/o	3.3
Central void diameter [mm]	1.4
Central void material	dry air
Cladding outside diameter [mm]	9.1
Cladding thickness [mm]	0.69
Cladding material	Zr+1% Nb
Cladding density [kg/m^3]	n/a
Gap material	He
Moderator material	H_2O

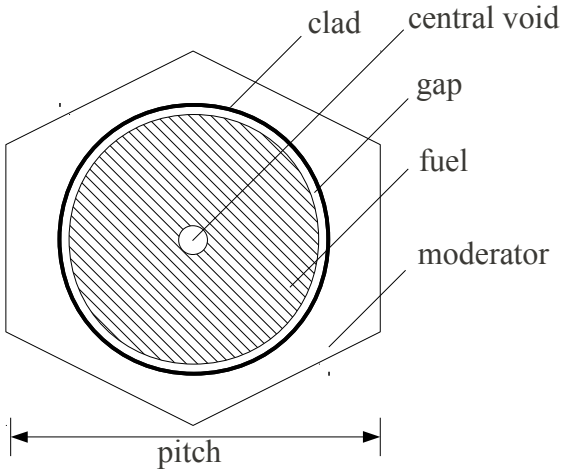

Reactor conditions	HZP	HFP
Fuel temperature [K]	552.150	900.0
Cladding temperature [K]	552.150	600.0
Moderator temperature [K]	552.150	560.0
Moderator density [g/cm^3]	767.000	752.5
Reactor power [kW]	3.000	3000

Figure 3.9: Schematic of the Kozloduy-6 VVER lattice cell

3.4.5 OECD/NEA UAM benchmark cases results

Both the best-estimate and uncertainty quantification results for the UAM test cases are described in this section.

Lattice cell	XSDRNPM	NEWT
PB-2 BWR	1.33856	1.33892
TMI-1 PWR	1.42367	1.42397
K-6 VVER	1.33149	1.34040

Table 3.11: SCALE 5.1 best-estimate predictions of k_∞, using *44GROUPNDF5* library

The uncertainty of k_∞ was calculated by TSUNAMI-1D using an adjoint sensitivity technique, and by SCALE-SS generating two-thousand statistical samples of all nuclides that possessed covariance. Cross-sections were sampled one at a time so that the contribution to k_∞ arising from each multi-group reaction or parameter could be separately quantified.

PB-2 nuclide	reaction/ parameter	TSUNAMI-1D $\%\Delta k/k$	SCALE-SS-1D (XSDRNPM) $\%\Delta k/k$	SCALE-SS-2D (NEWT) $\%\Delta k/k$
U^{238}	(n,γ)	0.3609	3.0254	2.9943
U^{235}	$\bar{\nu}$	0.2715	0.2726	0.2437
U^{235}	(n,γ)	0.1612	0.1636	0.1775
U^{235}	$(n,fission)$	0.1076	0.1056	0.1048
U^{235}	χ	0.0720	0.0813	0.0768
O^{16}	(n,α)	0.0525	0.0539	0.0501
U^{238}	$\bar{\nu}$	0.0396	0.0418	0.0399
U^{238}	$(n,fission)$	0.0496	0.0467	0.0462
H^1	elastic scatter	0.0322	0.0328	0.0322
H^1	(n,γ)	0.0282	0.0278	0.0275
O^{16}	elastic scatter	0.0137	0.0110	0.0119

Table 3.12: Major contributions to uncertainty in PB-2 k_∞

Tables 3.12 through 3.14 show the largest individual contributions to k_∞ uncertainty resulting from uncertain multi-group input cross-sections and parameters. For many input parameters, there was reasonable agreement between SCALE-SS and TSUNAMI-1D. Some disparity is expected due to subtle differences in the capabilities and approximations of each code. For example, as described in chapter 2, TSUNAMI-1D employs first-order perturbation theory, whereas the statistical sampling procedure

TMI-1 nuclide	reaction/ parameter	TSUNAMI-1D $\%\Delta k/k$	SCALE-SS-1D (XSDRNPM) $\%\Delta k/k$	SCALE-SS-2D (NEWT) $\%\Delta k/k$
U^{238}	(n,γ)	0.2937	2.3844	2.3726
U^{235}	$\bar{\nu}$	0.2646	0.2627	0.2688
U^{235}	(n,γ)	0.2428	0.2747	0.2669
U^{235}	$(n,fission)$	0.1280	0.1345	0.1327
U^{235}	χ	0.0610	0.0767	0.0760
O^{16}	(n,α)	0.0528	0.0526	0.0518
U^{238}	$\bar{\nu}$	0.0359	0.0380	0.0356
U^{238}	$(n,fission)$	0.0415	0.0392	0.0393
H^{1}	elastic scatter	0.0308	0.0317	0.0316
H^{1}	(n,γ)	0.0189	0.0192	0.0194
O^{16}	elastic scatter	0.0123	0.0103	0.0104

Table 3.13: Contributions to uncertainty in TMI-1 k_∞

K-6 nuclide	reaction/ parameter	TSUNAMI-1D $\%\Delta k/k$	SCALE-SS-1D (XSDRNPM) $\%\Delta k/k$	SCALE-SS-2D (NEWT) $\%\Delta k/k$
U^{238}	(n,γ)	0.3502	2.5470	2.5260
U^{235}	$\bar{\nu}$	0.2715	0.2696	0.2679
U^{235}	(n,γ)	0.1836	0.1993	0.1947
U^{235}	$(n,fission)$	0.1101	0.1163	0.1135
U^{235}	χ	0.0626	0.0725	0.0766
O^{16}	(n,α)	0.0509	0.0512	0.0505
U^{238}	$\bar{\nu}$	0.0365	0.0357	0.0365
U^{238}	$(n,fission)$	0.0471	0.0419	0.0446
H^{1}	elastic scatter	0.0314	0.0334	0.0308
H^{1}	(n,γ)	0.0257	0.0254	0.0265
O^{16}	elastic scatter	0.0124	0.0104	0.0103

Table 3.14: Contributions to uncertainty in K-6 k_∞

of SCALE-SS implicitly captures all higher-order terms. Also, the calculation of sensitivities by TSUNAMI-1D assumes that perturbations of cross-sections do not cause related perturbations on neutron flux, which is a phenomena that is also captured by SCALE-SS. Lastly, the resonance parameter treatment by SCALE-SS includes several necessary approximations, as outline in section 3.4.3. Therefore, differences in calculated uncertainties for multi-group inputs that are strongly self-shielded, particularly by resolved resonances, should not be surprising, in general. What is notable is the large discrepancy in k_∞ uncertainty using SCALE-SS caused by the (n, γ) cross-section of U^{238}, which is caused almost entirely by uncertainties in the resolved resonance range. In LWR thermal reactor fuel mixtures, U^{238} is of especially low dilution, implying that resonance self-shielding effects for cross-sections of this nuclide are strong, and the self-shielded cross-sections will vary substantially compared to their infinite-dilution counterparts. Also, of the resolved U^{238} resonances, the partial width corresponding to the (n, γ) cross-section, Γ_γ, is large compared to the other partial widths, Γ_n and Γ_f, which is in violation of the assumptions introduced when deriving the resonance parameter correction in equation (3.4.24).

The multi-group inputs that contribute significant uncertainty to k_∞ for the LWR fuel cells are also those that correspond to the primary fission-source ($U^{235}_{n,f}$, $U^{235}_{\bar{\nu}}$, U^{235}_{χ}, $U^{238}_{n,f}$, $U^{238}_{\bar{\nu}}$, U^{238}_{χ}), neutron absorption ($U^{238}_{n,\gamma}$, $U^{235}_{n,\gamma}$, $H^{1}_{n,\gamma}$) and neutron slowing-down ($H^{1}_{elastic}$, $O^{16}_{elastic}$) terms in the neutron transport equation. This is a logical result, since the reactions in question are highly linked to k_∞. It is also noteworthy that when comparing uncertainties between LWR fuel cell types, the contribution by each input shows only small variation, and that the rank of importance of each uncertain input is identical. Likewise, the one-dimensional equivalent models of the fuel cells showed excellent agreement with the true, two-dimensional geometry in tems of relative uncertainty. This is the case even for the Kozloduy-6 VVER cell, which showed a 5 mk difference in the best-estimate k_∞ prediction depending on dimensionality. In fact, the relative uncertainties of k_∞ for each fuel cell model in tables 3.12 through 3.14 show close consistency despite the dissimilar value in the underlying best-estimate values of k_∞ shown in table 3.11.

Despite the clear error in propagating $U^{238}_{n,\gamma}$ cross-section covariance in the resolved resonance range, SCALE-SS demonstrates that the statistical sampling procedure can, in general, be a useful and capable tool in performing lattice physics uncertainty analysis. As the only noteworthy discrepancies between the statistical sampling method and the adjoint-based TSUNAMI method were related to self-shielding, it suggests that the key to propagating all multi-group input uncertainties accurately is the correct adjustment of related inputs, such as resonance parameters. However, the resonance parameters used by NITAWL for self-shielding by the Nordheim integral method are not well-suited to adjustments derived from perturbations in multi-group cross-sections. As a result of the difficulties with NITAWL, another transport code involving different resonance parameters was adopted for the lattice uncertainty investigations in this dissertation.

3.5 DINOSAUR

The main focus of this dissertation was the development of DINOSAUR, and its application to LWR and CANDU lattice physics uncertainty propagation. DINOSAUR propagates uncertainties using both a statistical sampling and direct numerical perturbation technique. After the successful demonstration of the statistical sampling method using SCALE (as well as the evident importance of resonance parameter correction), the statistical sampling method was deployed with the Canadian Industry Standard Toolset (IST) lattice code DRAGON. As with SCALE-SS, DINOSAUR creates new multi-group nuclear data libraries whose data has been modified compared to a set of reference data. The solution of the lattice physics equations applied to each new library is performed using the code DRAGON. The resonance parameters used by DRAGON for self-shielding are better suited to corrections due to multi-group perturbation, and thus DRAGON resonance parameters are adjusted by DINOSAUR to provide correct consideration of self-shielding effects on the evolution of covariance through the lattice calculation sequence.

DRAGON is a modular lattice code that solves lattice problems by executing a calculation sequence. An input deck is used to specify problem-specific parameters such as the geometry to be solved and the composition and temperatures of material mixtures, as well as to describe how the calculation is to be performed, by specifying execution parameters for each module that is employed. A flow diagram of a typical DRAGON lattice calculation sequence is shown in figure 3.10. Some steps of the lattice sequence can be accomplished by several different modules in DRAGON, the choice of which depends on problem-specific considerations, and therefore not every DRAGON sequence is identical. Figure 3.10 is an example of one possible sequence, and happens to be the one used for the DRAGON lattice calculations performed in this dissertation.

Several nuclear data library formats are supported by DRAGON. The library used in this dissertation is the *IAEA* 69-group library in a WIMS-D4 format. The *IAEA* library is freely available from the International Atomic Energy Agency (IAEA) along with associated documentation. The WIMS-D4 library format is included in the IAEA documentation. A detailed format description of the library is essential when modifying the library data with sampled or numerically perturbed values.

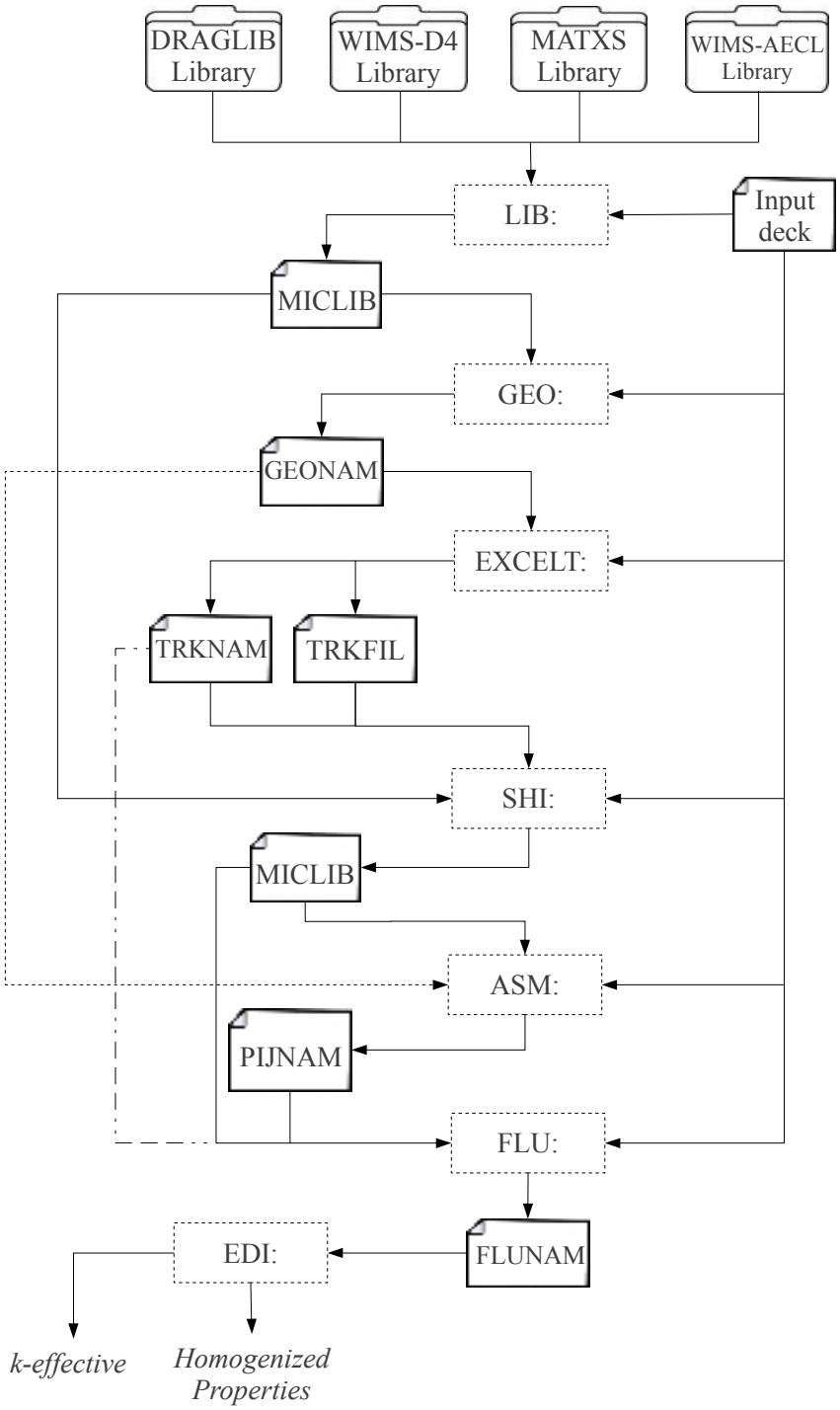

Figure 3.10: DRAGON lattice calculation sequence

Item	Description
DRAGLIB	Multi-group cross-section library in the DRAGLIB format
MATXS	Multi-group cross-section library in the MATXS format
WIMS-D4	Multi-group cross-section library in the WIMS-D4 format
WIMS-AECL	Multi-group cross-section library in the WIMS-AECL format
LIB:	Interpolates microscopic cross-sections and calculates macroscopic cross-sections for each mixture
GEO:	Reads lattice cell geometry, associates macroscopic cross-sections with spatial regions
EXCELT:	Tracking module for 2D and 3D geometries
SHI:	Performs self-shielding calculations; shielded cross-sections written to MICLIB
ASM:	Generates collision probability matrix
FLU:	Solves the neutron transport equation
EDI:	Editing module for recording problem data
MICLIB	Contains microscopic and macroscopic cross-sections
GEONAM	Contains geometry data
TRKNAM	Contains region volumes, surface area vectors and other tracking information
TRKFIL	Contains track lengths
PIJNAM	Contains collision probability matrices
FLUNAM	Contains transport solution

Table 3.15: DRAGON lattice sequence component description

3.5.1 WIMSD4-format IAEA library

During the 1990s, the IAEA identified the need to update the aging WIMS-D4 libraries with the latest nuclear data. It subsequently launched the WIMS Library Update Project (WLUP) to produce new WIMS-D4 format libraries that would replace the existing WIMS-D4 library, which was based on evaluated nuclear data from the early 1960s. The resulting 69 energy group *IAEA* library contains data for 173 materials, whose data sources are several evaluated nuclear data files, including ENDF/B-VI, JENDL-3.2, FOND-2.2, CENDL-2.1, CENDL-3 and JEF-2.2. A full list of materials and other library data is available in WLUP documentation.

Validation of the library was performed as part of the WLUP project by using library data to predict lattice parameters of over 200 benchmark cases of varying

Group	Upper energy limit (eV)	Group	Upper energy limit(eV)	Group	Upper energy limit(eV)
1	1.00E+007	25	2.77E+001	49	3.50E-001
2	6.07E+006	26	1.60E+001	50	3.20E-001
3	3.68E+006	27	9.88E+000	51	3.00E-001
4	2.23E+006	28	4.00E+000	52	2.80E-001
5	1.35E+006	29	3.30E+000	53	2.50E-001
6	8.21E+005	30	2.60E+000	54	2.20E-001
7	5.00E+005	31	2.10E+000	55	1.80E-001
8	3.03E+005	32	1.50E+000	56	1.40E-001
9	1.83E+005	33	1.30E+000	57	1.00E-001
10	1.11E+005	34	1.15E+000	58	8.00E-002
11	6.73E+004	35	1.12E+000	59	6.70E-002
12	4.09E+004	36	1.10E+000	60	5.80E-002
13	2.48E+004	37	1.07E+000	61	5.00E-002
14	1.50E+004	38	1.05E+000	62	4.20E-002
15	9.12E+003	39	1.02E+000	63	3.50E-002
16	5.53E+003	40	9.96E-001	64	3.00E-002
17	3.52E+003	41	9.72E-001	65	2.50E-002
18	2.24E+003	42	9.50E-001	66	2.00E-002
19	1.43E+003	43	9.10E-001	67	1.50E-002
20	9.07E+002	44	8.50E-001	68	1.00E-002
21	3.67E+002	45	7.80E-001	69	5.00E-003
22	1.49E+002	46	6.25E-001		1.00E-005
23	7.55E+001	47	5.00E-001		
24	4.81E+001	48	4.00E-001		

Table 3.16: *IAEA* energy group boundaries

configurations. The WIMS-D4 code using the *IAEA* library predicted the reactivity of H_2O moderated UO_2 (<6 wt% U^{235}) critical experimental assemblies to within 1% for most cases. For D_2O moderated UO_2 critical lattices, the predicted values fell within the experimental uncertainties for all eleven benchmark cases. The validation conducted by the IAEA WLUP participants demonstrates that the *IAEA* library is adequate for use in both LWR and heavy water reactor (HWR) analysis.

Cross-Sections

There is a fixed number of cross-sections and multi-group parameters stored in the *IAEA* library (see table 3.17), which is rigidly enforced by the WIMS-D4 format. The cross-sections that are included are those that are necessary for solving the lattice equations with little redundancy or additional information present.

Every material in the library (except dosimetry materials) possesses XT, XA and P_0 data in 69 energy groups. Fissionable nuclides also have associated XF and VF data, and common moderating materials (H^1, H^2 O^{16}, C^{12}) possess a P_1 scattering matrix. A sole fission spectrum, χ, is contained in the library and is nuclide-independent, having been constituted from the weighted averaging of the spectra of U^{235} (54%), U^{238} (8%) and Pu^{239}(38%). The spectrum is recorded only for the fastest 27 energy groups, with no data fields allocated for the appearance of fission neutrons in the remaining groups.

ID	Reaction/ parameter	Description
XT	(n, total)	Total neutron cross-section
XA	(n, abs)	Neutron absorption cross-section
XF	(n, f)	Fission cross-section
CHI	χ	Nuclide-independent spectrum of fission neutron initial energy
VF	$\bar{\nu}\sigma_f$	Fission yield cross-section
P_0	(n, n_o)	Group-to-group P_0 scattering cross-section matrix
P_1	(n, n_o)	Group-to-group P_1 scattering cross-section matrix

Table 3.17: *IAEA* cross-sections

Neutron producing processes, such as (n, 2n) and (n, 3n) are not explicitly referenced, so their influence is embedded in other stored data. The shedding of neutrons, when thought of as being opposite to absorbing neutrons, can equivalently be expressed as a negative absorption. Therefore, (n, 2n) and (n, 3n) are amalgamated with absorption reactions, but contribute their cross-section along with a negative sign.

$$XA \equiv \sigma_{(n,\gamma)} + \sigma_{(n,f)} + \sigma_{(n,\alpha)} + \sigma_{(n,p)} + \cdots - \sigma_{(n,2n)} - 2\sigma_{(n,3n)} \tag{3.5.1}$$

The (n, xn) processes are threshold reactions with considerable cross-sections in heavy nuclei that tend to eclipse other neutron absorption events. Therefore, the absorption cross-sections stored in *IAEA* are often negative for nonfissionable heavy nuclides in the fastest few energy groups, by virtue of the large cross-sections of (n, xn) at those energies and the formulation in equation (3.5.1). In the case of fissionable nuclides, the difference between the absorption and fission cross-sections, XA−XF, may be negative, similarly revealing the signature of (n, xn) cross-sections. For example, figures 3.11 through 3.13 show the cross-section of $U^{238}_{n,2n}$ and that of another significant absorption process, $U^{238}_{n,\gamma}$.

Likewise, the group-to-group scattering matrices in *IAEA* reflect contributions of (n, xn) neutron emissions.

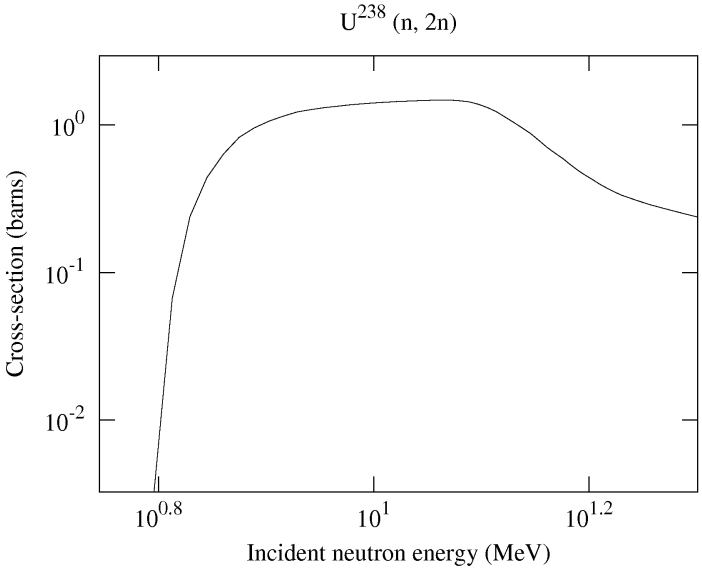

Figure 3.11: U^{238} (n, 2n) cross-section, ENDF/B-VI.8

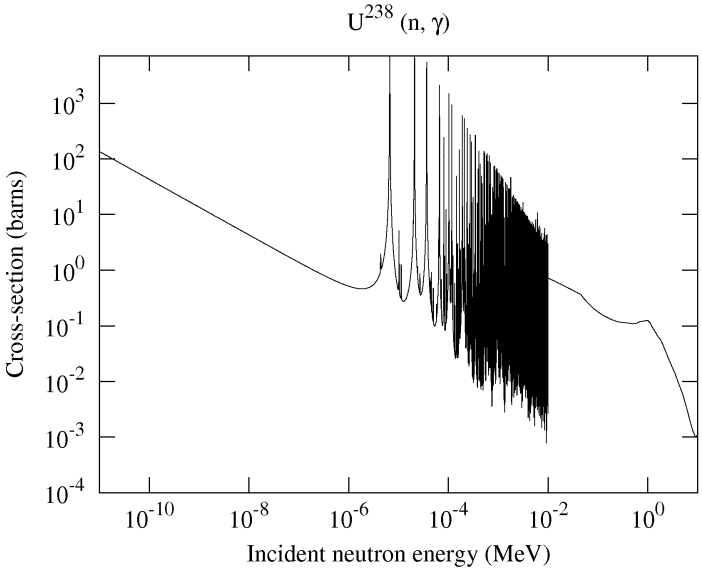

Figure 3.12: U^{238} (n, γ) cross-section, ENDF/B-VI.8

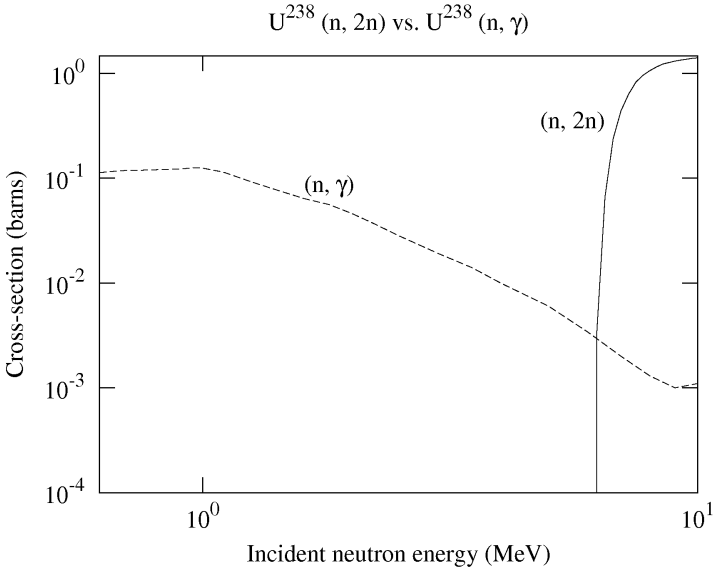

Figure 3.13: Cross-sections comparison near the U^{238} (n, 2n) threshold

$$P_{0,g\to g} \equiv \sigma_{s_0,g\to g} + 2\sigma_{(n,2n),g\to g} + 3\sigma_{(n,3n),g\to g} \tag{3.5.2}$$

Resonance Parameters

The resonance parameters in the *IAEA* library are fundamentally based on a Bondarenko-type method, similar to the Bondarenko Factors described in section 3.4.1, and consist of *resonance integrals* that are tabulated by temperature and background cross-section. A resonance integral is, in general, a function involving a continuous-energy cross-section integrated over the energies of one or more resonances. The most simple form of a resonance integral is merely the cross-section integrated over a single resonance.

$$I = \int_{res} \sigma(E)dE \tag{3.5.3}$$

More complicated resonance integrals involve the integration over multiple resonances, for example all the resonances in an energy group, of the product of a cross-section and weighting function (i.e. neutron flux),

$$I_g = \int_g \sigma(E)\phi(E)dE \tag{3.5.4}$$

Recall that a self-shielded, group cross-section is defined as,

$$\bar{\sigma}_g = \frac{\int_g \sigma(E)\phi(E)dE}{\int_g \phi(E)dE} \tag{3.5.5}$$

If the resonance integral in equation (3.5.4) is calculated over an entire energy group, then the self-shielded cross-section in equation (3.5.5) is reduced to,

$$\bar{\sigma}_g = \frac{I_g}{\int_g \phi(E)dE} \tag{3.5.6}$$

Moreover, in the resonance region, the neutron flux tends to vary as $1/E$, thus,

$$\bar{\sigma}_g = \frac{I_g}{ln(E_g/E_{g-1})} = \frac{I_g}{u_g} \tag{3.5.7}$$

Where, E_g and u_g are the upper-energy limit and lethargy width, respectively, of group g. As this simplified example demonstrates, the use of resonance integrals can be convenient when computing self-shielded cross-sections.

The resonance parameters stored in *IAEA*, which is a WIMS-D4 format library, are naturally intended to be compatible with the resonance self-shielding calculations performed by WIMS-D4, therefore a brief description of the WIMS self-shielding formulation is warranted in this section. Unlike the slowing-down equation solved by NITAWL (equation 3.4.2), which accounts for system heterogeneities by using a Dancoff factor, the basis of WIMS resonance self-shielding is the following expression for an infinite, homogeneous medium.

$$\Sigma_T(E)\phi(E) = \sum_i \frac{1}{1-\alpha_i} \int_E^{E/\alpha_i} \Sigma_s^i(E')\phi(E')\frac{dE'}{E'} \tag{3.5.8}$$

where,

$$\alpha_i = \left(\frac{A_i - 1}{A_i + 1}\right)^2 \tag{3.5.9}$$

and,

A_i	is the equivalent number of neutron masses of nuclide i
Σ_T	is the total macroscopic cross-section of the mixture
Σ_s^i	is the macroscopic scattering cross-section of nuclide i, assumed to be isotropic
ϕ	is the neutron flux

After the application of several simplifying assumptions, which are described elsewhere[62], the expressions for the self-shielded cross-sections are ultimately reduced to,

$$\bar{\sigma}_a(T,\sigma_b) = \frac{I_a(T,\sigma_b)}{1-\frac{I_a(T,\sigma_b)}{\sigma_b}} \tag{3.5.10}$$

$$\bar{\sigma}_{\nu f}(T,\sigma_b) = \frac{I_{\nu f}(T,\sigma_b)}{1-\frac{I_{\nu f}(T,\sigma_b)}{\sigma_b}} \tag{3.5.11}$$

where,

$\bar{\sigma}_a$	is the shielded absorption cross-section
$\bar{\sigma}_{\nu f}$	is the shielded fission yield cross-section
I_a	is the absorption resonance integral
$\mathrm{I}_{\nu f}$	is the fission yield resonance integral
T	is temperature
σ_b	is equal to $\delta_r \sigma_p^r + \sigma_o$
δ_r	is the Goldstein-Cohen intermediate resonance factor
σ_p^r	is the potential scattering cross-section of the resonant absorber
σ_o	is the background cross-section arising from all other nuclides, with units of barns per absorber atom

The resonance integrals, I_a and $I_{\nu f}$ stored on the library have been calculated in a somewhat circular way,

$$I_a(T,\sigma_b) = \frac{\bar{\sigma}_a(T,\sigma_b)\sigma_b}{\bar{\sigma}_a(T,\sigma_b)+\sigma_b} \tag{3.5.12}$$

$$I_{\nu f}(T,\sigma_b) = \frac{\bar{\sigma}_{\nu f}(T,\sigma_b)\sigma_b}{\bar{\sigma}_a(T,\sigma_b)+\sigma_b} \tag{3.5.13}$$

The shielded absorption and fission yield cross-sections of equations (3.5.12) and (3.5.13) have been calculated for each group of the reference *IAEA* library by the GROUPR module of the cross-section processing code NJOY[8] according to the formulation shown below.

$$\bar{\sigma}(T,\sigma_b) = \frac{\int_g \frac{\sigma(T,\mu)d\mu}{\sigma_t(T,\mu)+\sigma_b}}{\int_g \frac{d\mu}{\sigma_t(T,\mu)+\sigma_b}} \tag{3.5.14}$$

For problem temperatures and dilutions other than the those for which the resonances integrals have been tabulated, an interpolation strategy is used to estimate values of resonance integrals that correspond to the problem specifications.

3.5.2 69GROUPV6REC covariance library

The 69-group *IAEA* library demands an identically-sized covariance matrix that holds the associated uncertainty information. A covariance matrix of the correct size can be generated by one of two ways. The matrix can be collapsed by a flux-weighting directly from the high-resolution ENDF data files to the desired group structure by using a cross-section processing code such as the ERRORR module of NJOY. Alternatively, an existing multi-group covariance library can be linearly interpolated to a new energy group structure that does not vary radically from the original in terms of the number of groups as well as the total energy range spanned collectively by all groups. The latter approach was adopted for this work. While the collapsing of a new covariance directly from the nuclear data files is more mathematically rigorous, the resulting covariance would not have been subjected to the level of scrutiny, evaluation, or calibration that was afforded to, for example, the *44GROUPV6REC* library from its evaluators at ORNL. Therefore, all of the mathematical approximation that accompanied a linear interpolation of the covariance was deemed to be less important than the expert judgement buried in the 44-group ORNL covariance library.

The code ANGELO2 [63] was used to perform a covariance interpolation from the 44-group structure (see table 3.4) of *44GROUPV6REC* to the 69-group structure (see table 3.16) of the *IAEA* library. A limitation of the ANGELO2 code is its inability to process covariance data between cross-sections of different nuclides. Aside from the omission of nuclide-to-nuclide covariances, the uncertainty content of the interpolated library is identical to the original, and thus *69GROUPV6REC* contains covariances for the same nuclides and cross-sections listed in table 3.7.

3.5.3 Procedures and rules

DINOSAUR propagates uncertainties by varying the values of variables used as inputs during successive calls to the lattice code DRAGON. The varied nuclear data inputs are stored in a collection of new multi-group libraries, and varied model parameter inputs are stored on a collection of DRAGON input decks. In a similar manner as SCALE-SS, there is minimal direct interaction between the uncertainty propagation routines of DINOSAUR and the lattice solver itself. The lattice uncertainty propagation sequence of DINOSAUR consists of eleven modules that perform a variety of functions, and is shown in figure 3.14.

Uncertainty propagation procedure

DINOSAUR has the capability to propagate nuclear data uncertainties using both a statistical sampling and a direct numerical perturbation approach. The statistical sampling method of DINOSAUR is essentially identical to that of SCALE-SS, but with the additional capability of sampling data according to a uniform distribution. Naturally, when nuclear data is modified by DINOSAUR, either through direct per-

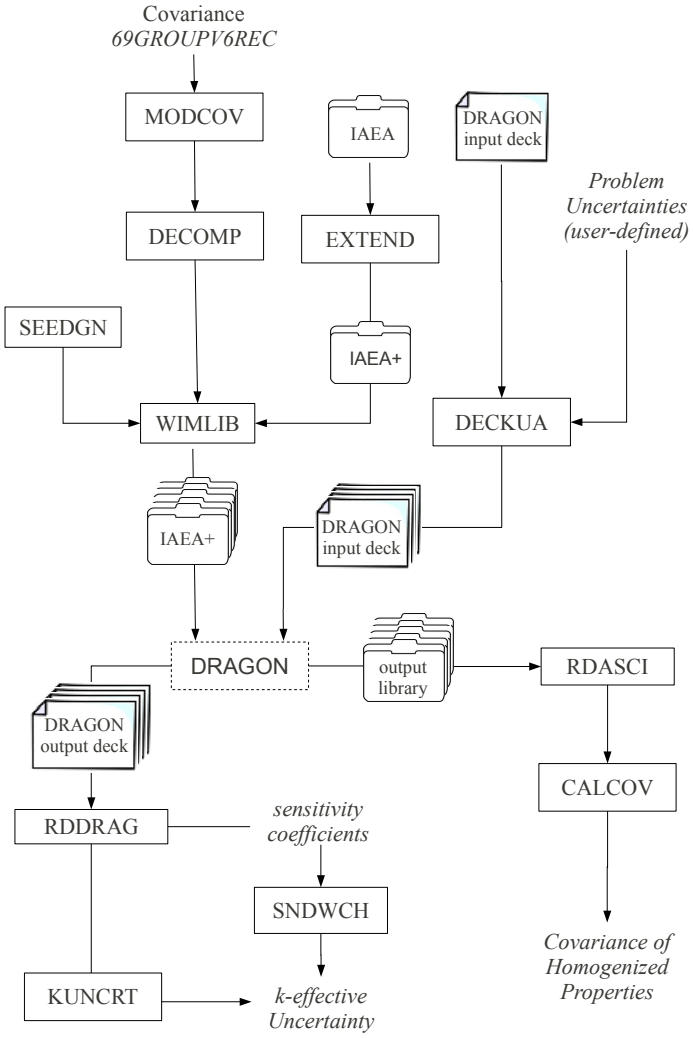

Figure 3.14: DINOSAUR uncertainty propagation sequence

turbation or statistical sampling, a set of consistency rules are enforced to ensure that dependent quantities such as aggregate cross-sections and resonance parameters are adjusted to reflect the changes in the sampled or perturbed inputs.

When activated in direct numerical perturbation mode, DINOSAUR follows a series of calculation steps, with one parameter perturbed at a time, first across all energy groups, and then repeating such calculations for all reactions and all isotopes. DINOSAUR creates, for a single given reaction $\big($e.g. (n, γ)$\big)$, 69 new WIMS-D4 format libraries, with each library containing a perturbed value of that cross-section in a single energy group. This is achieved by multiplying the value in question by a perturbation factor, $(1+\delta)$, that is supplied by the user of DINOSAUR. DINOSAUR subsequently calls the code DRAGON 69 times, with each DRAGON call reading one of the perturbed libraries. The resulting changes in k_∞ indicate its sensitiv-

Item	Description
IAEA	Multi-group cross-section library in the WIMS-D4 format
69GROUPV6REC	Covariance matrix in 69 energy groups
Input Deck	Problem-specific modelling parameters
Problem Uncertainties	Probability distributions of input deck modelling parameters
MODCOV	Translates the covariance from its ENDF format to a format used by DINOSAUR
DECOMP	Performs an eigenvalue decomposition of the covariance
EXTEND	Increases the byte length of the IAEA library to accommodate a 69-group fission spectrum, χ
IAEA+	IAEA library with extended fission spectrum
SEEDGN	Generates a set of unique random seeds when DINOSAUR is launched in multi-threaded mode
WIMLIB	Generates a set of random or perturbed WIMS-D4 libraries based on a reference library
DECKUA	Generates a set of random DRAGON input decks based on a reference deck
DRAGON	DRAGON lattice calculation sequence, equivalent to figure 3.10
Output deck	DRAGON lattice sequence output summary
RDDRAG	Extracts k_∞ from output deck, and calculates sensitivities when in perturbation mode
KUNCRT	Calculates $\Delta^2 k$ statistically from a population of k_∞
Sensitivity coefficients	Partial derivatives, dimensionless sensitivity coefficients and sensitivities per unit lethargy
SNDWCH	Calculates $\Delta^2 k$ using the sandwich rule
Output Library	Homogenized multi-group cross-section library in ASCII format
RDASCI	Parses output libraries and extracts homogenized cross-sections and flux
CALCOV	Calculates covariance and correlation matrices for homogenized cross-sections and flux

Table 3.18: DINOSAUR uncertainty propagation sequence component description

ity with respect to each input, which are subsequently used with the covariance *69GROUPV6REC* to calculate the uncertainty of k_∞, $\Delta^2 k$, arising from the cross-section using the sandwich rule. For lattice calculations like those shown in chapter 4 and chapter 5, there are about twenty reactions of statistical significance (spanning all isotopes), which demand approximately 1400 (20×69) DRAGON calculations. The current implementation of the sandwich rule in DINOSAUR neglects the effects of covariance between reactions, therefore, the calculation of the total $\Delta^2 k$ uncertainty reported by DINOSAUR in direct numerical perturbation mode is estimated by taking the root-sum-of-squares of the uncertainty contribution of each cross-section, which is a precise determination if and only if the reaction cross-sections are independent. As shown in chapters 4 and 5, the good agreement between the total cross-section uncertainty from the direct numerical perturbation mode and the statistical sampling mode (which *does* account for reaction-to-reaction covariance), indicates that such covariance is not a dominant effect in the overall uncertainties of cross-sections on lattice reactivity.

Whether propagating uncertainties through statistical sampling or direct numerical perturbation, the reference *IAEA* must be subject to a minor correction on its fission spectrum, χ. Initially the reference library contains a spectrum record length sufficient to store χ values for 27 energy groups. The DINOSAUR module EXTEND lengthens the library, modifying all relevant format flags and record length indicators, so that the spectrum spans all 69 groups. The newly formed groups are then set to an identical nonzero quantity that is two orders of magnitude smaller than the smallest pre-existing value found in the first 27 groups. The entire spectrum is then renormalized. The extension of the spectrum in this manner is necessary to accommodate potentially large uncertainties associated with the fission spectrum at low energies, and the artificial increase in thermal spectrum has been found to be sufficiently small as to not change the best-estimate calculation of k_∞ when applied to several thermal LWR test cases.

In addition to propagating uncertainties associated with variables in the *IAEA* multi-group nuclear library, DINOSAUR has the capability to propagate uncertainties in DRAGON problem-specific input deck parameters, such as material temperatures and densities, component geometries and so on. The user can create a table of distributions and associate each distribution with one or more parameters that appear in a DRAGON input deck. Each distribution is specified by a distribution type (Gaussian or uniform), relative variance and mean. DINOSAUR will then create a collection of random input decks whose uncertain parameters are statistically sampled according to their specified distributions in a similar manner as is performed when sampling multi-group nuclear data.

Cross-Section Consistency Rules

The cross-section consistency rules enforced when DINOSAUR makes changes to WIMS-D4 format libraries have some commonalities with the corresponding rules

used by SCALE-SS, but include an additional set of assumptions. Namely, in addition to updating aggregate cross-sections with new totals derived from changes to fundamental cross-sections, DINOSAUR must first derive fundamental cross-sections from the reference aggregate cross-sections. Unlike the AMPX-format library accessed by SCALE, the WIMS-D4 library does not store records of most fundamental multigroup parameters. Only the fission cross-section, (n, fission), and fission neutron yield, $\bar{\nu}$, are explicitly or implicitly described in their entirety. Other fundamental processes, such as (n, γ), (n, 2n) and elastic scattering must be estimated from the library's aggregate cross-sections, (n, total) and (n, absorb), while exploiting pertinent underlying theory to compose sound assumptions when necessary.

ID	Description	Rule
XS	(n, n_o)	Elastic scatter set to XS = XT - XA
X2N	(n, 2n)	For each group, equal to the magnitude of XG, only when XG is negative
XG	(n, γ)	Set to XG = XA - XF + X2N
	(n, α)	Alpha production assumed zero
	(n, n$'\gamma$)	Inelastic scattering assumed zero
NU	$\bar{\nu}$	Set to ratio of XV/XF
CHI	χ	Linked to a single fissionable nuclide (i.e. U^{235})

Table 3.19: DINOSAUR fundamental cross-section rules

The first rule in table 3.19 states that elastic scattering is the balance between the absorption and total cross-sections. Strictly, this difference is in fact the sum of both elastic and inelastic scattering. However, the inelastic scattering cross-section tends to be small for low mass number nuclides, and hence for the moderating materials that dominate the slowing-down behavior of the system. Inelastic scattering does not exist at all in the case of hydrogen-1. Even for heavy nuclides, such as U^{238}, the inelastic cross-section only becomes appreciable compared to its elastic counterpart at energies near 1 MeV and higher. The elastic and inelastic cross-sections for these materials is shown in figures 3.15 through 3.17.

The second rule involves the (n, 2n) cross-section. Recall from equation (3.5.1) in section 3.5.1 that the net effect of (n, xn) reactions is incorporated into the absorption cross-section, XA. Due to the nature of (n, xn), they typically are associated with large cross-sections above their threshold energies for heavy nuclei, that drives XA below zero, or alternately, to a value less than XF for fissionable nuclei. Since, for heavy nuclei, (n, 2n) in particular tends to be so large compared to other neutron absorbing reactions, the approximation is made that (n, 2n) represents the entire absorption cross-section where it exists, and other absorbing reactions such as (n, γ) are neglected and assumed to be zero.

The next three rules are related to the second, and sets the radiative capture cross-section equal to the difference between the total absorption cross-section, XA,

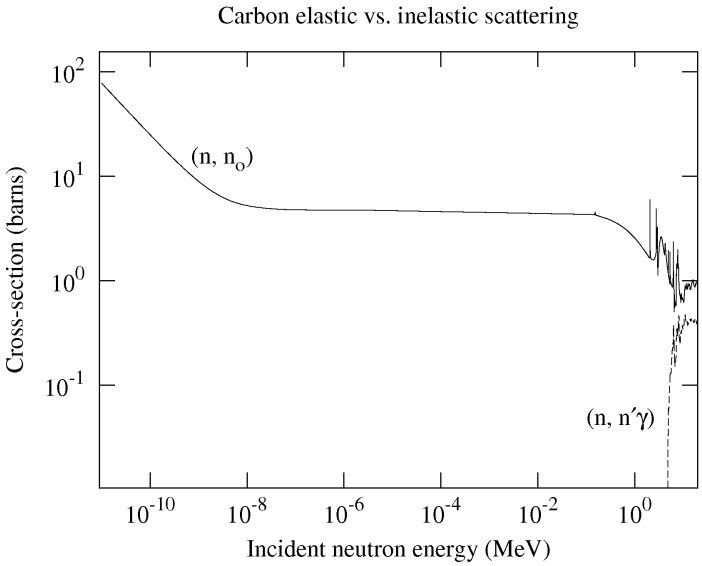

Figure 3.15: Elemental carbon scattering cross-sections, ENDF/B-VI.8

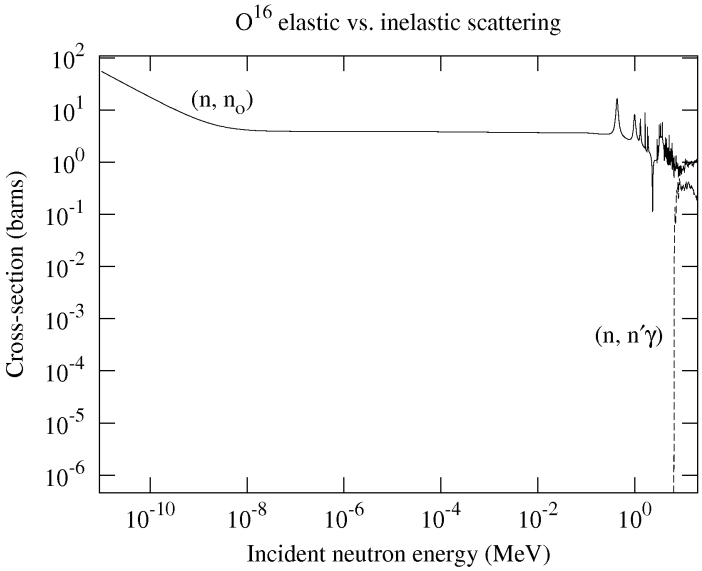

Figure 3.16: O^{16} scattering cross-sections, ENDF/B-VI.8

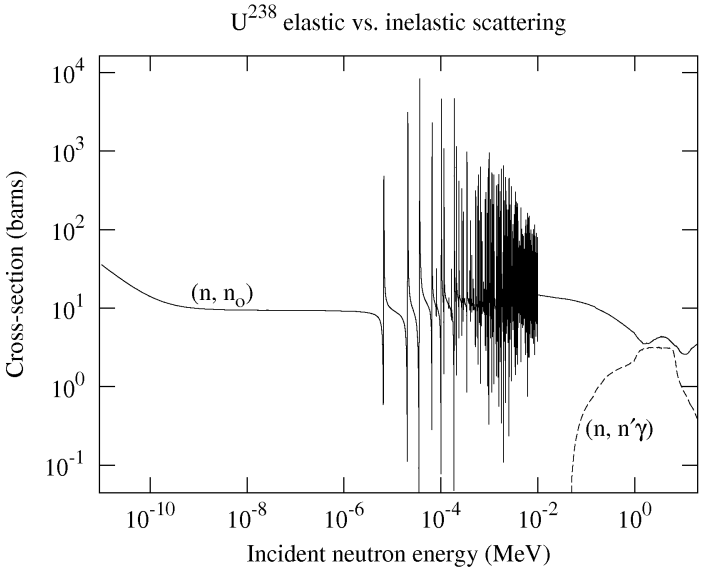

Figure 3.17: U^{238} scattering cross-sections, ENDF/B-VI.8

and the magnitude of the fission cross-section XF and the (n, 2n) cross-section, X2N, that was computed according to the second rule. This rule can be stated equivalently by defining the capture cross-section, XG, to be zero whenever X2N is nonzero, and to be the difference between XA and XF otherwise. For a given nuclei, in no energy group can XA and X2N be simultaneously nonzero. Estimating the capture cross-section in this way is implicitly assuming that other absorbing reactions such as (n, α), (n, 3n) and (n, p) all cause negligible contributions to the absorption cross-section compared to (n, γ) and (n, 2n). While not entirely justifiable at all energies, no better assumption can be made given the multi-group information that is present in a WIMS-D4 format library.

The rule for defining the fission neutron yield, $\bar{\nu}$, is straightforward and without approximation, and is merely the recognition of the ratio of the fission yield cross-section, VF, and fission cross-section, XF, both of which are stored for all energy groups in the library.

The final rule concerns the problem-independent, library fission spectrum, χ. To propagate spectrum uncertainties, the spectrum must be associated with a single fissionable nuclide, in order to establish which covariance data should be used to represent the uncertainty of the spectrum. For thermal, uranium-fueled LWR lattices, nearly all the fissions are of U^{235} nuclei, therefore the assumption can be made that the U^{235} covariance be applied to the library fission spectrum. This selection of nuclide is not mandatory, however, and is left to the discretion fo the user of DINOSAUR.

Once the fundamental parameters, XS, XG, X2N, XF and NU have been determined or estimated, they can be modified by DINOSAUR through either statis-

tical sampling or direct numerical perturbation. Afterwards, the inverse of the rules in table 3.19 are implemented to re-calculate the aggregate cross-sections using the new totals of the modified fundamental data. Changes to the scattering cross-section are reflected by a corresponding consistency adjustment to the group-to-group scattering tables in a way identical to SCALE-SS, which is described in general in section 3.3.1.

Resonance Parameter Consistency Rules

The resonance parameter consistency rules used in DINOSAUR result in adjustments to the resonance integrals shown in equations (3.5.12) and (3.5.13), that are derived from changes in the weighted multi-group cross-sections. Continuous-energy cross-sections are used as an intermediary parameter when relating the integrals to the weighted group cross-sections, similar to the equations that related the SCALE Bondarenko Factors to the same. Recall the self-shielded, homogeneous medium cross-sections in equation (3.5.14) that are computed by the GROUPR module of NJOY, and used in the calculation of the *IAEA* library resonance integrals. Given the derivation of a perturbed continuous energy cross-section in equation (3.4.13) of section 3.4.3, a perturbed GROUPR self-shielded cross-section can be defined as,

$$\bar{\sigma}'(T,\sigma_b) = \frac{\int_g \frac{(1+\delta)\sigma(T,\mu)d\mu}{\sigma_t(T,\mu)+\delta\sigma+\sigma_b}}{\int_g \frac{d\mu}{\sigma_t(T,\mu))+\delta\sigma+\sigma_b}} \tag{3.5.15}$$

$$= (1+\delta)\frac{\int_g \frac{\sigma(T,\mu)d\mu}{\sigma_t(T,\mu)+\delta\sigma+\sigma_b}}{\int_g \frac{d\mu}{\sigma_t(T,\mu))+\delta\sigma+\sigma_b}} \tag{3.5.16}$$

$$= (1+\delta)\frac{\int_g \frac{\sigma(T,\mu)d\mu}{\sigma_t(T,\mu)+\sigma'_b}}{\int_g \frac{d\mu}{\sigma_t(T,\mu))+\sigma'_b}} \tag{3.5.17}$$

$$= (1+\delta)\bar{\sigma}(T,\sigma'_b) \tag{3.5.18}$$

where,

$1+\delta$	is a perturbation factor which was applied to the weighted cross-section, σ
μ	is neutron lethargy $\big($see equation (3.4.14)$\big)$
$\sigma(T,\mu)$	is the unperturbed continuous-energy cross-section
$\sigma_t(T,\mu)$	is the unperturbed continuous-energy total cross-section
$\bar{\sigma}(T,\sigma_b)$	is the unperturbed shielded cross-section in group g evaluated at σ_b and T
σ_o	is the unperturbed background cross-section
σ'_b	is the *effective* perturbed background cross-section, $\sigma'_b = \sigma_b + \delta\sigma$
T	is temperature
$\bar{\sigma}'(T,\sigma_b)$	is the perturbed shielded cross-section in group g evaluated at σ_o and T

The familiar consequence again emerges that the perturbing of a weighted cross-section requires the evaluation of the shielded cross-section at a modified background, σ'_o. This is accomplished in DINOSAUR by a multi-step procedure. First, the unperturbed self-shielded absorption and fission yield cross-sections are calculated by re-arranging equations (3.5.12) and (3.5.13) and solving for σ_a and $\sigma_{\nu f}$,

$$\bar{\sigma}_a(T,\sigma_b) = \frac{I_a(T,\sigma_b)\sigma_b}{\sigma_b - I_a(T,\sigma_b)} \tag{3.5.19}$$

$$\bar{\sigma}_{\nu f}(T,\sigma_b) = \frac{I_{\nu f}(T,\sigma_b)\sigma_b}{\sigma_b - I_a(T,\sigma_b)} \tag{3.5.20}$$

where, $I_a(T,\sigma_b)$ and $I_{\nu f}(T,\sigma_b)$ are found in the table of resonance integrals, and σ_b and T are provided by the library as resonance table indexing parameters. Each $\bar{\sigma}(T,\sigma_o)$ that is implicitly given in the resonance integral tables must be substituted by $\bar{\sigma}(T,\sigma'_o = \sigma_o + \delta\sigma_t)$. DINOSAUR calculates the values of $\bar{\sigma}(T,\sigma'_o)$ by linearly interpolating between the given values of $\bar{\sigma}(T,\sigma_o)$. After DINOSAUR has interpolated for $\bar{\sigma}(T,\sigma'_o)$, they are used in the calculation of perturbed self-shielded cross-sections, as shown below.

$$\bar{\sigma}'(T,\sigma_b) = (1+\delta)\bar{\sigma}(T,\sigma'_b) \tag{3.5.21}$$

which are subsequently used to re-calculate new integrals for the resonance table.

$$I'_a(T,\sigma_b) = \frac{\bar{\sigma}'_a(T,\sigma_b)\sigma_b}{\bar{\sigma}'_a(T,\sigma_b)+\sigma_b} = \frac{(1+\delta_a)\bar{\sigma}_a(T,\sigma'_b)\sigma_b}{(1+\delta_a)\bar{\sigma}_a(T,\sigma'_b)+\sigma_b} \tag{3.5.22}$$

$$I'_{\nu f}(T,\sigma_b) = \frac{\bar{\sigma}'_{\nu f}(T,\sigma_b)\sigma_b}{\bar{\sigma}'_a(T,\sigma_b)+\sigma_b} = \frac{(1+\delta_{\nu f})\bar{\sigma}_{\nu f}(T,\sigma'_b)\sigma_b}{(1+\delta_a)\sigma_a(T,\sigma'_b)+\sigma_b} \tag{3.5.23}$$

where the parameters δ_a and $\delta_{\nu f}$ relate to the individual changes in both the absorption and fission yield cross-sections, keeping in mind that DINOSAUR may sample many cross-sections simultaneously. The resonance parameter consistency rules used by DINOSAUR are the implementations of equations (3.5.21) through (3.5.23).

Chapter 4

OECD/NEA UAM benchmark cases results

The code DINOSAUR, which is fully described in chapter 3, was used to generate uncertainty solutions for three light water reactor test cases of the OECD/NEA Uncertainty Analysis in Modelling benchmark. The LWR test cases include BWR, PWR, and VVER pin cell models, whose specifications can be found in figures 3.7 through 3.9 in section 3.4.4. The statistical sampling method, sampling from both normal and uniform distributions, was used to calculate the total uncertainty associated with k_∞, as well as covariance matrices for two-group, spatially-homogenized cross-sections and neutron flux by taking 1024 samples while varying all input cross-sections simultaneously. Additionally, the individual contributions to k_∞ uncertainty was quantified by taking 128 samples for each cross-section, while varying that cross-section alone.

The direct numerical perturbation method was also used to calculate k_∞ uncertainty contributions, as well as its sensitivity to group values of all major uncertainty contributors. Perturbations were performed by subjecting cross-section group values to a multiplicative scaling that varied according to its sensitivity with k_∞ – cross-sections characterized by small sensitivity were perturbed by a larger amount to achieve a sufficiently large change in k_∞ to adequately assess the underlying partial derivative. The most sensitive cross-sections were scaled by 1%, with the scaling gradually increasing to 100% for the decreasingly sensitive cross-sections.

Present in the following sections of this chapter are evaluations of lattice output uncertainties for each LWR cell, consisting of: the relative standard deviation of k_∞, partitioned by its individual uncertainty components; sensitivity profiles of k_∞ with respect to all relevant multi-group inputs; and covariance and correlation matrices for spatially homogenized, two-group lattice properties. The two-group lattice cell output properties of concern are macroscopic total (Σ_T), scatter (Σ_S), absorption (Σ_A), and fission yield ($\nu\Sigma_F$) cross-sections, whose fast/thermal boundary is set to 0.625 eV. Tables of uncertainty contributions to k_∞ as well as sensitivity plots to group-wise cross-sections are shown for each LWR cell in sections 4.2 through 4.4,

and subsequent discussion of all case results can be found in section 4.5.

4.1 Simulation and modelling parameters

The DRAGON lattice sequence that was used by DINOSAUR during the uncertainty propagation procedure is shown in figure 3.10. Thirty integration line angles, and a tracking line density of sixty per centimetre were used as EXCELT tracking parameters for the flux solution by the FLU module on a finely discretized geometry. The SHIBA module performed resonance self-shielding on a more coarse geometry and tracking system. Isotropic return (white) boundary conditions were applied to every lattice cell under investigation.

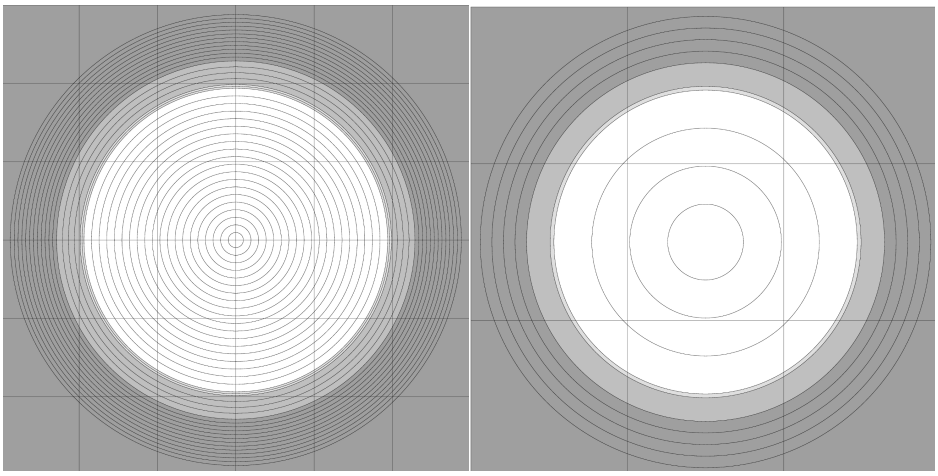

(a) flux solution (b) self-shielding

Figure 4.1: PB-2 DRAGON model discretization

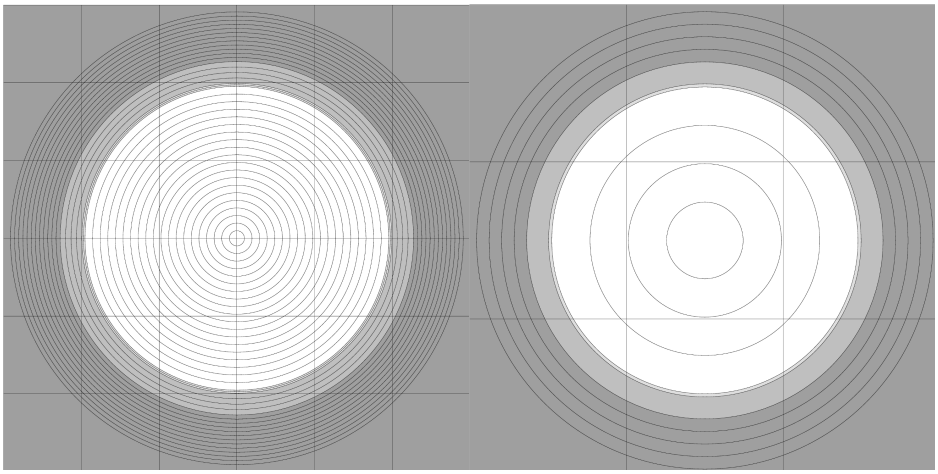

(a) flux solution (b) self-shielding

Figure 4.2: TMI-1 DRAGON model discretization

Lattice cell	Hot zero power	Hot full power
PB-2 BWR	1.33909	1.21328
TMI-1 PWR	1.42480	1.40340
K-6 VVER	1.36718	1.34899

Table 4.1: Best-estimate predictions of k_∞

The best-estimate predictions of k_∞ computed by the DRAGON lattice sequence is shown in table 4.1 for HZP and HFP conditions. The decreases in reactivity associated with HFP cases is the result of Doppler broadening of intermediate-energy radiative capture resonances in fuel and clad material, and a decrease in moderator densities. The latter effect is most pronounced in the case of the PB-2 BWR cell, which is characterized by a 40% coolant/moderator void at full power.

4.2 Peach Bottom unit 2 Boiling Water Reactor

The contributions to PB-2 BWR k_∞ uncertainty at HZP and HFP are shown in tables 4.2 and 4.3, respectively. Dimensionless sensitivity profiles of k_∞ to uncertainty contributors can be found in figures 4.3 to 4.23.

nuclide	reaction/ parameter	Statistical Uniform %Δk/k	Statistical Gaussian %Δ k/k	Direct Perturbation %Δ k/k
All	All	1.0041	1.0043	1.0347
U^{238}	(n, γ)	0.9031	0.8771	0.8734
U^{235}	(n, γ)	0.4160	0.4680	0.4415
U^{235}	(n, fission)	0.2656	0.2486	0.2653
U^{235}	$\bar{\nu}$	0.1513	0.1364	0.1376
U^{238}	$\bar{\nu}$	0.1205	0.1243	0.1178
H^{1}	(n, γ)	0.0517	0.0532	0.0514
O^{16}	(n, γ)	0.0493	0.0431	0.0475
Zr^{Nat}	(n, γ)	0.0461	0.0387	0.0455
U^{238}	(n, fission)	0.0421	0.0427	0.0414
U^{238}	scatter	0.0216	0.0223	0.0215
H^{1}	scatter	0.0181	0.0170	0.0169
O^{16}	scatter	0.0118	0.0106	0.0117
Sn^{118}	(n, γ)	0.0082	0.0090	0.0089
U^{234}	(n, γ)	0.0056	0.0061	0.0065
Hf^{178}	(n, γ)	0.0028	0.0028	0.0032
Cr^{52}	(n, γ)	0.0025	0.0023	0.0025
Zr^{Nat}	scatter	0.0015	0.0017	0.0016
Fe^{Nat}	(n, γ)	0.0011	0.0012	0.0012
U^{235}	scatter	0.0008	0.0007	0.0008

Table 4.2: Contributions to uncertainty in PB-2 k_∞ at HZP

nuclide	reaction/ parameter	Statistical Uniform %Δ k/k	Statistical Gaussian %Δ k/k	Direct Perturbation %Δ k/k
All	All	1.3660	1.3432	1.3865
U^{238}	(n, γ)	1.2278	1.2081	1.2429
U^{235}	(n, γ)	0.4464	0.4606	0.4939
U^{235}	(n, fission)	0.2511	0.2982	0.2747
U^{235}	$\bar{\nu}$	0.1646	0.1730	0.1334
U^{238}	$\bar{\nu}$	0.1350	0.1383	0.1682
U^{238}	(n, fission)	0.0626	0.0610	0.0623
O^{16}	(n, γ)	0.0489	0.0511	0.0507
Zr^{Nat}	(n, γ)	0.0426	0.0471	0.0491
U^{238}	scatter	0.0373	0.0412	0.0382
H^{1}	scatter	0.0250	0.0225	0.0228
H^{1}	(n, γ)	0.0240	0.0246	0.0263
O^{16}	scatter	0.0203	0.0190	0.0197
Sn^{118}	(n, γ)	0.0118	0.0138	0.0133
U^{234}	(n, γ)	0.0077	0.0079	0.0086
Hf^{178}	(n, γ)	0.0035	0.0039	0.0042
Zr^{Nat}	scatter	0.0032	0.0038	0.0037
Cr^{52}	(n, γ)	0.0021	0.0020	0.0022
U^{235}	scatter	0.0013	0.0013	0.0015
Fe^{Nat}	(n, γ)	0.0010	0.0010	0.0010
Fe^{Nat}	scatter	0.0001	0.0001	0.0001

Table 4.3: Contributions to uncertainty in PB-2 k_∞ at HFP

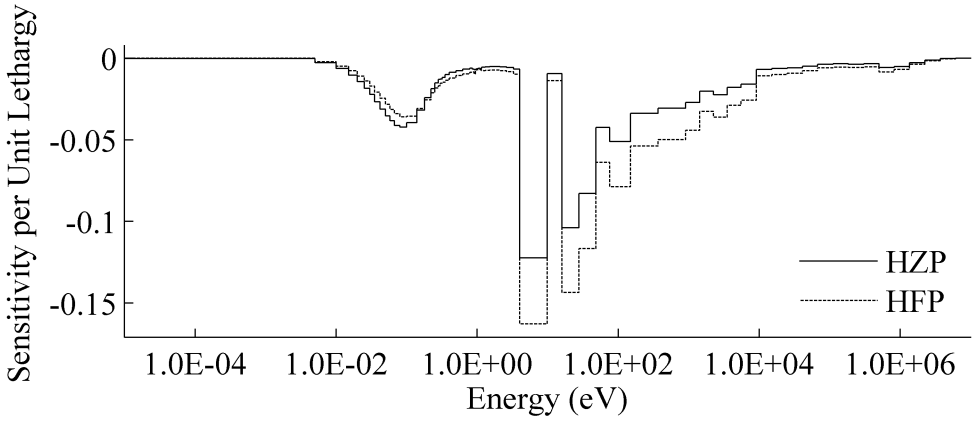

Figure 4.3: Sensitivity profile of PB-2 k_∞ to U^{238} (n, γ)

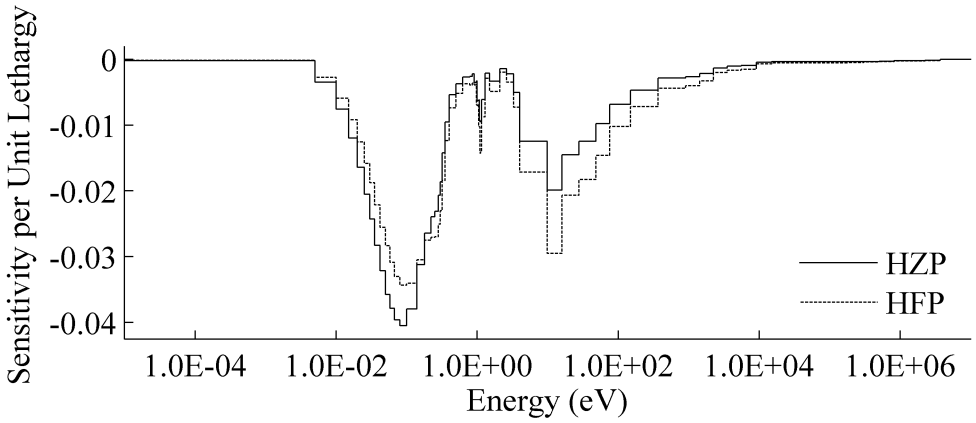

Figure 4.4: Sensitivity profile of PB-2 k_∞ to U^{235} (n, γ)

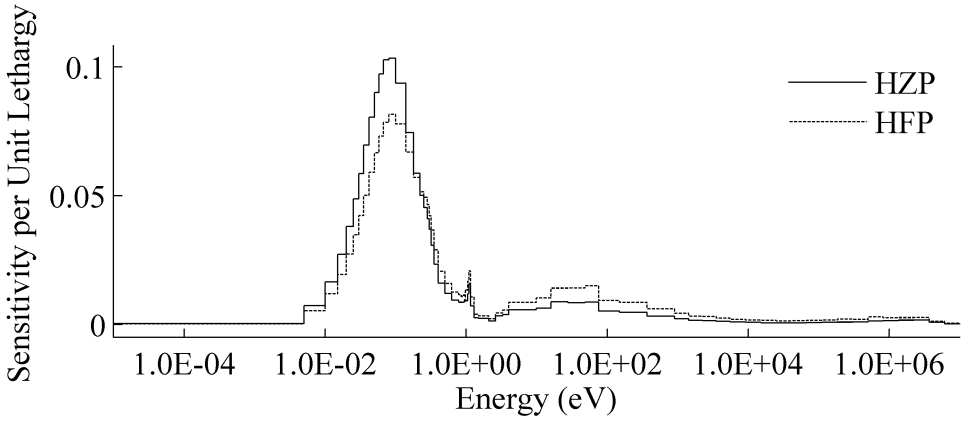

Figure 4.5: Sensitivity profile of PB-2 k_∞ to U^{235} (n, fission)

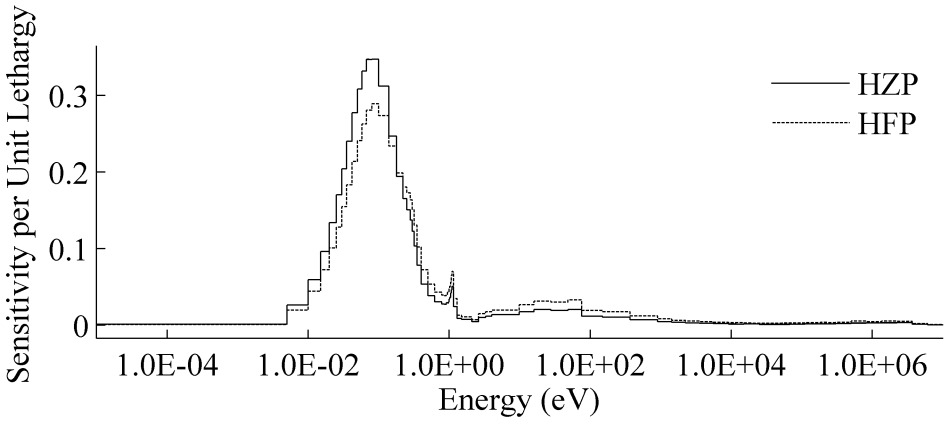

Figure 4.6: Sensitivity profile of PB-2 k_∞ to U^{235} $\bar{\nu}$

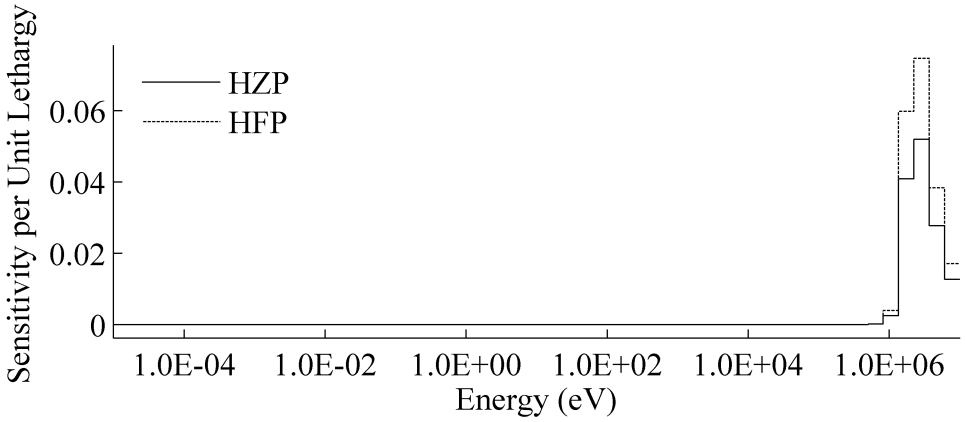

Figure 4.7: Sensitivity profile of PB-2 k_∞ to U^{238} $\bar{\nu}$

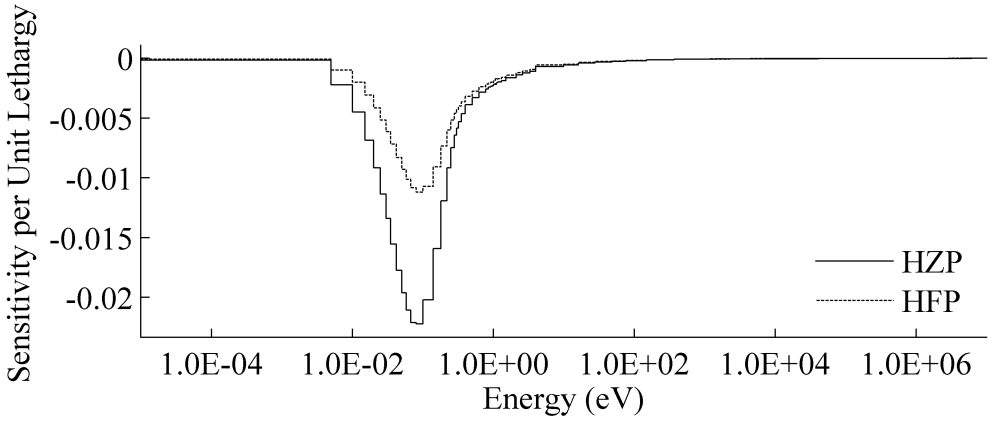

Figure 4.8: Sensitivity profile of PB-2 k_∞ to H^1 (n, γ)

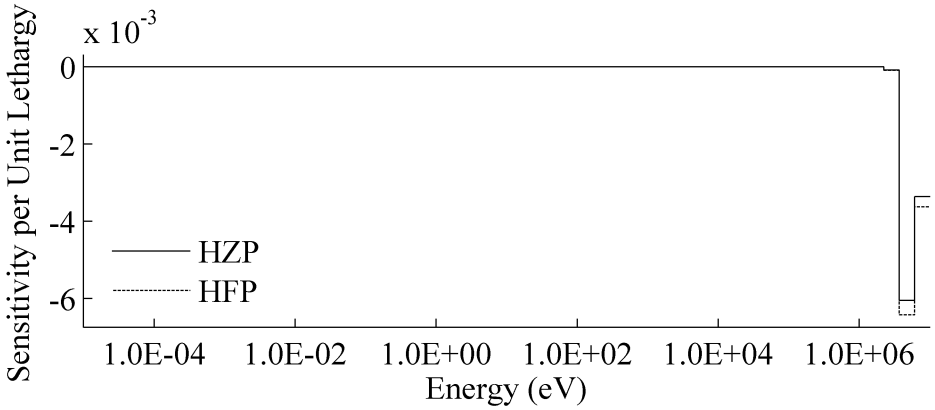

Figure 4.9: Sensitivity profile of PB-2 k_∞ to O^{16} (n, γ)

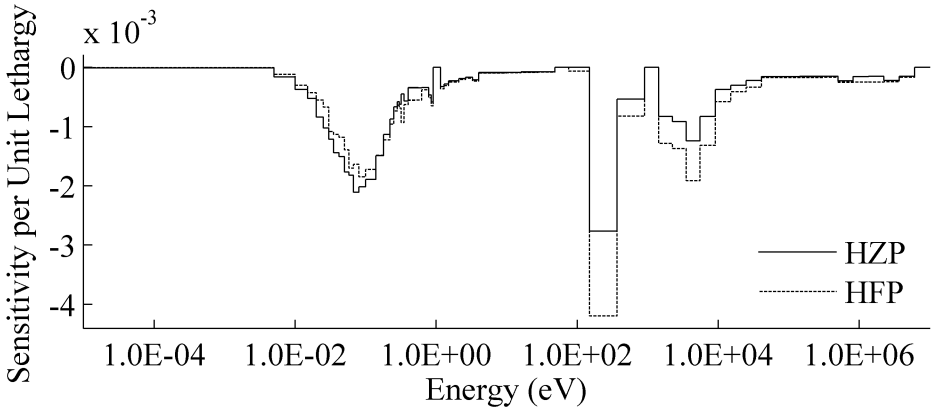

Figure 4.10: Sensitivity profile of PB-2 k_∞ to Zr^{Nat} (n, γ)

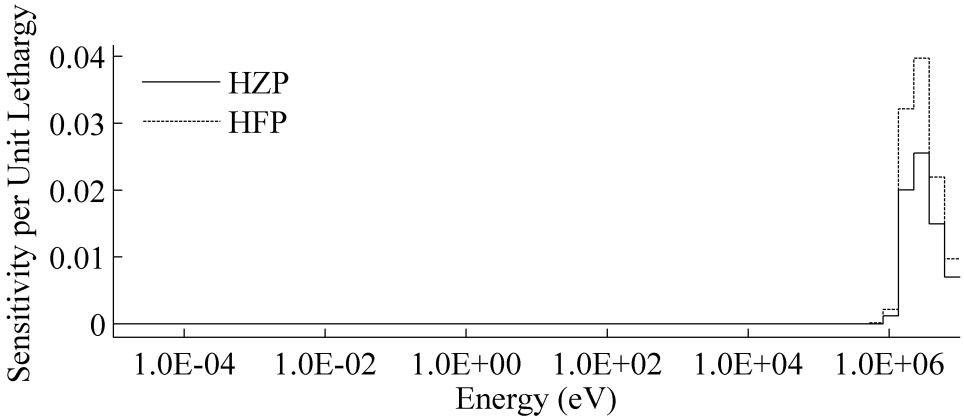

Figure 4.11: Sensitivity profile of PB-2 k_∞ to U^{238} (n, fission)

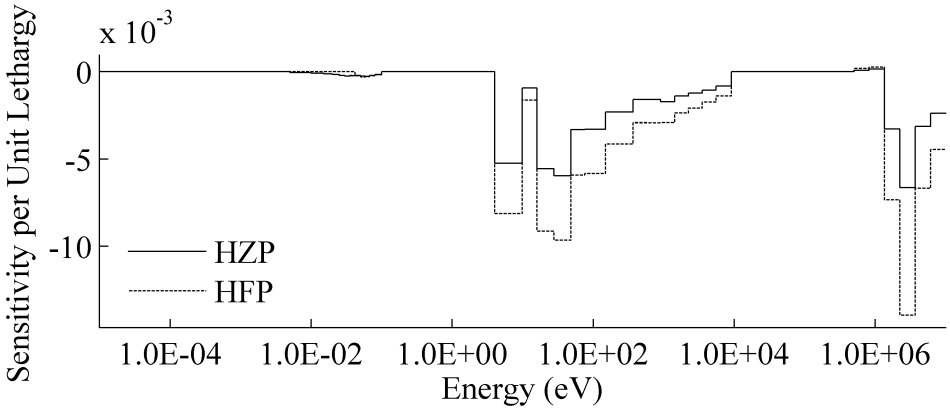

Figure 4.12: Sensitivity profile of PB-2 k_∞ to U^{238} scatter

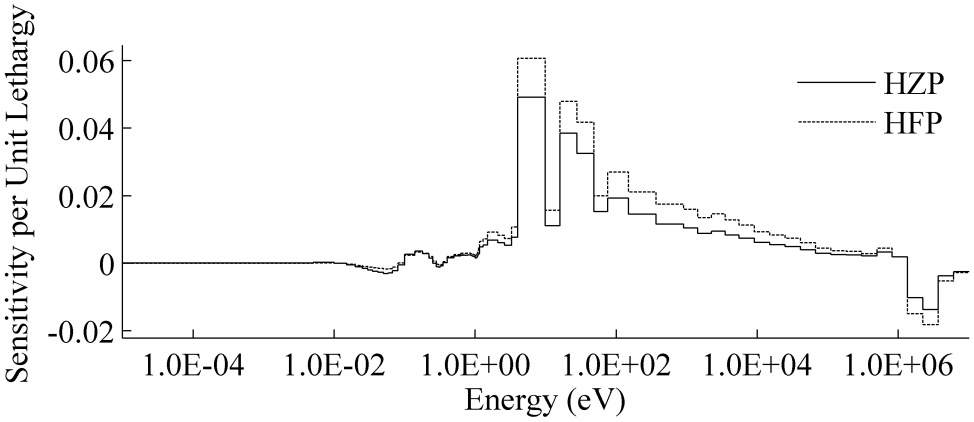

Figure 4.13: Sensitivity profile of PB-2 k_∞ to H^1 scatter

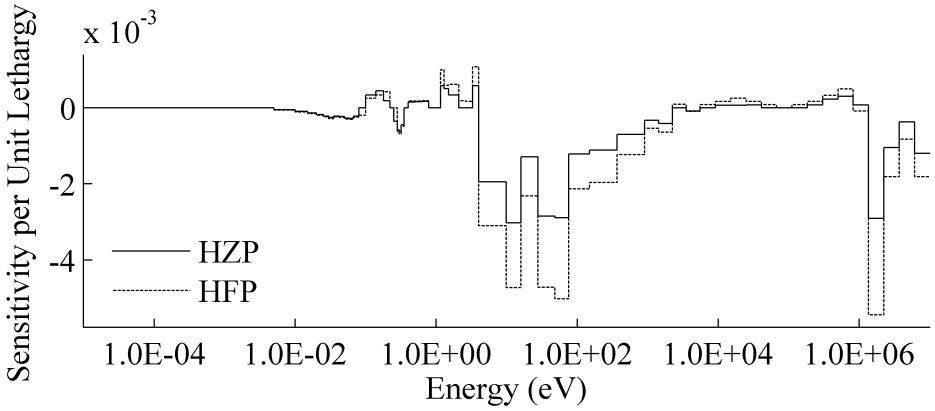

Figure 4.14: Sensitivity profile of PB-2 k_∞ to O^{16} scatter

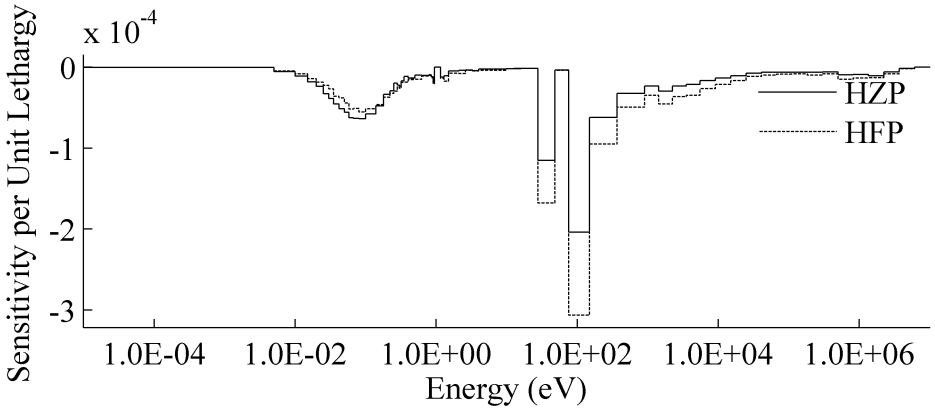

Figure 4.15: Sensitivity profile of PB-2 k_∞ to Sn^{118} (n, γ)

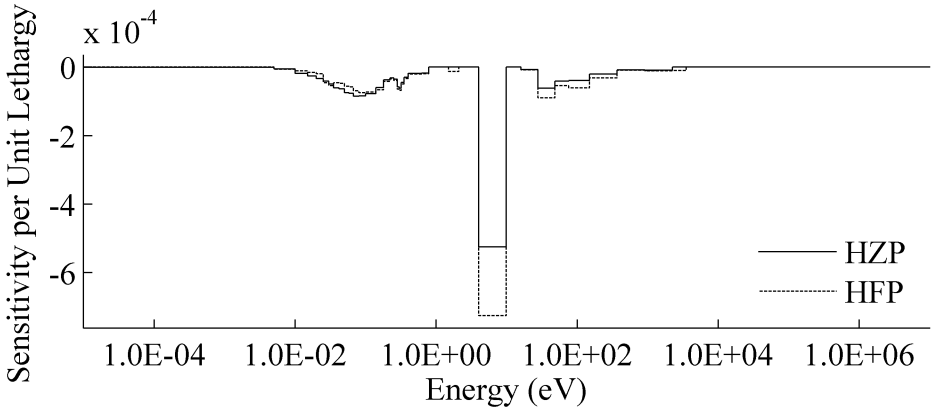

Figure 4.16: Sensitivity profile of PB-2 k_∞ to U^{234} (n, γ)

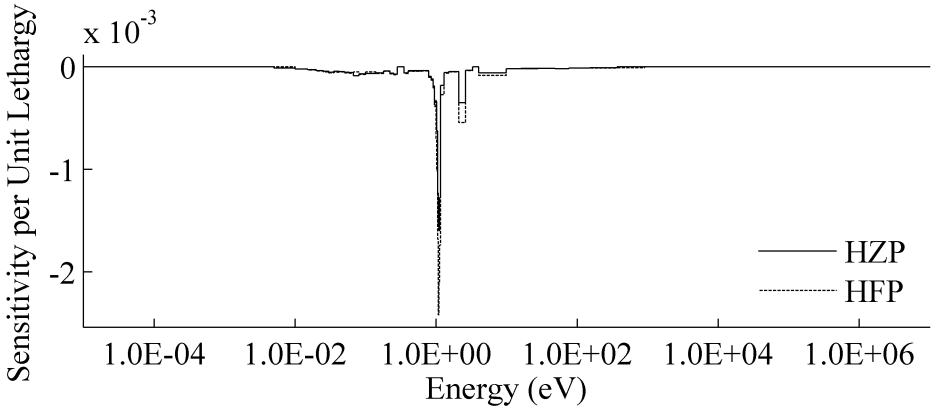

Figure 4.17: Sensitivity profile of PB-2 k_∞ to Hf^{178} (n, γ)

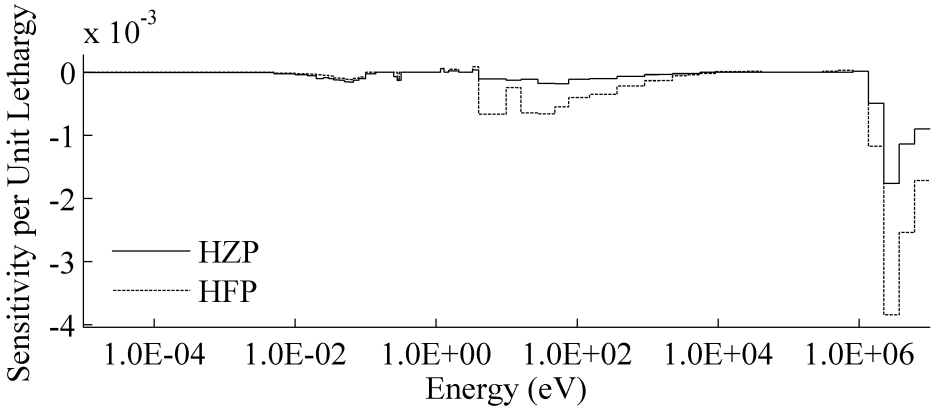

Figure 4.18: Sensitivity profile of PB-2 k_∞ to Zr^{Nat} scatter

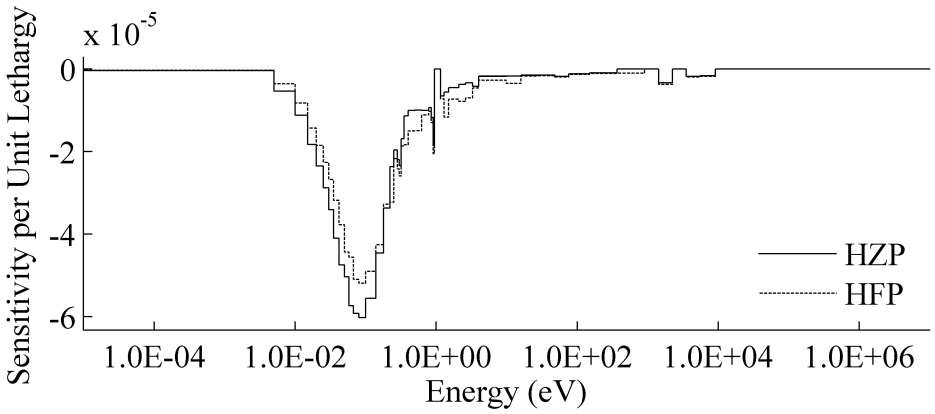

Figure 4.19: Sensitivity profile of PB-2 k_∞ to Cr^{52} (n, γ)

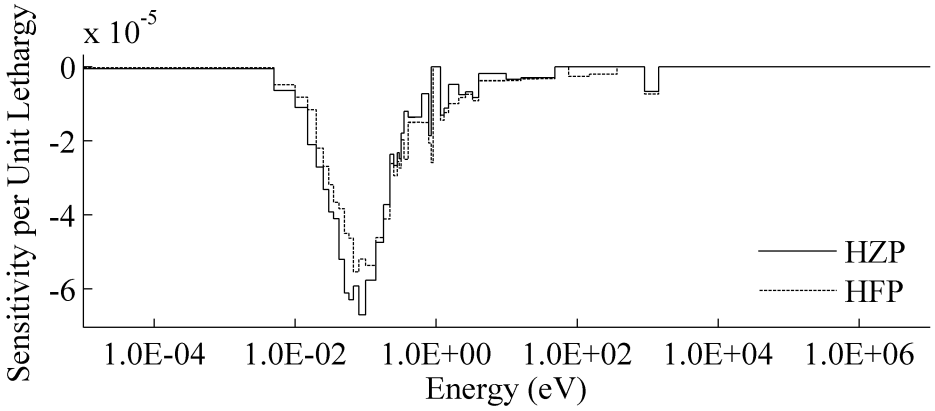

Figure 4.20: Sensitivity profile of PB-2 k_∞ to Fe^{Nat} (n, γ)

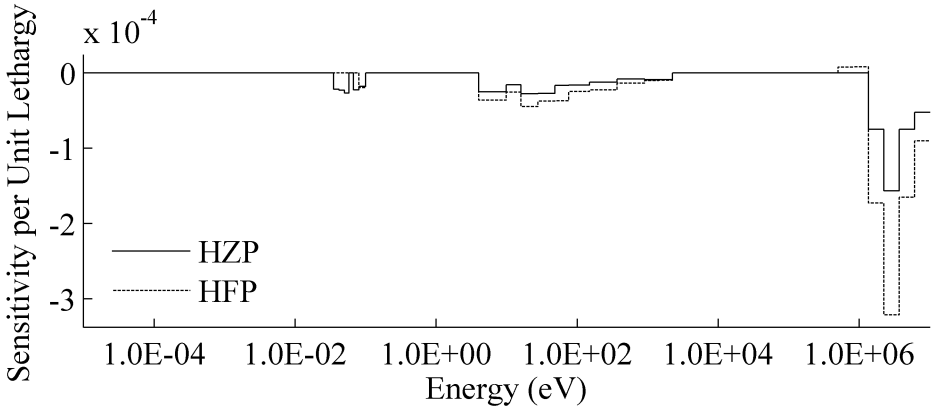

Figure 4.21: Sensitivity profile of PB-2 k_∞ to U^{235} scatter

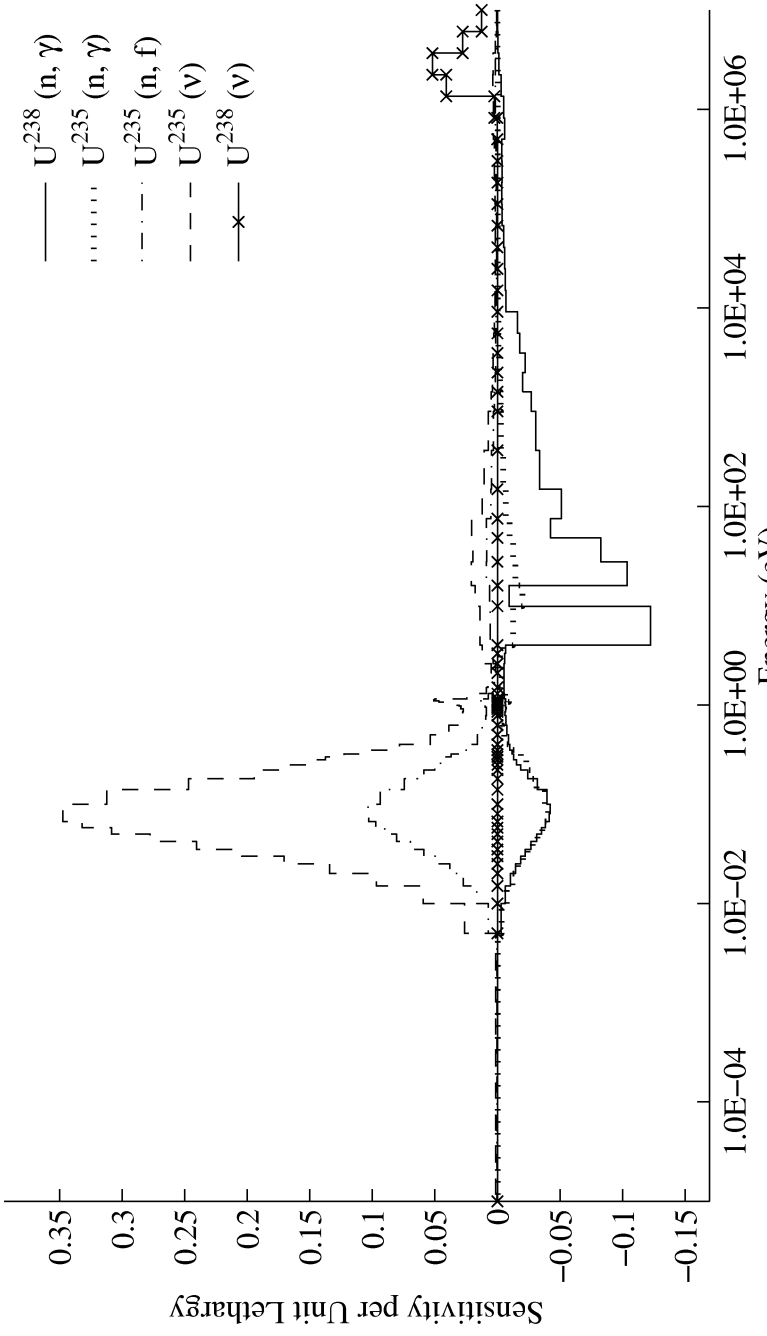

Figure 4.22: Sensitivity to major contributors of HZP PB-2 k_∞

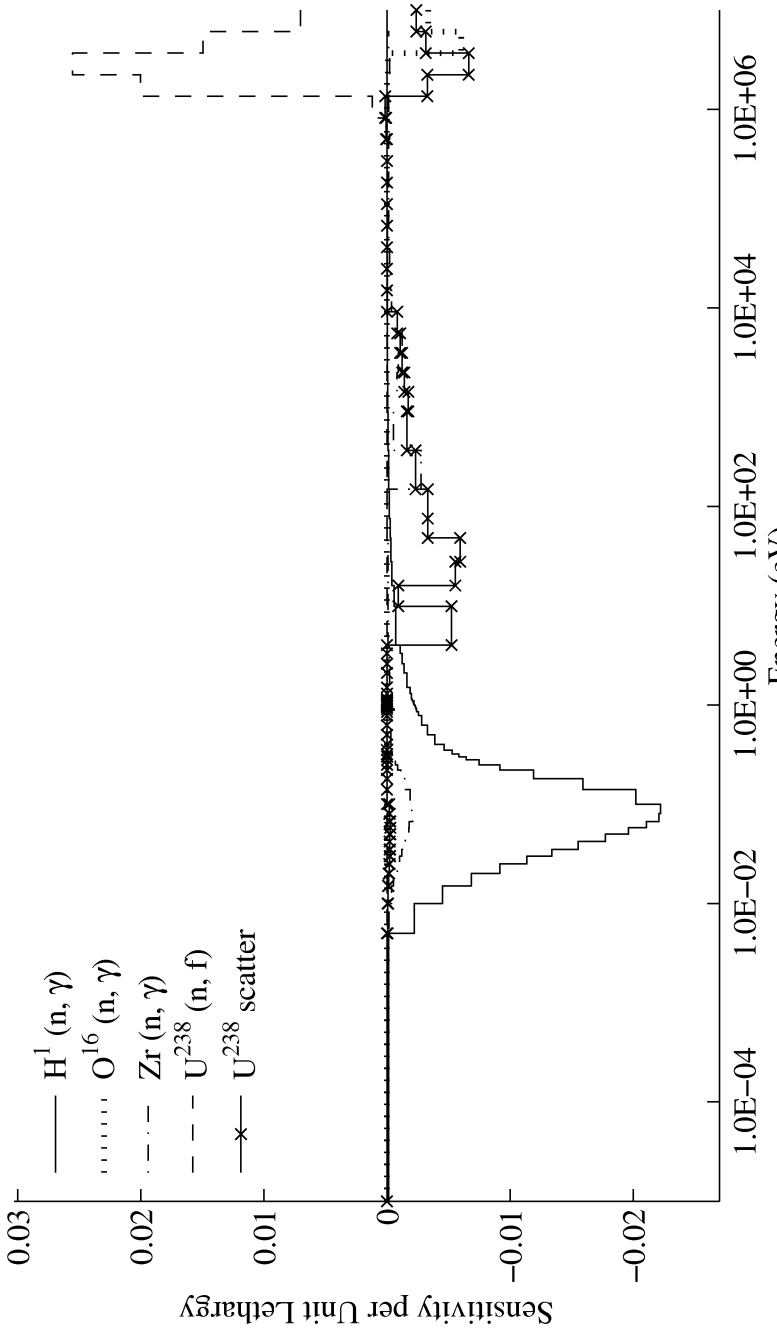

Figure 4.23: Sensitivity to minor contributors of HZP PB-2 k_∞

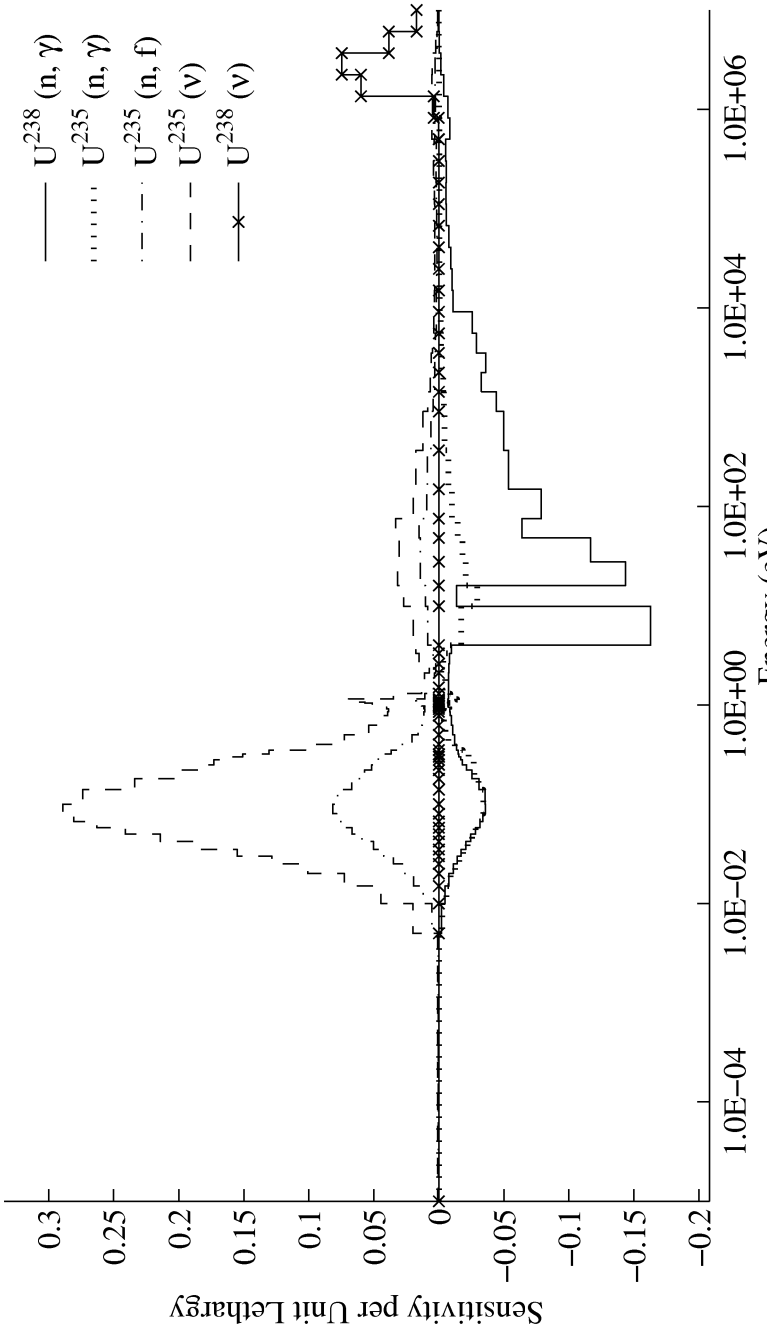

Figure 4.24: Sensitivity to major contributors of HFP PB-2 k_∞

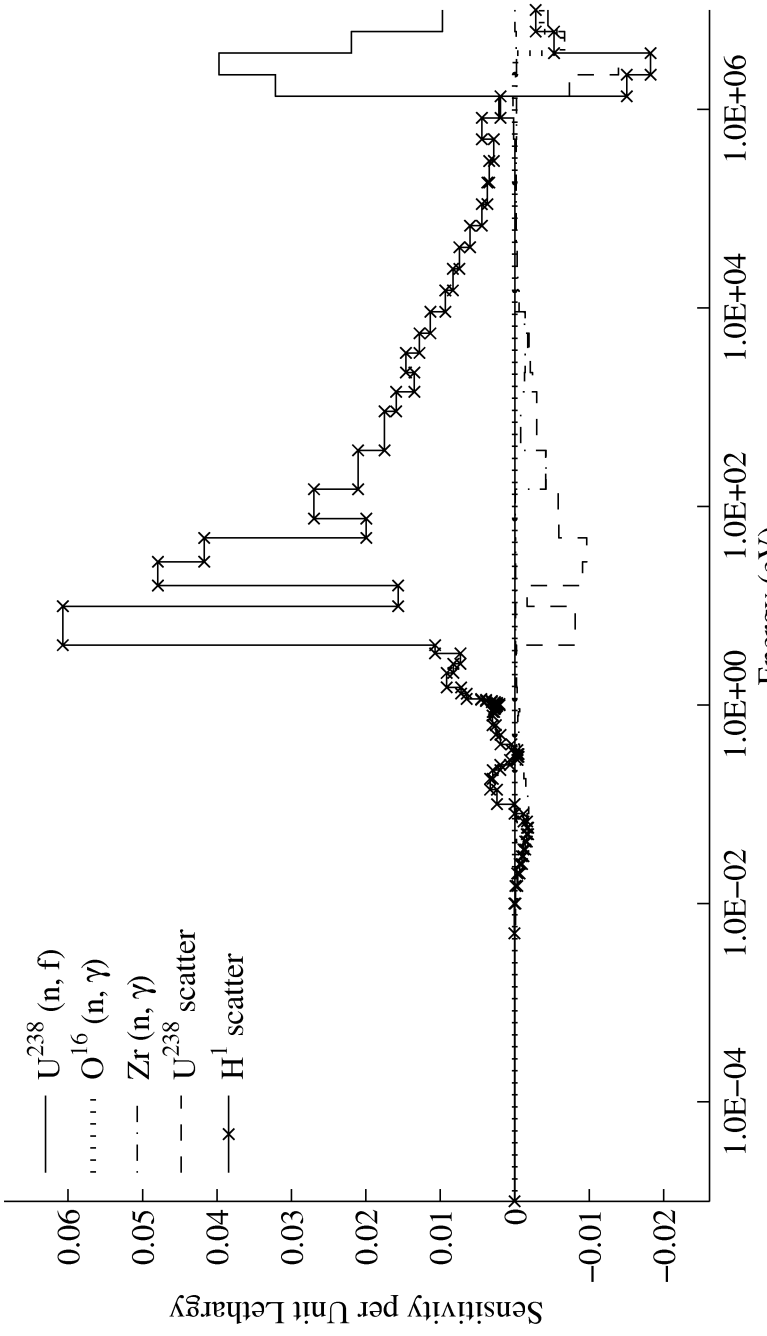

Figure 4.25: Sensitivity to minor contributors of HFP PB-2 k_∞

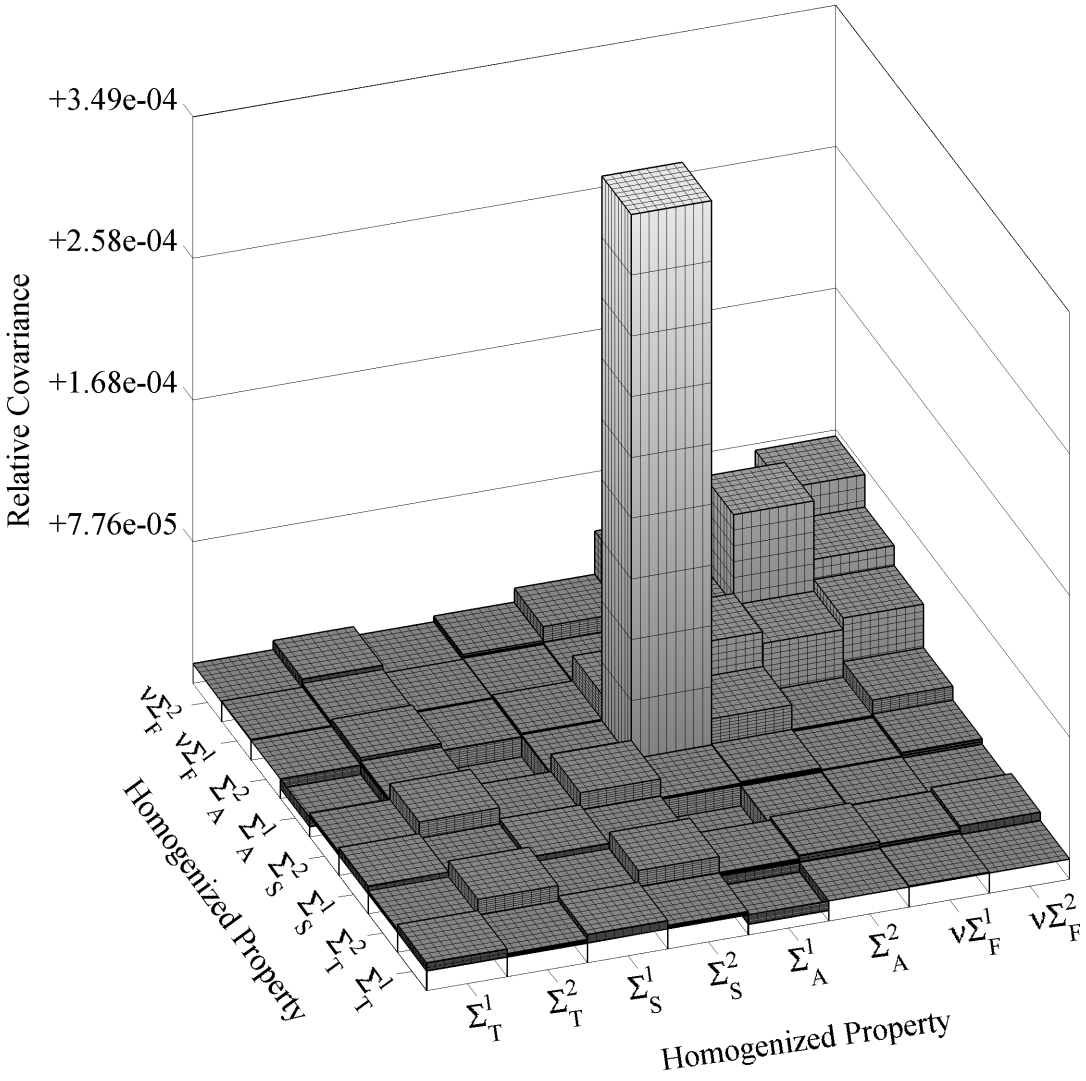

Figure 4.26: PB-2 HZP two-group homogenized lattice covariance

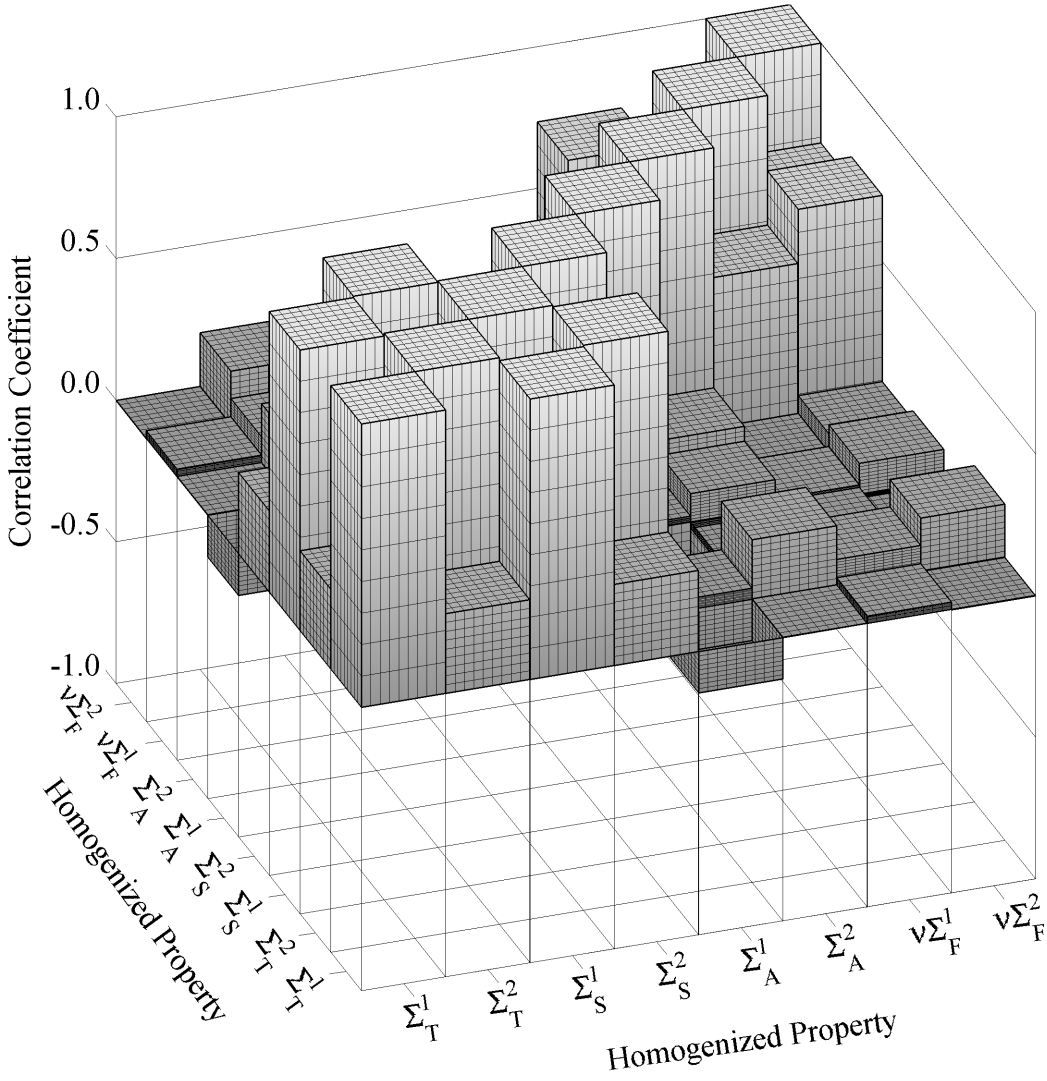

Figure 4.27: PB-2 HZP two-group homogenized lattice correlation

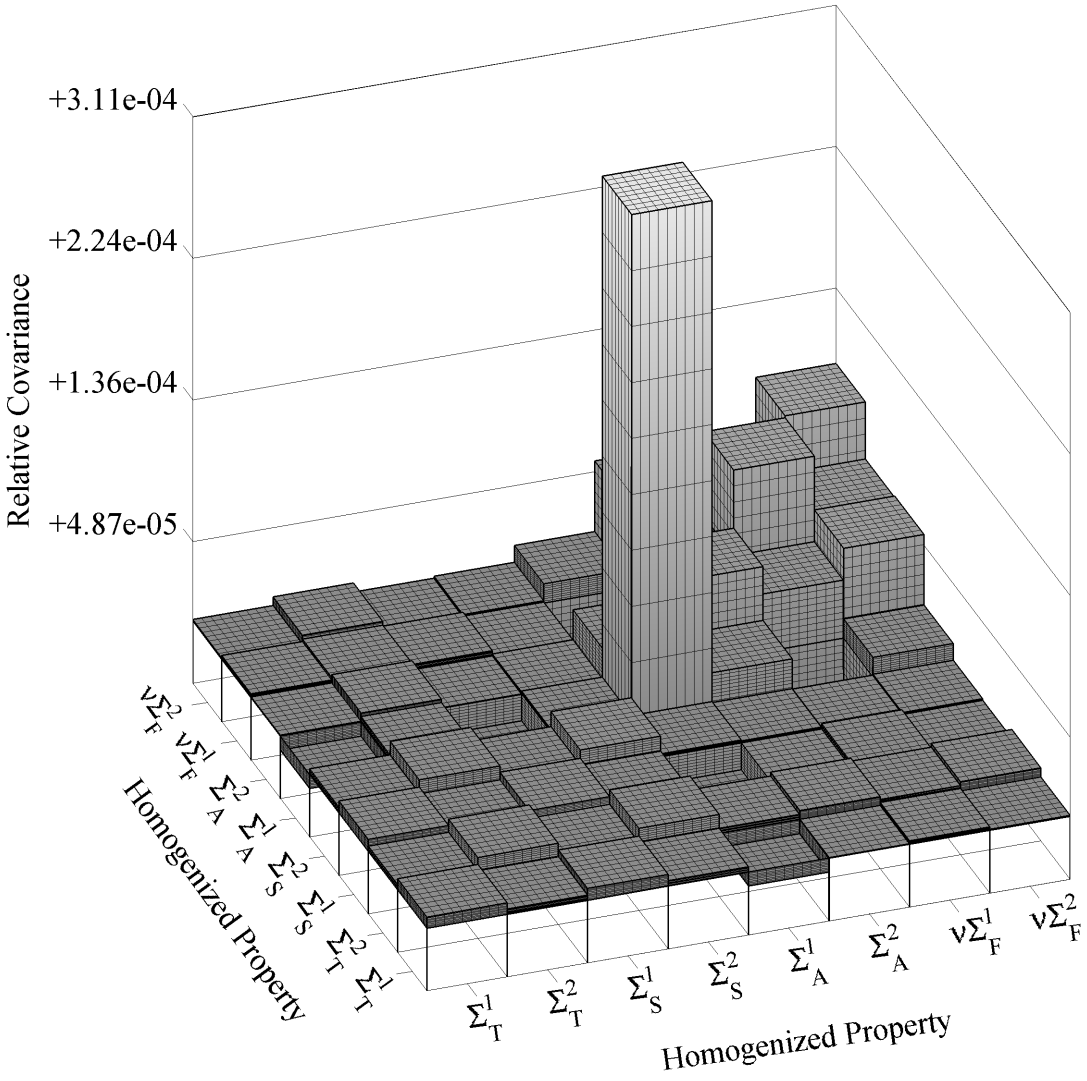

Figure 4.28: PB-2 HFP two-group homogenized lattice covariance

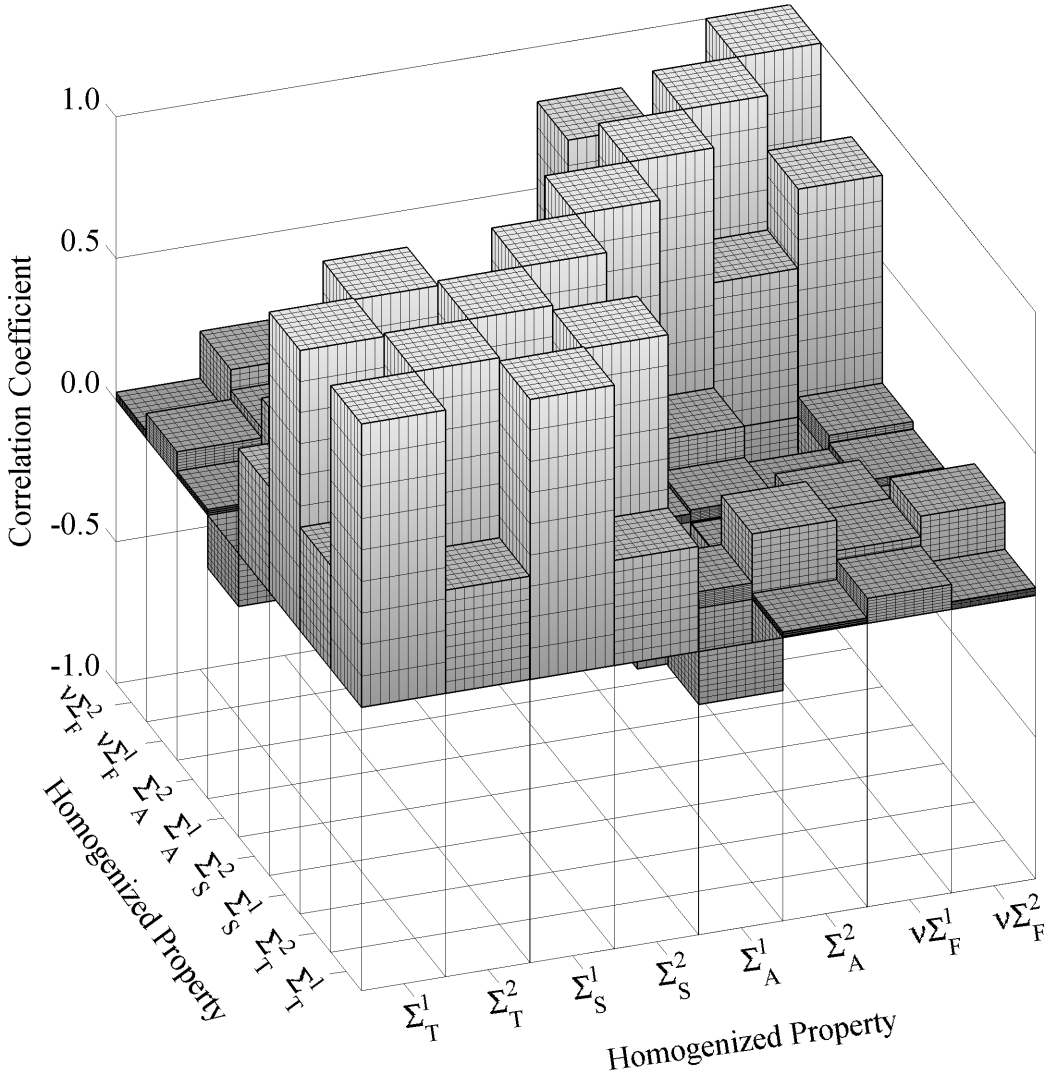

Figure 4.29: PB-2 HFP two-group homogenized lattice correlation

4.3 Three Mile Island unit 1 Pressurized Water Reactor

nuclide	reaction/ parameter	Statistical Uniform %Δk/k	Statistical Gaussian %Δ k/k	Direct Perturbation %Δ k/k
ALL	ALL	1.0250	1.0221	1.0386
U^{238}	(n, γ)	0.8703	0.8825	0.8412
U^{235}	(n, γ)	0.5035	0.4788	0.5254
U^{235}	(n, fission)	0.2248	0.2493	0.2423
U^{235}	$\bar{\nu}$	0.1499	0.1312	0.1384
U^{238}	$\bar{\nu}$	0.1106	0.1077	0.1065
O^{16}	(n, γ)	0.0466	0.0563	0.0466
H^{1}	(n, γ)	0.0361	0.0326	0.0326
U^{238}	(n, fission)	0.0361	0.0378	0.0357
Zr^{Nat}	(n, γ)	0.0259	0.0265	0.0228
H^{1}	scatter	0.0196	0.0160	0.0165
U^{238}	scatter	0.0176	0.0195	0.0180
O^{16}	scatter	0.0104	0.0092	0.0096
Sn^{118}	(n, γ)	0.0082	0.0084	0.0081
U^{234}	(n, γ)	0.0058	0.0054	0.0044
Hf^{178}	(n, γ)	0.0023	0.0020	0.0017
Zr^{Nat}	scatter	0.0016	0.0014	0.0014
Cr^{52}	(n, γ)	0.0014	0.0014	0.0014
Fe^{Nat}	(n, γ)	0.0010	0.0010	0.0009
U^{235}	scatter	0.0010	0.0011	0.0010

Table 4.4: Contributions to uncertainty in TMI-1 k_∞ at HZP

nuclide	reaction/ parameter	Statistical Uniform %Δk/k	Statistical Gaussian %Δ k/k	Direct Perturbation %Δ k/k
ALL	ALL	1.0553	1.0803	1.0965
U^{238}	(n, γ)	0.8331	0.8794	0.9002
U^{235}	(n, γ)	0.5398	0.5411	0.5429
U^{235}	(n, fission)	0.2524	0.2391	0.2421
U^{235}	$\bar{\nu}$	0.1249	0.1297	0.1381
U^{238}	$\bar{\nu}$	0.1074	0.1023	0.1092
O^{16}	(n, γ)	0.0480	0.0451	0.0509
U^{238}	(n, fission)	0.0363	0.0342	0.0367
H^{1}	(n, γ)	0.0320	0.0299	0.0312
Zr^{Nat}	(n, γ)	0.0271	0.0279	0.0398
U^{238}	scatter	0.0194	0.0210	0.0204
H^{1}	scatter	0.0192	0.0177	0.0173
O^{16}	scatter	0.0118	0.0124	0.0124
Sn^{118}	(n, γ)	0.0081	0.0089	0.0086
U^{234}	(n, γ)	0.0046	0.0054	0.0125
Hf^{178}	(n, γ)	0.0021	0.0022	0.0031
Zr^{Nat}	scatter	0.0015	0.0015	0.0016
Cr^{52}	(n, γ)	0.0013	0.0014	0.0015
U^{235}	scatter	0.0012	0.0011	0.0014
Fe^{Nat}	(n, γ)	0.0010	0.0010	0.0012
Fe^{Nat}	scatter	0.0000	0.0000	0.0001
U^{234}	scatter	0.0000	0.0000	0.0003

Table 4.5: Contributions to uncertainty in TMI-1 k_∞ at HFP

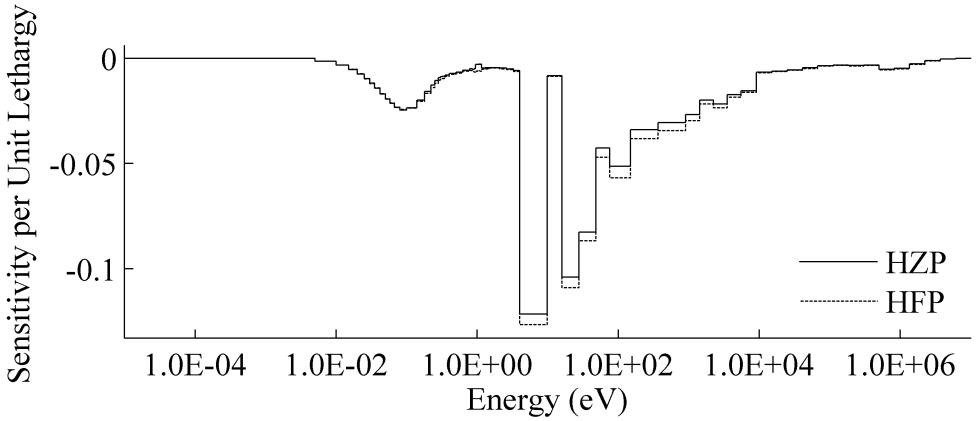

Figure 4.30: Sensitivity profile of TMI-1 k_∞ to U^{238} (n, γ)

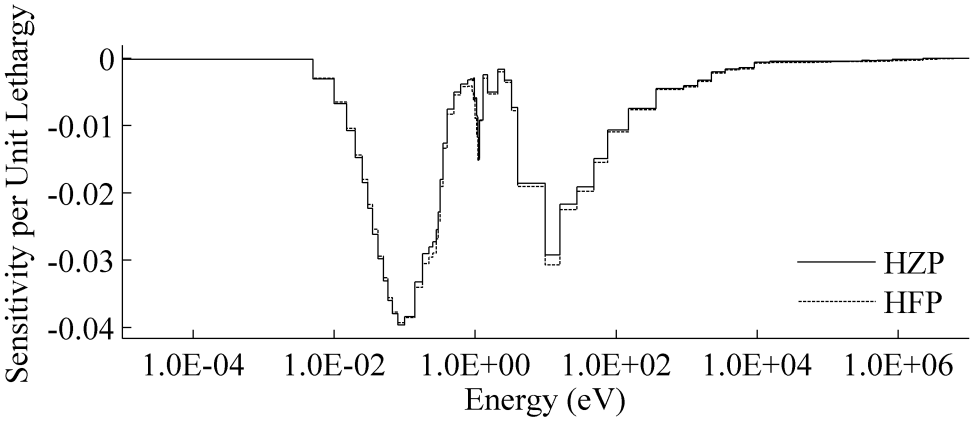

Figure 4.31: Sensitivity profile of TMI-1 k_∞ to U^{235} (n, γ)

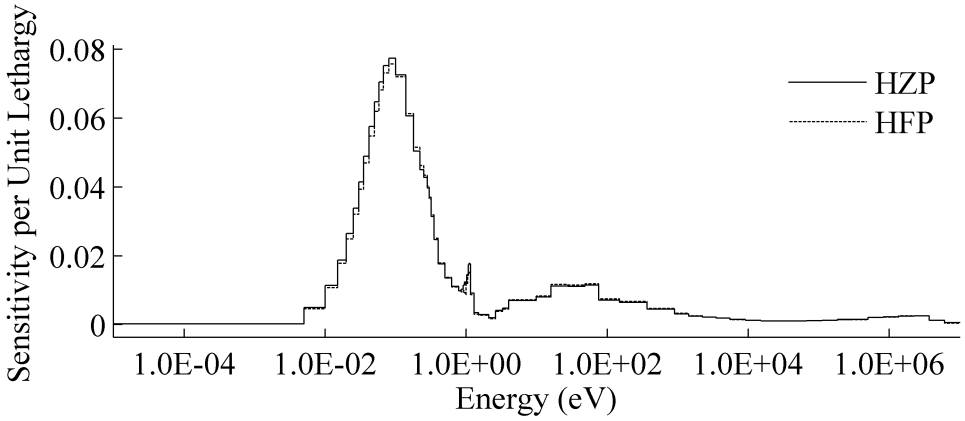

Figure 4.32: Sensitivity profile of TMI-1 k_∞ to U^{235} (n, fission)

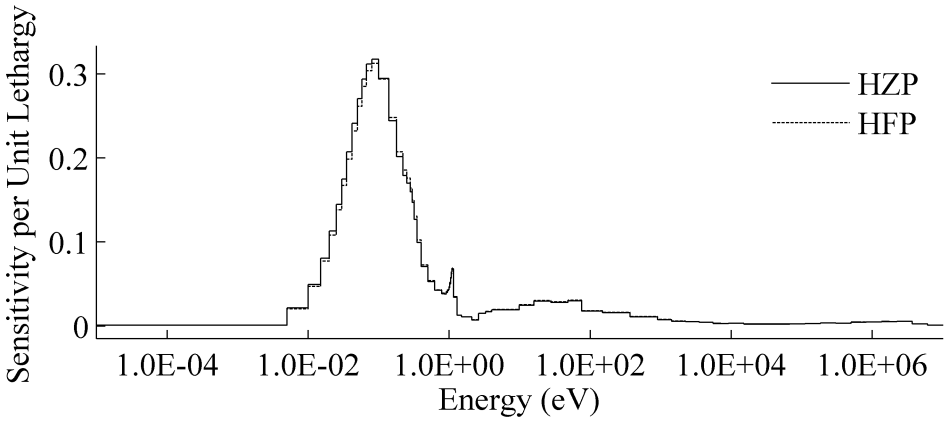

Figure 4.33: Sensitivity profile of TMI-1 k_∞ to U^{235} $\bar{\nu}$

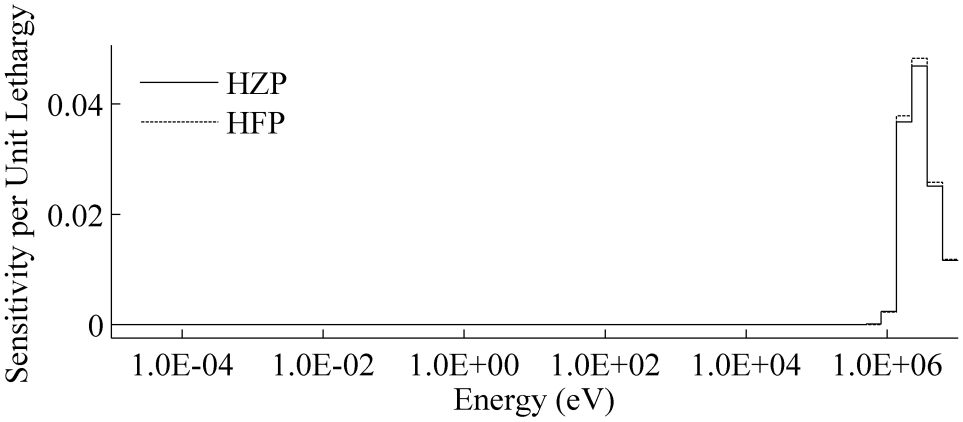

Figure 4.34: Sensitivity profile of TMI-1 k_∞ to U^{238} $\bar{\nu}$

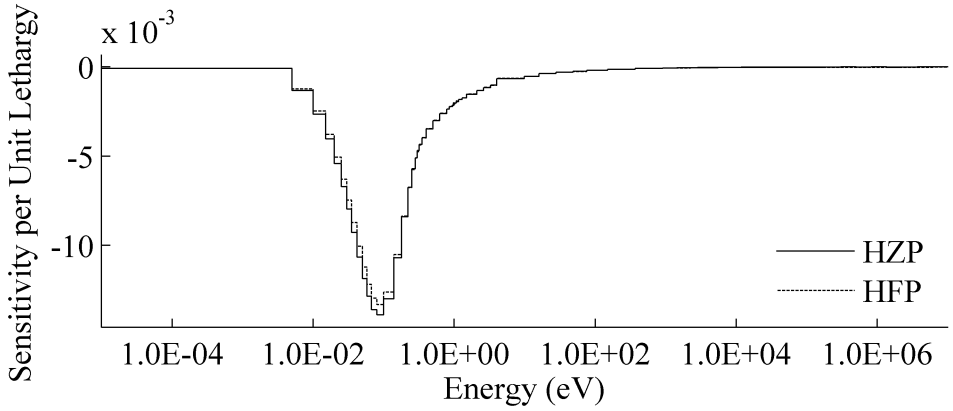

Figure 4.35: Sensitivity profile of TMI-1 k_∞ to H^1 (n, γ)

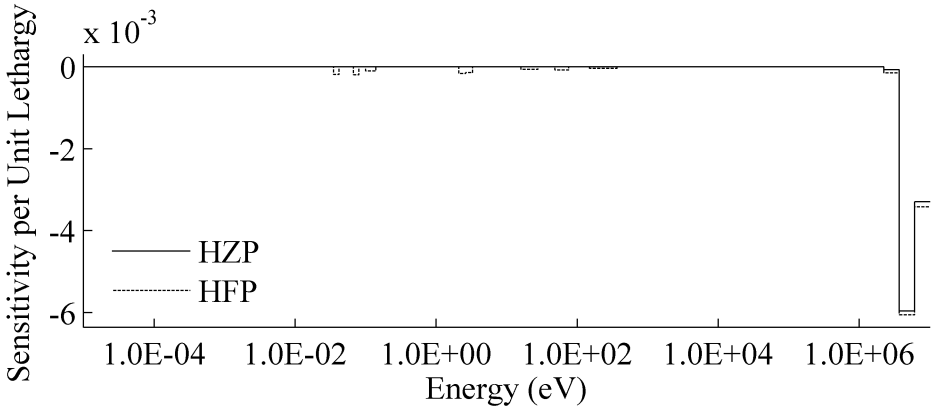

Figure 4.36: Sensitivity profile of TMI-1 k_∞ to O^{16} (n, γ)

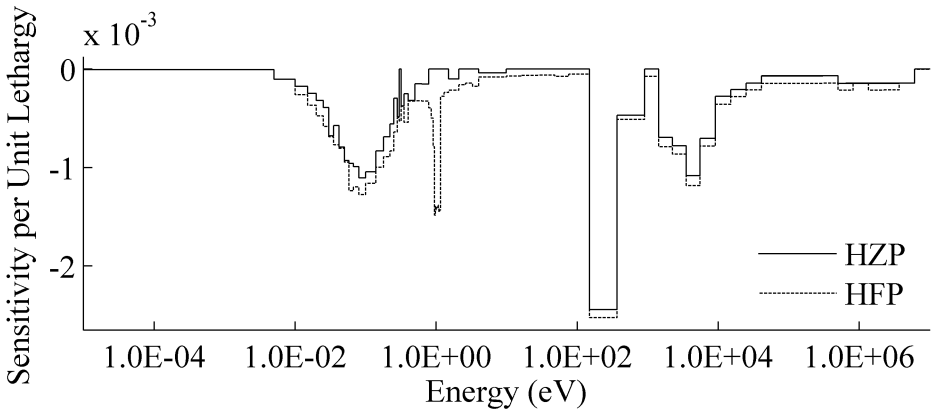

Figure 4.37: Sensitivity profile of TMI-1 k_∞ to Zr^{Nat} (n, γ)

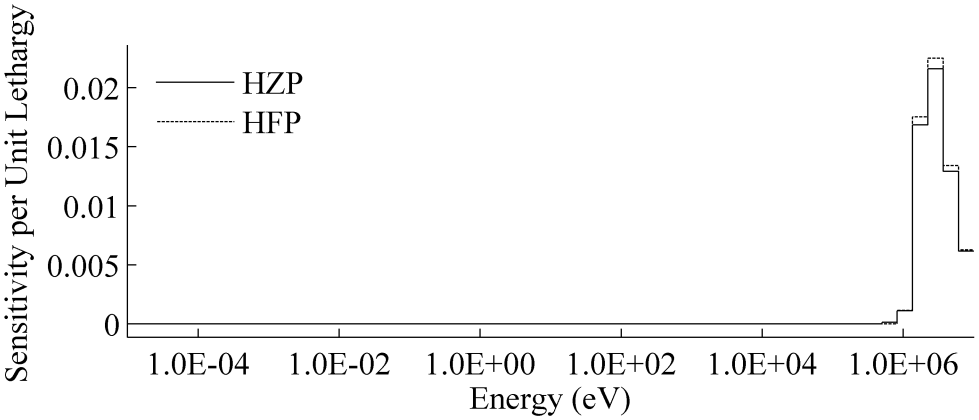

Figure 4.38: Sensitivity profile of TMI-1 k_∞ to U^{238} (n, fission)

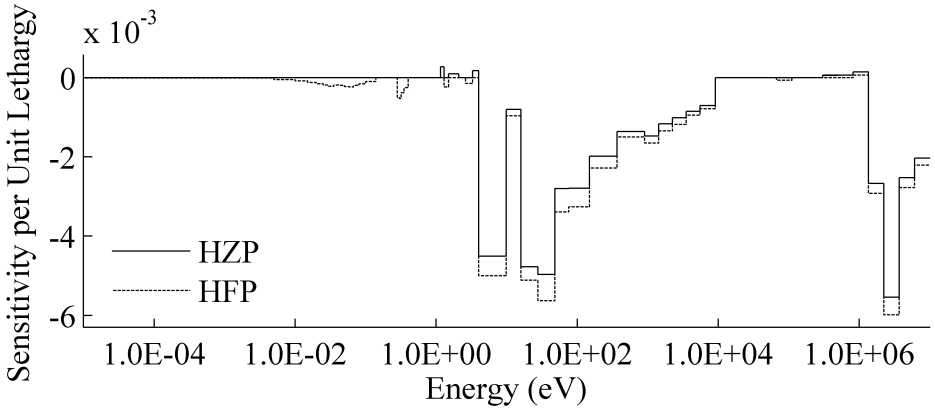

Figure 4.39: Sensitivity profile of TMI-1 k_∞ to U^{238} scatter

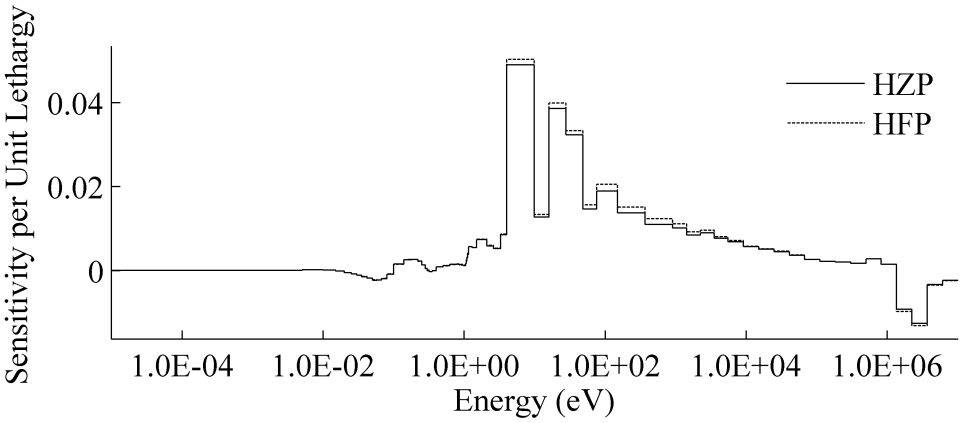

Figure 4.40: Sensitivity profile of TMI-1 k_∞ to H^1 scatter

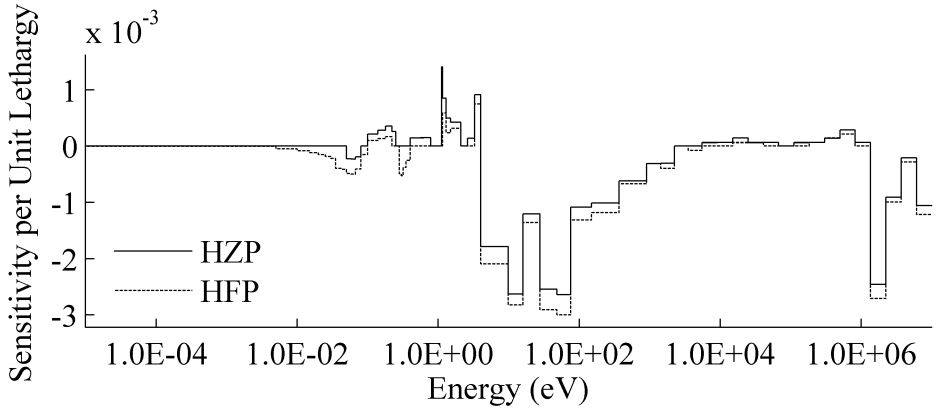

Figure 4.41: Sensitivity profile of TMI-1 k_∞ to O^{16} scatter

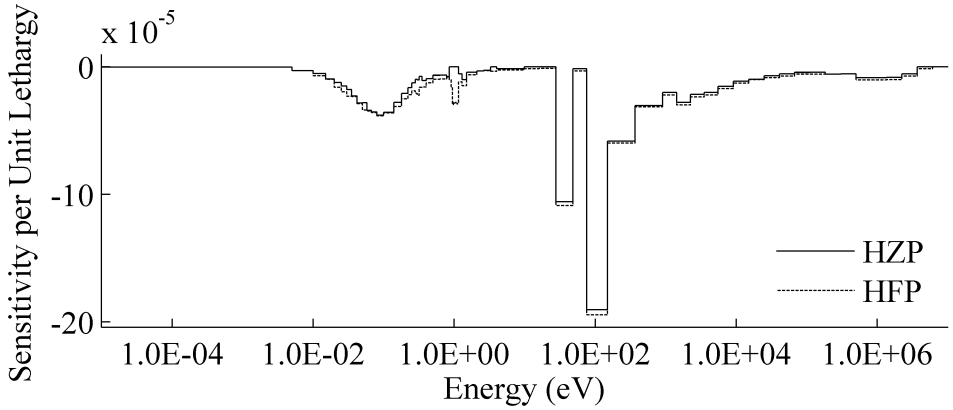

Figure 4.42: Sensitivity profile of TMI-1 k_∞ to Sn^{118} (n, γ)

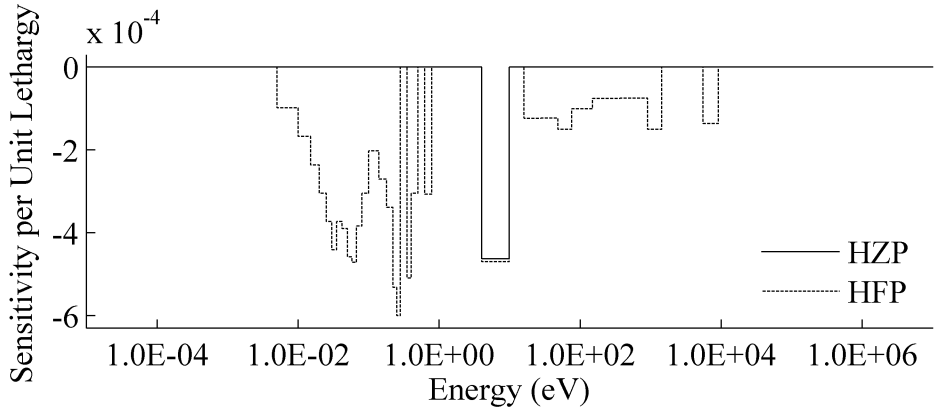

Figure 4.43: Sensitivity profile of TMI-1 k_∞ to U^{234} (n, γ)

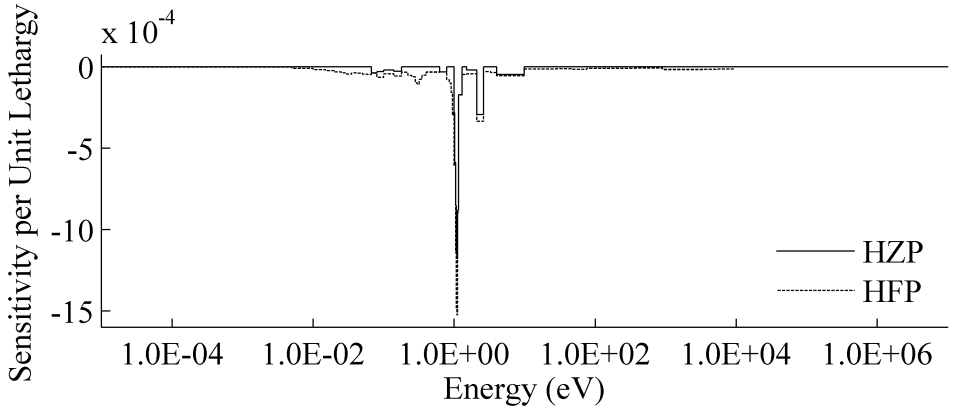

Figure 4.44: Sensitivity profile of TMI-1 k_∞ to Hf^{178} (n, γ)

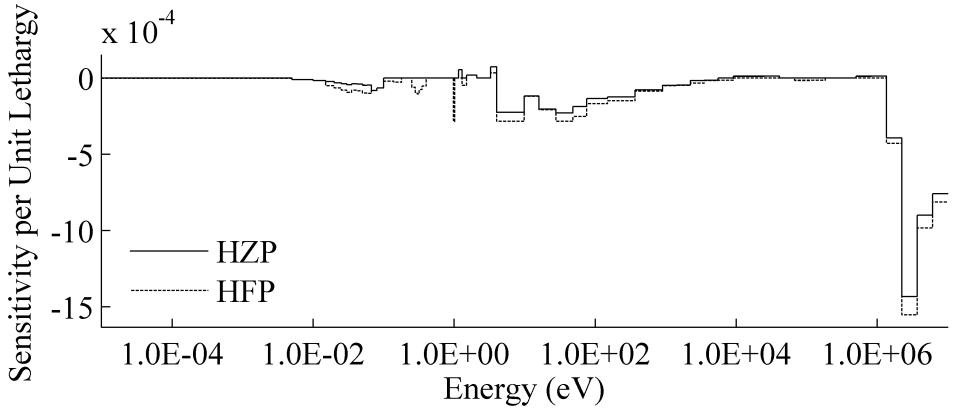

Figure 4.45: Sensitivity profile of TMI-1 k_∞ to Zr^{Nat} scatter

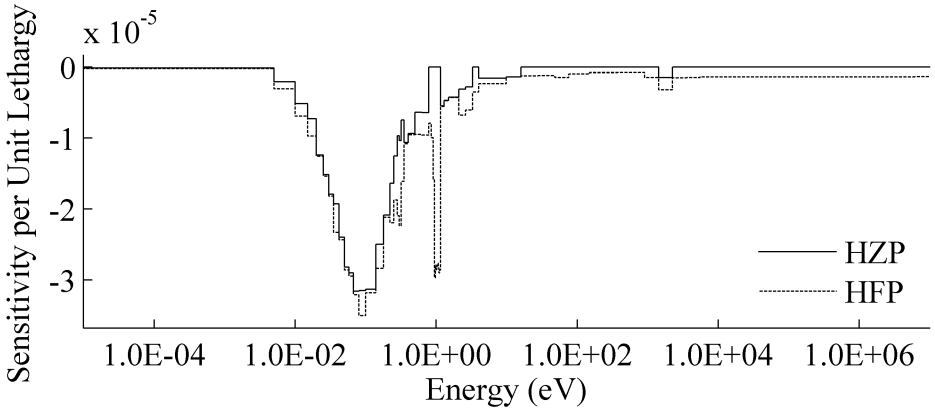

Figure 4.46: Sensitivity profile of TMI-1 k_∞ to Cr^{52} (n, γ)

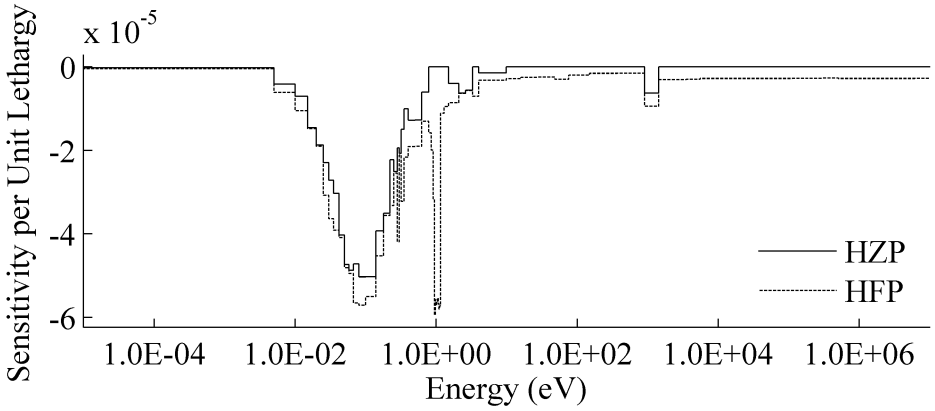

Figure 4.47: Sensitivity profile of TMI-1 k_∞ to Fe^{Nat} (n, γ)

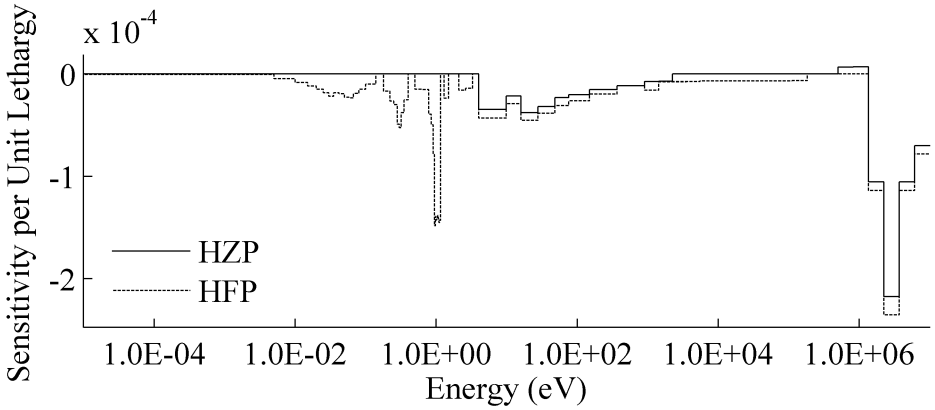

Figure 4.48: Sensitivity profile of TMI-1 k_∞ to U^{235} scatter

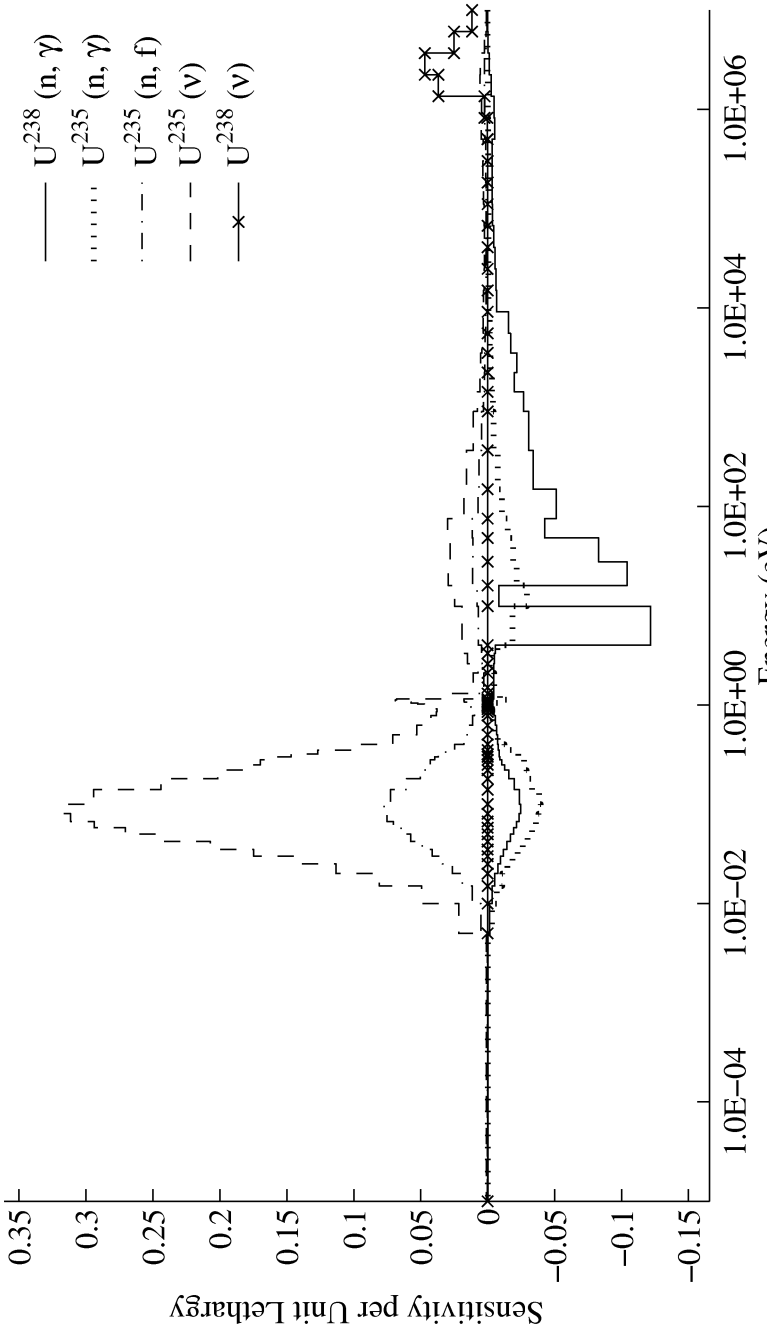

Figure 4.49: Sensitivity to major contributors of HZP TMI-1 k_∞

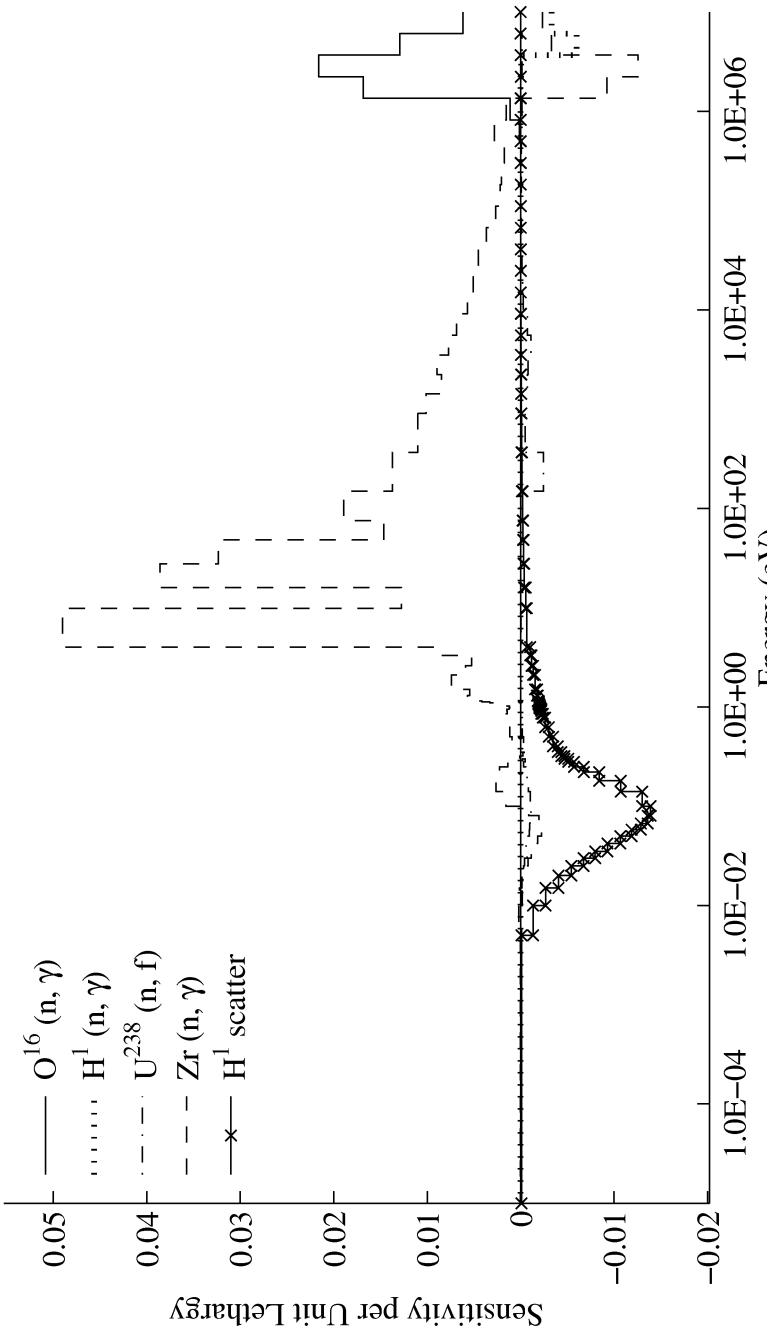

Figure 4.50: Sensitivity to minor contributors of HZP TMI-1 k_∞

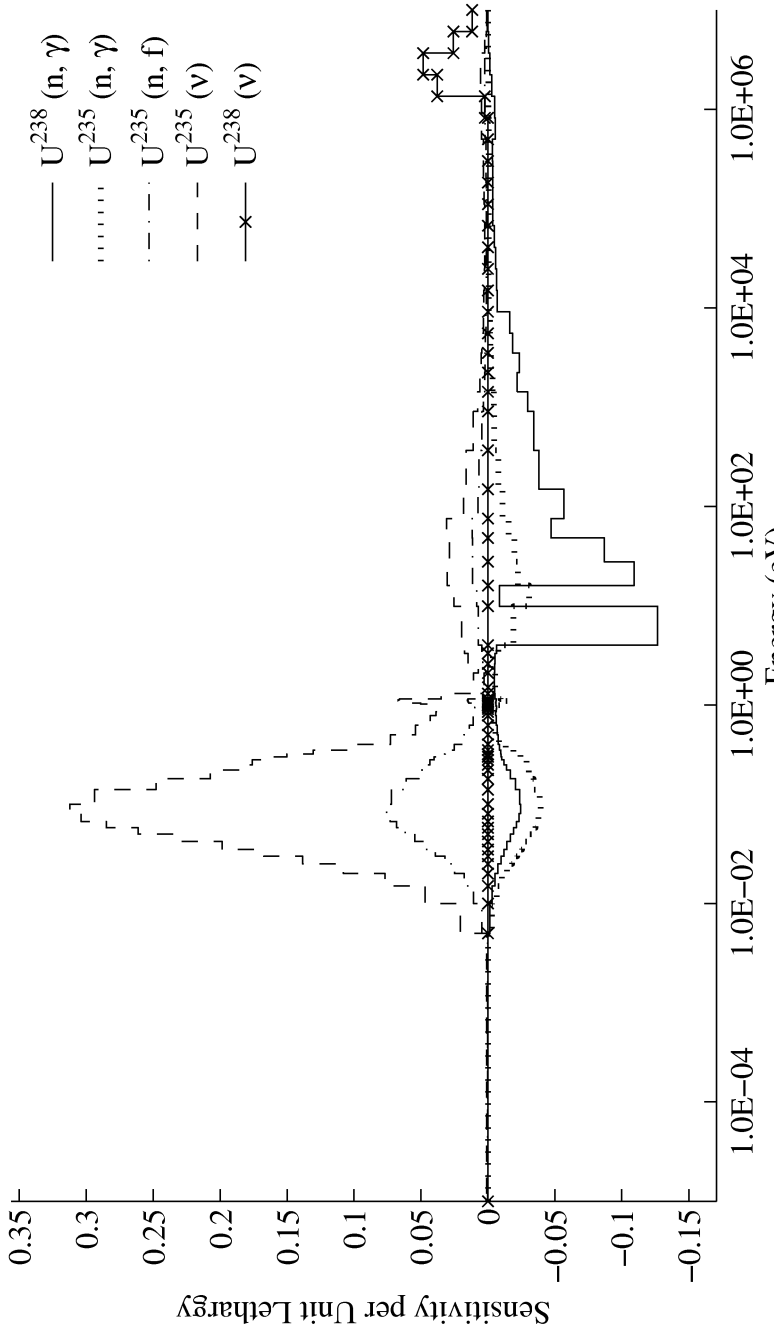

Figure 4.51: Sensitivity to major contributors of HFP TMI-1 k_∞

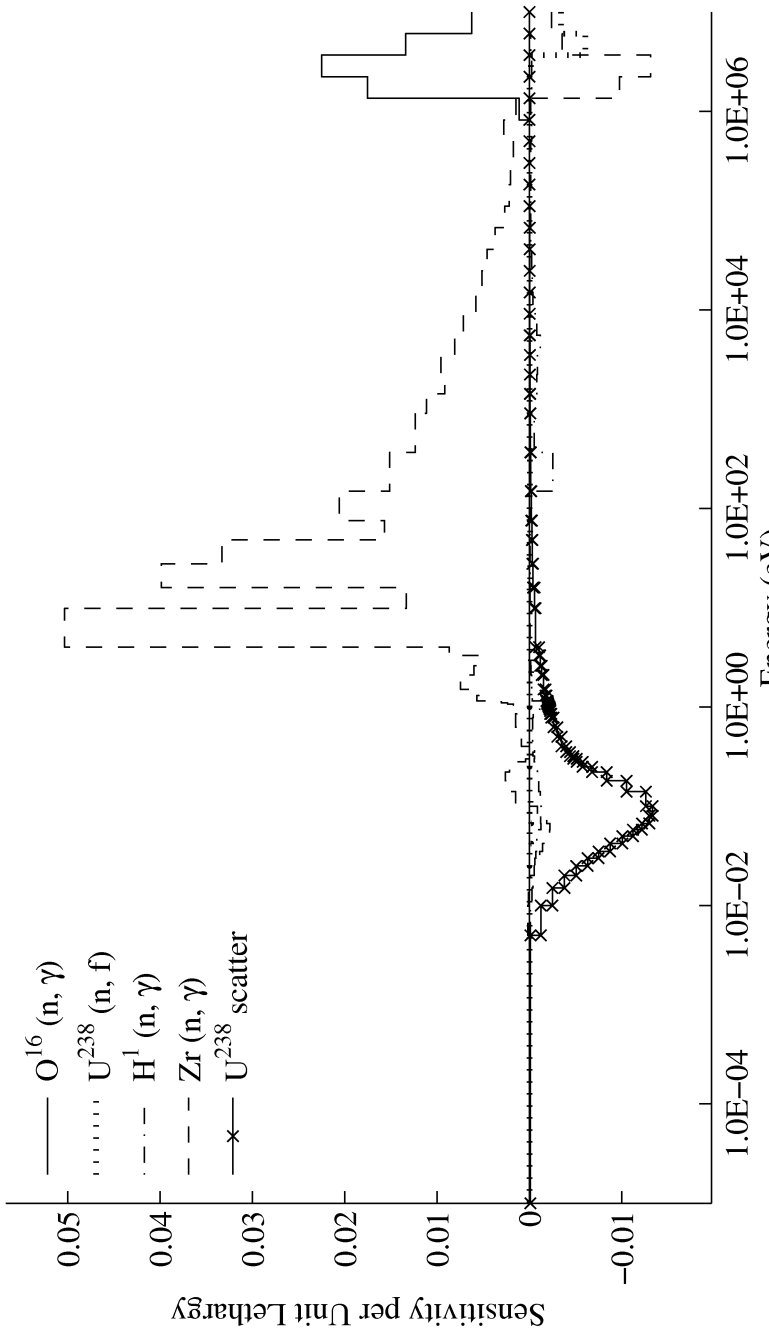

Figure 4.52: Sensitivity to minor contributors of HFP TMI-1 k_∞

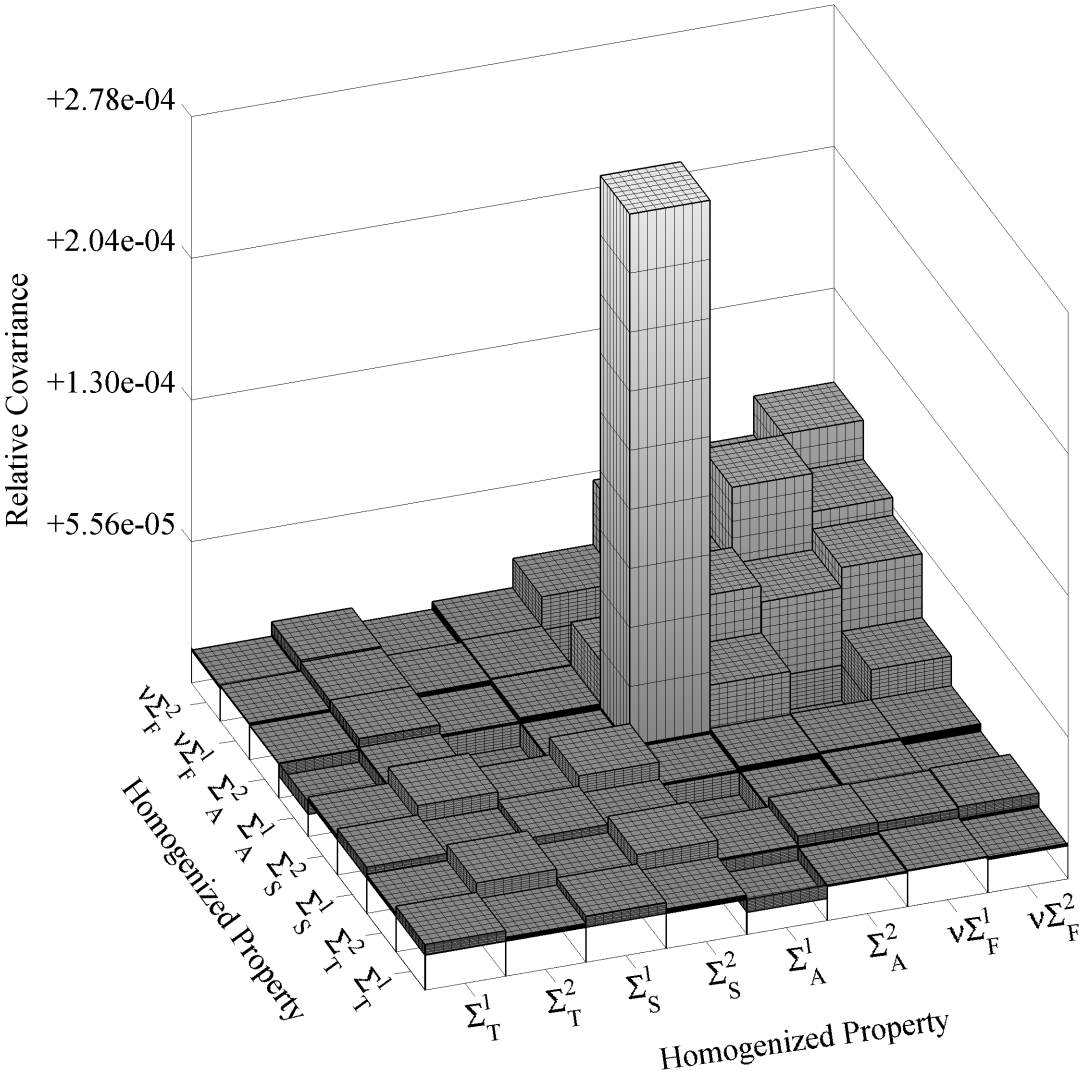

Figure 4.53: TMI-1 HZP two-group homogenized lattice covariance

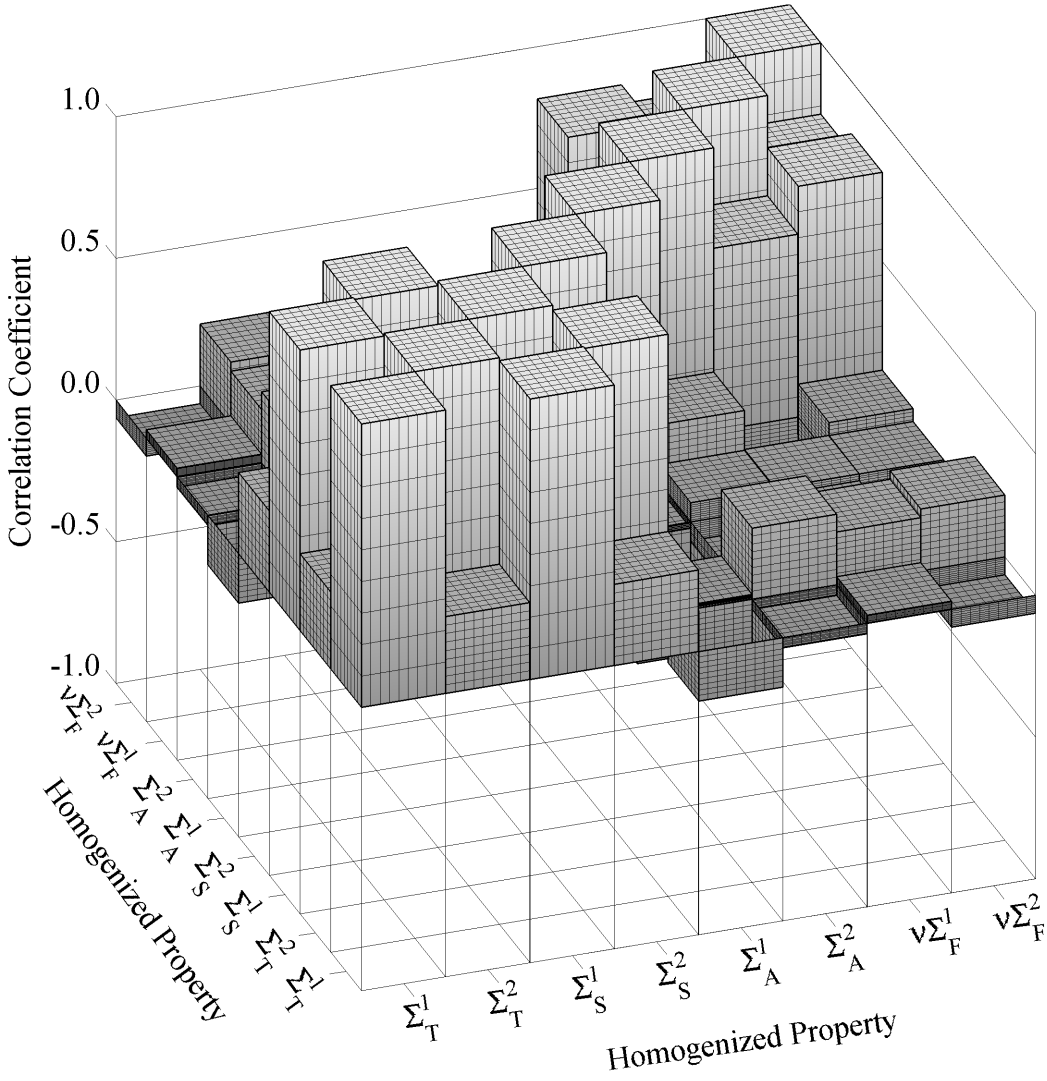

Figure 4.54: TMI-1 HZP two-group homogenized lattice correlation

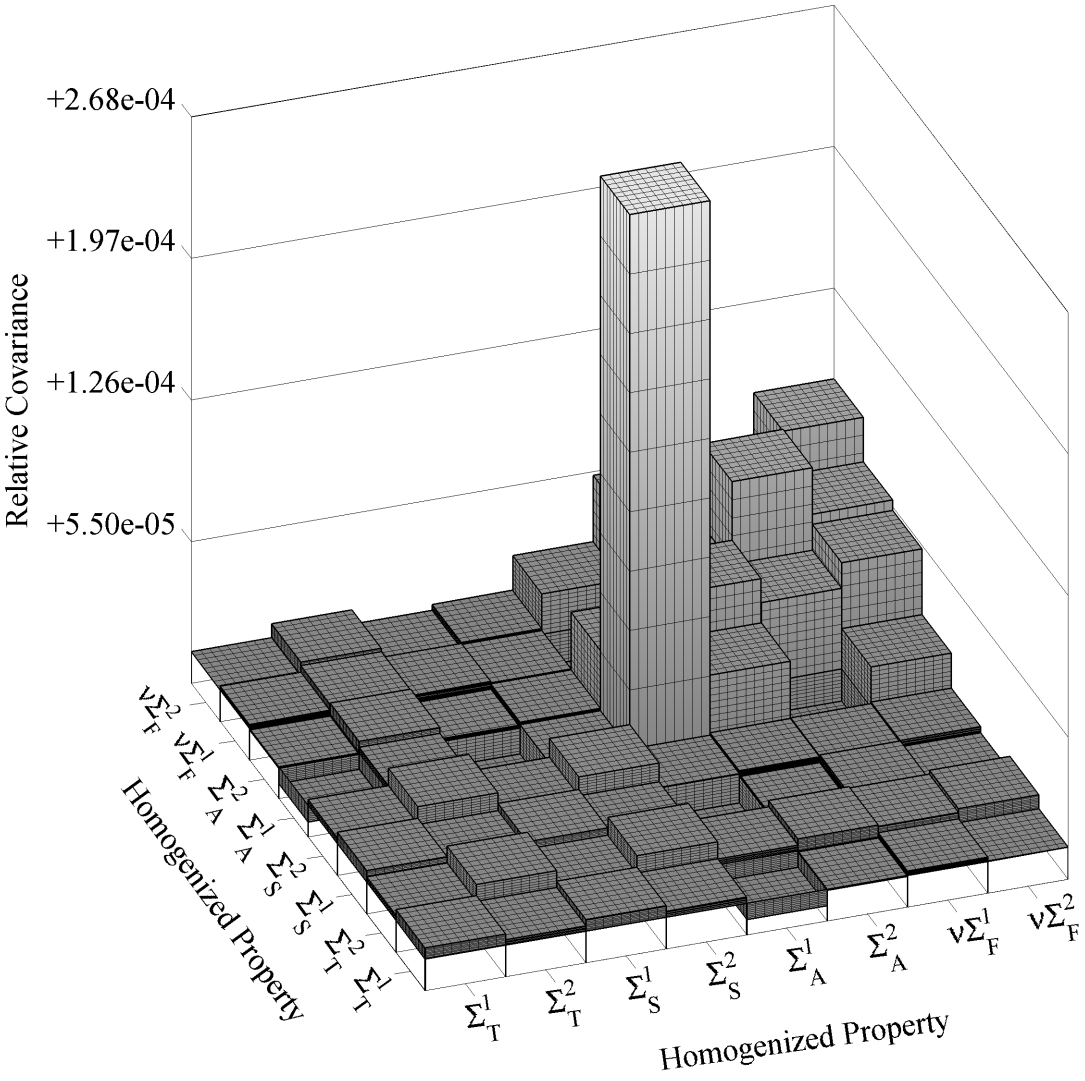

Figure 4.55: TMI-1 HFP two-group homogenized lattice covariance

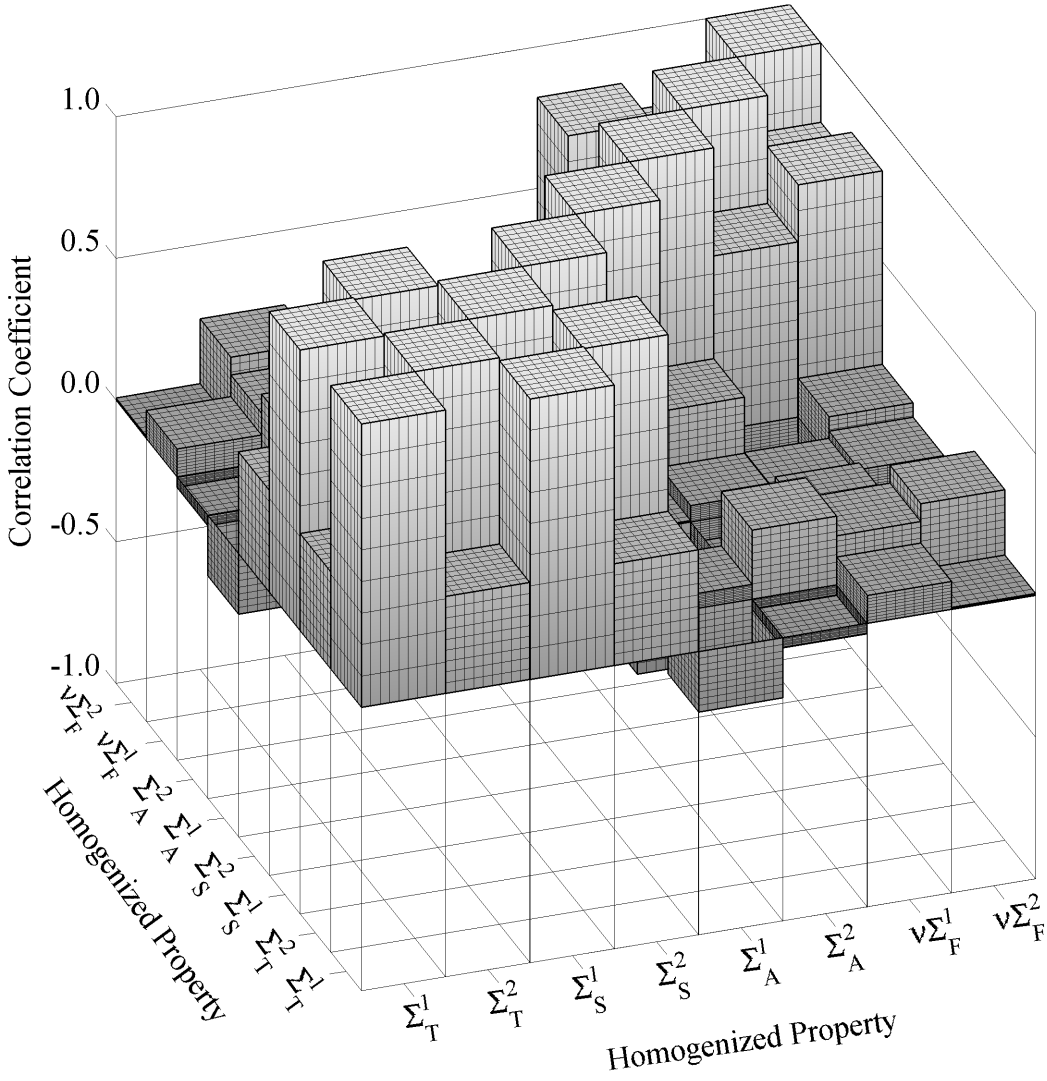

Figure 4.56: TMI-1 HFP two-group homogenized lattice correlation

4.4 Kozloduy unit 6 Vodo-Vodyanoi Energetichesky Reactor

nuclide	reaction/ parameter	Statistical Uniform %Δk/k	Statistical Gaussian %Δ k/k	Direct Perturbation %Δ k/k
ALL	ALL	0.9912	1.0155	1.0331
U^{238}	(n, γ)	0.7829	0.8738	0.8662
U^{235}	(n, γ)	0.4798	0.4961	0.4611
U^{235}	(n, fission)	0.2151	0.2526	0.2557
U^{235}	$\bar{\nu}$	0.1355	0.1348	0.1378
U^{238}	$\bar{\nu}$	0.1060	0.1085	0.1064
Zr^{Nat}	(n, γ)	0.0512	0.0481	0.0460
H^{1}	(n, γ)	0.0505	0.0472	0.0469
O^{16}	(n, γ)	0.0446	0.0429	0.0458
U^{238}	(n, fission)	0.0363	0.0364	0.0368
U^{238}	scatter	0.0185	0.0210	0.0201
H^{1}	scatter	0.0178	0.0166	0.0160
O^{16}	scatter	0.0108	0.0136	0.0114
Hf^{178}	(n, γ)	0.0096	0.0094	0.0100
U^{234}	(n, γ)	0.0056	0.0061	0.0062
Zr^{Nat}	scatter	0.0012	0.0015	0.0013
U^{235}	scatter	0.0007	0.0007	0.0007
Fe^{Nat}	(n, γ)	0.0004	0.0004	0.0004

Table 4.6: Contributions to uncertainty in K-6 k_∞ at HZP

nuclide	reaction/ parameter	Statistical Uniform %Δk/k	Statistical Gaussian %Δ k/k	Direct Perturbation %Δ k/k
ALL	ALL	1.0532	1.0617	1.0799
U^{238}	(n, γ)	0.9848	1.0128	0.9165
U^{235}	(n, γ)	0.4786	0.4362	0.4679
U^{235}	(n, fission)	0.2368	0.2329	0.2593
U^{235}	$\bar{\nu}$	0.1264	0.1308	0.1377
U^{238}	$\bar{\nu}$	0.1155	0.1092	0.1094
H^{1}	(n, γ)	0.0487	0.0441	0.0443
Zr^{Nat}	(n, γ)	0.0432	0.0492	0.0506
O^{16}	(n, γ)	0.0427	0.0482	0.0459
U^{238}	(n, fission)	0.0385	0.0373	0.0383
U^{238}	scatter	0.0222	0.0217	0.0223
H^{1}	scatter	0.0164	0.0180	0.0167
O^{16}	scatter	0.0133	0.0116	0.0132
Hf^{178}	(n, γ)	0.0101	0.0097	0.0104
U^{234}	(n, γ)	0.0051	0.0062	0.0066
Zr^{Nat}	scatter	0.0015	0.0014	0.0014
U^{235}	scatter	0.0007	0.0008	0.0008
Fe^{Nat}	(n, γ)	0.0004	0.0004	0.0005

Table 4.7: Contributions to uncertainty in K-6 k_∞ at HFP

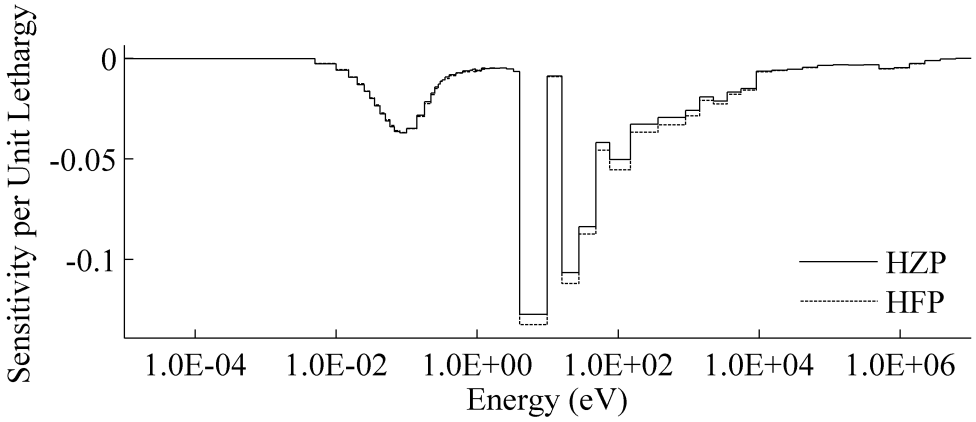

Figure 4.57: Sensitivity profile of K-6 k_∞ to U^{238} (n, γ)

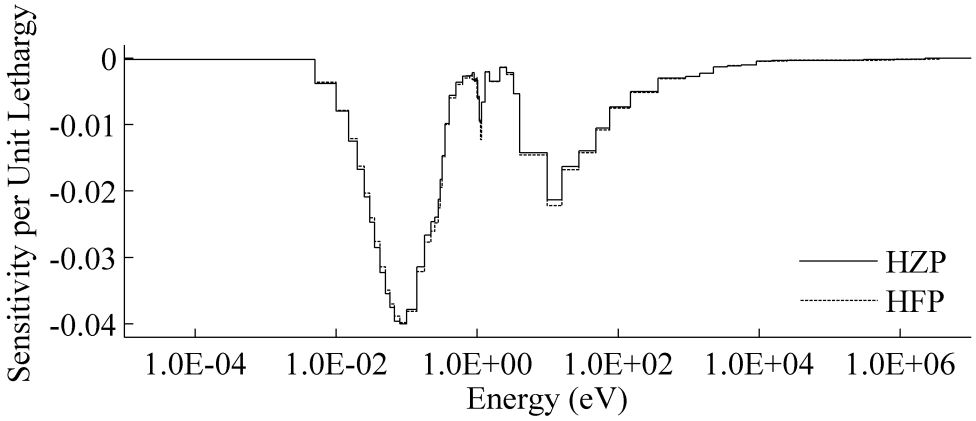

Figure 4.58: Sensitivity profile of K-6 k_∞ to U^{235} (n, γ)

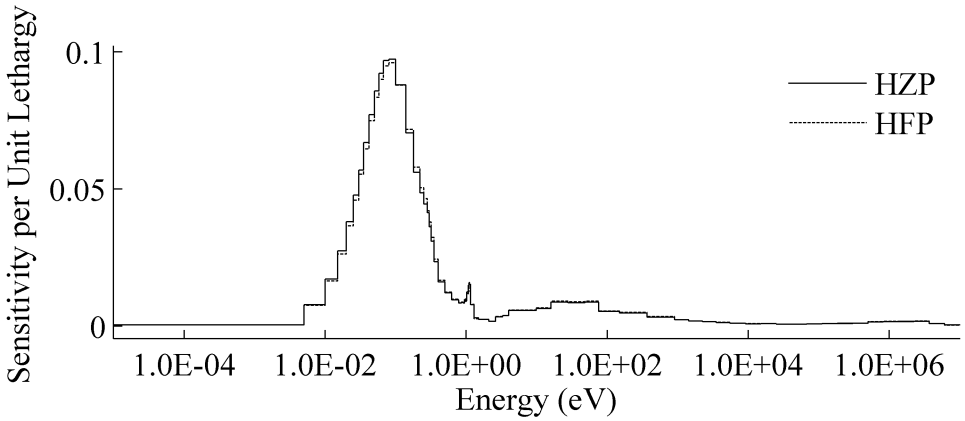

Figure 4.59: Sensitivity profile of K-6 k_∞ to U^{235} (n, fission)

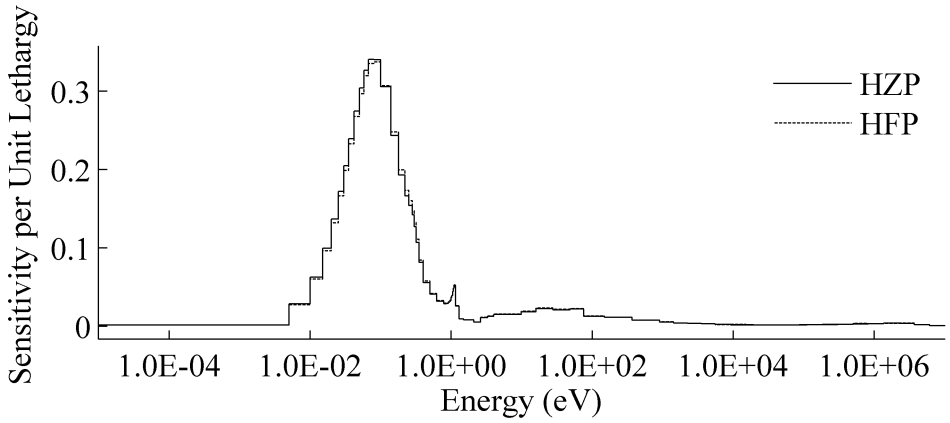

Figure 4.60: Sensitivity profile of K-6 k_∞ to U^{235} $\bar{\nu}$

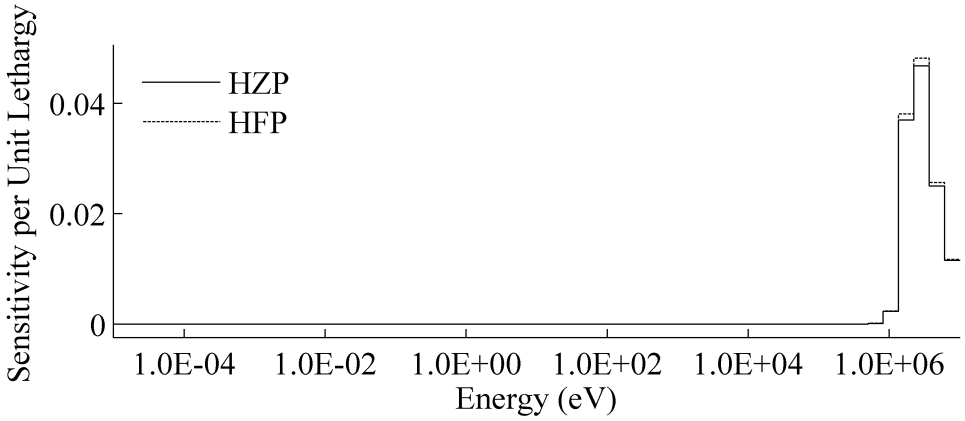

Figure 4.61: Sensitivity profile of K-6 k_∞ to U^{238} $\bar{\nu}$

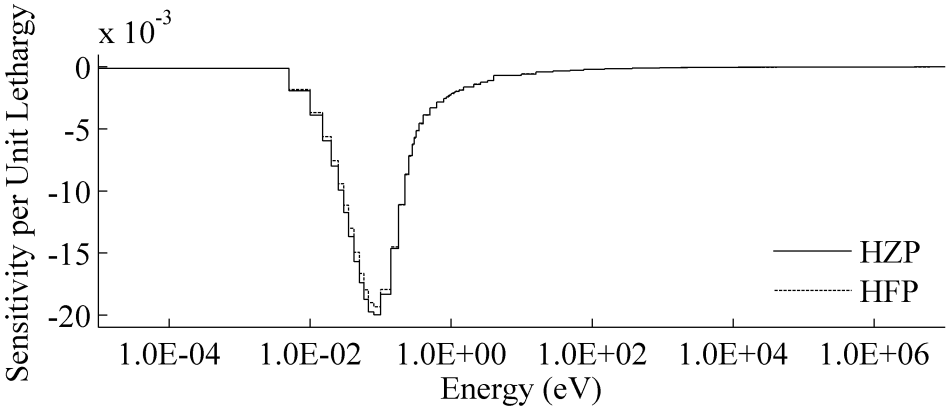

Figure 4.62: Sensitivity profile of K-6 k_∞ to H^1 (n, γ)

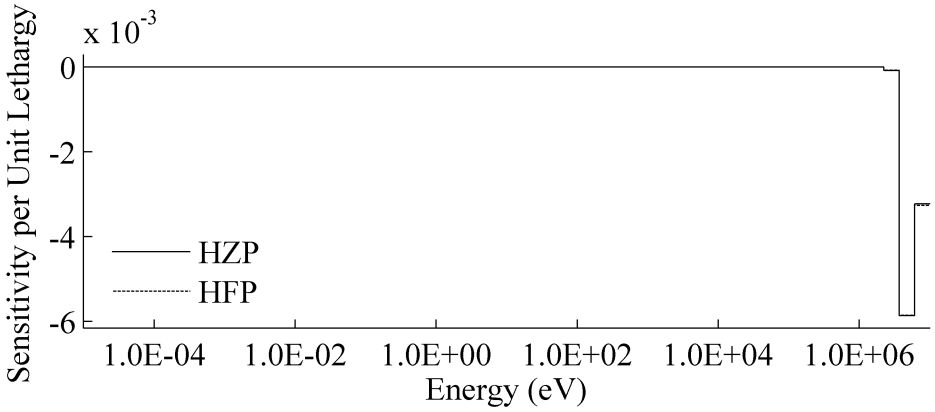

Figure 4.63: Sensitivity profile of K-6 k_∞ to O^{16} (n, γ)

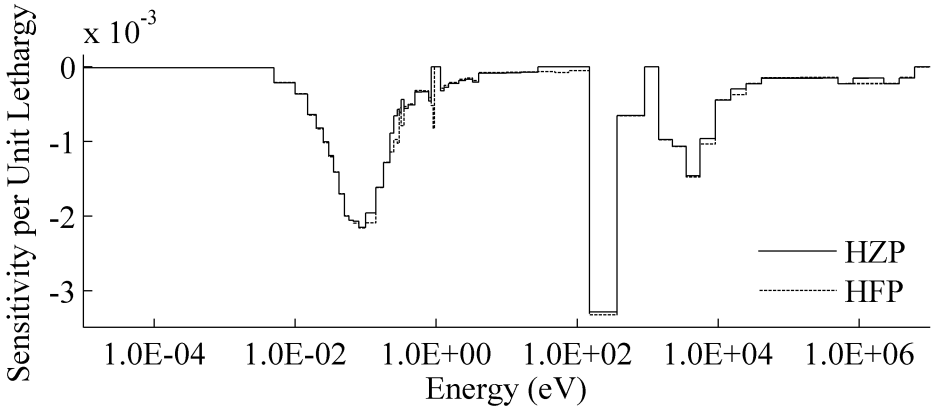

Figure 4.64: Sensitivity profile of K-6 k_∞ to Zr^{Nat} (n, γ)

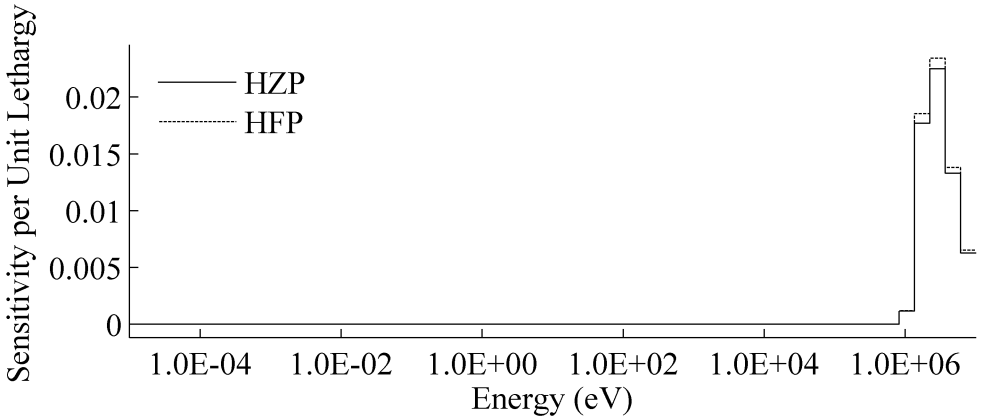

Figure 4.65: Sensitivity profile of K-6 k_∞ to U^{238} (n, fission)

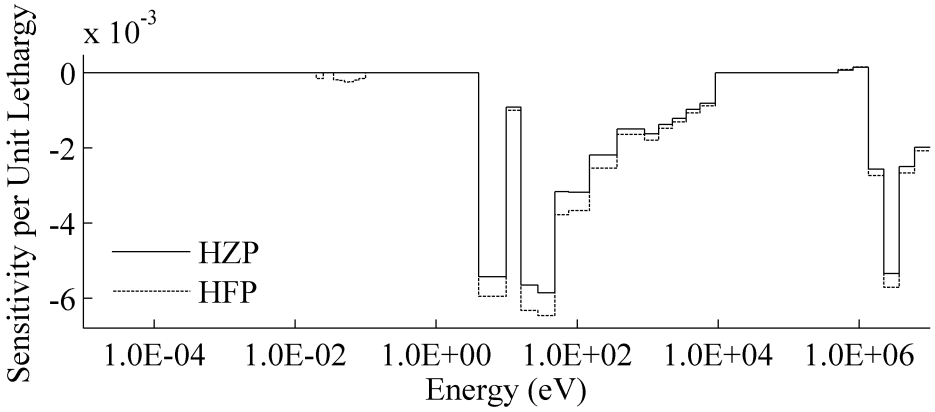

Figure 4.66: Sensitivity profile of K-6 k_∞ to U^{238} scatter

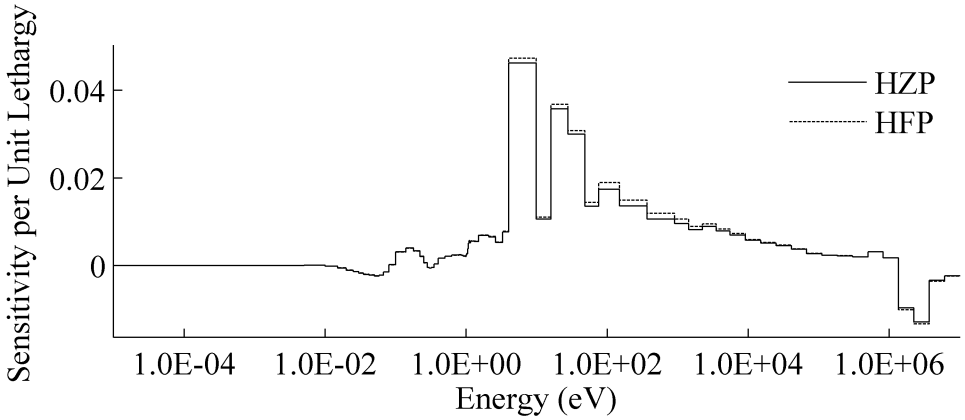

Figure 4.67: Sensitivity profile of K-6 k_∞ to H^1 scatter

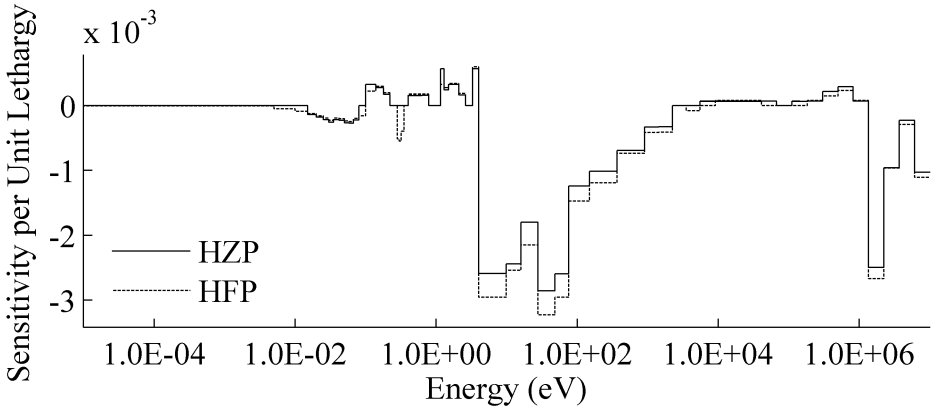

Figure 4.68: Sensitivity profile of K-6 k_∞ to O^{16} scatter

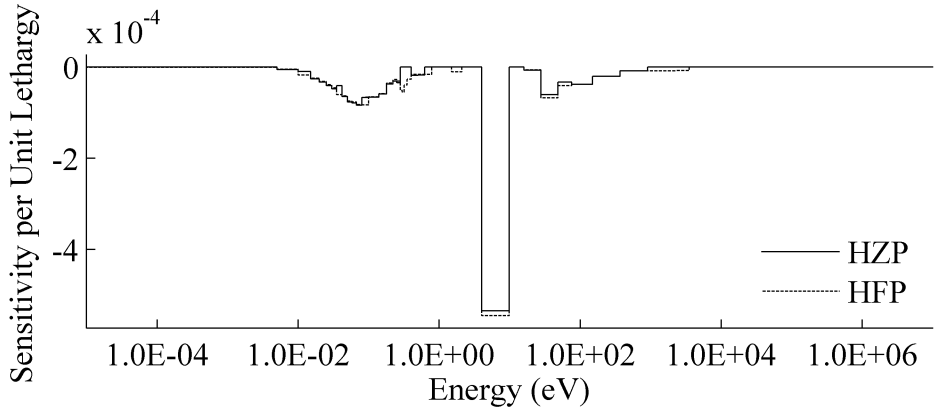

Figure 4.69: Sensitivity profile of K-6 k_∞ to U^{234} (n, γ)

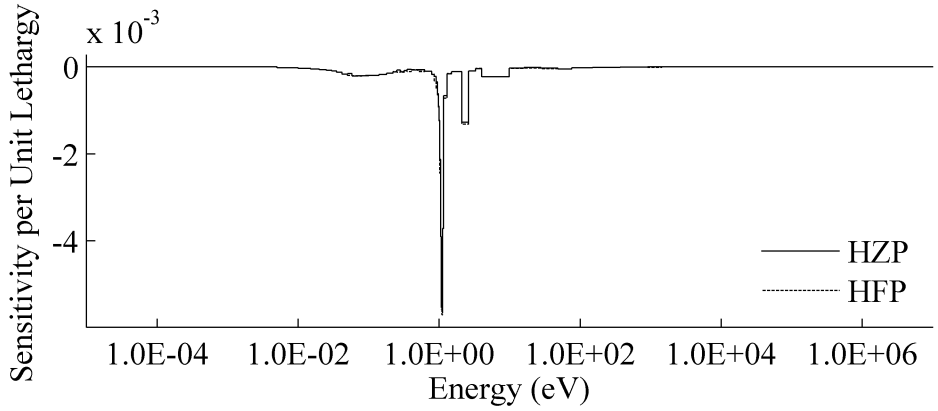

Figure 4.70: Sensitivity profile of K-6 k_∞ to Hf^{178} (n, γ)

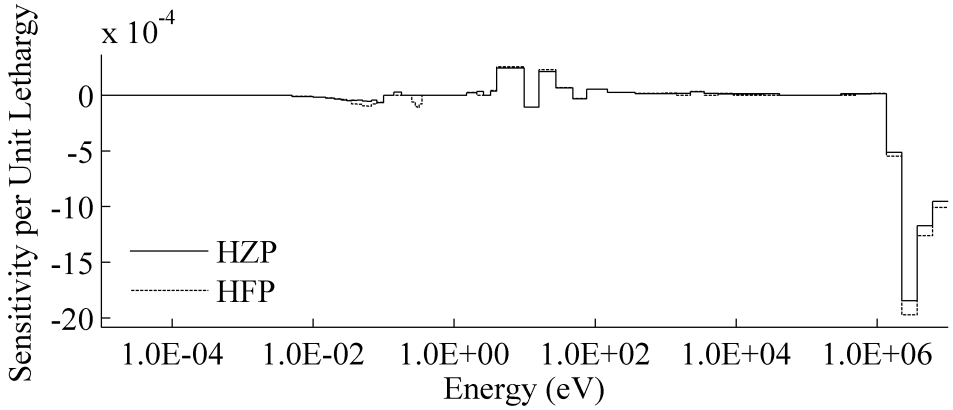

Figure 4.71: Sensitivity profile of K-6 k_∞ to Zr^{Nat} scatter

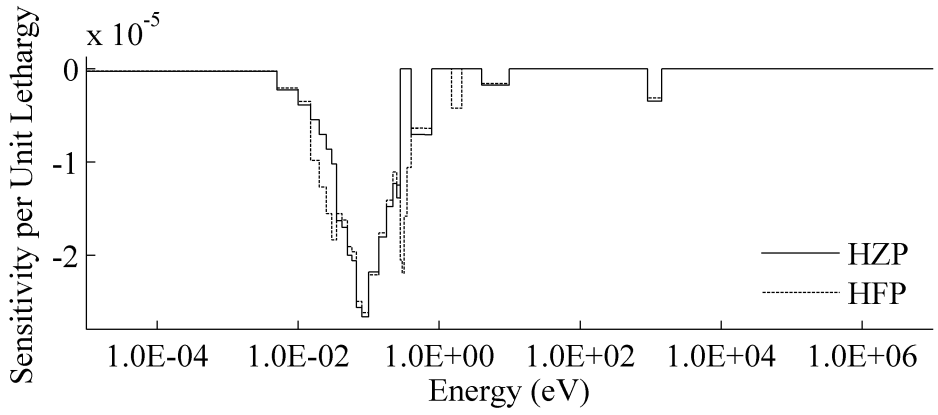

Figure 4.72: Sensitivity profile of K-6 k_∞ to Fe^{Nat} (n, γ)

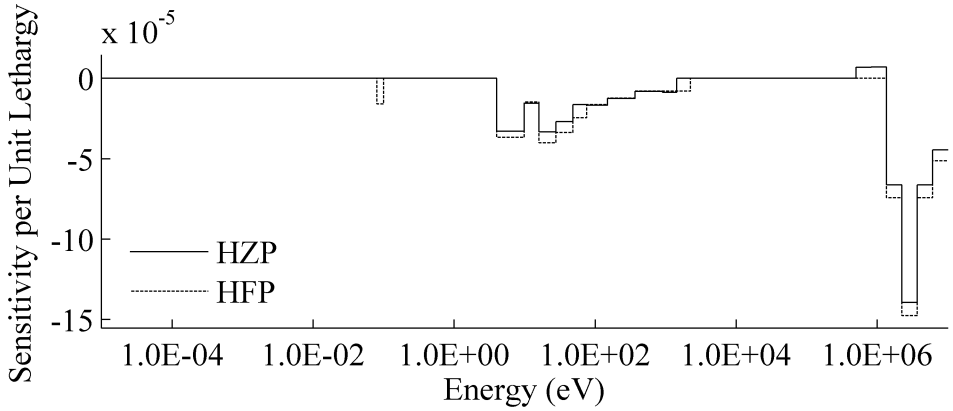

Figure 4.73: Sensitivity profile of K-6 k_∞ to U^{235} scatter

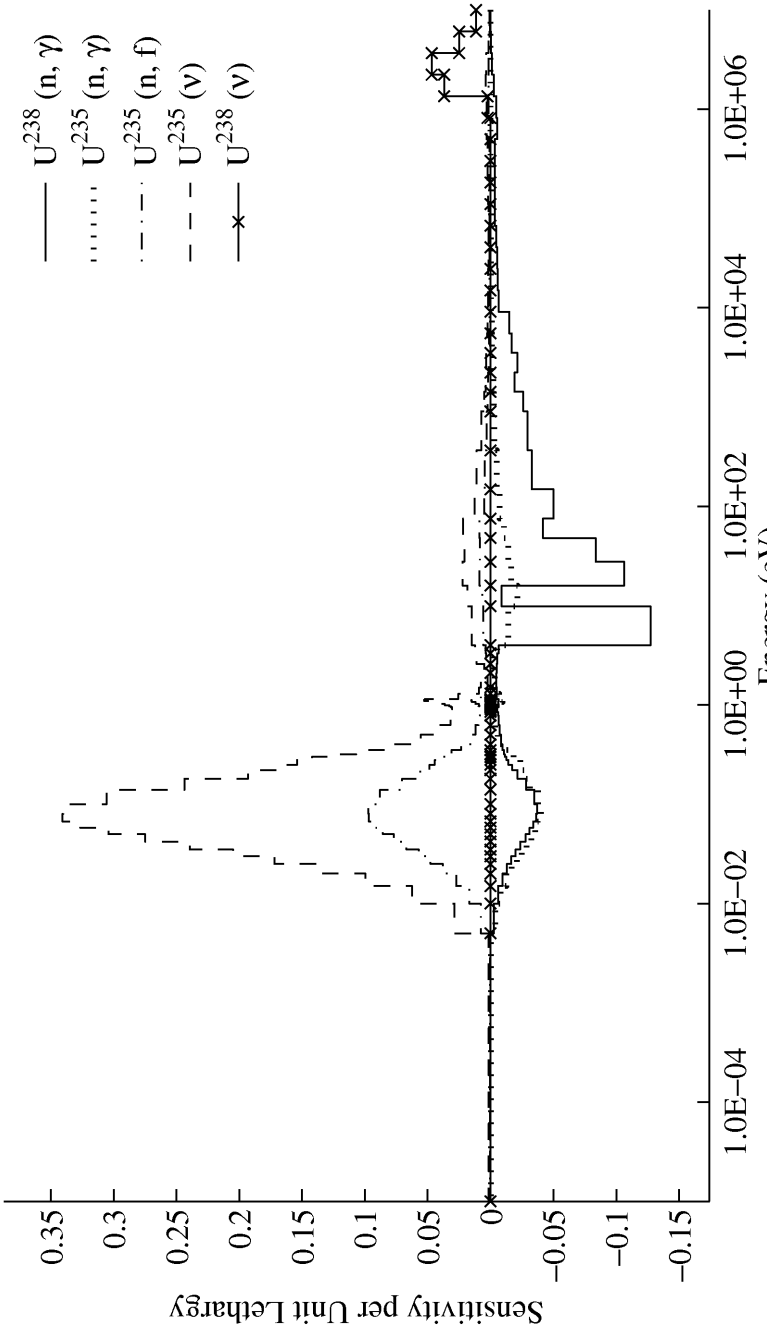

Figure 4.74: Sensitivity to major contributors of HZP K-6 k_∞

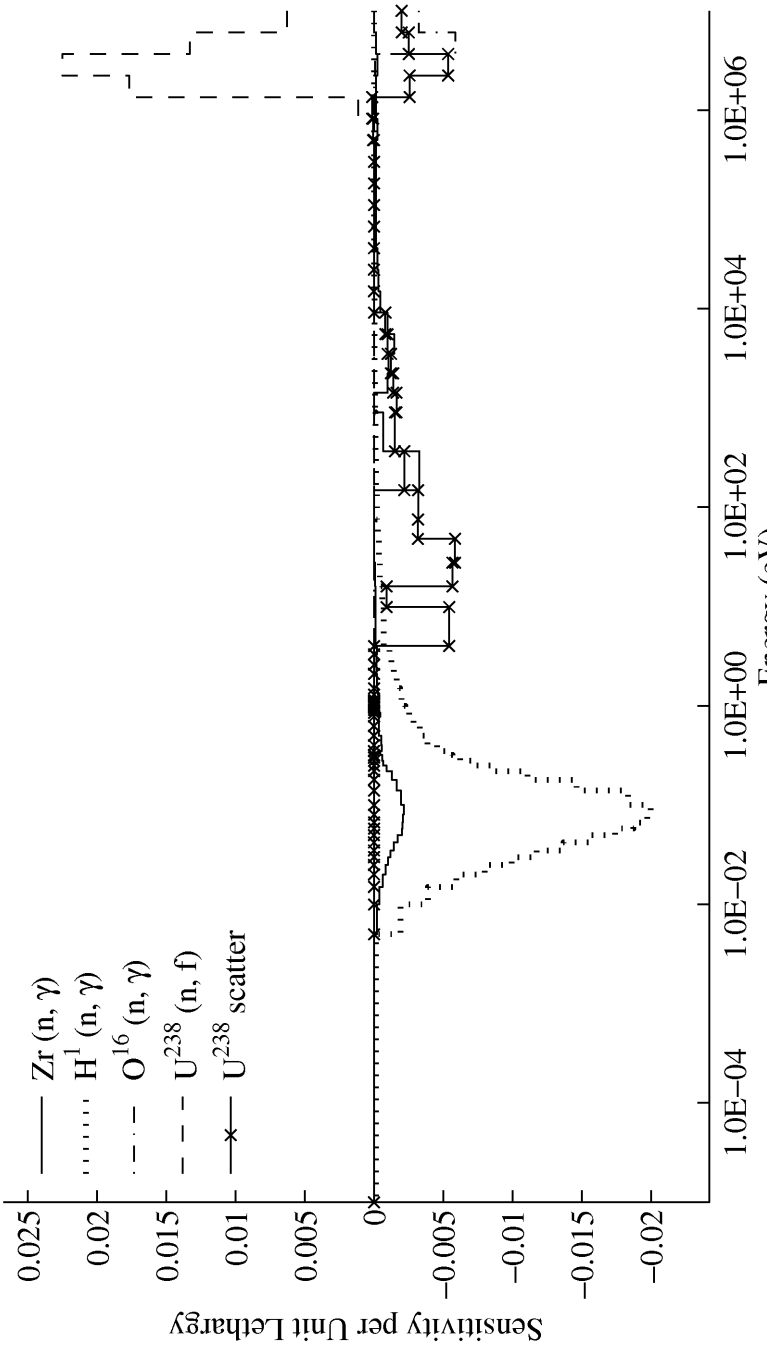

Figure 4.75: Sensitivity to minor contributors of HZP K-6 k_∞

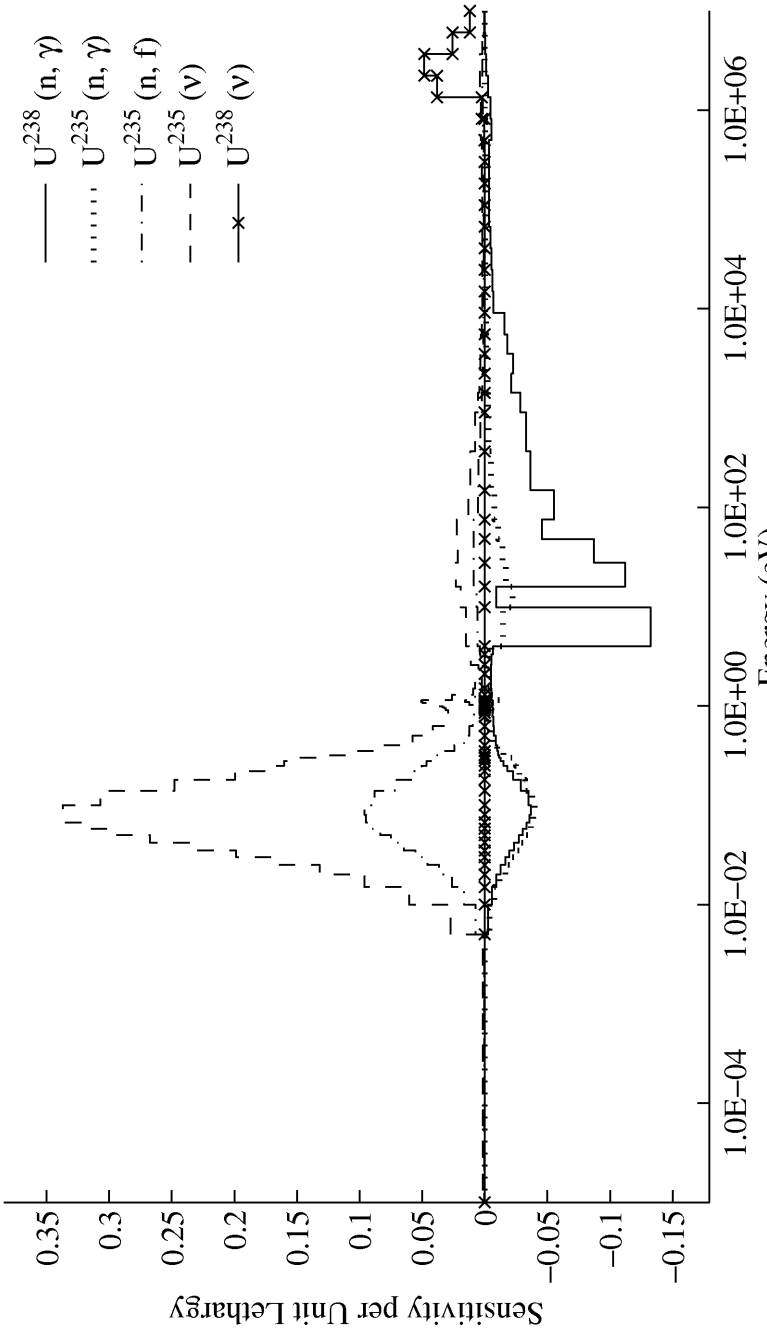

Figure 4.76: Sensitivity to major contributors of HFP K-6 k_∞

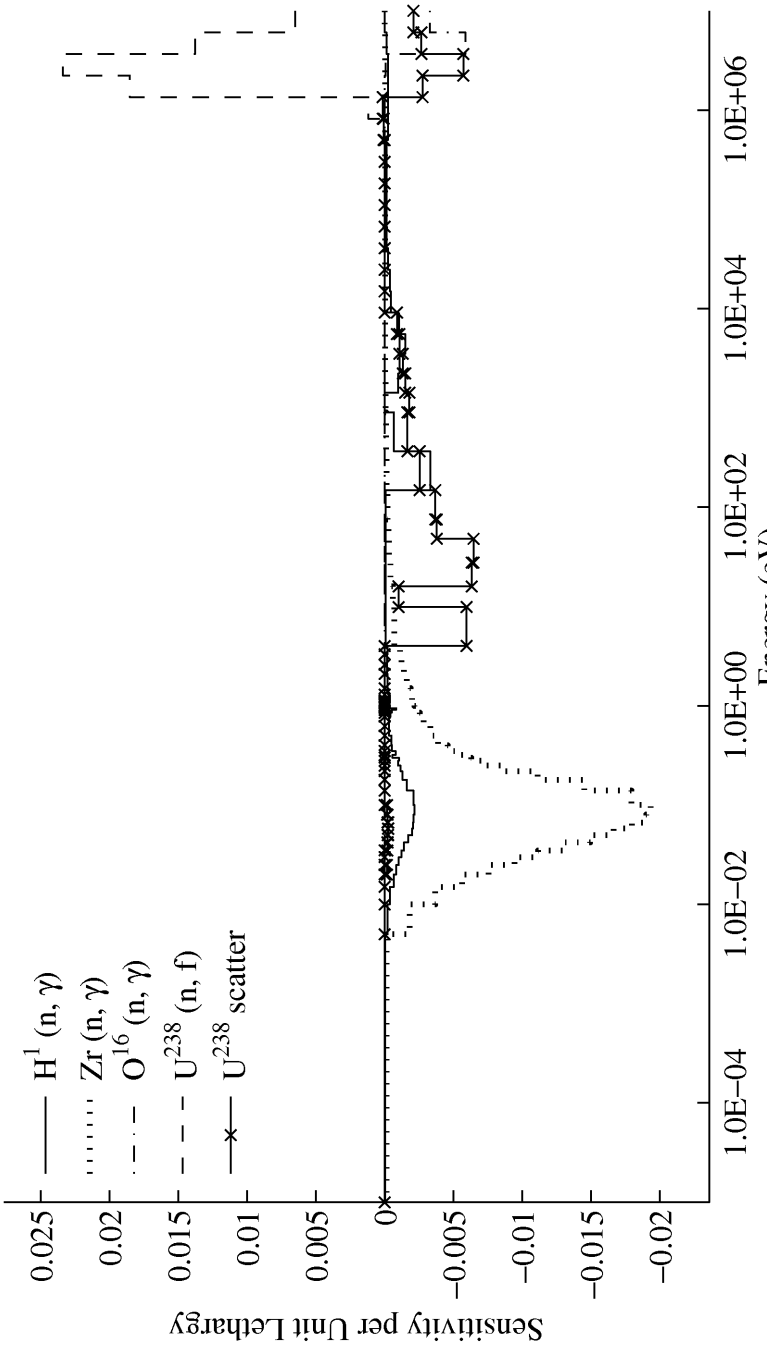

Figure 4.77: Sensitivity to minor contributors of HFP K-6 k_∞

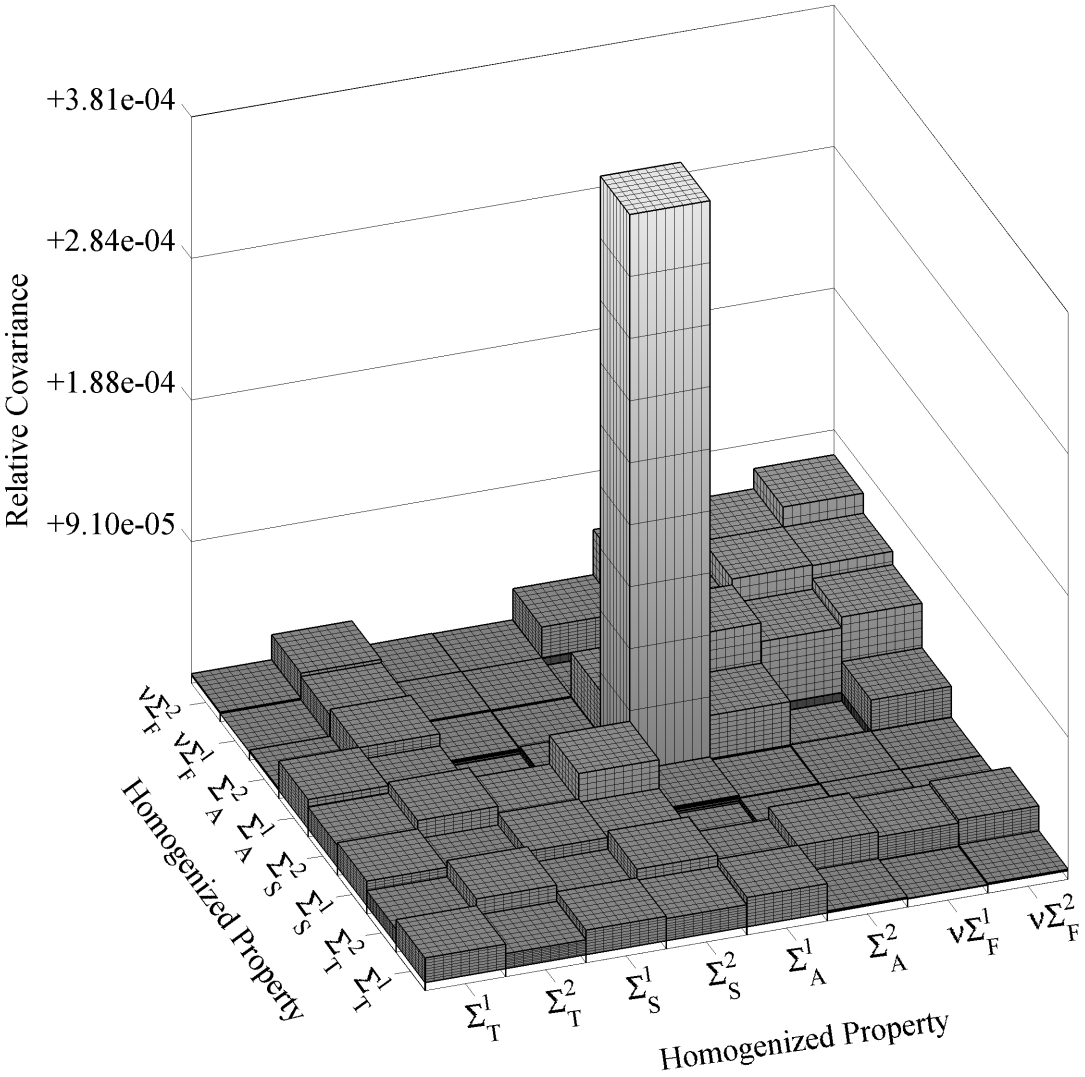

Figure 4.78: K-6 HZP two-group homogenized lattice covariance

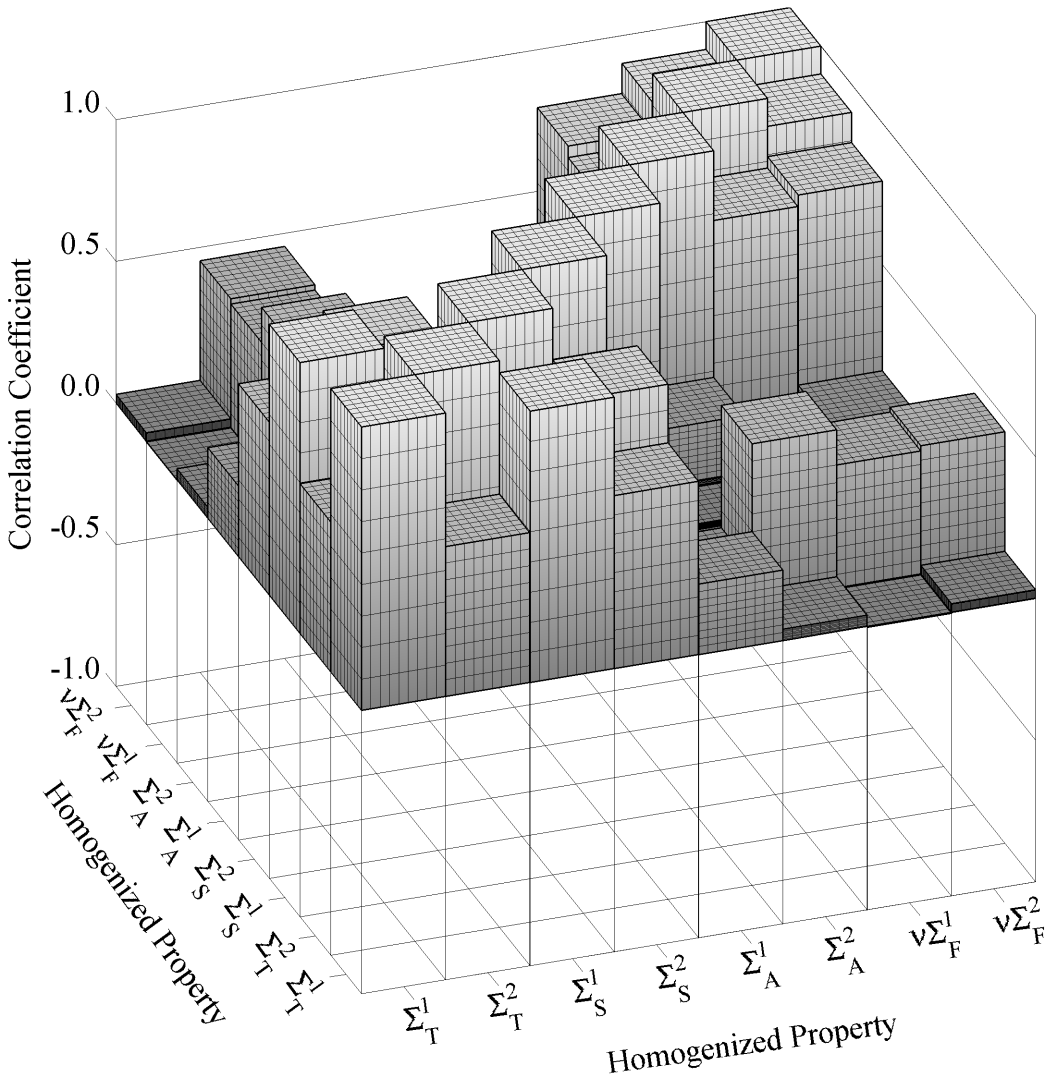

Figure 4.79: K-6 HZP two-group homogenized lattice correlation

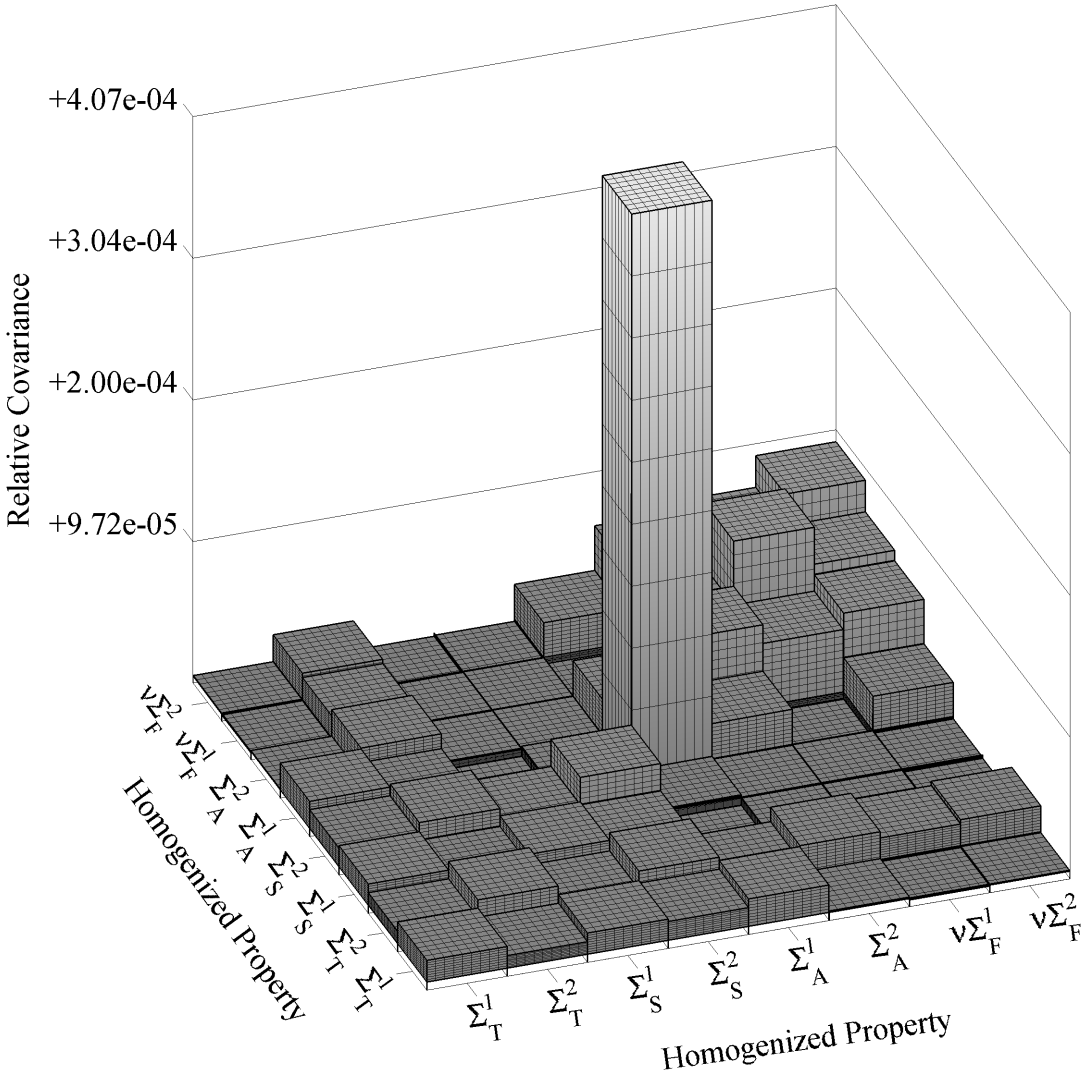

Figure 4.80: K-6 HFP two-group homogenized lattice covariance

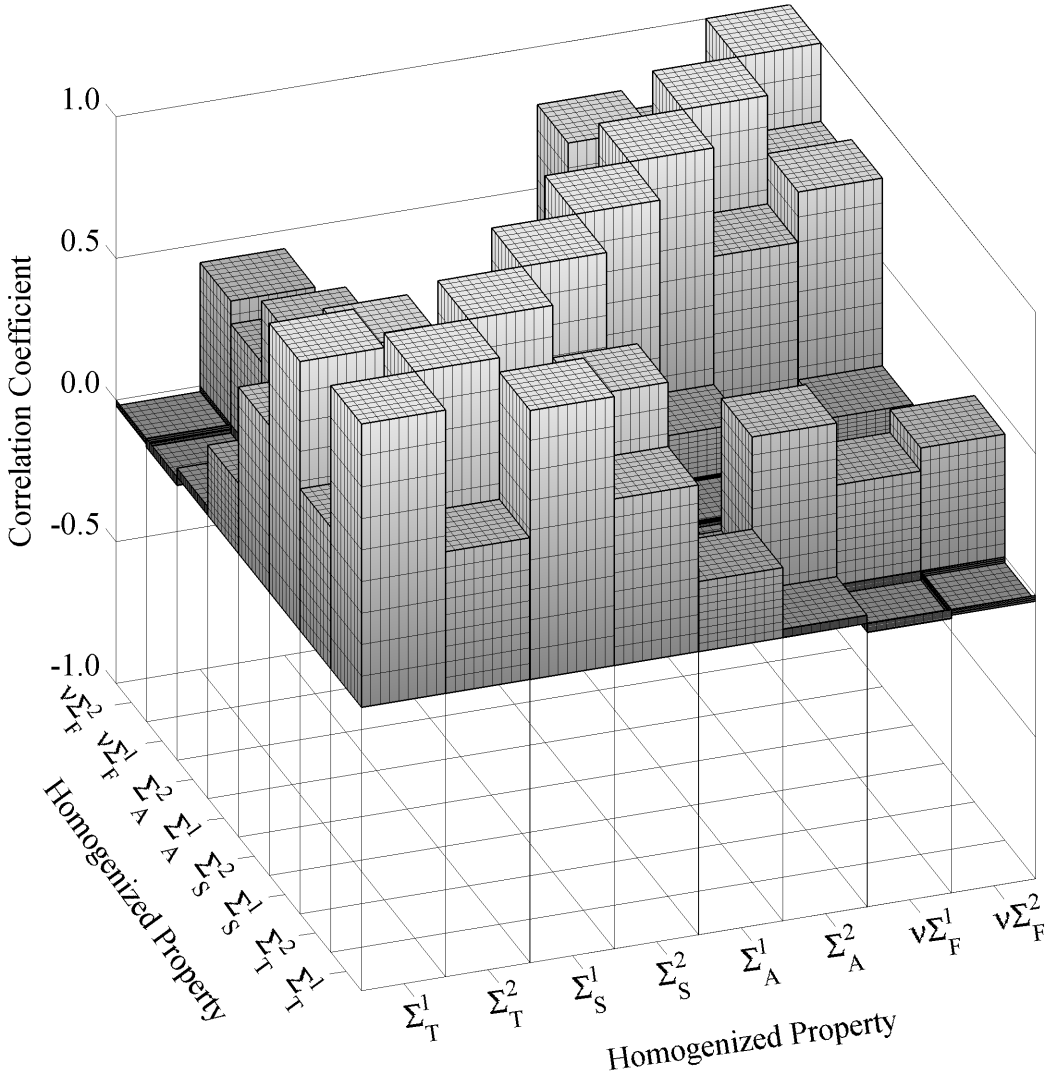

Figure 4.81: K-6 HFP two-group homogenized lattice correlation

4.5 UAM benchmark results discussion

The uncertainties associated with calculated lattice physics outputs shows remarkably little variation against the method of calculation. Uncertainty contributions derived by sampling from Gaussian and uniform distributions show virtually no statistically significant differences. Likewise, the uncertainty predictions made through direct numerical perturbation agree well with their statistically sampled counterparts. In the case of extremely small uncertainty contributors, however, for example those that contribute to $\Delta k/k$ a quantity less than 5E-5, precision limitations related to the solution of the system eigenvalue makes precise uncertainty quantification challenging, because even large changes in the values of these contributors leads to values of k_∞ that are inadequately dissimilar from the best-estimate solution. Thus, it is in the context of very small uncertainty contributors that noticeable discrepancies outside the expected statistical error are occasionally found.

In general, the agreement between direct perturbation uncertainty propagation and statistical propagation suggests that first-order, linear perturbation theory is reasonably suited to lattice calculations and introduces no unreasonable assumptions in regard to the relationship between k_∞ and neutron cross-sections.

The uncertainty associated with k_∞ also shows little variation between LWR reactor designs. Despite their differing pin radii, enrichment, material densities and operating temperatures, the rank of importance of most uncertainty contributors across the test cases are either identical, or statistically indistinguishable. The total uncertainty associated with the infinite multiplication constant due to nuclear data is approximately 1% for five of the six test cases. The singular exception is that of the PB-2 lattice at hot, full-power. The increased k_∞ uncertainty for the PB-2 HFP test case is almost entirely a consequence of an increase arising from the contribution of U^{238} (n, γ). Recall that this particular lattice cell is characterized by a 40% coolant void. The decrease in moderation resulting from the coolant's reduced atom density causes a hardening of the neutron flux spectrum, and thus increases the flux seen at intermediate and high energies (see figure 4.82), where k_∞ is most sensitive to U^{238} (n, γ), as shown in figure 4.3. Neglecting covariances between energy groups, it is possible to estimate the individual contributions to $\Delta k/k$ from a particular cross-section group value when the partial derivative and variance of the cross-section at that group is known. Figure 4.83 shows the per-group contributions of U^{238} (n, γ) to PB-2 k_∞ uncertainty, and the cumulative uncertainty starting at the thermal end of the spectrum and moving to the fast end. As expected, at HFP, there is less total contribution to uncertainty from thermal groups, and a large increase from higher energy groups.

Doppler broadening of resonances not only plays a role in decreasing the best-estimate prediction of k_∞ of the LWR lattice cells at HFP, but also leads to increased uncertainty contributions by strongly resonant cross-sections, particularly U^{238} (n, γ), U^{235} (n, γ), and Zr^{Nat} (n, γ). The change in contribution by these

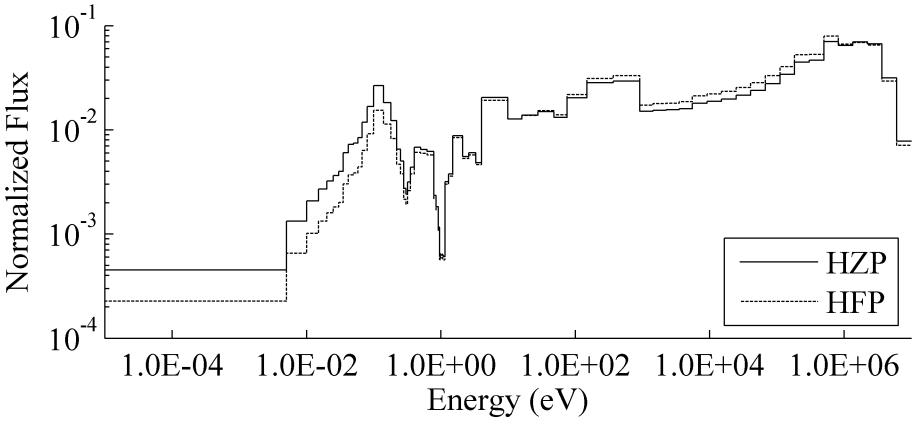

Figure 4.82: PB-2 normalized flux vs. energy group

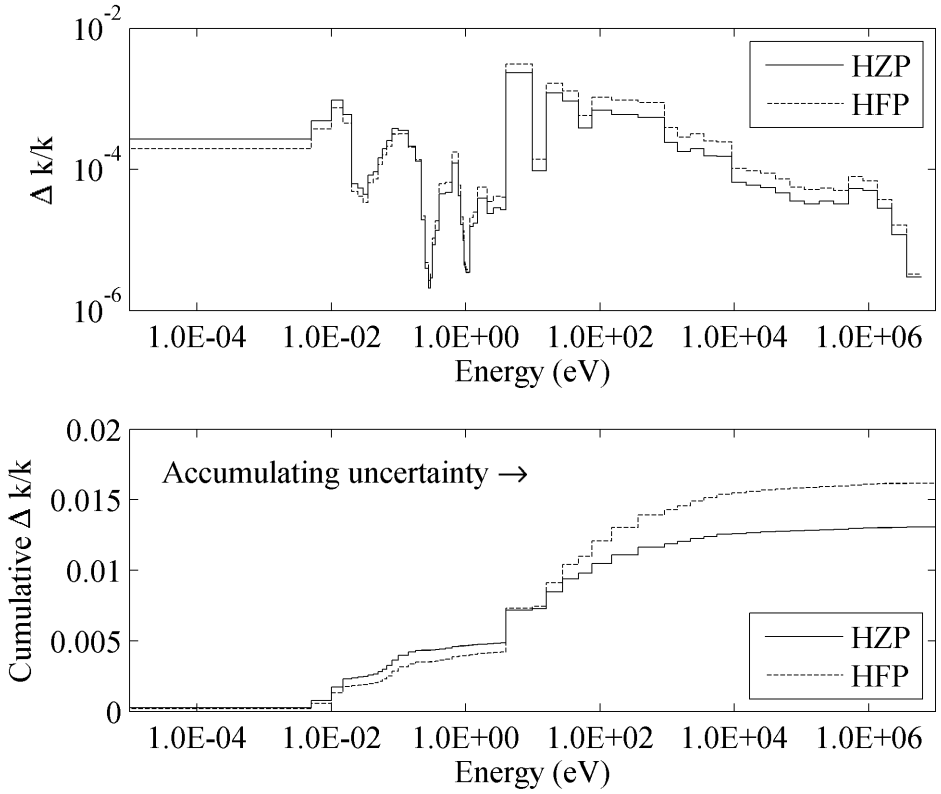

Figure 4.83: PB-2 $\Delta k_\infty/k_\infty$ contributions from uncorrelated U^{238} (n, γ) energy groups

reactions to $\Delta k/k$ is too subtle to be identified through the 128 statistical samples (the statistical uncertainty associated with 128 samples is larger than the effect of the power change), but is readily seen from the results of the direct numerical perturbation as shown in tables 4.4 and 4.5, for example.

Interesting observations related to neutron scattering can be made from the sensitivity studies performed using direct numerical perturbation. The sensitivity of k_∞ to energy-dependent scattering cross-sections is complex, but the general behaviour of neutrons in uranium-fueled thermal reactors can explain some trends related to the elaborate scattering sensitivity profiles shown in the previous section. When fast neutrons are scattered inside fuel material, reactivity suffers because the neutrons can be absorbed by large capture resonances at intermediate energies as they lose speed during collisions. Therefore, larger scattering cross-sections of fuel nuclides corresponds to lower reactivities and hence a negative sensitivity. As shown in the previous section, the sensitivity of k_∞ to scattering cross-sections of U^{238}, U^{235} and O^{16} are consistently negative. The sensitivity to the primary moderating material, H^1, shows a more nuanced and interesting profile, however. The sensitivity to H^1 scatter is positive over most of the energy spectrum, but negative at high energies. This may result from high-energy, fission neutrons that are being ejected from the fuel, which meet the moderator at the fuel/moderator interface, have potential to be reflected by the moderator back into the fuel from which the neutron was in the process of escaping. For the sake of supporting reactivity, fission neutrons should penetrate deep into the moderator before suffering collisions, allowing them to establish sufficient distance to the fuel material that they are unlikely to wander back before being fully thermalized. A low scattering cross-section at high energies makes the moderator more transparent to fast neutrons, and decreasing the chance of a collision in close proximity to the fuel interface. Consequently, it is reasonable for k_∞ to exhibit negative sensitivity to the H^1 scatter cross-section at high energies, because an increase of that cross-section increases neutron opacity of the moderator and reflection back to the fuel. Similarly, intermediate energies of the scatter cross-section are associated with a large, positive sensitivity, likely because it corresponds to a rapid thermalization of neutrons that are probably located far from fuel pins, since they would have already suffered several moderating collisions before reaching intermediate energies. The characteristics of zirconium scattering are similar, given that zirconium is concentrated at the fuel/moderator interface and has potential to be involved in fast neutron reflection. The sensitivity studies indicate that Zr^{Nat}, like H^1, is negatively related to k_∞ at high energies that correspond to fission neutrons.

The lattice output covariance matrices are a function of direct and indirect pathways of uncertainty propagation through the homogenization process. Note that the energy condensation of cross-sections to a two-group structure involves a flux-weighted averaging of multi-group cross-sections. The direct uncertainty pathway is through the multi-group cross-sections themselves. Naturally, if uncertainty exists in the quantities being averaged, there is a directly related uncertainty in the av-

erage quantity. Multi-group cross-section covariance also causes uncertainty on the multi-group neutron flux that is the solution of the lattice equations. Therefore, a component of the uncertainty on the two-group cross-sections is a consequence of the uncertain weighting function used to produce the two-group averaged values, referred to as the indirect effect.

The indirect uncertainty effects act to introduce additional covariance between cross-sections, because the perturbation on flux is propagated through all averaged quantities that employ the flux as a weighting function. Cross-sections in fast energy groups are more likely to cause indirect effects, and are also more prone to those effects, because the profile of fast flux is fairly unconstrained. Conversely, thermal flux is generally constrained to a Maxwellian distribution defined by the temperature of the moderator with limited potential variation, even when faced with changes in higher energy cross-sections. Essentially, neutrons in thermal equilibrium have had enough random collisions to 'forget' the cross-sections experienced at fast energies.

For example, the covariance matrix of the spatially homogenized, 69-group flux of the TMI-1 PWR case at hot, full-power is shown in figure 4.84, and the relative standard deviation of flux in each group in figure 4.85. It can be seen in those figures that there is a great deal more flux uncertainty in the thermal-energy portion of the energy spectrum. However, the thermal flux are all strongly correlated, as shown in figure 4.86, indicating that the profile of the thermal flux sees little variation; the thermal values tend to move in unison. In the fast region, however, a large anti-correlation exists between the flux above 367 eV (the first 20 groups) with those below. Therefore, there exists a large variation in the profile of fast flux, which is used as a weighting function to collapse the first 45 groups into a single fast group during energy condensation. Take the fast group of the 2-group, homogenized scattering cross-section, Σ_S^1, of TMI-1 HFP case as an example. The uncertainty of that homogenized cross-section will have contributions from several multi-group cross-sections belonging to several nuclides. Scattering cross-sections, such as H^1 (n, scatter) will provide a direct uncertainty component due to its multi-group uncertainties that are part of the weighted average of Σ_S^1. Additionally, non-scattering cross-sections, such as U^{238} (n, γ) will contribute uncertainty to Σ_S^1 by causing a related uncertainty on the fast flux that is used as a weighting function applied to microscopic scattering cross-sections. When examining the relative uncertainty in Σ_S^1 of TMI-1 HFP, $\Delta\Sigma_S^1/\Sigma_S^1$, the component from H^1 (n, scatter) was found to be 5.62E-04, whereas the component from U^{238} (n, γ) is 9.00E-4. Therefore, the radiative capture cross-section of U^{238} contributes 60% more uncertainty to the fast homogenized scattering cross-section than does the scattering cross-section of the primary moderating material, solely as a result of indirect uncertainty effects.

The output covariance matrices share a common feature that the largest uncertainty is associated with the fast group of the macroscopic absorption cross-section. The homogenized, 69-group absorption uncertainty is shown in figure 4.87. The 69-group absorption covariance shows that even before the flux-weighted aver-

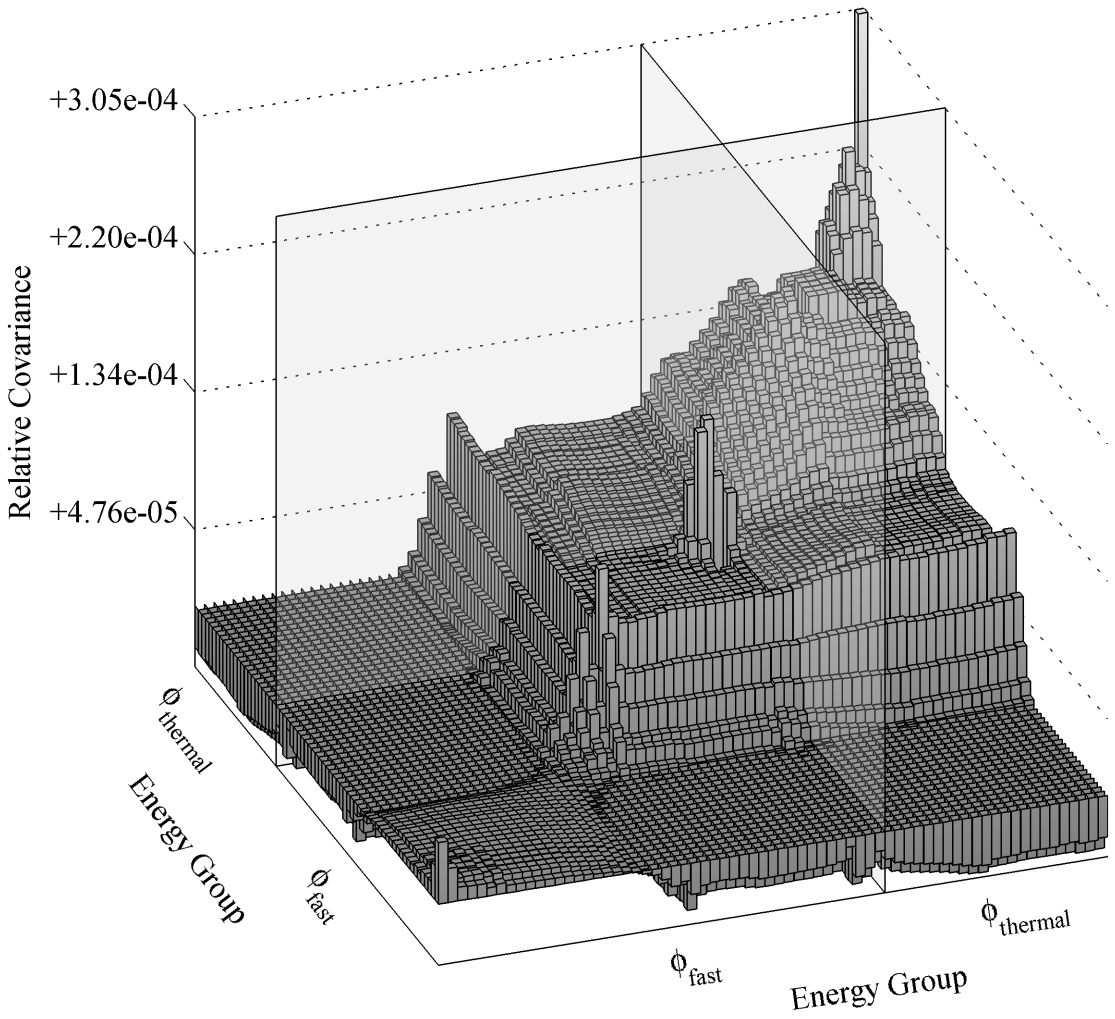

Figure 4.84: TMI-1 HFP 69-group homogenized, normalized flux covariance

aging of group values, there is substantially greater uncertainty associated with fast absorption. The increased high-energy uncertainty is further bolstered by the indirect uncertainty effects that also generally arise at high energies.

From the homogenized correlation matrices, a naturally large dependency is observed between total and scattering cross-sections of the same group. This is merely a consequence of the spatially homogenized scattering cross-section being an order of magnitude larger than the absorption cross-section, and thus being nearly equal to the total cross-section. There is a strong correlation between the absorption and fission yield cross-sections for a similar reason; fission is a nontrivial component in the calculation of absorption. Conversely, the correlations between scattering and absorption cross-sections are small, and are driven mainly by indirect uncertainty effects in the weighting function.

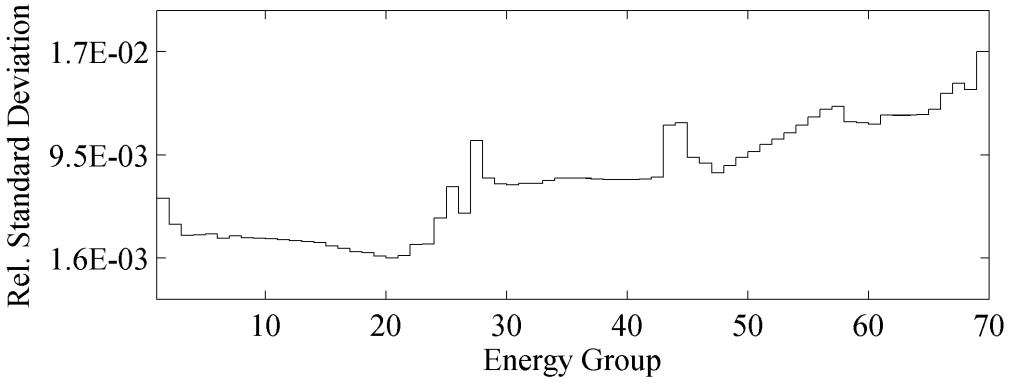

Figure 4.85: TMI-1 HFP 69-group homogenized flux uncertainty

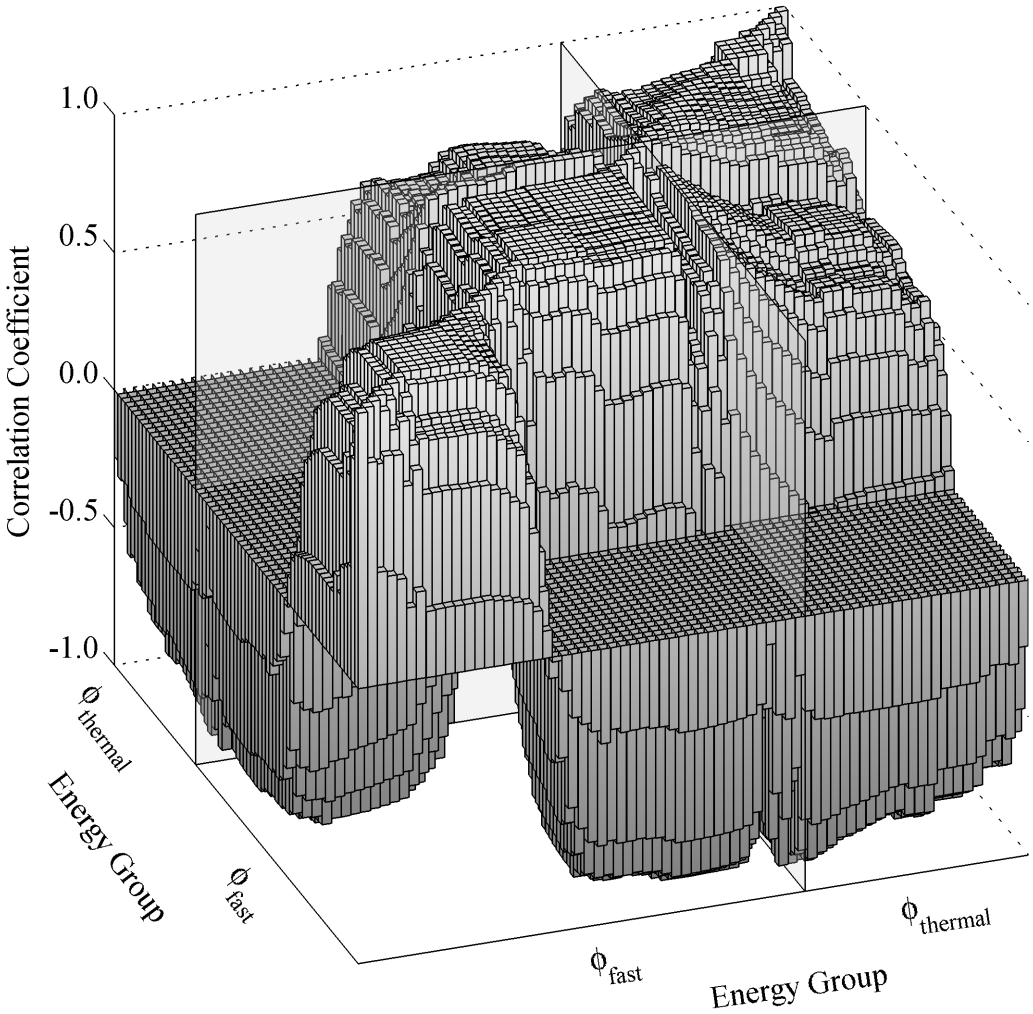

Figure 4.86: TMI-1 HFP 69-group homogenized, normalized flux correlation

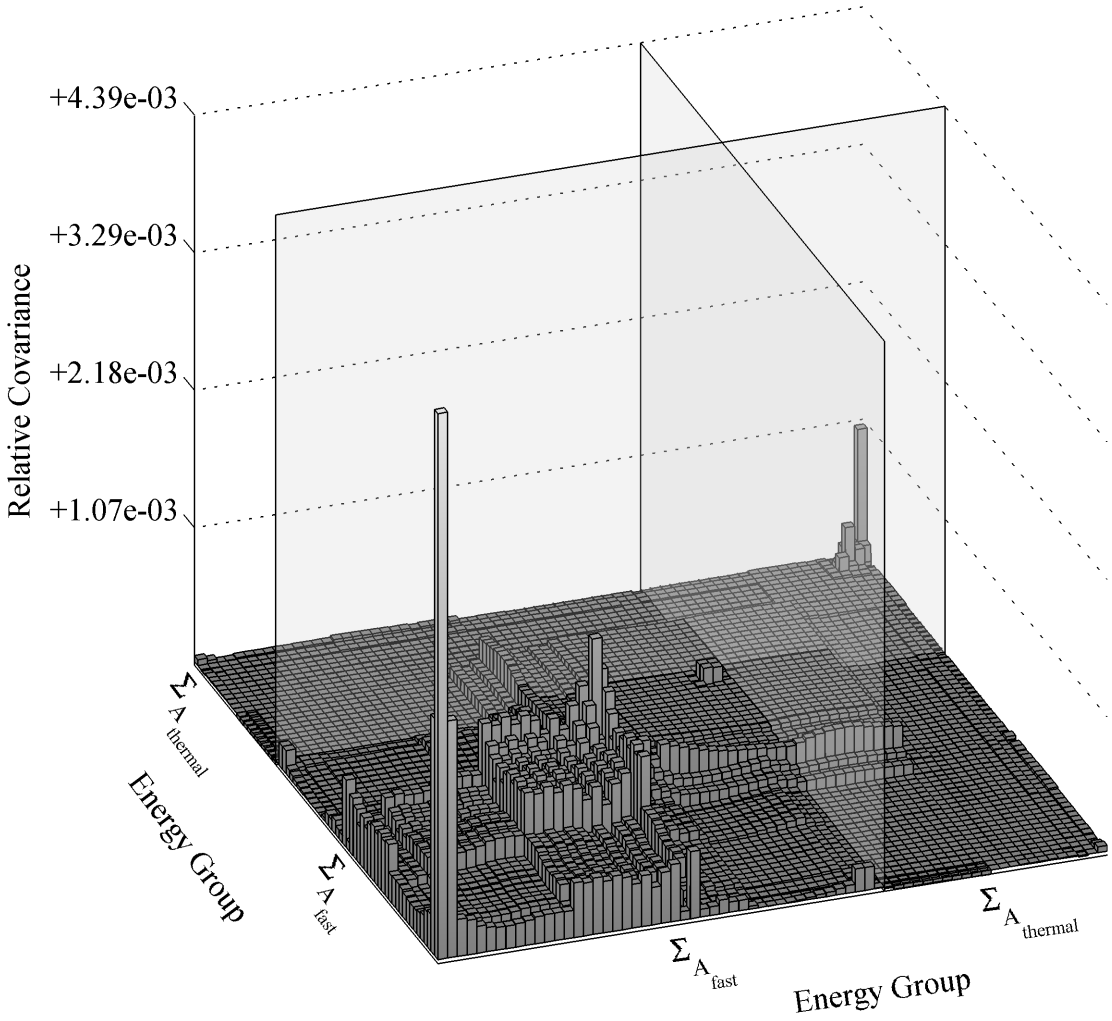

Figure 4.87: TMI-1 HFP 69-group homogenized absorption covariance

Chapter 5

CANDU lattice

This chapter details the results of DINOSAUR uncertainty propagation applied to a representative model of a CANDU® 37-element fuel bundle in an infinite lattice configuration. To the extent that certain specific design specifications of the CANDU® bundle are proprietary intellectual property, the model used in this work is an approximate equivalent, whose specifications are similar yet not necessarily identical to that of any bundle that is actually in service, and is referred to simply as a *generic* CANDU® bundle.

Like the uncertainty propagation and sensitivity analysis that was performed for UAM LWR cells, the generic CANDU bundle was subjected to a statistical sampling of cross-sections according to normal and uniform probability distributions, and direct numerical perturbations were used to establish sensitivity profiles to important multi-group data. Studies were conducted beginning-of-cycle (BoC) fuel and end-of-cycle (EoC) fuel after 180 days of burnup at a constant, high power. Uncertainties associated with k_∞ and atomic number densities of bundle materials, fission products and activation products were calculated as a function of burnup. Note that mid-burnup models are, by definition, evaluated at full-power, as is the EoC lattice.

In addition to the treatment of physics uncertainties, the DECKUA module of DINOSAUR was used to statistically propagate uncertainties in the temperatures of the fuel, coolant and moderator of the CANDU® lattice at hot, full-power. Only uniform probability distributions were used for temperature sampling. Also, sensitivity of k_∞ to changes in material temperatures was computed manually using numerical perturbation. As temperature uncertainty contributions are not yet addressed in the UAM benchmark, corresponding temperature uncertainty analysis was not included in chapter 4.

5.1 Simulation and modelling parameters

The specifications used for generic CANDU® modelling in this discretization are shown in tables 5.1 through 5.3. The spatial discretization of the DRAGON models for neutron transport and resonance self-shielding are shown in figures 5.1 and 5.2. As always, isotropic return boundary conditions are applied to the outer cell boundary. The best-estimate predictions of k_∞ are shown in table 5.4.

The sampling of material temperatures was performed without recalculation of material densities based on the new temperatures in order to isolate the effects of temperature uncertainties on microscopic cross-sections as a result of their dependency on temperature through Doppler broadening. A density change, which can equivalently be regarded as a fractional change in all macroscopic cross-sections, can already be deduced from the sensitivity analysis conducted for each cross-section. The Doppler broadening dependency, however, represents a separate mechanism for uncertainty propagation in lattice physics that deserved an explicit and dedicated examination. Lattice components whose temperatures are related (e.g. moderator with calandria rube, and coolant with pressure tube and fuel clad) had their temperatures varied in a way consistent with a full correlation. For example, as coolant temperature was varied, pressure tube temperature was varied identically. The relative standard deviation applied as inputs to fuel, moderator and coolant temperature were assumed to be 2%. Although high-fidelity estimates of CANDU® temperature uncertainties are absent in literature, estimates of LWR fuel temperature uncertainties range from 2%[64] to over 25%[65], depending on reactor operating conditions. The statistical propagation of each of the three uncertain input temperatures involved 1056 random samples.

Parameter	Value
Lattice pitch [cm]	28.575
Fuel pellet diameter [mm]	12.24
Fuel pellet material	UO_2
Fuel density [g/cm^3]	10.4
Fuel enrichment, w/o	0.7
Cladding outside diameter [mm]	13.08
Cladding thickness [mm]	0.42
Cladding material	Zr alloy
Pressure tube material	Zr + 2% Nb alloy
Calandria tube material	Zr alloy
Cladding density [g/cm^3]	6.44
Gap material	CO_2
Moderator material	D_2O

Table 5.1: Generic CANDU® operating temperatures

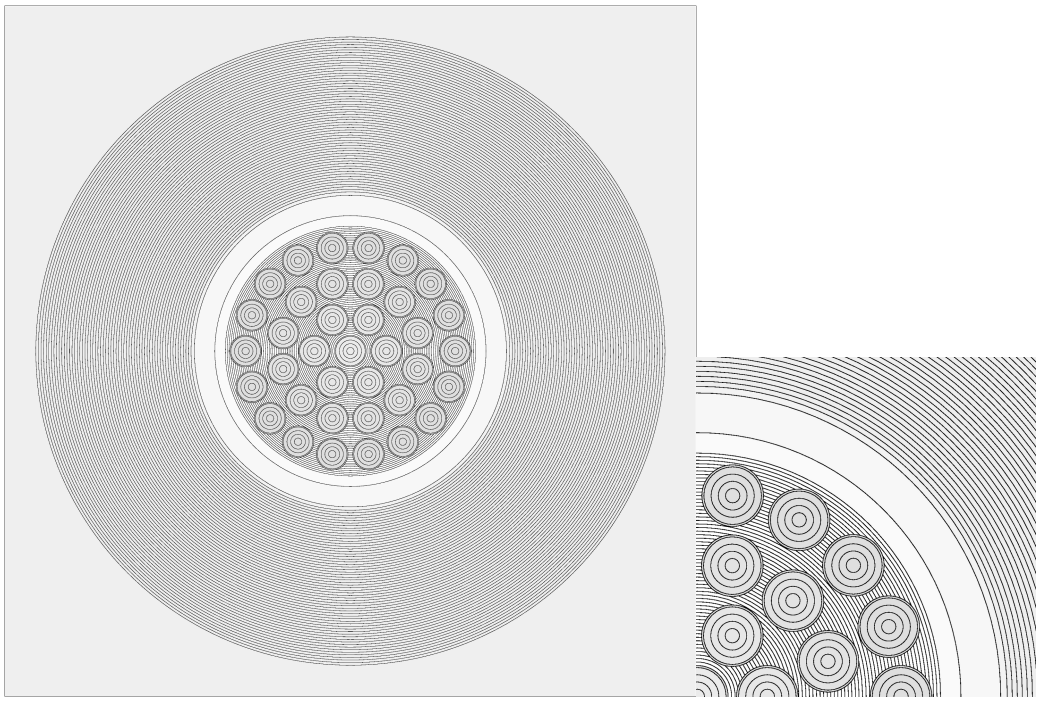

(a) flux solution (b) magnified

Figure 5.1: CANDU® DRAGON model discretization

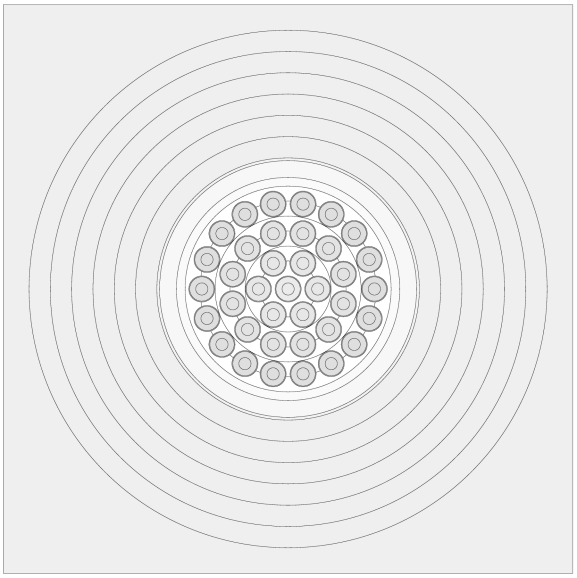

Figure 5.2: CANDU® DRAGON model discretization for self-shielding

Material	Nuclide	Percent weight
Zr alloy	Zr^{Nat}	99.71
	Fe^{Nat}	1.60
	Cr^{Nat}	1.10
	Ni^{Nat}	0.06
Zr + 2%Nb alloy	Zr^{Nat}	97.50
	Nb^{93}	2.50
Uranium fuel	U^{234}	0.00
	U^{235}	0.70
	U^{238}	99.30
Moderator	D_2O	99.8
	H_2O	0.2

Table 5.2: Generic CANDU® material compositions

Reactor conditions	HZP	HFP
Fuel temperature [K]	560.66	941.29
Cladding temperature [K]	560.66	560.66
Moderator temperature [K]	345.66	345.66
Moderator density [g/cm^3]	1.083	1.083

Table 5.3: Generic CANDU® operating temperatures

	BoC		EoC
Lattice cell	HZP	HFP	HFP
Generic CANDU®	1.12675	1.20613	0.98723

Table 5.4: Best-estimate predictions of CANDU® BoC k_∞

The effects of burnup, and the changing material composition that results, was studied only statistically using DINOSAUR. The multi-group nuclear data of all nuclides that appear during irradiation were subjected to 96 samples of statistical variation. On each sample of varied data, a full 180-day burnup calculation was conducted at a constant power of 900 kW/bundle. This is not a reflection of the true power irradiation of in-core bundles in operational CANDU® plants, in which fresh bundles start burning at low power (100 W to 200 W), and then ramp up to higher power ($<$ 900 W) before ultimately falling once again to low power. However, the

purpose of this burnup investigation is to study the effect of cross-sections on creation and removal rates of nuclides, and the influence of burnup product cross-sections on lattice parameters. The mapping of simulation burnup to in-core burnup histories of real bundles introduces an additional degree of freedom on lattice properties that was undesirable when attempting to isolate cross-section uncertainty consequences. Due to the large computational effort necessary to calculate 180 days of fuel burning, and the large number of nuclides that appear during burnup and contribute to lattice properties, a per-nuclide investigation by either a statistical sampling or direct numerical perturbation method was not feasible. A list of nuclides that appear during burnup as either fission products, activation products, or decay products are listed in table 5.5.

Kr^{36}	In^{115}	Nd^{143}	Eu^{153}	Ho^{165}	Pu^{240}
Mo^{95}	Sb^{125}	Nd^{145}	Eu^{154}	Er^{166}	Pu^{241}
Tc^{99}	Te^{127}	Pm^{147}	Eu^{155}	Er^{167}	Pu^{242}
Ru^{101}	I^{127}	Pm^{148}	Gd^{154}	Pa^{231}	Am^{241}
Ru^{103}	I^{135}	Pm^{149}	Gd^{155}	U^{232}	Am^{242}
Ru^{106}	Xe^{131}	Sm^{147}	Gd^{156}	U^{233}	Am^{243}
Rh^{103}	Xe^{134}	Sm^{148}	Gd^{157}	U^{234}	Cm^{242}
Rh^{105}	Xe^{135}	Sm^{149}	Gd^{158}	U^{236}	Cm^{243}
Pd^{105}	Xe^{136}	Sm^{150}	Dy^{160}	U^{237}	Cm^{244}
Pd^{107}	Cs^{133}	Sm^{151}	Dy^{161}	Np^{237}	
Pd^{108}	Cs^{134}	Sm^{152}	Dy^{162}	Np^{239}	
Ag^{109}	Cs^{135}	Eu^{151}	Dy^{163}	Pu^{238}	
Cd^{113}	Cs^{137}	Eu^{152}	Dy^{164}	Pu^{239}	

Table 5.5: Nuclides in *IAEA* that appear during CANDU® burnup

5.2 BoC lattice

Fresh, generic CANDU® lattice cells were evaluated at HZP and HFP conditions. In a similar manner as the LWR analysis, 1024 samples were taken when sampling all cross-sections simultaneously. When individual contributions to k_∞ uncertainty were identified by sampling multi-group cross-sections one at a time, 128 samples were used for each investigation. The contributions to k_∞ uncertainty are shown in tables 5.6 and 5.7, and sensitivity profiles in figures 5.3 to 5.24.

nuclide	reaction/ parameter	Statistical Uniform %Δk/k	Statistical Gaussian %Δ k/k	Direct Perturbation %Δ k/k
ALL	ALL	1.2642	1.2300	1.2451
U^{238}	(n, γ)	1.0877	1.1130	1.1492
U^{235}	(n, fission)	0.2774	0.2609	0.2791
U^{235}	(n, γ)	0.2708	0.2957	0.2887
U^{235}	$\bar{\nu}$	0.1465	0.1421	0.1426
Zr^{Nat}	(n, γ)	0.1323	0.1392	0.1420
H^{2}	(n, γ)	0.1091	0.1058	0.0949
U^{238}	$\bar{\nu}$	0.1011	0.0995	0.0909
O^{16}	(n, γ)	0.0710	0.0635	0.0665
H^{2}	scatter	0.0615	0.0666	0.0650
U^{238}	(n, fission)	0.0383	0.0365	0.0364
U^{238}	scatter	0.0156	0.0142	0.0144
O^{16}	scatter	0.0109	0.0117	0.0109
Cr^{52}	(n, γ)	0.0077	0.0076	0.0077
H^{1}	(n, γ)	0.0047	0.0047	0.0046
Fe^{Nat}	(n, γ)	0.0040	0.0044	0.0040
Zr^{Nat}	scatter	0.0016	0.0014	0.0016
H^{1}	scatter	0.0002	0.0002	0.0002
U^{235}	scatter	0.0002	0.0002	0.0002

Table 5.6: Contributions to uncertainty in CANDU k_{∞} at HZP (BoC)

nuclide	reaction/ parameter	Statistical Uniform %Δk/k	Statistical Gaussian %Δ k/k	Direct Perturbation %Δ k/k
ALL	ALL	1.2640	1.3143	1.2741
U^{238}	(n, γ)	1.1963	1.2052	1.1837
U^{235}	(n, fission)	0.2789	0.2576	0.2645
U^{235}	(n, γ)	0.2779	0.2966	0.2946
U^{235}	$\bar{\nu}$	0.1374	0.1423	0.1417
Zr^{Nat}	(n, γ)	0.1269	0.1466	0.1369
H^{2}	(n, γ)	0.1095	0.1051	0.0912
U^{238}	$\bar{\nu}$	0.0937	0.0913	0.0904
H^{2}	scatter	0.0674	0.0633	0.0647
O^{16}	(n, γ)	0.0668	0.0727	0.0664
U^{238}	(n, fission)	0.0395	0.0377	0.0361
O^{16}	scatter	0.0204	0.0197	0.0091
U^{238}	scatter	0.0164	0.0144	0.0139
Cr^{52}	(n, γ)	0.0076	0.0077	0.0005
H^{1}	(n, γ)	0.0042	0.0048	0.0045
Fe^{Nat}	(n, γ)	0.0037	0.0040	0.0040
Zr^{Nat}	scatter	0.0016	0.0016	0.0016
H^{1}	scatter	0.0003	0.0003	0.0002
U^{235}	scatter	0.0002	0.0002	0.0002

Table 5.7: Contributions to uncertainty in CANDU k_{∞} at HFP (BoC)

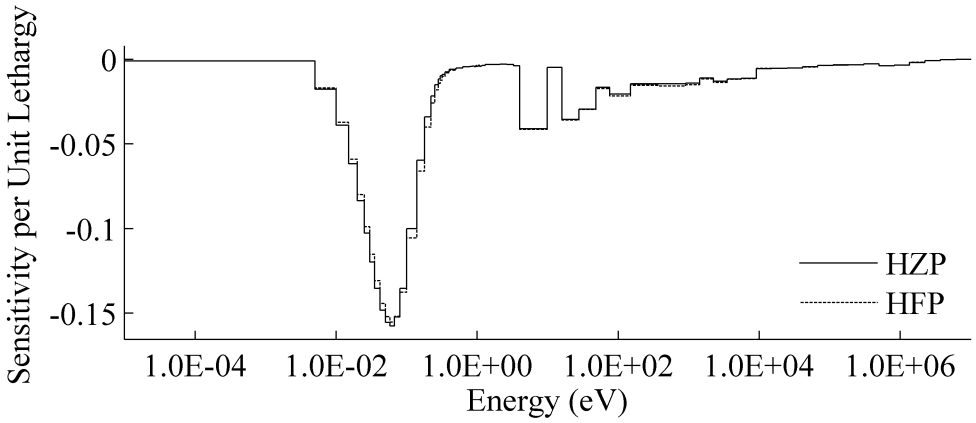

Figure 5.3: Sensitivity profile of CANDU® k_∞ to U^{238} (n,γ)

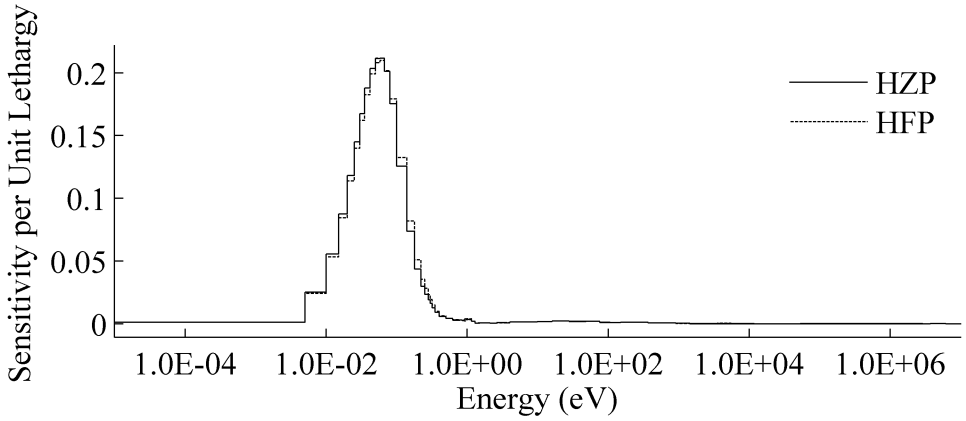

Figure 5.4: Sensitivity profile of CANDU® k_∞ to U^{235} (n, fission)

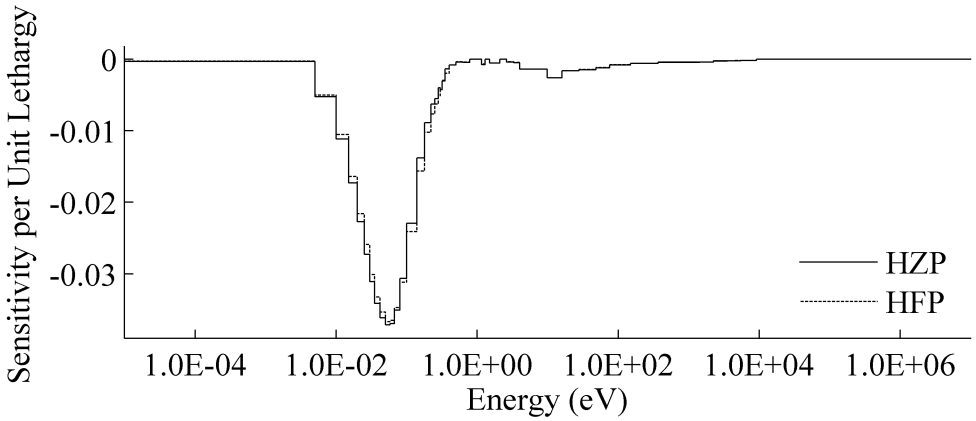

Figure 5.5: Sensitivity profile of CANDU® k_∞ to U^{235} (n, γ)

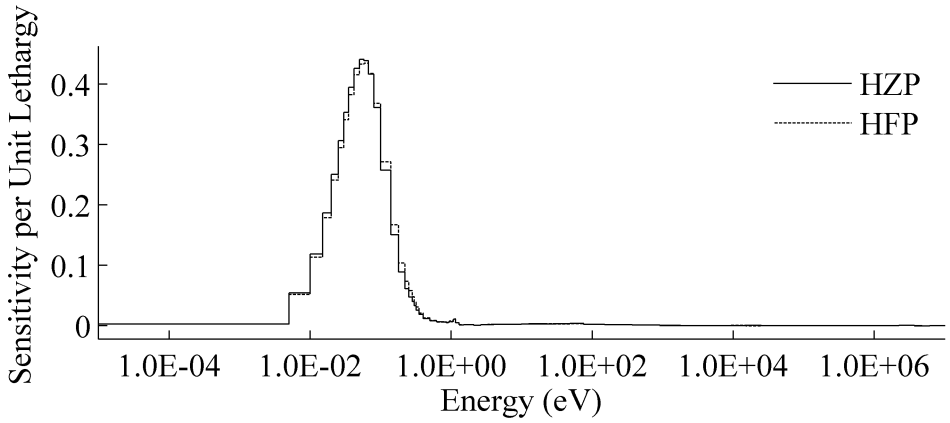

Figure 5.6: Sensitivity profile of CANDU® k_∞ to U^{235} $\bar{\nu}$

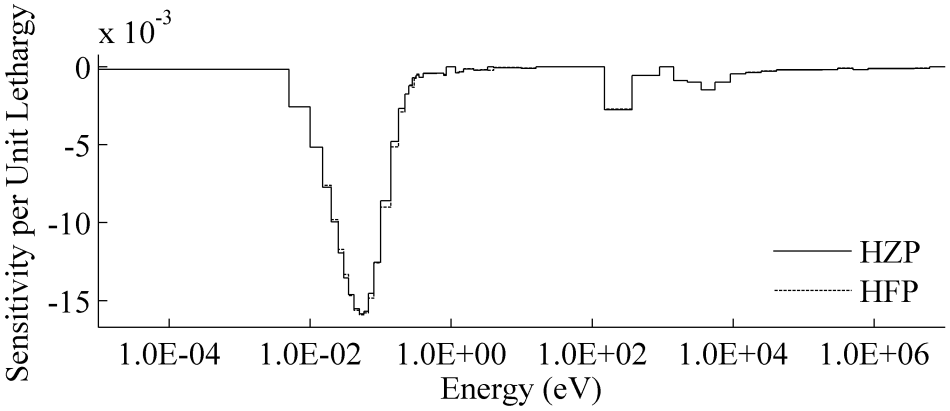

Figure 5.7: Sensitivity profile of CANDU® k_∞ to Zr^{Nat} (n, γ)

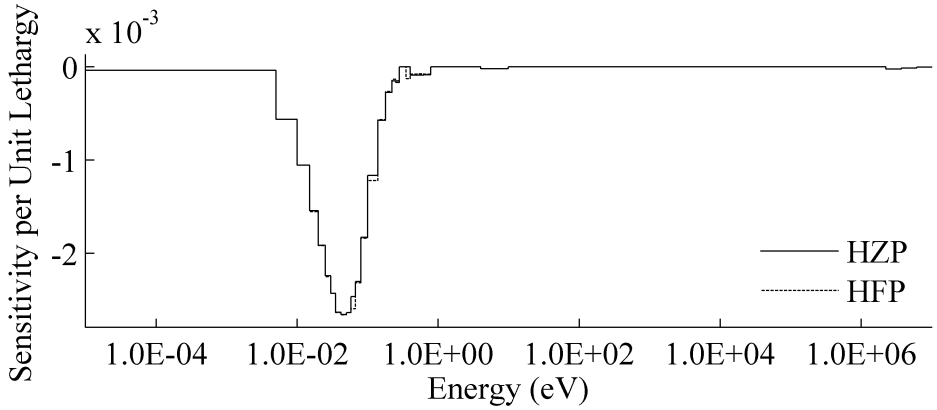

Figure 5.8: Sensitivity profile of CANDU® k_∞ to H^2 (n, γ)

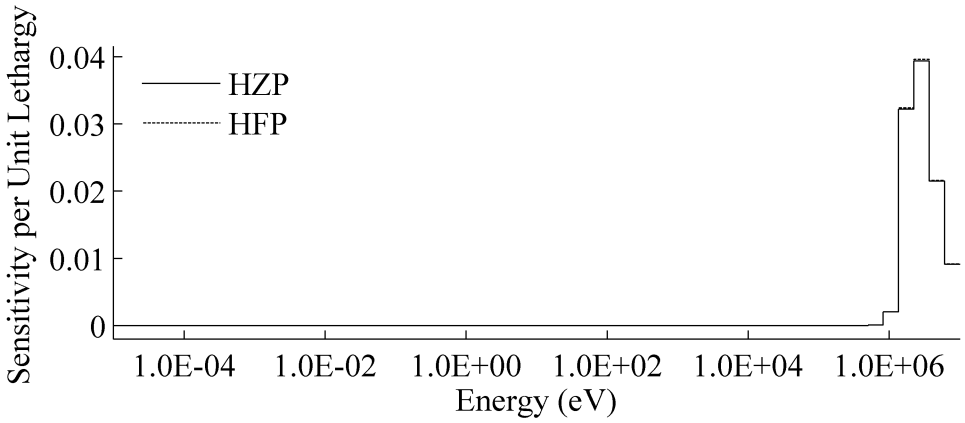

Figure 5.9: Sensitivity profile of CANDU® k_∞ to U^{238} $\bar{\nu}$

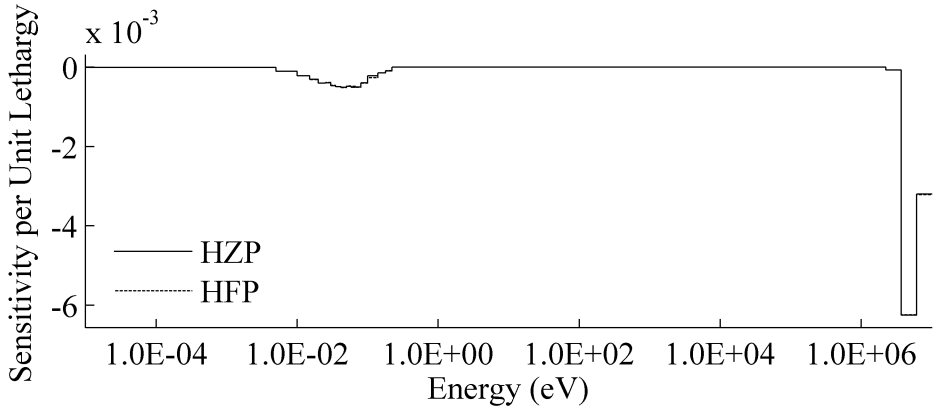

Figure 5.10: Sensitivity profile of CANDU® k_∞ to O^{16} (n, γ)

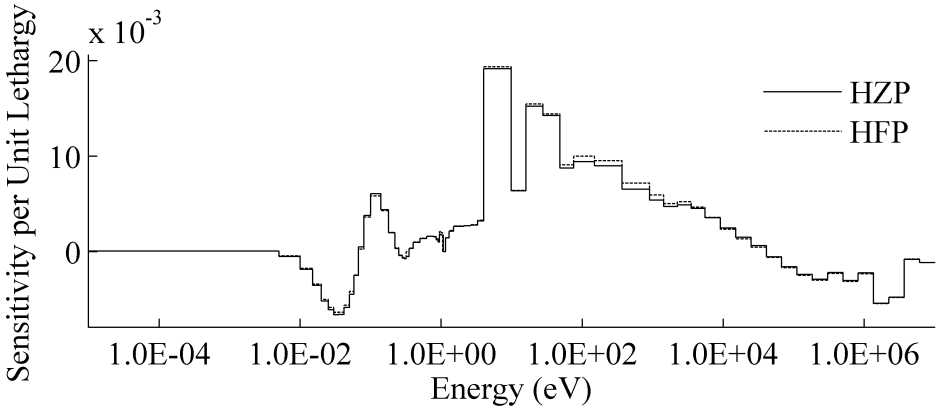

Figure 5.11: Sensitivity profile of CANDU® k_∞ to H^2 scatter

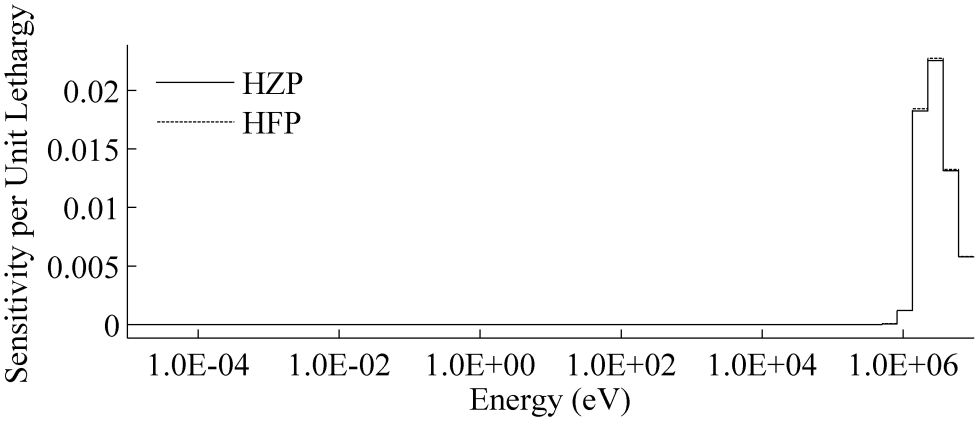

Figure 5.12: Sensitivity profile of CANDU® k_∞ to U^{238} (n, fission)

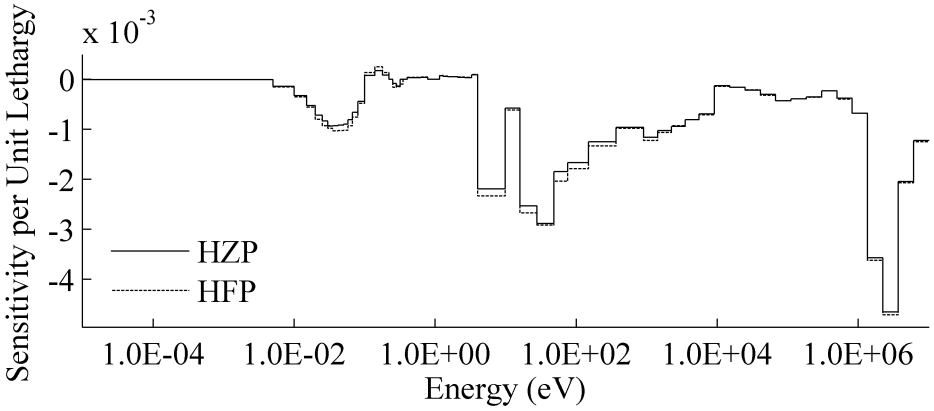

Figure 5.13: Sensitivity profile of CANDU® k_∞ to U^{238} scatter

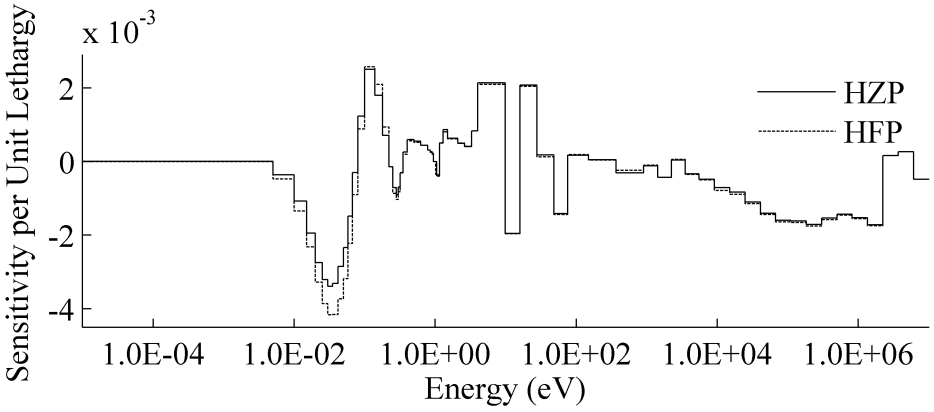

Figure 5.14: Sensitivity profile of CANDU® k_∞ to O^{16} scatter

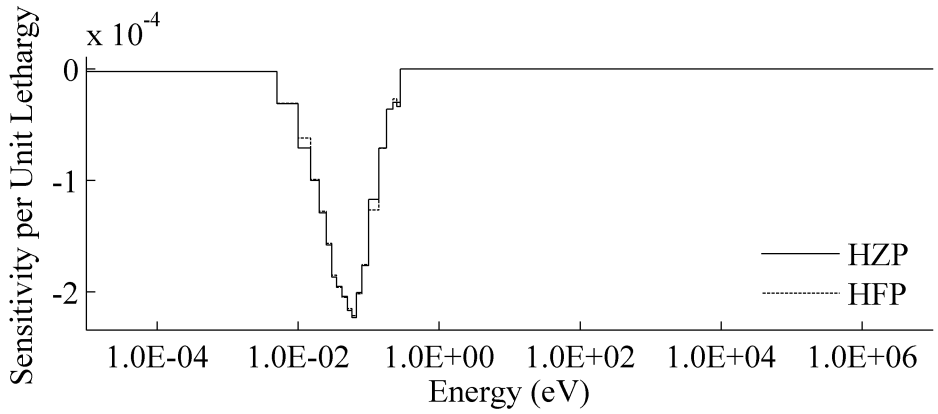

Figure 5.15: Sensitivity profile of CANDU® k_∞ to Cr^{52} (n, γ)

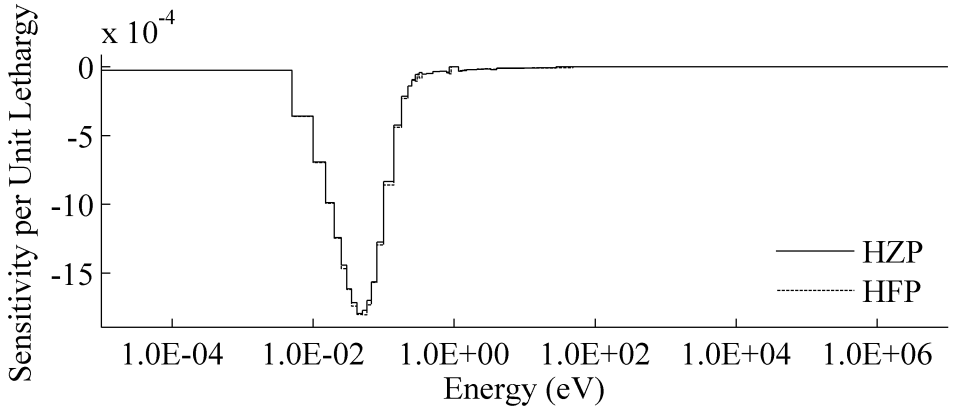

Figure 5.16: Sensitivity profile of CANDU® k_∞ to H^1 (n, γ)

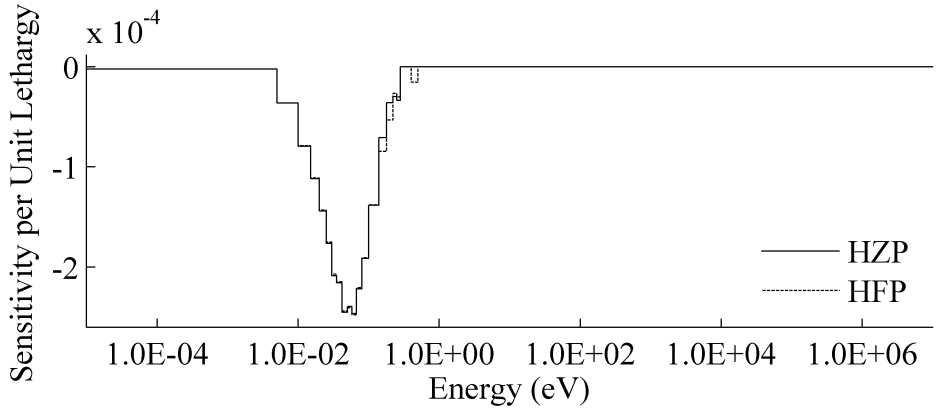

Figure 5.17: Sensitivity profile of CANDU® k_∞ to Fe^{Nat} (n, γ)

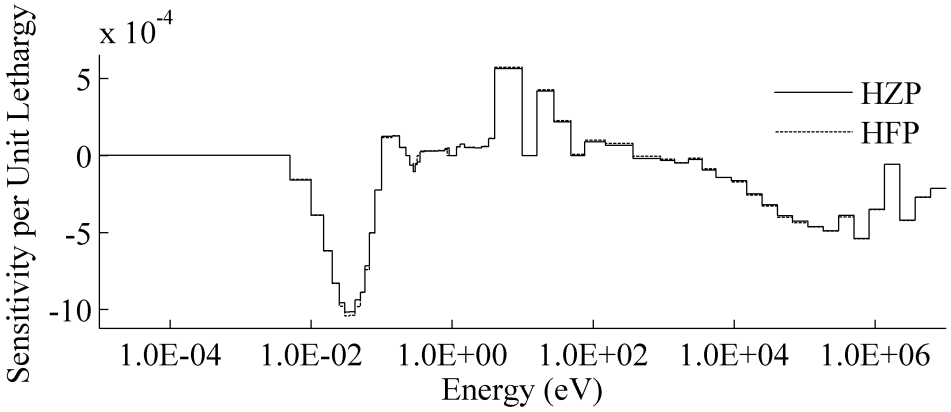

Figure 5.18: Sensitivity profile of CANDU® k_∞ to Zr^{Nat} scatter

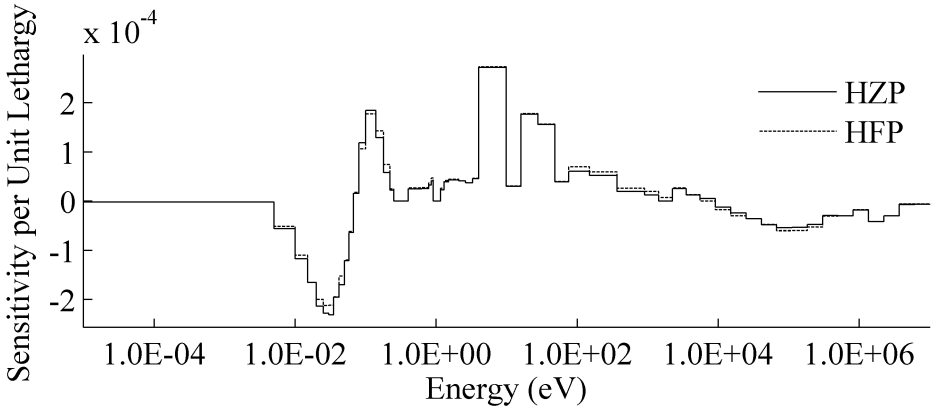

Figure 5.19: Sensitivity profile of CANDU® k_∞ to H^1 scatter

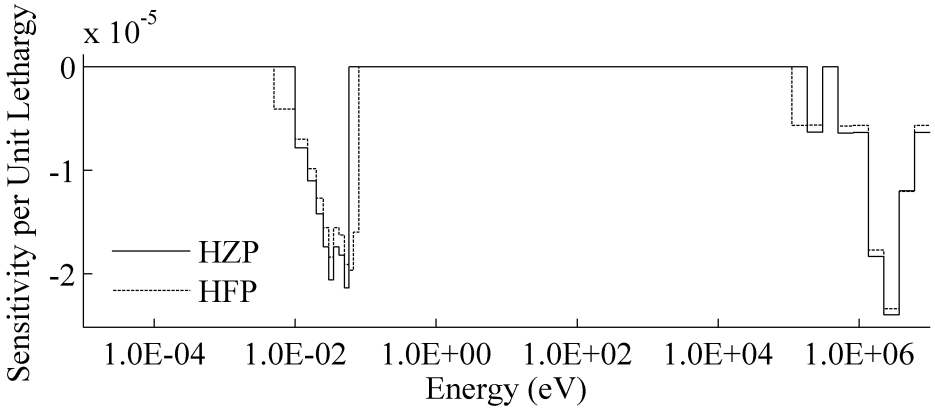

Figure 5.20: Sensitivity profile of CANDU® k_∞ to U^{235} scatter

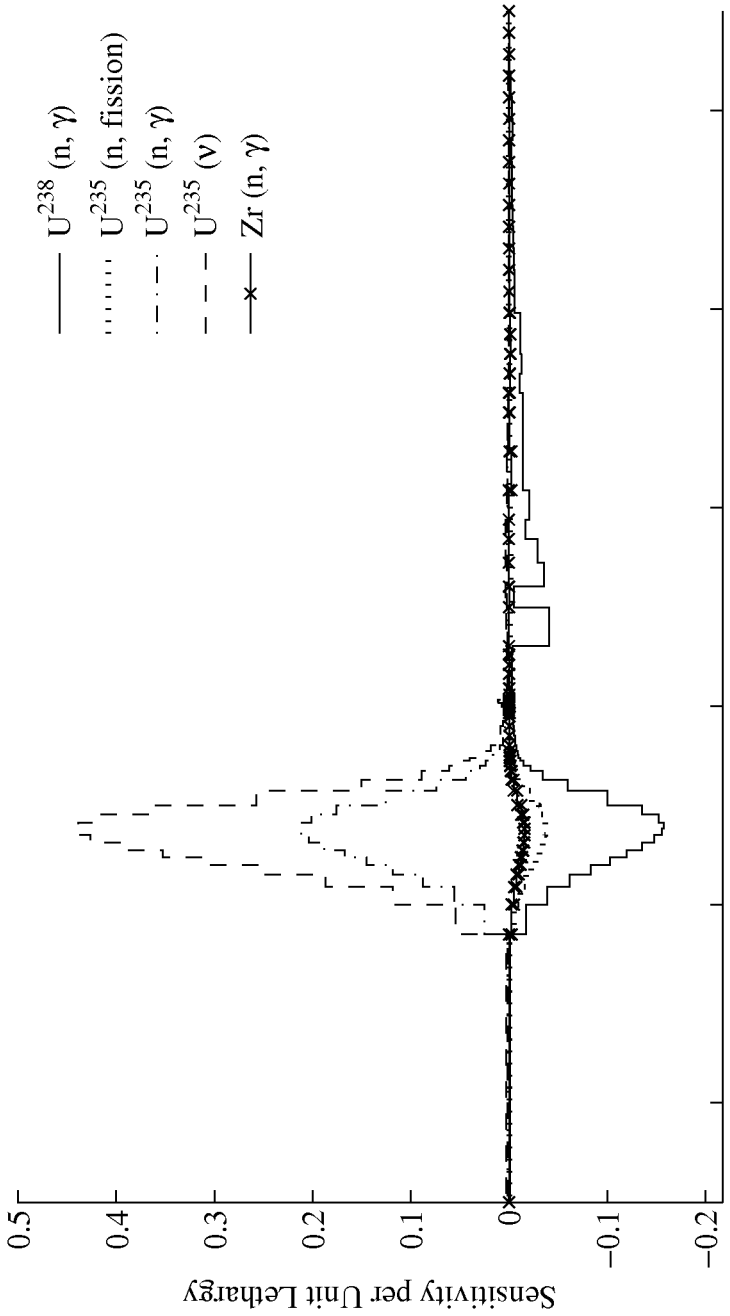

Figure 5.21: Sensitivity to major contributors of HZP CANDU® $\Delta k_\infty/k_\infty$

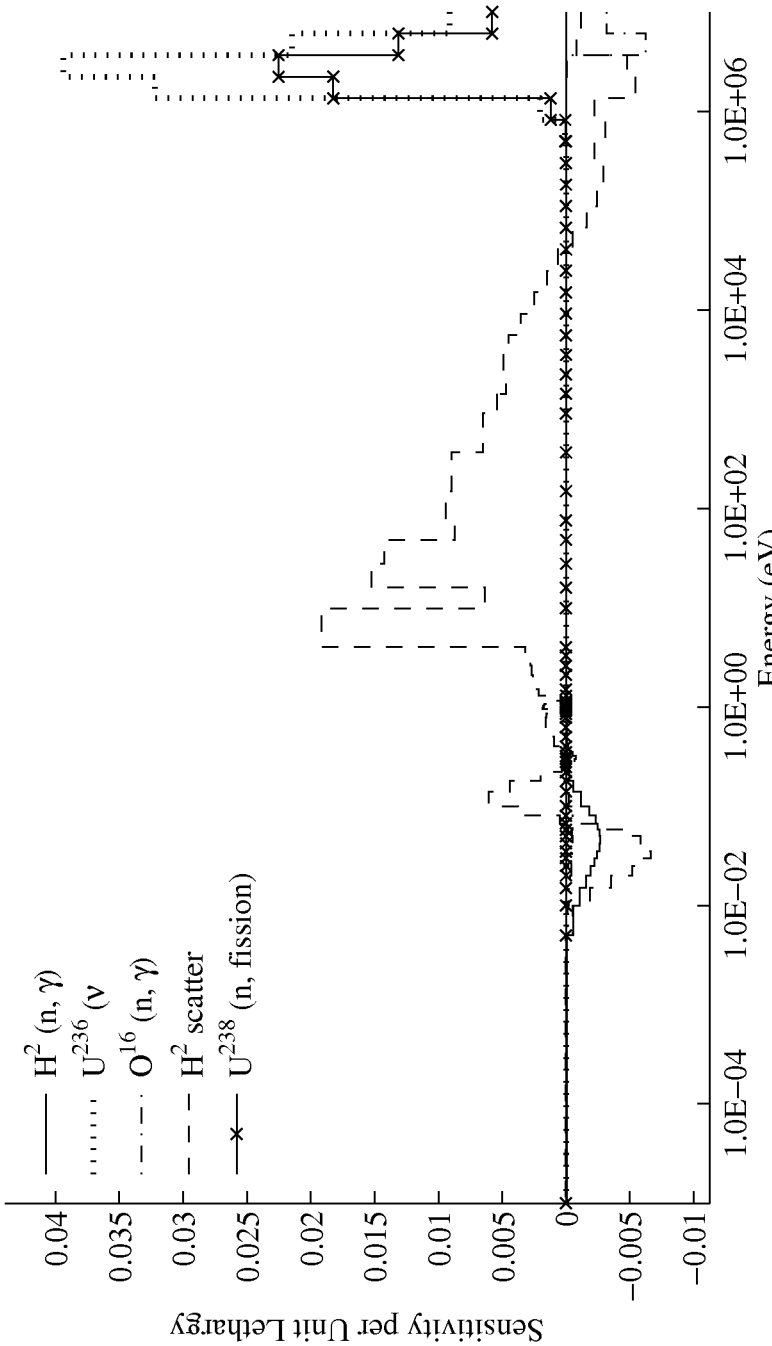

Figure 5.22: Sensitivity to minor contributors of HZP CANDU® $\Delta k_\infty/k_\infty$

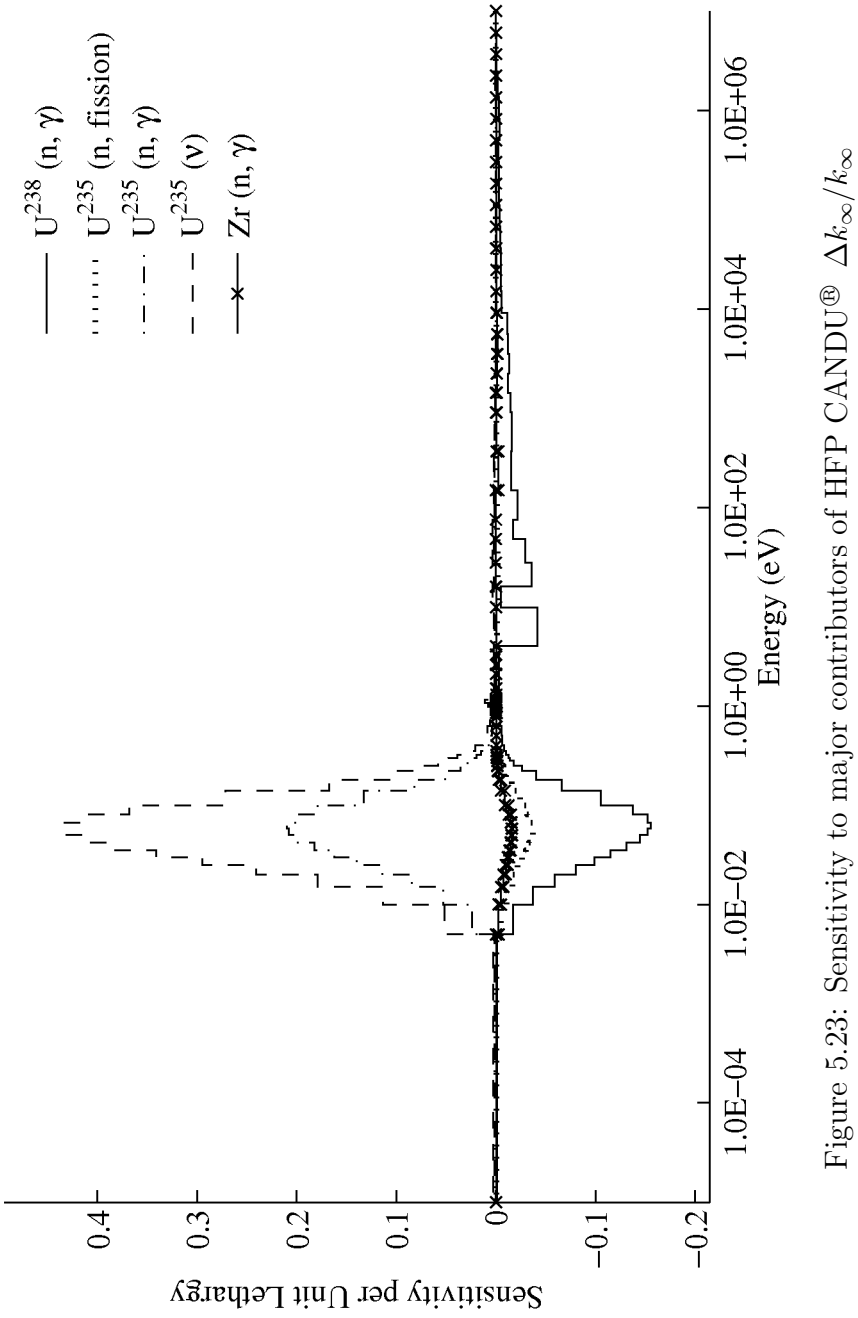

Figure 5.23: Sensitivity to major contributors of HFP CANDU® $\Delta k_\infty/k_\infty$

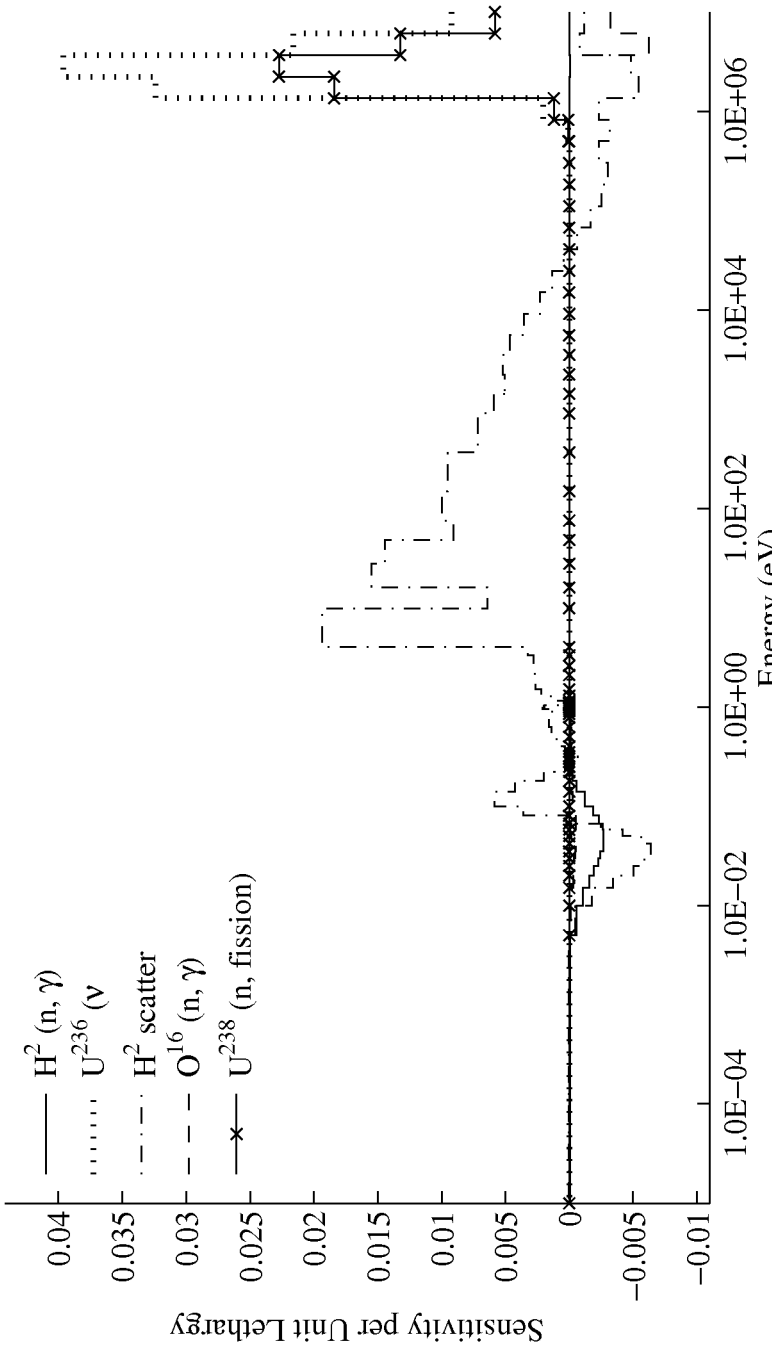

Figure 5.24: Sensitivity to minor contributors of HFP CANDU® $\Delta k_\infty/k_\infty$

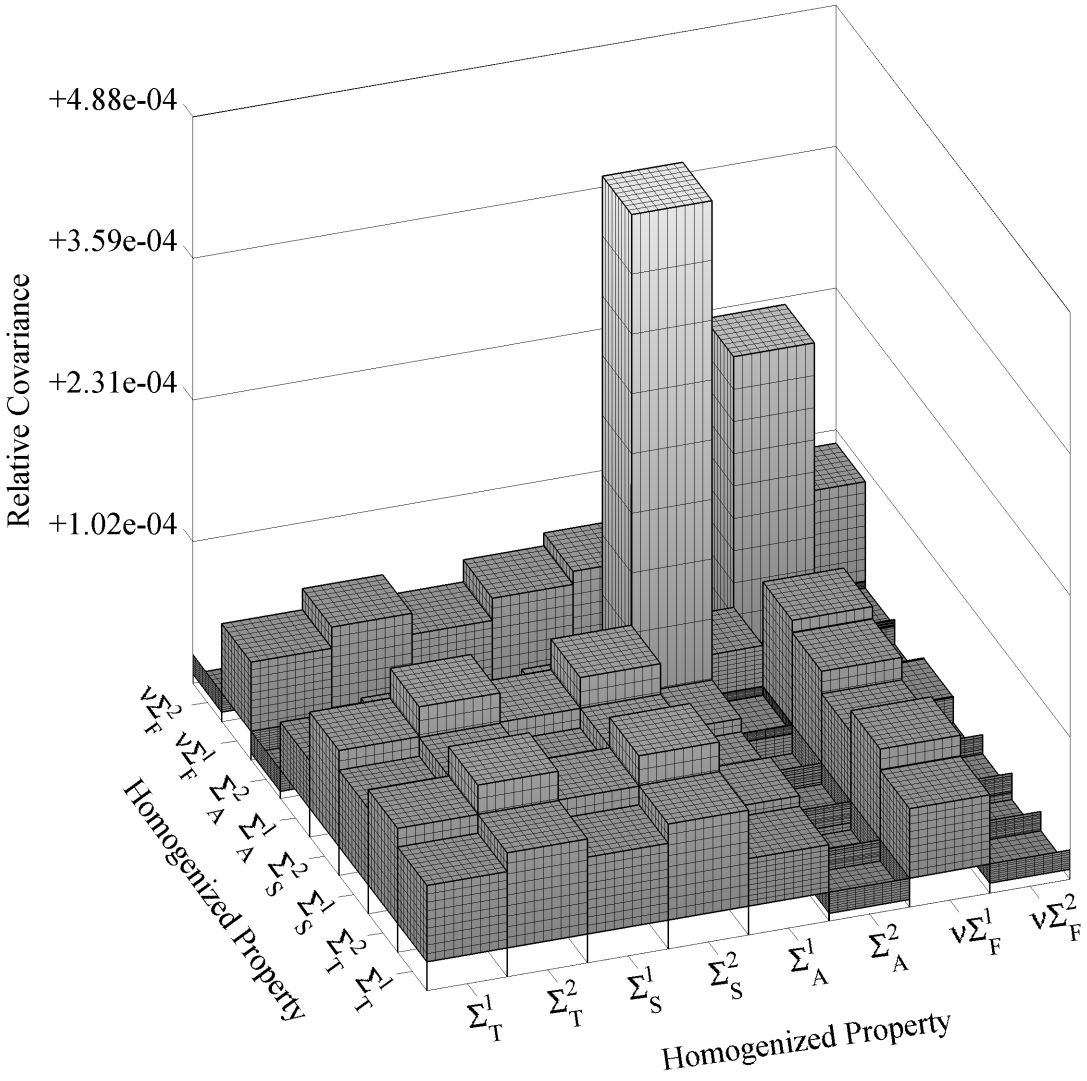

Figure 5.25: CANDU® HZP two-group homogenized lattice covariance (BoC)

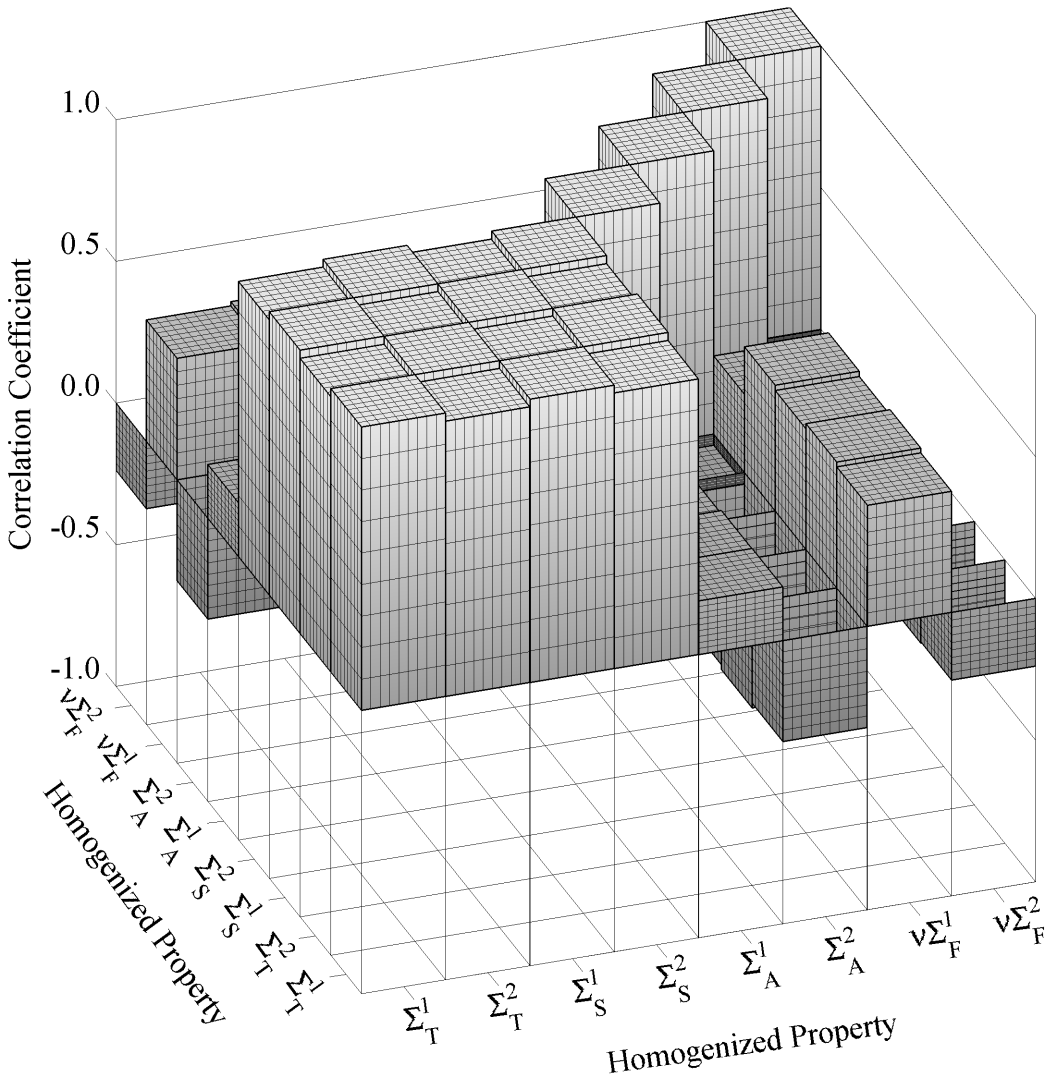

Figure 5.26: CANDU® HZP two-group homogenized lattice correlation (BoC)

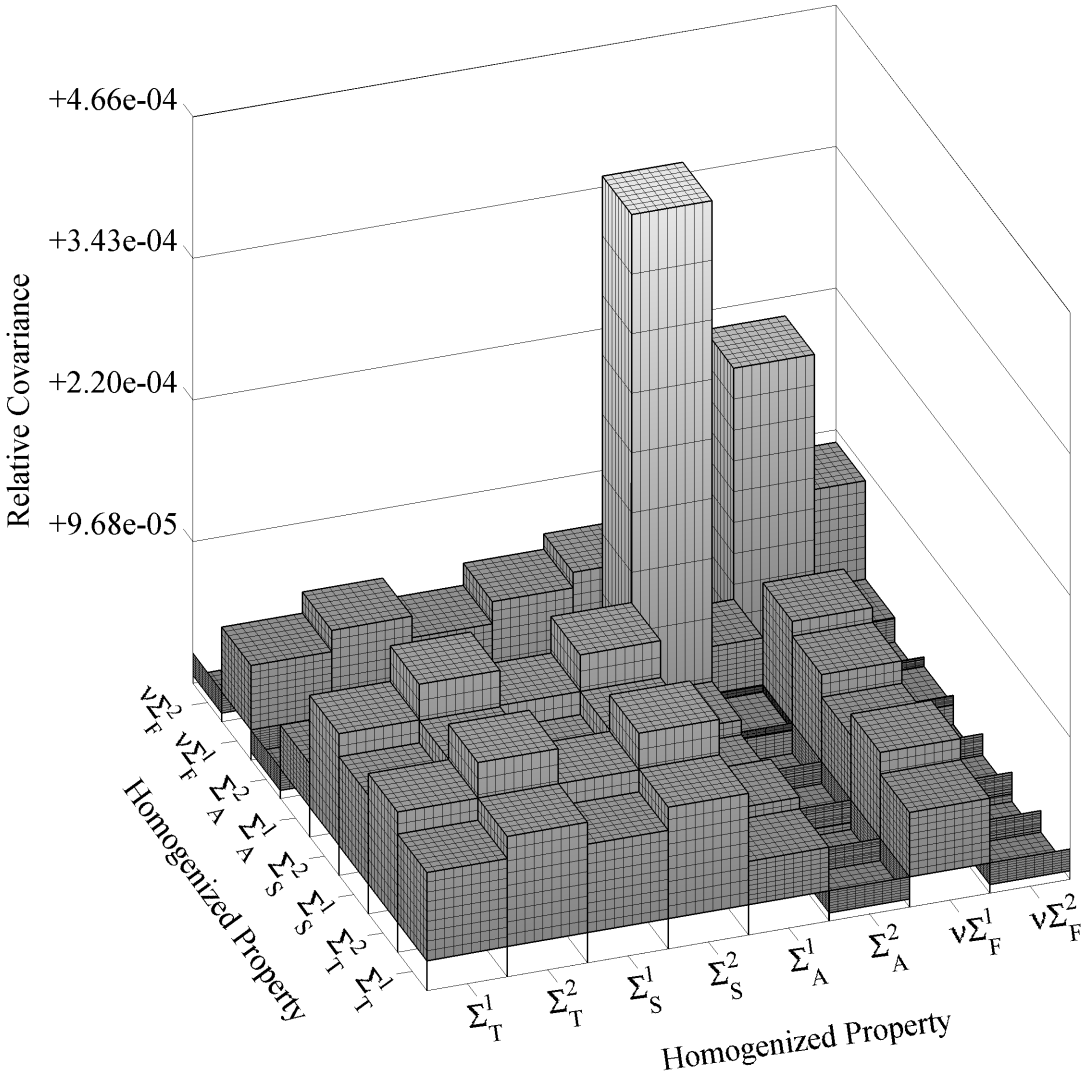

Figure 5.27: CANDU® HFP two-group homogenized lattice covariance (BoC)

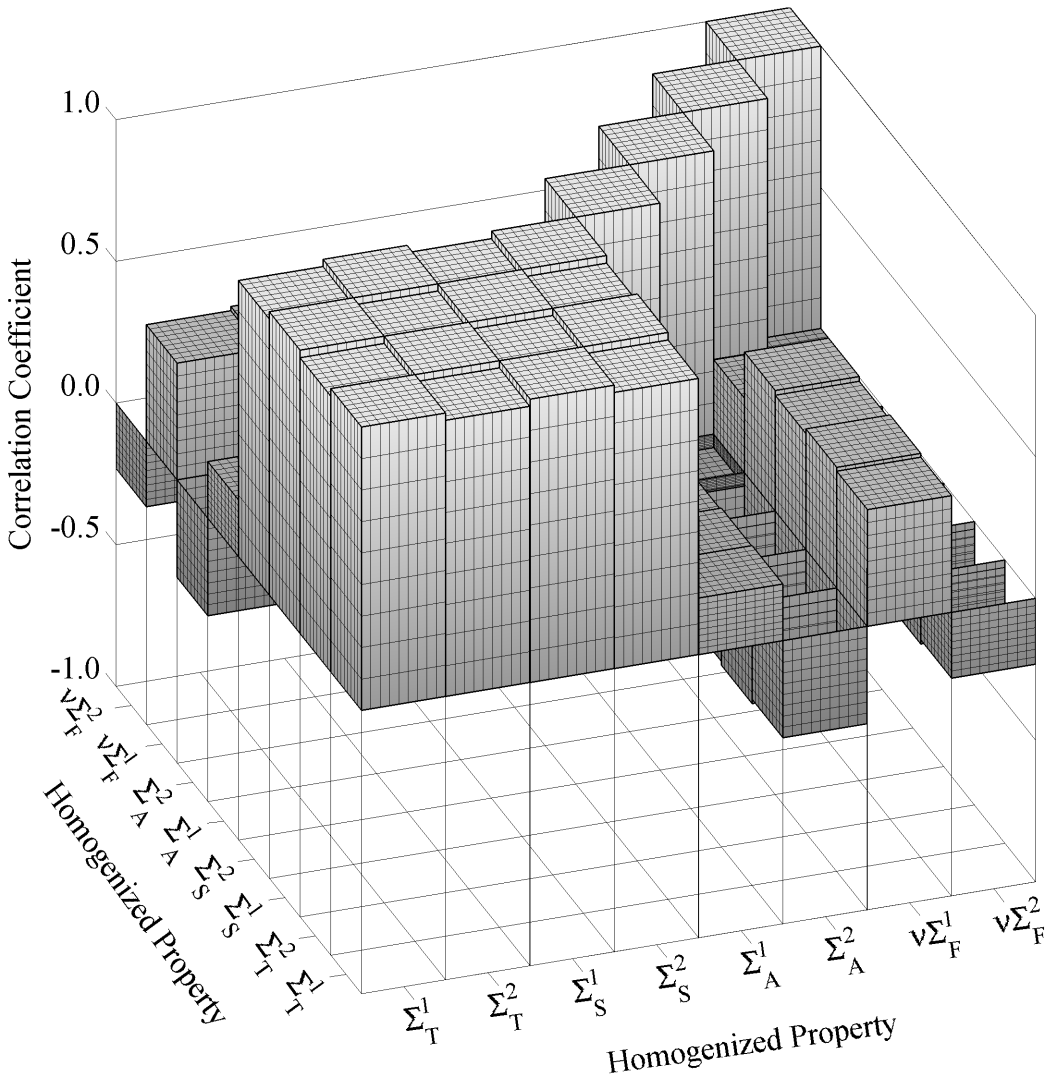

Figure 5.28: CANDU® HFP two-group homogenized lattice correlation (BoC)

Temperature Uncertainties Propagation

A summary of sensitivity and uncertainty results associated with input temperatures is shown in table 5.8. Homogenized, few-group covariance and correlation matrices resulting from each uncertain input temperature are shown in figures 5.30 to 5.35.

	Input temperature		
Item	Fuel	Moderator	Coolant
$\Delta k/k$ Statistical	0.0239%	0.0137%	0.0127%
$\Delta k/k$ Perturbation	0.0240%	0.0132%	0.0127%
dk/dT	-1.43E-5	-2.14E-5	-1.28E-5
Sensitivity	-1.20E-2	-6.59E-3	-6.41E-3

Table 5.8: Material temperature uncertainty propagation results

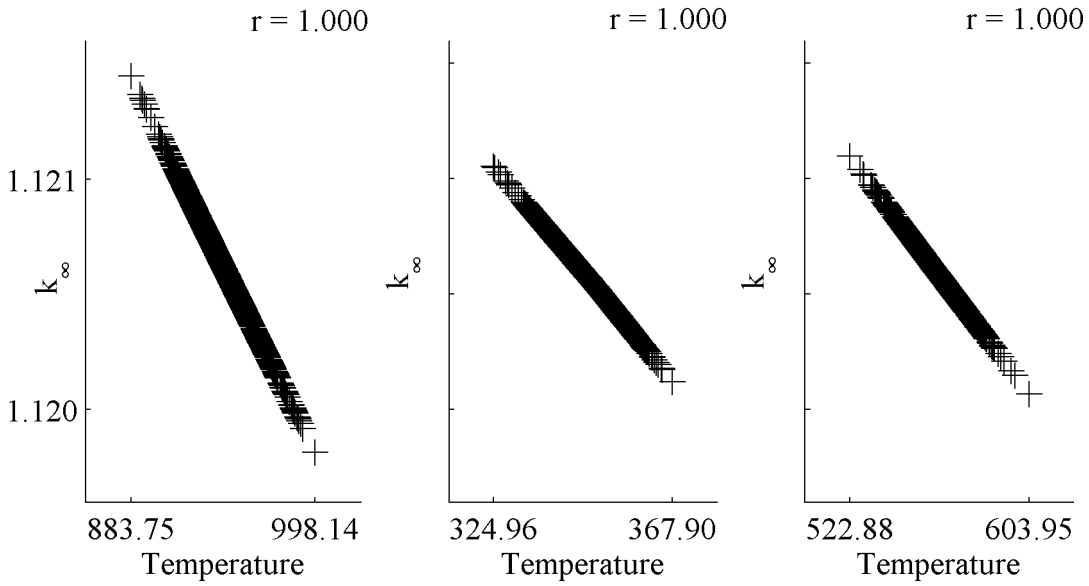

(a) Fuel (b) Moderator (c) Coolant

Figure 5.29: CANDU® k_∞ vs. input temperatures

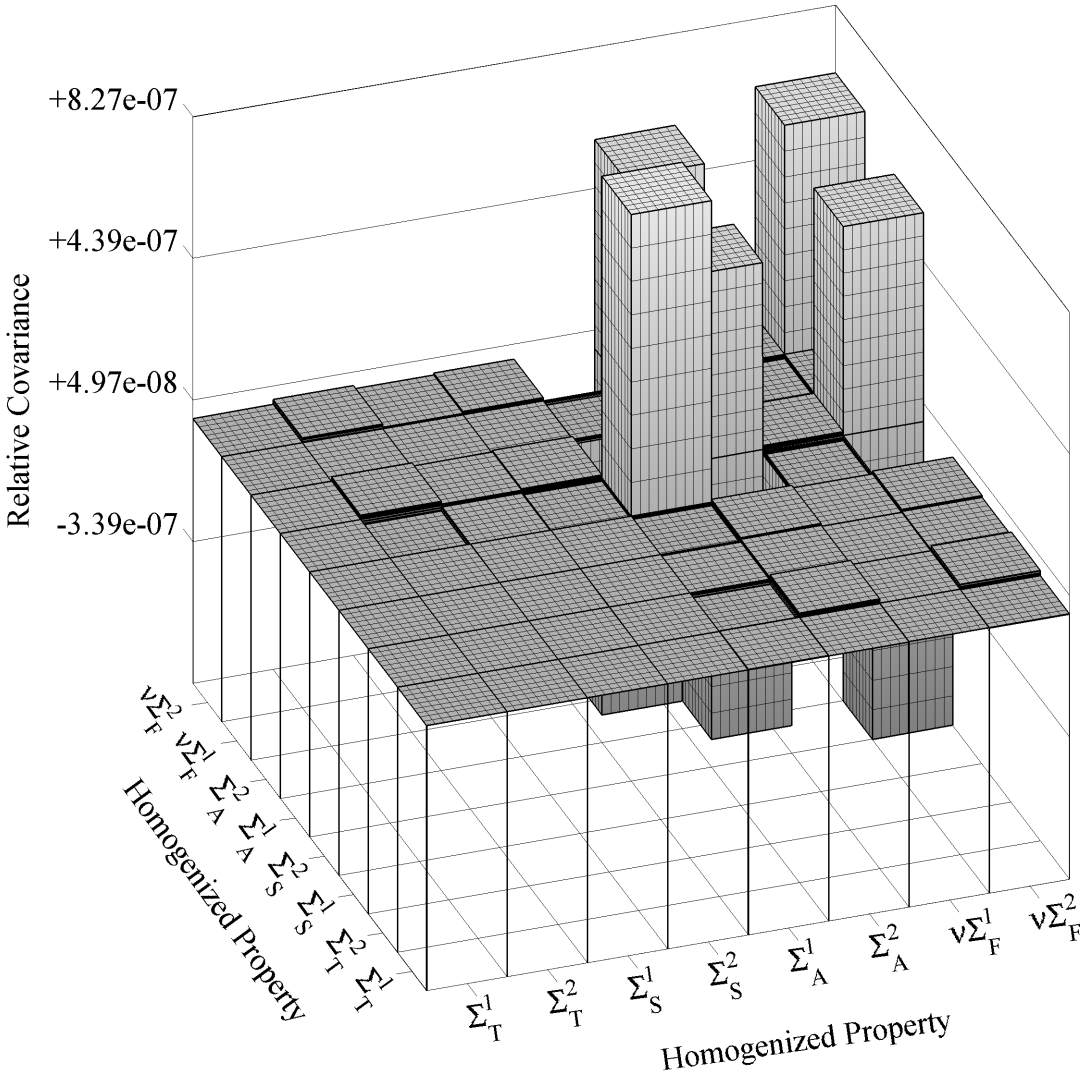

Figure 5.30: CANDU® homogenized covariance due to fuel temperature

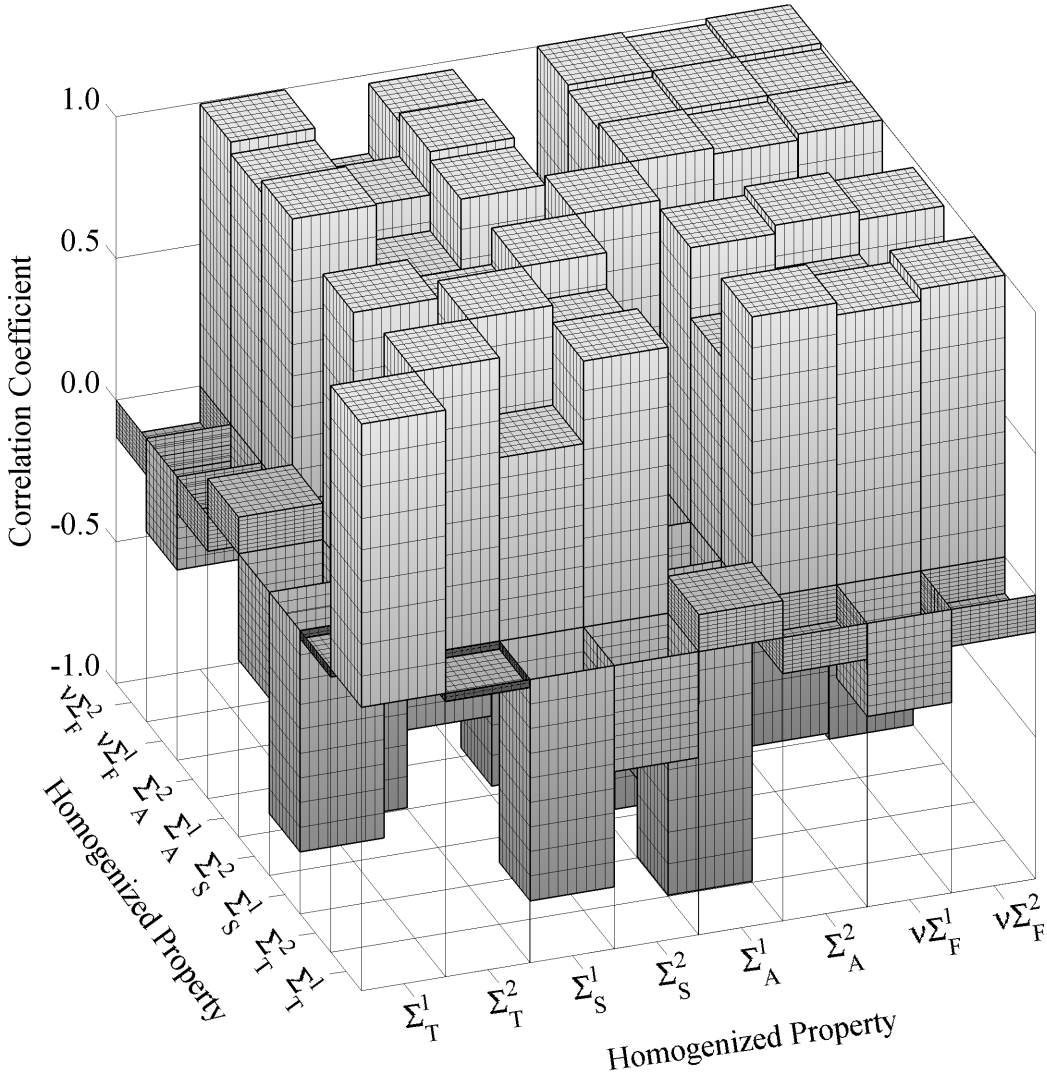

Figure 5.31: CANDU® homogenized correlation due to fuel temperature

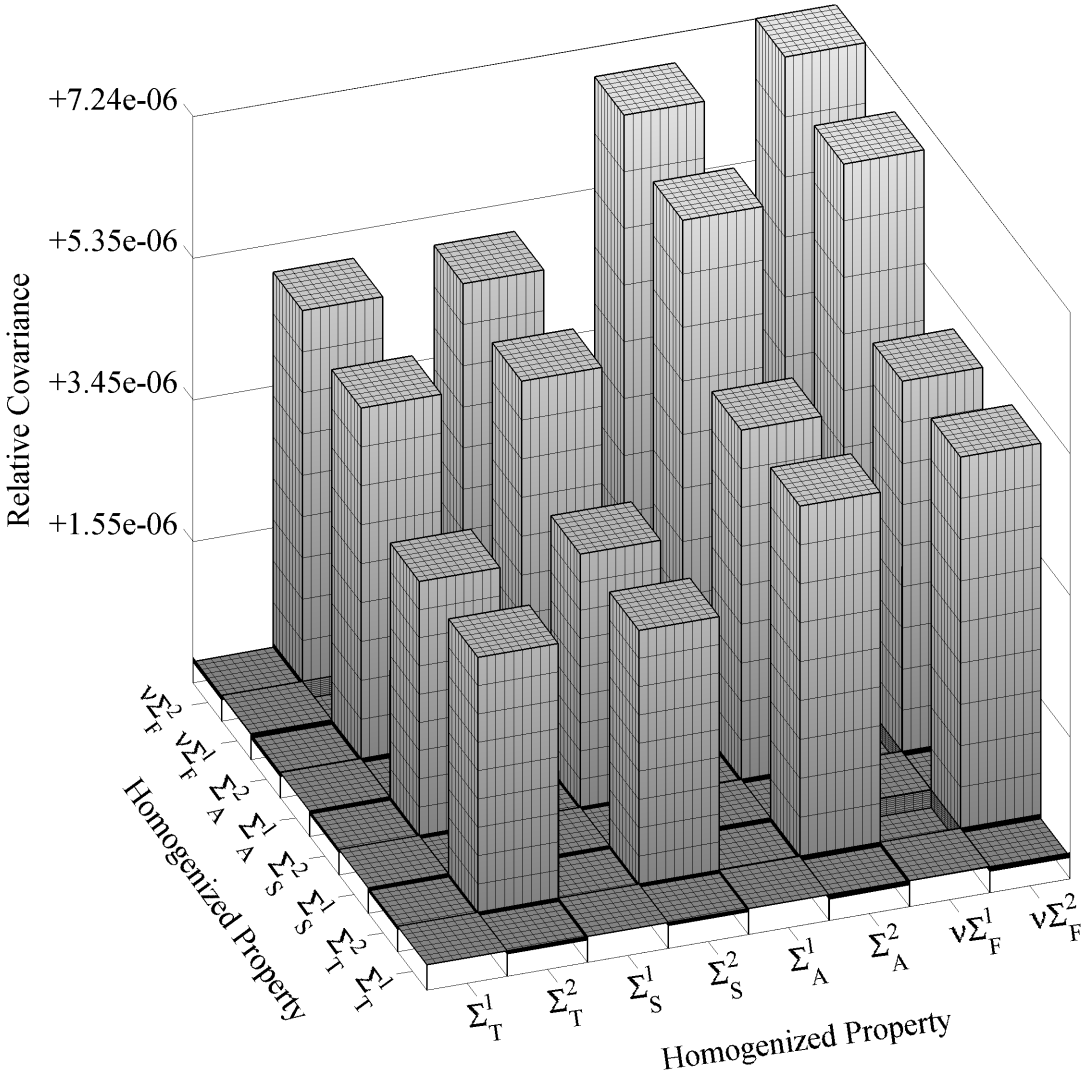

Figure 5.32: CANDU® homogenized covariance due to moderator temperature

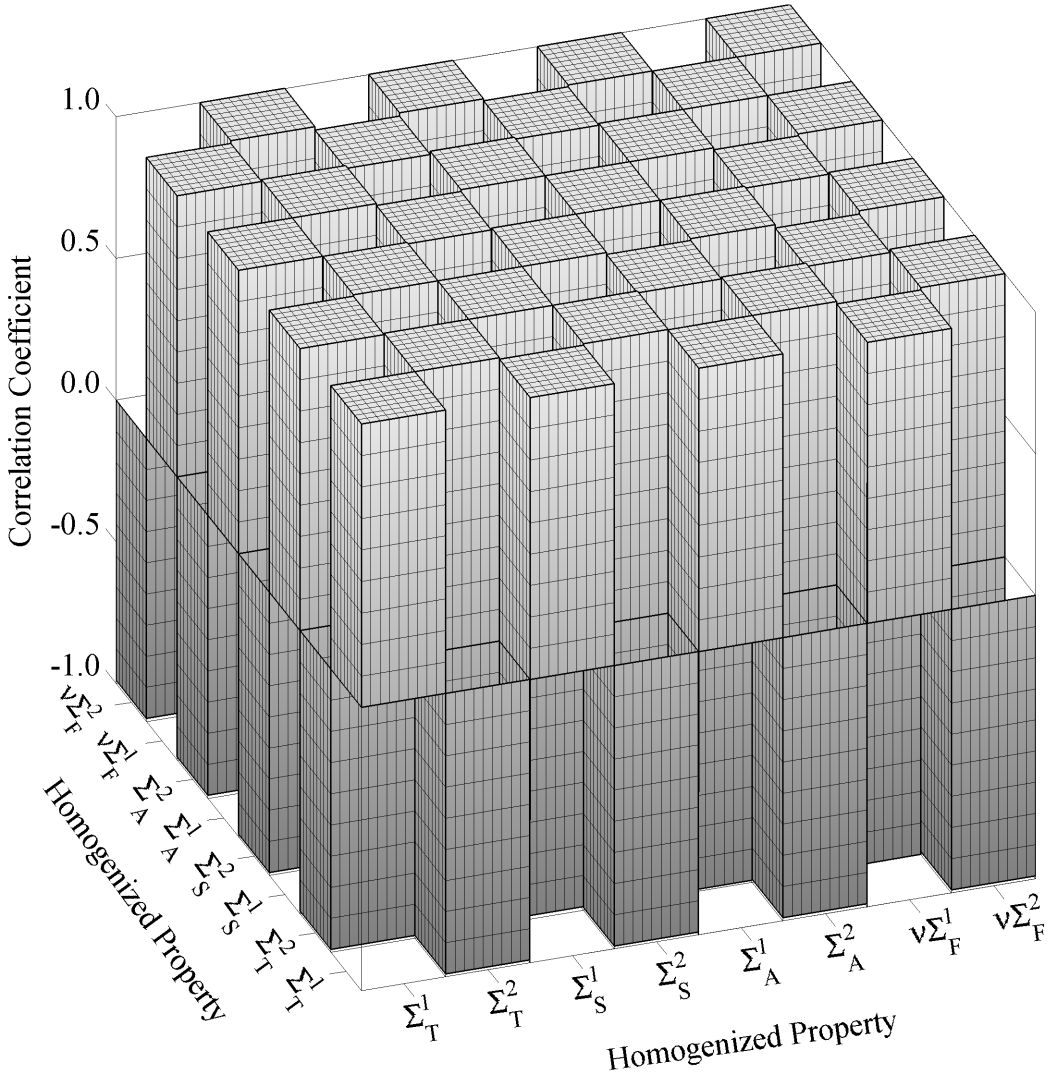

Figure 5.33: CANDU® homogenized correlation due to moderator temperature

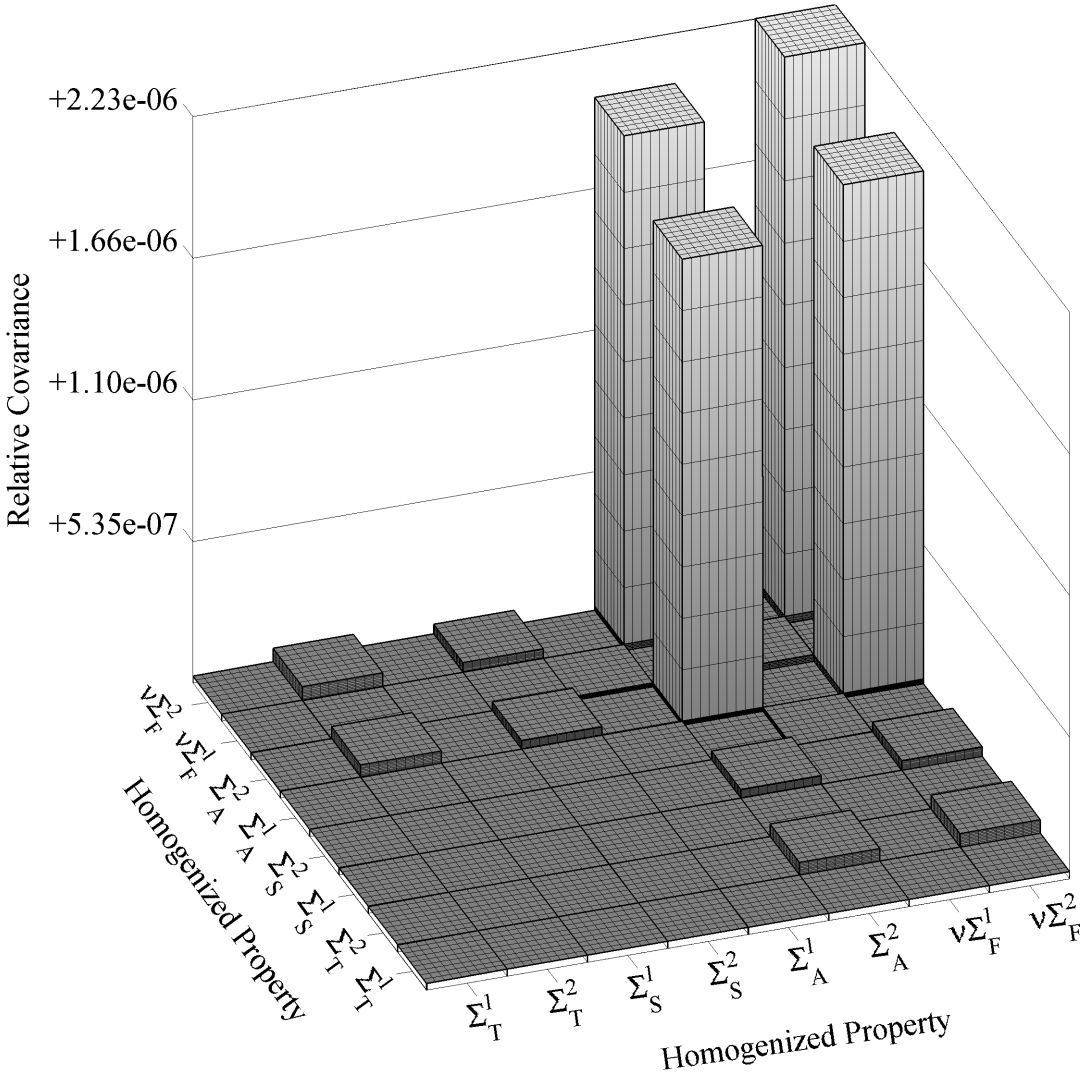

Figure 5.34: CANDU® homogenized covariance due to coolant temperature

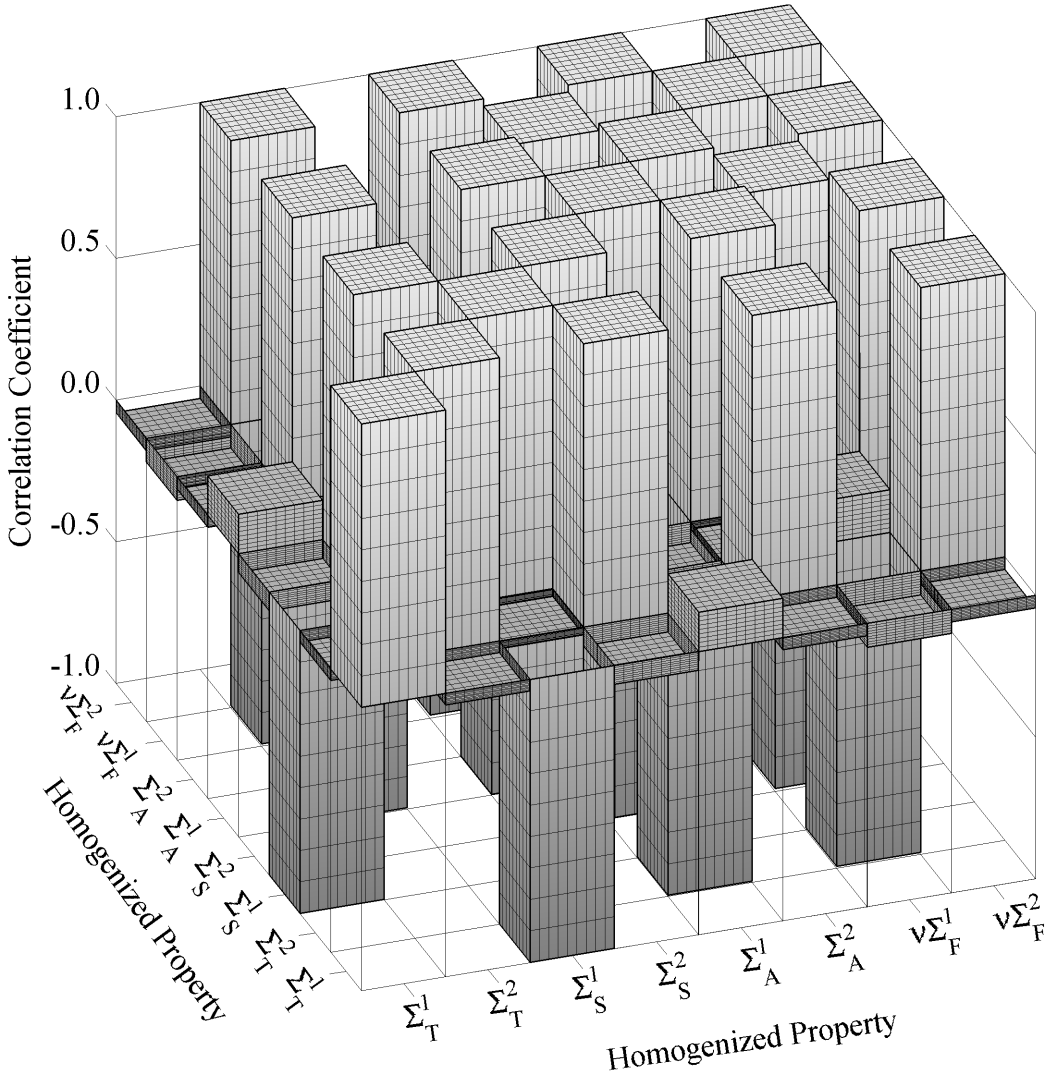

Figure 5.35: CANDU® homogenized correlation due to coolant temperature

5.3 BoC results discussion

Uncertainty in the infinite multiplication constant of the generic CANDU® lattice is typically much larger than the LWR cells investigated in chapter 4, with the only comparable case being that of the PB-2 BWR at hot, full-power with substantial coolant void. However, whereas the PB-2 uncertainty, which is driven by U^{238} (n, γ), is primarily a result of under-moderation due to coolant void, the large contribution from that cross-section to the uncertainty of CANDU® k_∞ can be attributed to its larger relative contribution to thermal reaction rates in CANDU® fuel compared to LWRs and is therefore essentially an enrichment phenomena.

Cross-Section Sensitivity and Uncertainty

The sensitivity of CANDU® k_∞ to multi-group cross-sections varies substantially compared to the UAM lattices which feature an LWR neutron spectrum. The best-estimate, normalized neutron flux of CANDU® and TMI-1 at HFP are shown in figure 5.36, and the relative ratio of normalized flux of the two cells in figure 5.37. There is substantially greater thermal flux in the CANDU® lattice at energies up to 0.28 eV, and substantially less flux at energies above that threshold, compared to the PWR. This is reflected in the sensitivities of CANDU® k_∞ to multi-group cross-sections, which tend to be large below 0.28 eV. The difference is plainly seen for the sensitivity to U^{238} (n, γ), the most important uncertainty contributor, in contrast to the same sensitivity in the context of LWR lattices. The PB-2, TMI-1 and K-6 sensitivity profiles to that reaction, shown in figures 4.3, 4.30, and 4.57, exhibits large peaks at intermediate and high energies that are absent from the corresponding CANDU® sensitivity profile in figure 5.3. Similarly, an increase in thermal sensitivity can be readily observed with respect to several other cross-sections as well $\big($e.g. Zr^{Nat} (n, γ), O^{16} (n, n_o), Fe^{Nat} (n, γ)$\big)$.

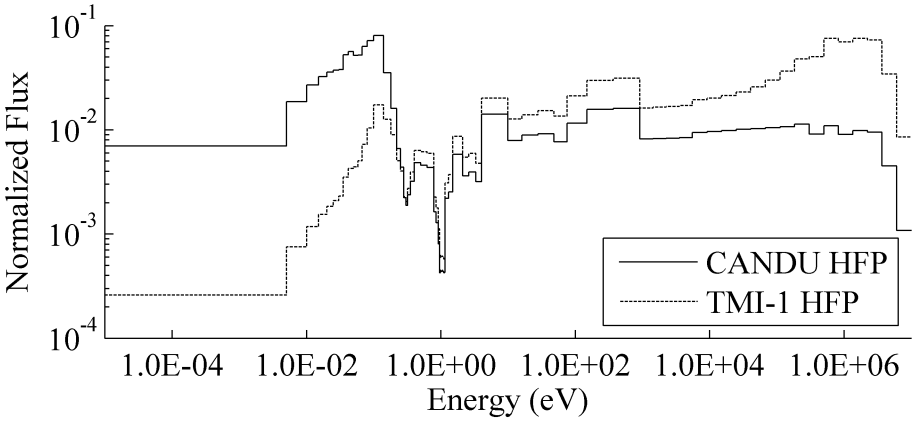

Figure 5.36: CANDU® and TMI-1 normalized neutron flux

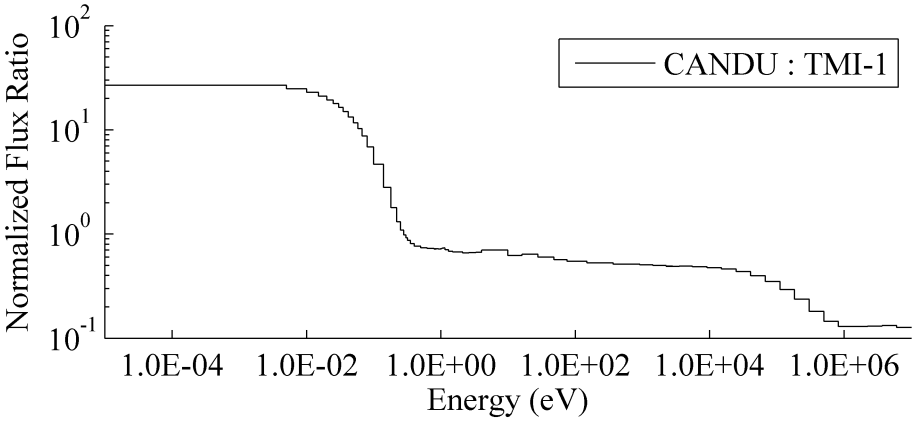

Figure 5.37: CANDU® flux to TMI-1 flux ratio

Naturally, since the CANDU® lattice is heavy water moderated, the sensitivity to H^1 cross-sections is reduced by an order of magnitude or more compared to LWR cells. However, an interesting sensitivity profile to deuterium exists. Note the k_∞ sensitivity to H^2 scattering cross-section is negative at very high energies, as shown in figure 5.11, which is expected given the coolant's potential to reflect fission neutrons at the fuel/coolant interface, and is positive at the intermediate energies which correspond to the thermalizing of neutrons far from the fuel. However, at even lower energies, the sensitivity again becomes negative. This is likely the result of the temperature disparity between the coolant, which lies inside the pressure tube, and moderator, which lies outside of the calandria tube. The coolant's higher temperature substantially increases the possibility of neutron up-scattering within a short distance of the fuel. Up-scatter events imposed on neutrons that initially are of the thermal distribution associated with the cooler moderator, will push the neutrons to higher energies; energies at which the fission-to-capture ratio of fuel material tends to be lower. The negative thermal sensitivity caused by the up-scatter effect is entirely absent for the LWR cells, whose moderator and coolant are the same.

Microscopic cross-section uncertainties cause more covariance on CANDU® lattice outputs (i.e. k_∞ and homogenized, few-group cross-sections) than they do for LWR cells. The moderately large uncertainty contribution from H^2 scatter pushes the CANDU® homogenized scattering cross-section covariance higher, and the total cross-section covariance higher along with it. The larger fast-group absorption and fission uncertainties are attributable to contributions from U^{238} (n, γ) and U^{235} (n, fission), respectively, which contribute more to CANDU ® $\Delta k/k$. than LWR $\Delta k/k$, as shown in tables 4.4 and 5.6, for example.

Temperature Sensitivity and Uncertainty

The relationship between reactivity and temperatures of fuel, moderator, and coolant were found to be remarkably linear. An analysis of 1056 samples of each (scatter plots shown in figure 5.29), resulted in a calculated correlation that was, to a high precision, equal to unity. This indicates that a first order perturbation system is an excellent approximation for material temperature uncertainty propagation. The sensitivities of k_∞ with respect to temperatures are such that even large temperature uncertainties would contribute an amount of uncertainty to k_∞ that is of only moderate importance compared to contributions from cross-section uncertainties.

Fuel Temperature Uncertainty Effects

The homogenized, two-group covariance matrix of the lattice that results from fuel temperature uncertainty is straightforward to interpret given the data available on the *IAEA* library that is temperature-dependent. Multi-group cross-sections are temperature-dependent in the last (slowest) 42 energy groups, up to 4 eV. Above 4 eV, there are temperature-dependent resonance integrals for 13 groups, up to 9.112 keV. The fastest groups, from 9.112 keV to 2 MeV are entirely temperature-independent. Therefore, in the homogenized two-group cross-sections, there can emerge variation in the broad thermal group due to the thermal-dependency of multi-group data across the entire range of the broad group. However, variation in the broad fast group emerges only from whatever little temperature variation exists from 0.625 eV to 4 eV, in combination with the temperature variation of resonance integrals, which ultimately stem from Doppler broadening of resonance peaks. In the case of CANDU® fuel material, the two nuclides principally responsible for reaction rates are U^{235}, involved primarily at thermal energies, and U^{238}, which dominates effects at fast and epithermal energies, and whose effects are also present at thermal energies. Therefore, uncertainty in the fast group of homogenized absorption and fission cross-sections resulting from fuel temperature uncertainty will be driven by U^{238} effects, and likewise, the thermal group uncertainty driven by a collection of nuclides. The capture cross-section of U^{238} features a large number of very strong, densely packed resonances, which cause significant uncertainty to arise in the Σ_A^1 homogenized cross-section in figure 5.30. However, the fission resonances of U^{238} are weak and sparsely populated. Consequently, there are no fission resonance integrals of U^{238} stored in the *IAEA* library, and hence no temperature-dependent variation of data above 4.0 eV, which leads to $\bar{\nu}\Sigma_F^1$ having no significant uncertainty. Both broad-group thermal cross-sections, Σ_A^2 and $\bar{\nu}\Sigma_F^2$ show covariance in figure 5.30 due to the temperature-dependent variation of thermal data of all fuel nuclides.

Moderator Temperature Uncertainty Effects

In a well-thermalized lattice, neutrons that escape resonance absorption will be slowed through elastic collisions with moderating nuclei and eventually reach a thermal equilibrium with the moderator material, taking on an energy distribution of the Maxwell-Boltzmann type. Uncertainty associated with moderator temperature propagates to uncertainty in the neutron energy distribution, which in turn introduces uncertainty in few-group cross-sections that are averaged using an energy-varying flux profile as a weighting function. Since the effect of moderator temperature is almost entirely limited to thermal equilibrium phenomena, the fast flux is subject to virtually no variation, which can be seen by the trivial covariance associated with fast cross-sections in figure 5.32. The fast group homogenized scattering cross-section shows less covariance than does the absorption and fission yield, because microscopic scattering cross-sections tend to be flat and slowly varying at low energies compared to absorption cross-sections, and therefore less sensitive to changes in weighting function.

The correlation shown in figure 5.29b implies a negative coefficient of reactivity with respect to moderator temperature. The negative reactivity exists for lattices of fresh fuel because the fission cross-section of the fissile material, U^{235}, decreases with increasing neutron energy in the neighborhood of 0.03 eV, which is the mean kinetic energy of neutrons thermalized to a temperature of 345 K. However, as fuel is burned and plutonium accumulates, the temperature reactivity has potential to change and become less negative, due to a significant Pu^{239} resonance located at 0.296 eV that causes its fission cross-section to increase with increasing neutron energies in the neighborhood of thermal equilibrium.

Coolant Temperature Uncertainty Effects

The uncertainty of coolant temperature effects the incidence of up-scatter occurring to thermal neutrons entering the fuel channel from the moderator. The up-scatter uncertainty leads to a small uncertainty in the thermal flux profile seen by fuel nuclides, and therefore a small uncertainty on the homogenized thermal group cross-section. Because most scatter reactions take place in the moderator rather than the coolant, the relative uncertainty associated with the cell-homogenized scatter cross-section is nearly zero, as shown in figure 5.34.

5.4 EoC and mid-burnup lattice results

The lattice k_∞ against burnup is shown in figure 5.38. The solid line in the figure indicates the best-estimate prediction of k_∞, while dashed lines represent the 0.95/0.95 two-sided confidence limits calculated using Wilks' forumula. The variation of relative k_∞ uncertainty with burnup is shown in figure 5.39. Spatially homogenized, two-group cross-section covariance and correlation matrices corresponding to the state of the

lattice after the 180 days of burnup are shown in figures 5.40 and 5.41, respectively.

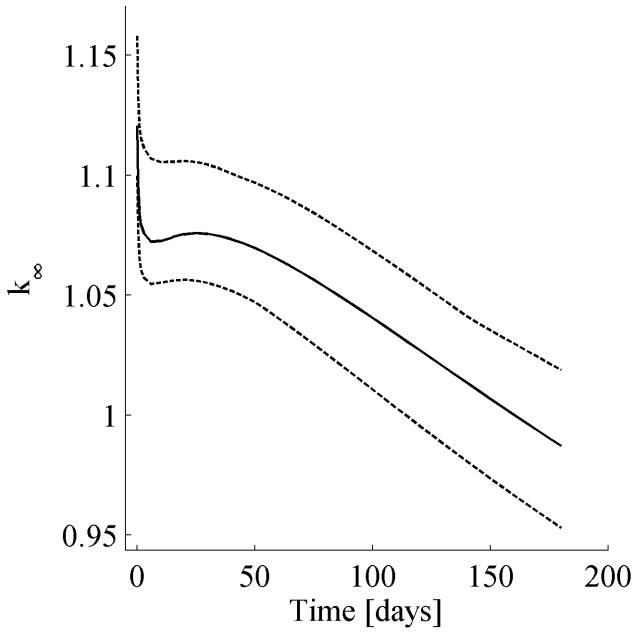

Figure 5.38: CANDU® k_∞ versus burnup, with 95^{th} percentile confidence limits

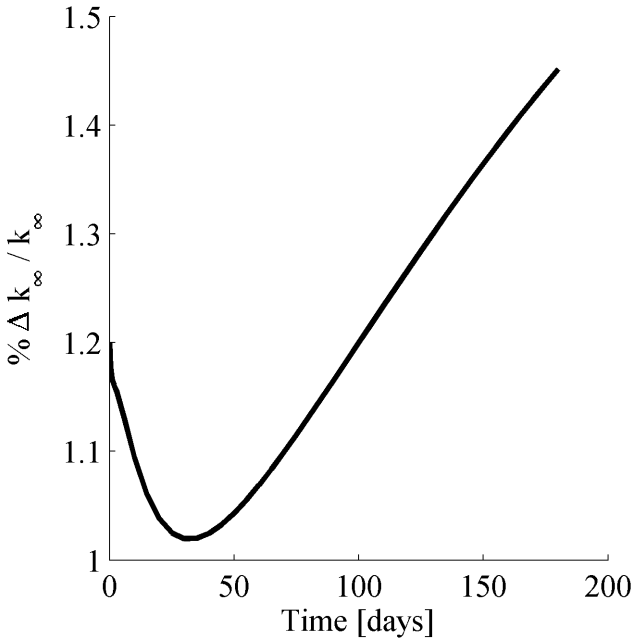

Figure 5.39: CANDU® k_∞ uncertainty versus burnup

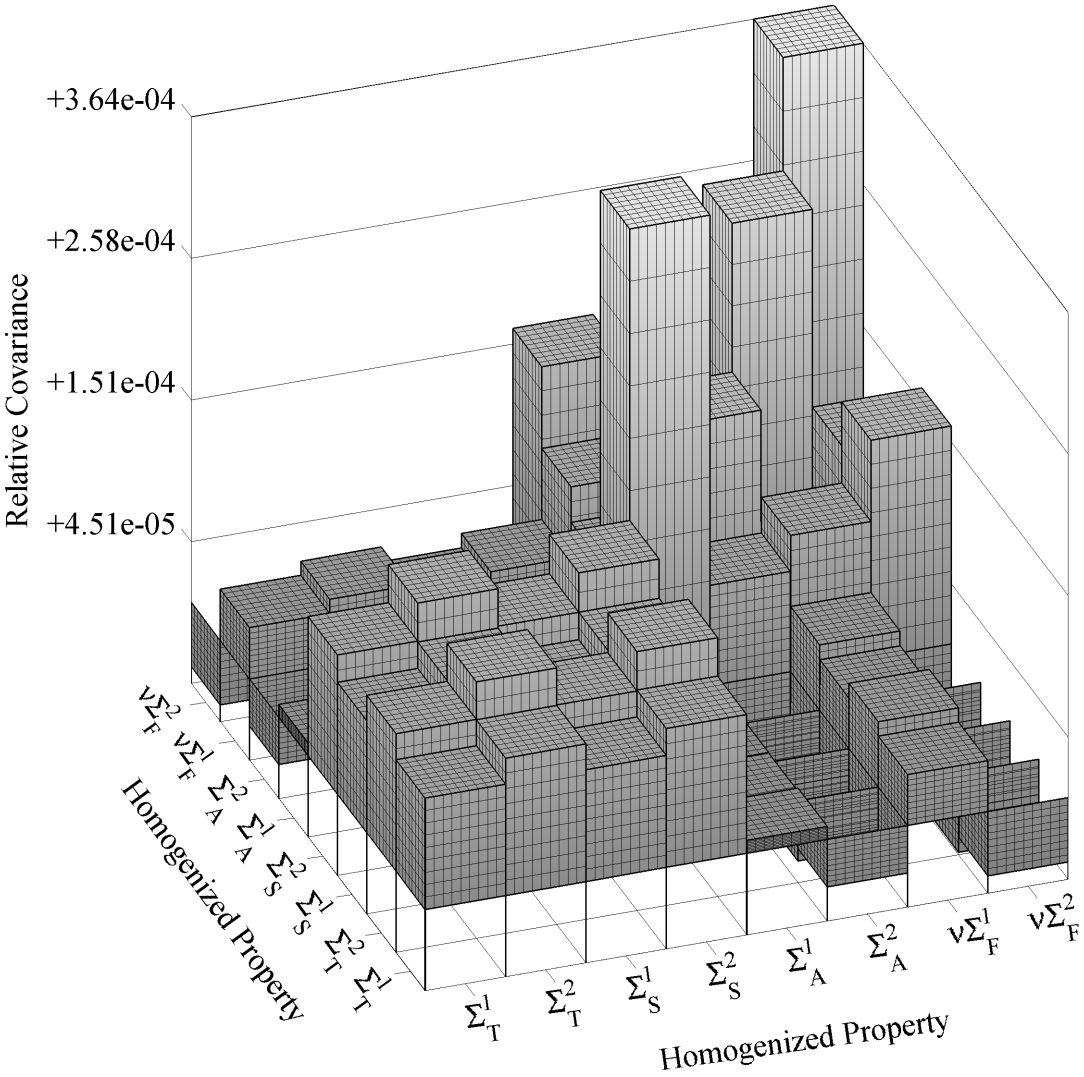

Figure 5.40: CANDU® EoC homogenized relative covariance

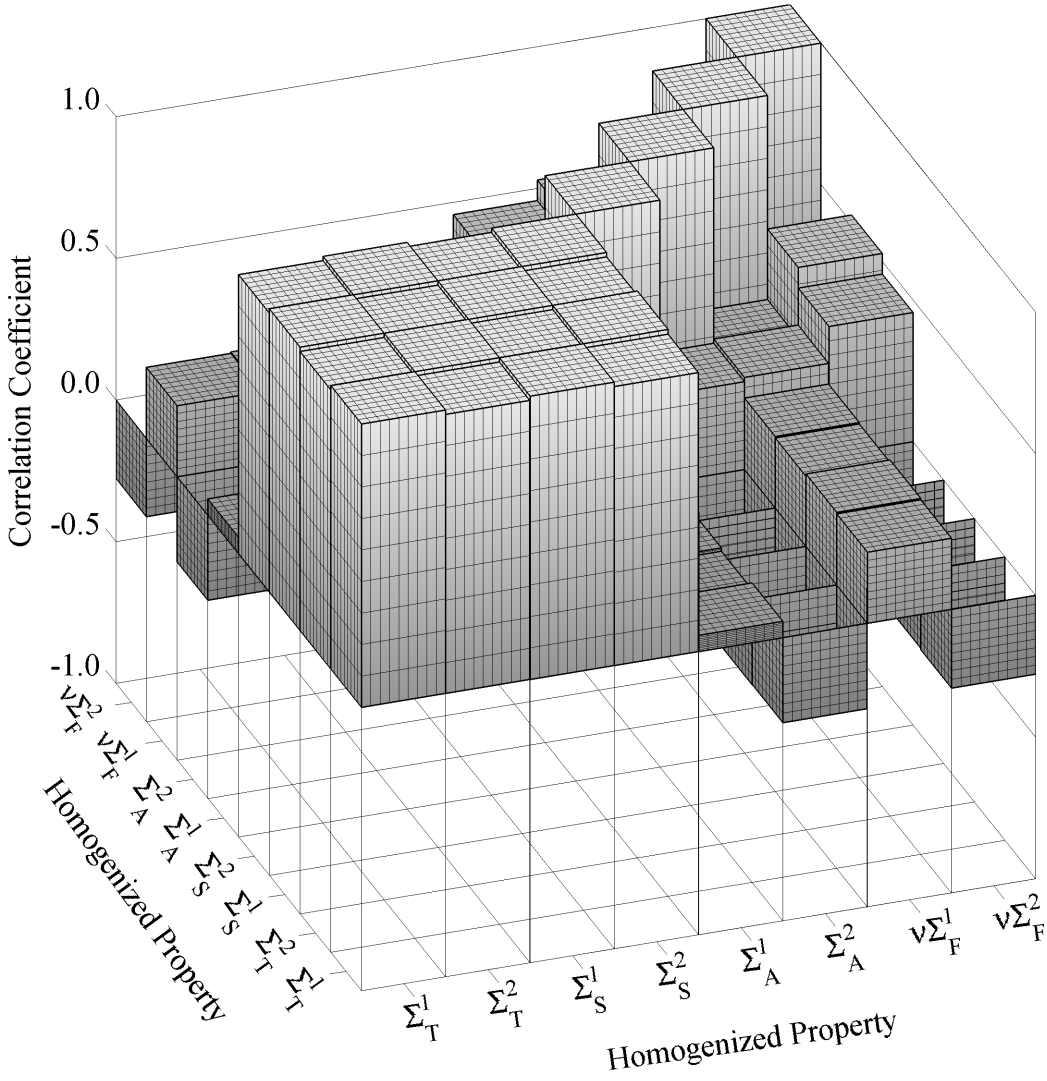

Figure 5.41: CANDU® EoC homogenized correlation

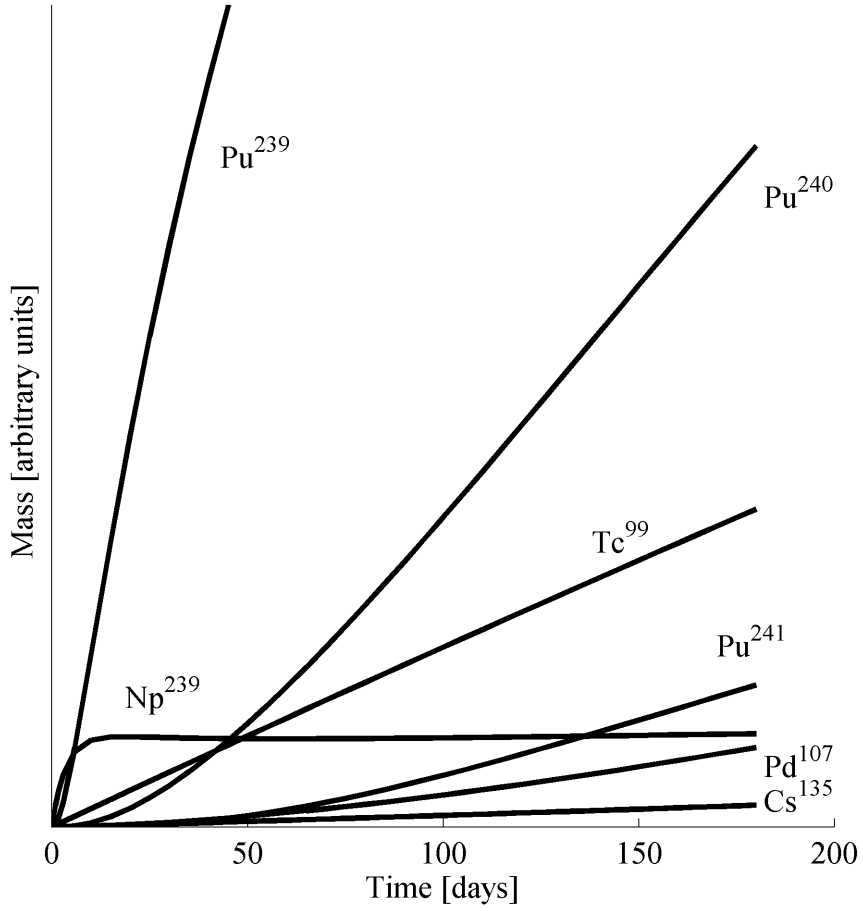

Figure 5.42: CANDU® best-estimate selected nuclide mass

The mass of all 82 lattice nuclides were recorded at each burnup timestep. Figure 5.42 shows the best-estimate prediction of mass for several fission and activation products, and figure 5.43 shows the mass of the same nuclides when predicted with 96 statistical samples of cross-sections. Nuclide concentrations, when average over the full lattice cell volume, are shown in detail for selected nuclides in figures 5.45 through 5.65, where best-estimate predictions are drawn with solid lines, and 0.95/0.95 confidence limits with dashed lines.

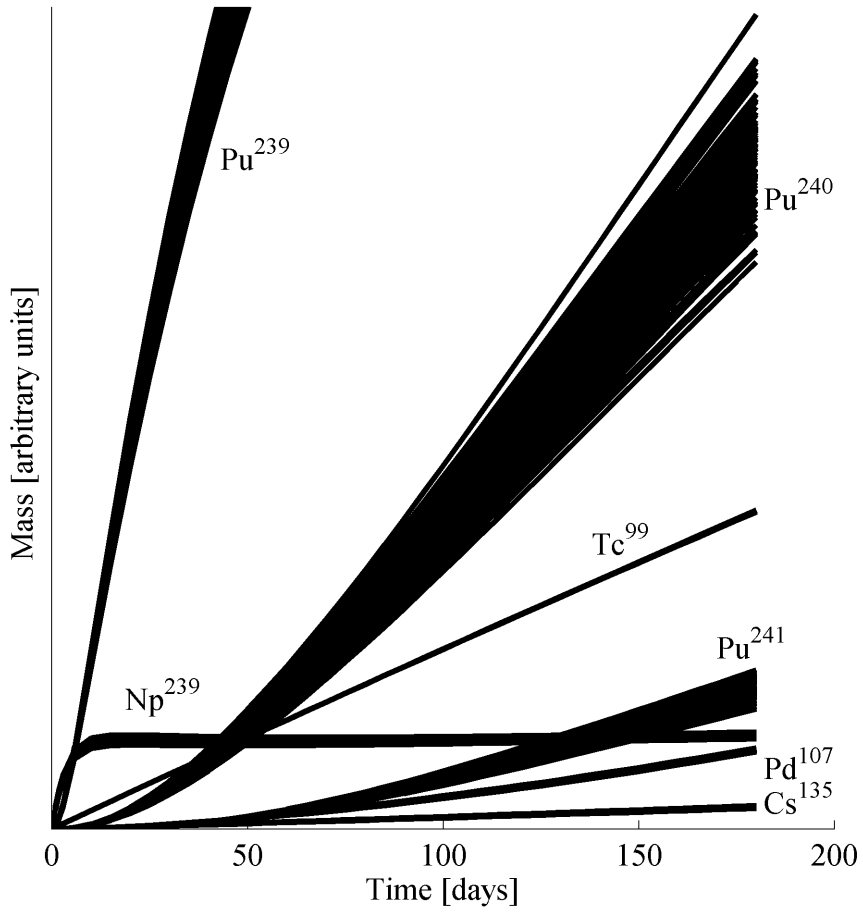

Figure 5.43: CANDU® statistical samples of selected nuclide mass

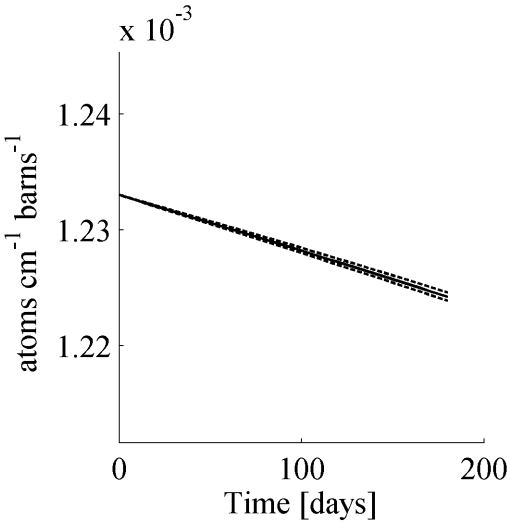

Figure 5.44: U^{238} conc. vs. burnup

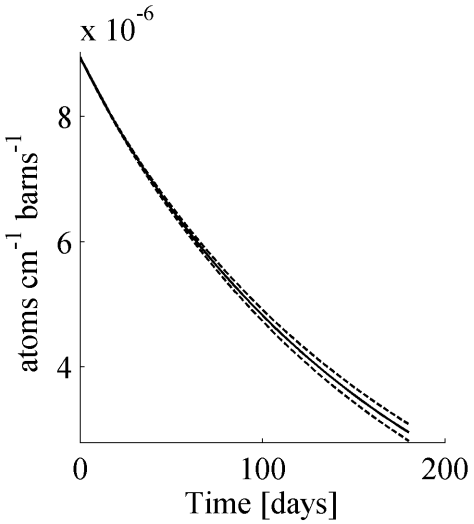

Figure 5.45: U^{235} conc. vs. burnup

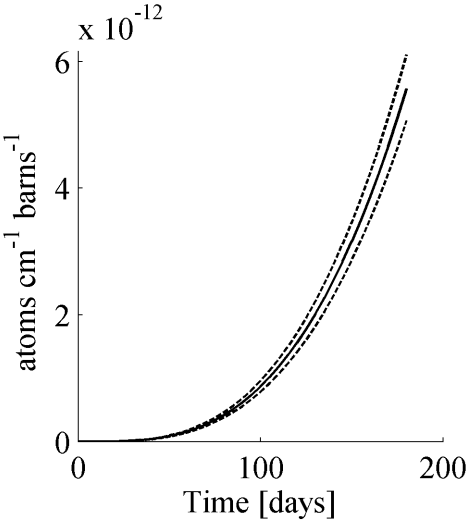

Figure 5.46: U^{234} conc. vs. burnup

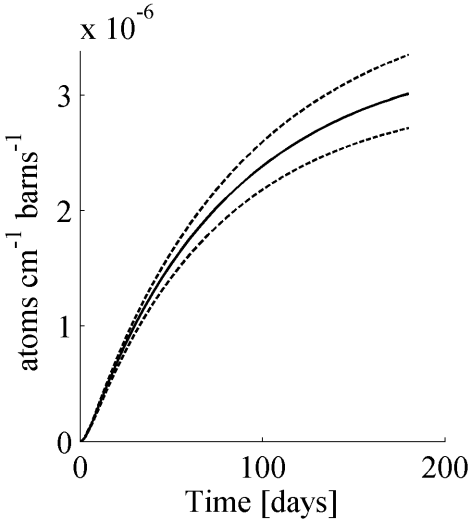

Figure 5.47: Pu^{239} conc. vs. burnup

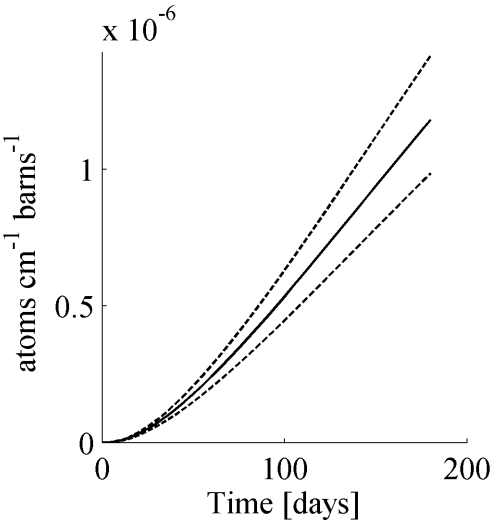

Figure 5.48: Pu^{240} conc. vs. burnup

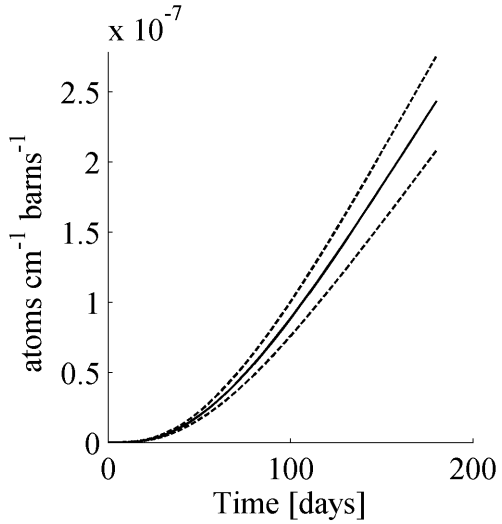

Figure 5.49: Pu^{241} conc. vs. burnup

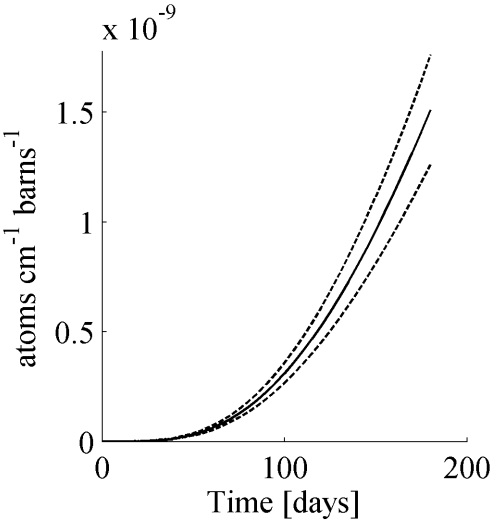

Figure 5.50: Am^{241} conc. vs. burnup

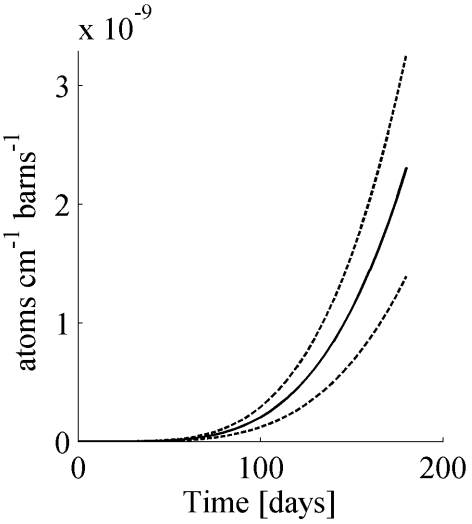

Figure 5.51: Am^{242} conc. vs. burnup

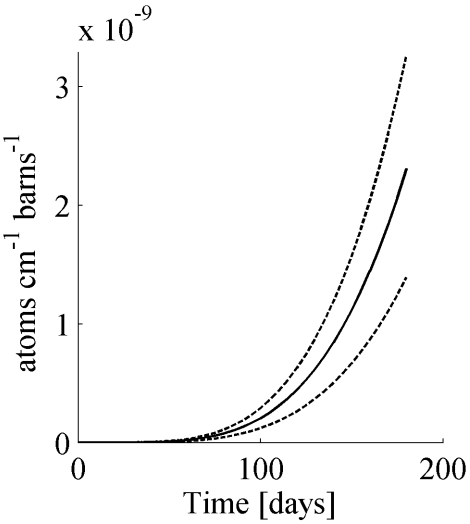

Figure 5.52: Am^{243} conc. vs. burnup

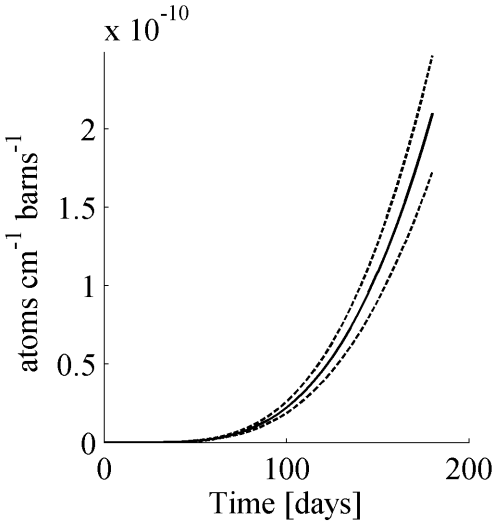

Figure 5.53: Cm^{242} conc. vs. burnup

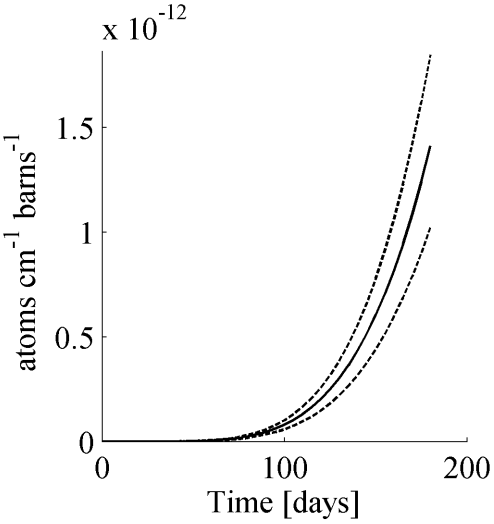

Figure 5.54: Cm^{243} conc. vs. burnup

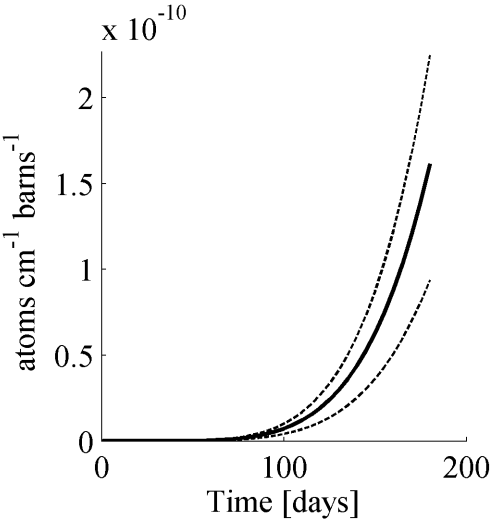

Figure 5.55: Cm^{244} conc. vs. burnup

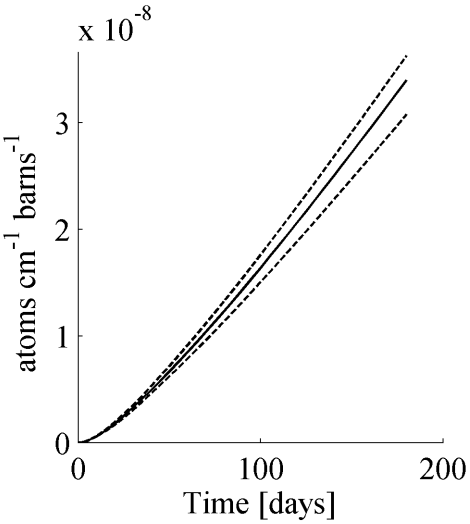

Figure 5.56: Np^{237} conc. vs. burnup

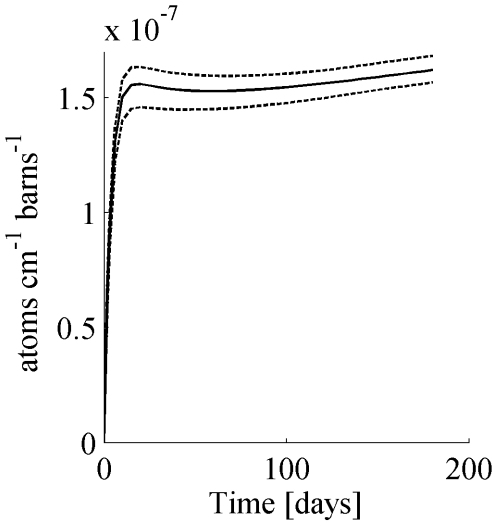

Figure 5.57: Np^{239} conc. vs. burnup

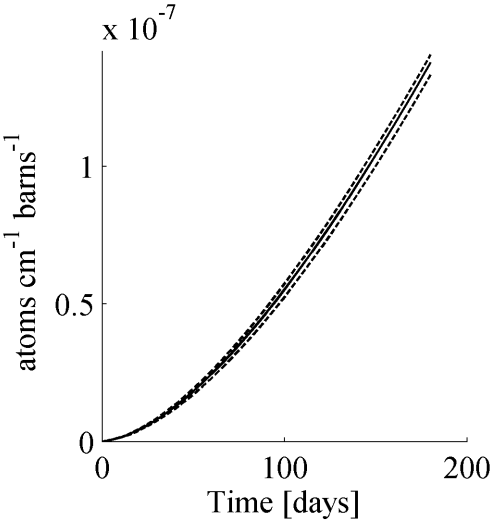

Figure 5.58: Pd^{107} conc. vs. burnup

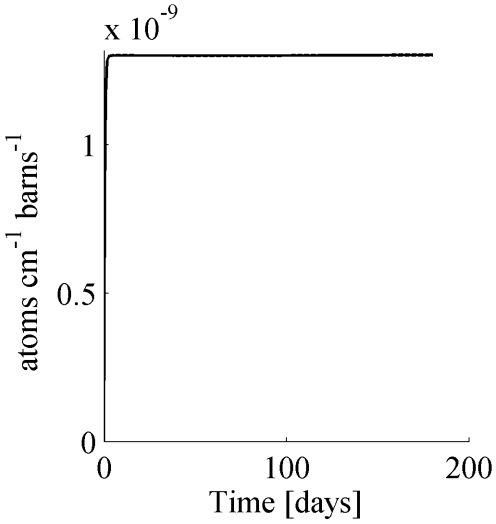

Figure 5.59: I^{135} conc. vs. burnup

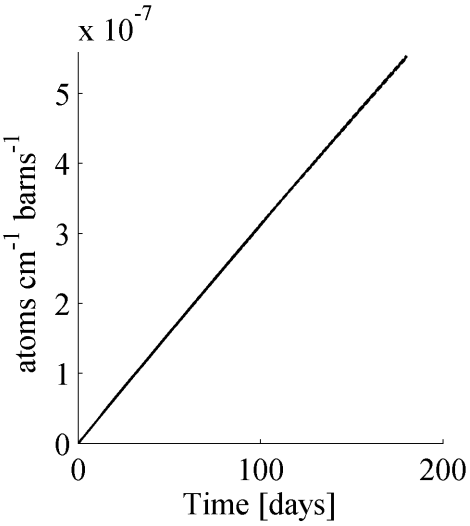

Figure 5.60: Tc^{99} conc. vs. burnup

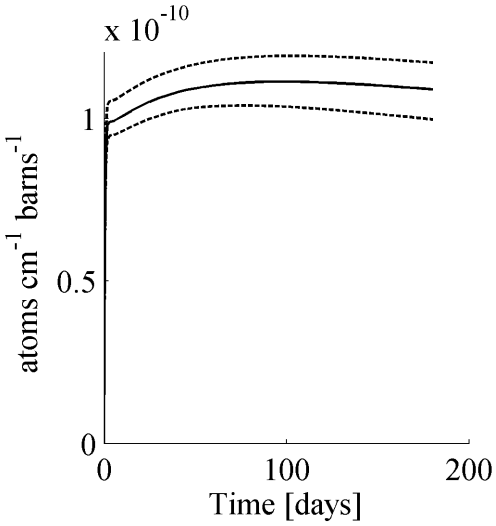

Figure 5.61: Xe^{135} conc. vs. burnup

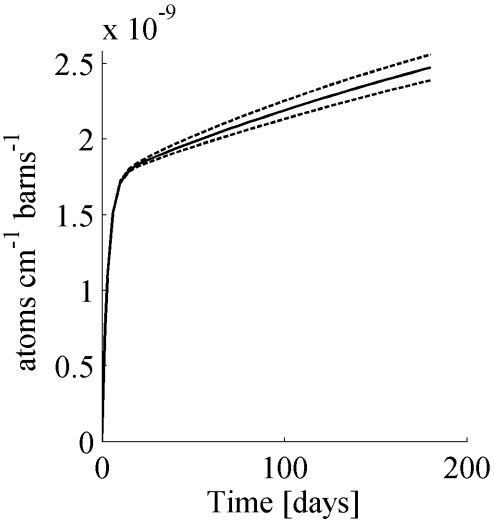

Figure 5.62: Sm^{149} conc. vs. burnup

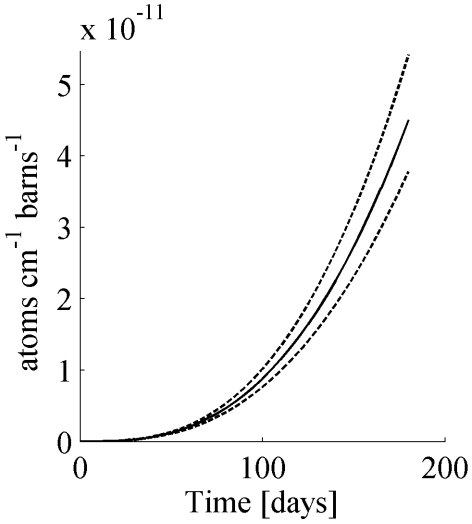

Figure 5.63: Gd^{157} conc. vs. burnup

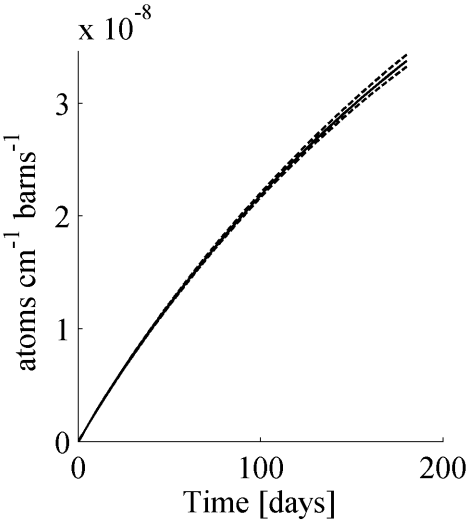

Figure 5.64: Kr^{83} conc. vs. burnup

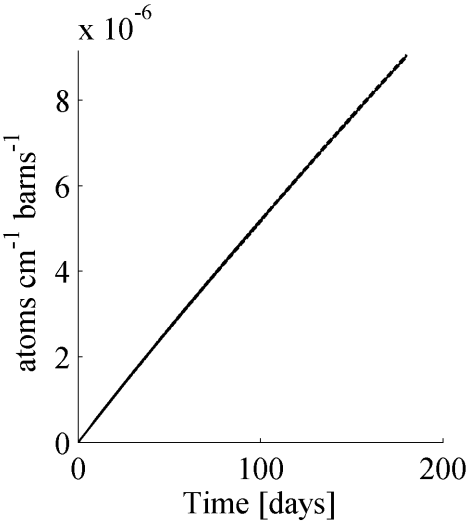

Figure 5.65: Lumped fission product conc. vs. burnup

5.5 EoC results discussion

Although the yield fractions and decay rates of nuclides on the *IAEA* library were not modified, uncertainty arises in the atomic densities of lattice nuclides during burnup as a result of uncertain multi-group cross-sections. The production rates of activation and fission products inherit uncertainty from their respective capture and fission cross-sections, as do all nuclides in their subsequent decay chains. Similarly, the removal rate of nuclides also varies as the rate of radiative capture, and also the fission rate if the nuclides are so capable. An additional indirect effect exists, in that the uncertain cross-sections result in an uncertain neutron flux distribution, which is equally involved in determining reaction rates.

As burnup starts, the multiplication constant of the infinite lattice rapidly declines as fission product poisons are born. The poison nuclides will gradually settle at steady-state concentrations, including, notably, Xe^{135}, which will typically do so after a period of several days at constant power. Plutonium-239, resulting from U^{238} neutron capture, simultaneously accumulates in the fuel and its large fission-to-capture ratio offers an improvement to reactivity that eventually outweighs the poison effect of fission products as their net concentration growth rate slows. The resulting *plutonium peak* in reactivity can be observed as a local maximum in figure 5.38 at approximately 20 days of burning at 900 kW per bundle; approximately 800 MW-days per tonne of fuel. The time at which the plutonium peak is encountered in operational CANDU® cores is a function of bundle power histories, which as previously noted, are not constant at 900 kW. As more fission poisons, whose steady-state settling times are characterized by long time constants, continue to accumulate and Pu^{239} is both

Ge^{72}	Kr^{84}	Nb^{94}	In^{113}	Te^{130}	Nd^{144}
Ge^{73}	Kr^{86}	Mo^{96}	Sn^{115}	I^{129}	Nd^{146}
Ge^{74}	Rb^{85}	Mo^{97}	Sn^{117}	Xe^{128}	Nd^{148}
Ge^{76}	Rb^{87}	Ru^{99}	Sn^{118}	Xe^{130}	Nd^{150}
As^{75}	Sb^{86}	Ru^{100}	Sn^{119}	Xe^{132}	Sm^{154}
Se^{76}	Sb^{87}	Ru^{102}	Sn^{126}	Ba^{134}	Gd^{152}
Se^{77}	Sr^{88}	Ru^{104}	Sb^{121}	Ba^{135}	Gd^{160}
Se^{78}	Y^{89}	Pd^{104}	Sb^{123}	Ba^{136}	Tb^{159}
Se^{80}	Zr^{90}	Pd^{106}	Te^{122}	Ba^{137}	Tb^{160}
Se^{82}	Zr^{91}	Pd^{110}	Te^{123}	Ba^{138}	
Br^{79}	Zr^{92}	Cd^{111}	Te^{124}	Ce^{140}	
Br^{81}	Zr^{93}	Cd^{112}	Te^{125}	Ce^{142}	
Kr^{80}	Zr^{94}	Cd^{114}	Te^{126}	Pr^{141}	
Kr^{82}	Zr^{96}	Cd^{116}	Te^{128}	Nd^{142}	

Table 5.9: *IAEA* lumped fission product contents

burned and transmuted to Pu^{240}, the reactivity again falls and continues to decrease for the remainder of the irradiation. The reactivity decrease over the full length of the 180 days at 900 kW/bundle burnup is 121 milli-k.

Not all fission products are explicitly recorded in the *IAEA* library. Some are treated as an aggregate *lumped fission product* (LFP), which is a construct representing an amalgam of properties of 79 fission product nuclides. The properties of the lumped nuclides are weighted in atom density according to their relative yields from three parent fissile nuclides, U^{235}, U^{238} and Pu^{239} assuming fractional fission rates of 54%, 8% and 38%, respectively. Lumped nuclide cross-sections are weighted in energy assuming infinite dilution and a temperature of 700 K, by the same weighting function used for all other library nuclides. The nuclides whose properties constitute the LFP are shown in table 5.9. The rationale behind the inclusion of nuclides in the FLP with associated selection criteria can be found in *WLUP* literature[62]. The LFP has no associated covariance matrix in the *69GROUPV6REC* covariance library as it is not a nuclide, however, an LFP covariance could be calculated from those of its constituent nuclides if the atom weighting function is precisely known. In this burnup uncertainty study, without detailed weighting functions, no LFP covariance could be reasonably assembled and it is therefore treated as having no associated cross-section uncertainty.

The variation of k_∞ uncertainty shown in figure 5.39 reveals a surprising uncertainty characteristic of the lattice during burnup. The relative uncertainty in reactivity falls quickly at the beginning of the irradiation and reaches a global minimum of just less than 1.02% $\Delta k_\infty/k_\infty$ at 30 days of irradiation, corresponding to approximately 1193 MW-days per tonne of burnup. The change in uncertainty was

tested for correlation with various individual isotope concentrations, but no significant correlation was observed. The variation of k_∞ uncertainty with burnup is, therefore, likely emerging from a complex set of competing phenomena involving several isotopes. Behaviour of $\Delta k_\infty / k_\infty$ has two dominant features, the decline during the first 30 days of burnup followed by a steady rise, and each stage can be analyzed separately to some degree, in an effort to determine its underlying causes, as though they are two independent components in superposition.

Recall the rapid accumulation of fission product poisons beginning at the onset of fuel irradiation. As their concentrations grow, they become responsible for an increasing frequency of parasitic absorptions of neutrons, which dulls the sensitivity of k_∞ to U^{238} (n, γ), since it is accountable for a smaller fraction of total absorption reaction rate. Naturally, as the sensitivity to U^{238} capture diminishes, sensitivities to fission product absorptions rises. However, fission product capture cross-sections tend to have less relative uncertainty than that of U^{238} (n, γ). Therefore, in terms of the total absorption rate, high-uncertainty captures by U^{238} are substituted with low-uncertainty captures of fission product nuclides such as Xe^{135}, Sm^{149}, and with LFP captures, which have no quantified uncertainty whatsoever. Now considering the inverse side of neutron multiplication, the relative fission rate of U^{235} decreases as Np^{239} decays to the fissile Pu^{239}, whose fission cross-section uncertainty is significantly larger than that of U^{235}. In this case, it is low-uncertainty reactions that are substituted with high-uncertainty reactions. Relative multi-group uncertainties for several selected nuclide cross-sections can be found in appendix A.

Speaking more generally, the uncertainties associated with actinide cross-sections tend to be large. As burnup continues and actinides are produced in increasing quantities, reaction rate uncertainties will tend to grow. Additionally, uncertainties cascade over time due to indirect effects; uncertain flux yields uncertain nuclide densities which yield uncertain flux. After 20 days of irradiation, the benefit to prediction confidences due to decreasing U^{238} capture sensitivity is overwhelmed by the increased uncertainties arising from indirect effects and other actinide uncertainties.

Chapter 6

Conclusions

The objective of this work was to conduct lattice physics sensitivity and uncertainty analysis on LWR and CANDU® systems by developing and applying new methods that comprehensively addresses all relevant sources of uncertainties. These uncertainties play a prominent role in steady-state reactor physics calculations such as those used for maximum power license compliance, as well as for transients such as anticipated operational occurrences (AOO) and design basis accidents (DBA). Rigorous integration of these uncertainties has been limited in the past by computational resources. However, using modern computational tools and large parallel computational abilities have allowed us to resolve such uncertainties for the first time.

Sources of uncertainty must not be limited to merely physics parameters such as cross-sections, but include model parameters such as material temperature and density of coolant and moderator. While several previous works have focused on a limited number of output variables of interest (such as k_∞), little work has examined the uncertainties in homogenized, few-group properties, and neutron flux. The treatment of resonance self-shielding effects on lattice uncertainties – a phenomena oft-neglected during lattice uncertainty investigations – was also a requirement of this work, to achieve a completeness of the analysis and to preserve applicability of the tool to nuclear systems that feature especially low material dilution, and hence a large degree of self-shielding. CANDU® lattice analysis additionally demands two-dimensional as well as three-dimensional capabilities.

In order to achieve the objectives, a new tool was developed using a Monte Carlo statistical approach. Verification of the tool was performed for pin-cell geometries of several reactor types through comparison to adjoint-based sensitivity approaches (e.g., the commercial code TSUNAMI, which is part of the SCALE code package). At each point in the verification, care was taken to ensure consistency in input ENDL and uncertainty covariance libraries. Additional verification using numerical perturbation sensitivity methods were also performed using additional tools developed in this thesis. This work was submitted to the OECD/NEA UAM benchmark and was a significant contribution to that international work.

Beyond the verification, the Monte Carlo tool was used to perform the first uncertainty analysis for CANDU® lattice calculations which could address not just nuclear data uncertainties, but those also associated with lattice parameters including coolant, moderator and fuel temperature. Sensitivity coefficients were also determined for key parameters. Finally, integrated uncertainties were determined for all key output variables and few-group cross-sections based on a combination of all multi-group physics parameter and physical input uncertainties. This thesis provides the only results from Canada contributed to the UAM international benchmark and includes the first published few-group cross-section uncertainties and covariance for CANDU® lattice physics.

This work offers unique contributions to the field of lattice physics uncertainty analysis that can be categorized in two ways. One set of contributions relates to the methodology and tools that were developed to conduct the analysis while satisfying the above requirements. Other contributions arise through the subsequent analysis of four specific lattice systems using the methodology and tools that were developed.

On the Methodology and Toolset

With respect to the methodology, the work described in this dissertation offers a unique approach to lattice uncertainty analysis that address all implicit sensitivity effects resulting from resonance self-shielding of cross-sections (which are often neglected by other methods), by employing a novel set of resonance parameter corrections that are derived according to reactor theory from perturbations in multi-group data. The toolset DINOSAUR performs statistical sampling and direct numerical perturbation of lattice inputs, and conducts all related parameter corrections, including those pertaining to resonance parameters, and is coupled to the lattice code DRAGON, which is part of the Canadian Industry Standard Toolset.

A statistical sampling approach was employed by DINOSAUR to propagate uncertainties of both physics and model parameters, with a separate direct numerical perturbation approach to generate sensitivity profiles and ranks of importance of inputs. By virtue of the coupling to DRAGON, the uncertainty propagation conducted by DINOSAUR is unique in that it can be applied to one, two and three-dimensional nuclear geometries, all using deterministic solutions of the transport equation. When this work was commenced, the available mainstream tool, TSUNAMI, was restricted to only 1D and 3D geometries[1], and furthermore, 3D geometries required a Monte Carlo rather than deterministic solution to the transport equation. Resonance self-shielding effects are fully addressed by a unique approach that involves the adjustment of resonance integrals derived from perturbations in multi-group cross-sections. A separate approach, which was also described in this dissertation, involves a differ-

[1]As discussed in chapter 2, TSUNAMI-2D was developed concurrently with this work and was recently released in July 2011.

ent set of resonance parameters for self-shielding by the Nordheim integral treatment, and highlights the challenges of performing comprehensive lattice physics uncertainty analysis with multi-group data libraries that were never intended to facilitate such an endeavour.

Physics and model parameter uncertainties can be simultaneously or individually propagated using DINOSAUR. By model parameter, what is meant is any parameter that is defined in the input deck of the lattice simulation, including material temperatures, densities, isotopics, and geometries (e.g. fuel pin diameters). Model parameters are statistically sampled by DINOSAUR according to user-defined probability distributions in a similar manner as physics parameters (i.e. multi-group cross-sections). The treatment of both model and physics parameters implies that every potential source of uncertainty in lattice physics can be addressed during analysis.

At the time this work began, mainstream tools were focused on quantifying uncertainty of the lattice k_∞, and not other lattice calculation outputs including homogenized, few-group cross-sections[2]. DINOSAUR has the capability to calculate covariance and correlation matrices for every output calculated during a best-estimate lattice calculation. The evolution of lattice properties and their associated uncertainties during burnup can be predicted using DINOSAUR. Adjoint-based methods face challenges in predicting such burnup-related uncertainties, which are straightforwardly obtained with DINOSAUR's statistical sampling method. Furthermore, DINOSAUR offers several advantages over adjoint-based sensitivity and uncertainty tools, in terms of: the diversity of input parameters and output responses for which uncertainties can be examined, computational efficiency when investigating a large number of responses and/or parameters, the parallelizability of the underlying methodology, and the capture of all high-order terms of the responses as a function of parameters.

On the Analysis

DINOSAUR was used to conduct sensitivity and uncertainty analysis on three LWR fuel cells, and a CANDU® lattice. In total, over 60,000 best-estimate and uncertainty lattice calculations were performed to generate the statistics of the lattice outputs and their sensitivities with respect to uncertain parameters. A summary of the contributions resulting from the analyses are presented in this section.

The statistical sampling used by DINOSAUR for each analysis in this dissertation was performed in duplicate, using distinct probability distributions for the input parameters – normal and uniform. The analyses demonstrate that the uncertainty results tend to be independent of the choice of input parameter distribution. Therefore, the uniform distribution is *preferred*, as it produces a set of random values that are the most tightly packed about the reference value, given a particular variance.

[2]Again, due to the rapid development of tools in part due to the OECD/NEA UAM benchmark, new tools, namely XSUSA, were later developed to quantify additional lattice output uncertainties.

Conversely, the tail ends of a Gaussian distribution have the potential to yield random parameter values that are so far from the reference value that numerical instabilities can arise during the solution of the transport equation working on those parameters. This is particularly true for cases where largely negative values are generated for a cross-section, which are clearly nonphysical.

With respect to the multiplication constant, k_∞, the ranking of importance of isotope physics parameters – the degree to which they contribute to k_∞ uncertainty – is fairly uniform between lattice cell types[3]. This broadly suggests that the ranking of importance of physics parameters is fairly constrained for thermal, uranium-fueled reactors. Fission and absorption parameters of the primary fissionable isotopes, U^{238} and U^{235} are consistently the top contributors to k_∞ uncertainty for lattices of fresh fuel. The large sensitivity of k_∞ to U^{238} (n, γ) conspires with that cross-section's significant covariance to make it the dominant source of k_∞ uncertainty for all the lattice cells that were investigated.

Physics parameters result in significant neutron flux uncertainty. It was found that the flux uncertainty contributes significantly to the uncertainty of few-group, homogenized cross-sections whose formulation incorporates the flux as a weighting function in their energy and volume averaging. Indeed, it was shown that this indirect pathway of cross-section uncertainty propagation can be more important to quantifying homogenized parameter uncertainties than the component contributed directly by the cross-sections that are averaged. In other words, the uncertainty associated with a weighted average can be more due to the uncertain weighting function (i.e. flux) than the uncertain parameters that are being averaged (i.e. cross-sections). Therefore, the consideration of flux uncertainties that arise from uncertainties in physics parameters is necessary to accurately quantify the covariance of lattice calculation outputs.

This dissertation constitutes what is probably the most rigorous CANDU® lattice physics sensitivity and uncertainty analysis ever conducted, which includes a study of the evolution of lattice uncertainties as a result of burnup. Even with no consideration given to uncertainties of isotope yield fractions and decay rates, considerable uncertainties were found in CANDU® properties during burnup. Such burnup related uncertainties result wholly from the uncertainties in fission and absorption rates of isotopes, leading to uncertain isotope concentrations and uncertain neutron flux at each timestep. A decrease in k_∞ uncertainty is seen at the onset of burnup, most likely due to the rapid accumulation of fission products, followed by a steady rise in uncertainty that is likely attributable to the slow buildup of transuranic actinides.

For CANDU® lattices, when isolating the effect of temperature uncertainties to the Doppler broadening of cross-sections (i.e. de-coupled from corresponding material density changes), the resulting uncertainties associated with lattice outputs are small in magnitude compared to those that result from multi-group cross-section covariance. Thermal uncertainties would need to be exorbitantly large ($\approx \pm 20\%$) to

[3]A natural and obvious exception applies to those isotopes that are not common to each system.

achieve uncertainty contributions to lattice properties that are of significance compared to the contributions from multi-group cross-section uncertainties. Temperature uncertainties of that magnitude are unreasonably large for typical, steady-state operations, but may be realized during some transients that correspond to accident conditions.

6.1 Future work

A challenge emerged during the development of DINOSAUR that is related to the uncertainty library *44GROUPV6REC* and the reference library *IAEA* not spanning a common set of parameters. Whereas the covariance matrices correspond to many partial cross-sections, such as (n, γ), (n, α), (n, 2n), etc., the *IAEA* library tends to include aggregate cross-sections such as (n, total) and (n, absorption) instead. Therefore, assumptions had to be made regarding the degree to which each partial cross-section contributed to the aggregate cross-sections, in order to apply their individual covariances in a sensible way. While the assumptions that were made are rather reasonable, they constitute an area of potential improvement.

Future work must be conducted to eliminate the need for assuming the relative magnitudes of various partial cross-sections. A new library, based on the latest data evaluations (i.e. ENDF/B-VII) will be generated using the NJOY cross-section processing code. The new library will not be of the constrained WIMS-D4 format, but rather a different format in which all important partial cross-sections are uniquely represented. DINOSAUR will be extended to perform statistical sampling and direct numerical perturbation on the new library, which will subsequently be converted to the DRAGON-readable WIMS-D4 format. This approach will ensure that the aggregate cross-sections of the WIMS-D4 library correctly capture the effects of each partial cross-section according to their true relative contributions. The adoption of ENDF/B-VII physics data will improve the quality of best-estimate lattice calculations, and will also be consistent with the latest covariance evaluations from Oak Ridge National Laboratory, *44GROUPCOV*.

6.2 Recommendations for future work

A widely adopted strategy in performing lattice physics uncertainty analysis, including the strategy adopted in this work, is to employ multi-group covariance matrices – such as the 44-group matrices evaluated by ORNL – as the basis for propagating physics uncertainties through the lattice calculation sequence. To the extent that some lattice sequences involve energy group structures that differ from the ORNL 44-group structure, interpolation of the covariance is required. A feature of multi-group covariances, such as *44GROUPV6REC*, is that they are a product of all underlying physics uncertainty effects, including: resonance parameter uncertainties; continuous-

energy cross-sections and weighting functions; and so on. To address the implicit uncertainty effects of resonance self-shielding, one must work backwards, using formulations that relate the variation in multi-group data to variations in the resonance parameters used for self-shielding. This is a rather clunky and circular procedure.

From the experience gained during the work of this dissertation, there is the following recommendation for future work. Exploiting the flexibility of the statistical sampling approach, uncertainty propagation can begin at the level of continuous-energy nuclear data files, rather than at the level of multi-group libraries. The ENDF/B-VII data files include covariance matrices on a very fine energy mesh, for cross-sections as well as resonance parameters. Therefore, the fine mesh covariances can be used to generate statistical samples of the entire ENDF/B-VII evaluation. For each randomly generated variation of ENDF/B-VII, standard cross-section processing can be performed. After processing, the resulting libraries will consist of multi-group data and resonance parameters that will necessarily be entirely consistent with the variations in continuous-energy data in the randomly generated ENDF/B-VII. A full best-estimate calculation, from lattice physics to full-core diffusion can be carried out for each variation, thus growing a population of reactor physics outputs whose uncertainties can be statistically calculated. The number of statistical variations of the ENDF/B-VII evaluation depends only on the desired confidence associated with subsequent reactor physics calculations. This approach, while more demanding in terms of the statistical sampling, requires the fewest number of assumptions regarding the relationships between parameters – especially those between multi-group cross-sections and resonance parameters.

Bibliography

[1] D. Cacuci, ed. *Handbook of Nuclear Engineering*. Vol. I - IV. New York: Springer, 2010.

[2] Brookhaven National Laboratory. "ENDF-6 Formats Manual: Data Formats and Procedures for the Evaluated Nuclear Data File ENDF/B-VI and ENDF/B-VII," Document ENDF-102, June 2009.

[3] A. Koning, R. Forrest, M. Kellett et al., eds. "The JEFF-3.1 Nuclear Data Library," JEFF Report 21, OECD/NEA, 2006.

[4] K. Shibata, O. Iwamoto, T. Nakagawa, et al. "JENDL-4.0: A New Library for Nuclear Science and Engineering," *Journal of Nuclear Science and Engineering*, Vol. 48, No. 1, pp.1-30, 2011.

[5] V. McLane. "EXFOR Basics: A Short Guide to the Nuclear Reaction Data Exchange Format," IAEA-NDS-206, BNL-NCS-63380-2000/05-Rev., International Atomic Energy Agency (IAEA), 2001.

[6] S.F. Mughabghab. *Atlas of Neutron Resonances, Fifth Edition: Resonance Parameters and Thermal Cross Sections*, Amsterdam: Elsevier Science, 2006.

[7] J.F. Briesmeister, ed. "MCNP – A General Monte Carlo N-Particle Transport Code – Version 4C," LA-13709-M, Los Alamos National Laboratory, March, 2000.

[8] R.E. MacFarlane, D.W. Muir and R.M. Boicourt. "The NJOY Nuclear Data Processing System: User's Manual," Los Alamos National Laboratory report, LA–9303-M, Vols. I to IV, May 1982.

[9] D. G. Madland. "New Fission-Neutron-Spectrum Representation for ENDF," Los Alamos National Laboratory report, LA–9285-MS, April 1982.

[10] J. J. Duderstadt, L. J. Hamilton. *Nuclear Reactor Analysis*, John Wiley and Sons, 1976.

[11] L. P. Abagyan, N. O. Bazazyants, I. I. Bondarenko, M. N. Nikolaev. *Group Constants for Nuclear Reactor Calculations*, New York: Consultants Bureau, 1964.

[12] C. Cercignani. *The Boltzmann Equation and Its Applications*, New York: Springer, 1987.

[13] D. J. Hughes. *Neutron Cross Sections*, Elsevier, 1957.

[14] M. Herman. MeV School. Lecture, Topic: "Covariance data". Argonne National Laboratory, Advanced Photon Source, Argonne, IL. Session #2-4, 18 July 2011.

[15] M.E. Dunn and N.M. Greene. "AMPX-2000: A Cross-Section Processing System for Generating Nuclear Data for Criticality Safety Applications," *Trans. Am. Nucl. Soc.*, No. 86, June 2002.

[16] D. Wiarda, M. E. Dunn. "PUFF-IV: A Code for Processing ENDF Uncertainty Data Into Multigroup Covariance Matrices," ORNL/TM-2006/147 ORNL, 2006.

[17] K. Ivanov et al. "Benchmark for Uncertainty Analysis in Modeling (UAM) for Design, Operation and Safety Analysis of LWRs," OECD Nuclear Energy Agency, Volume 1, Version 2.0, February 2011.

[18] Z. B. Alfassi. "Uncertainty analysis based on sensitivity analysis" in *Statistical Treatment of Analytical Data*. Oxford, U.K.: Blackwell Science, 2004.

[19] Q. Wang (2008). "Uncertainty quantification for unsteady fluid flow using adjoinst-based approaches". Doctoral dissertation. Stanford University, USA, 2008.

[20] F. R. Andrade Lima, et al. "Recent advances in perturbative methods applied to nuclear engineering problems," *Progress in Nuclear Energy*, Vol. 33, No. 1, pp. 23-97, 1998

[21] G. Aliberti, et al. "Nuclear data sensitivity, uncertainty and target accuracy assessment for future nuclear systems," *Annals of Nuclear Energy*, Vol. 33, pp. 700-733, 2006.

[22] M. Assawaroongruengchot and G. Marleau. "Perturbation Theory Based on the Method of Cyclic Characteristics," *Nuclear Science and Engineering*, Vol. 157, pp. 30–50, 2007.

[23] M. L. Williams, B. T. Rearden. "SCALE-6 sensitivity/uncertainty methods and covariance data," *Nuclear Data Sheets*, Vol. 109, Issue 12, pp. 2796-2800, December 2008.

[24] A. Bidaud et al., "Nuclear Data Uncertainty Analysis using the coupling of DRAGON with SUSD3D," *International Conference on Mathematics, Computational Methods & Reactor Physics (M&C 2009)*, Saratoga Springs, New York, May 3-7, 2009.

[25] A. Griewank. "On automatic differentiation" in M. Iri and K. Tanabe Eds., *Mathematical Programming: Recent Developments and Applications,* Dordrecht, Netherlands: Kluwer Akedemic Publishers, pp. 83–108, 1989.

[26] J. R. R. A. Martins, et al. "The complex-step derivative approximation." *ACM Transactions on Mathematical Software,* Vol. 29, No. 3, September 2003, pp. 245-262.

[27] C. Biscof and F. Dilley. "A compilation of automatic differentiation tools presented at the 1995 international convention on industrial and applied mathematics, Hamburg," *ACM SIGNUM Newsletter*, Vol. 30, Issue 3, July 1995.

[28] E. Laporte and P. Le Tallec. "Sensitivity analysis" in *Numerical methods in sensitivity analysis and shape optimization*, Boston: Birkhäuser, 2002.

[29] W. Wieselquist et al. "Towards an uncertainty quantification methodology with CASMO-5." *International Conference on Mathematics and Computational Methods Applied to Nuclear Science and Engineering (M&C2011)*, Rio de Janeiro, Brazil, May 8-12, 2011.

[30] Oak Ridge National Laboratory. "TSUNAMI-1D: Control Module for One-Dimensional Cross-Section Sensitivity and Uncertainty Analysis for Criticality," ORNL/TM-2005/39, Version 5.1, Vols. I, Book 2, Sect. C8, November 2006.

[31] Oak Ridge National Laboratory. "TSUNAMI-3D: Control Module for Three-Dimensional Cross-Section Sensitivity and Uncertainty Analysis for Criticality," ORNL/TM-2005/39, Version 5.1, Vols. I, Book 2, Sect. C9, November 2006.

[32] Oak Ridge National Laboratory. "SCALE: A Modular Code System for Performing Standardized Computer Anlyses for Licensing Evaluation," ORNL/TM-2005/39, Version 5.1, Vols. I-III, November 2006.

[33] Oak Ridge National Laboratory. "XSDRNPM: A One-Dimensional Discrete-Ordinates Code for Transport Analysis," ORNL/TM-2005/39, Version 5.1, Vols. II, Book 1, Sect. F3, November 2006.

[34] Oak Ridge National Laboratory. "KENO V.a: an improved Monte Carlo criticality program," ORNL/TM-2005/39, Version 5.1, Vols. II, Book 2, Sect. F11, November 2006.

[35] B. T. Rearden et al. "Advances in the TSUNAMI Sensitivity and Uncertainty Analysis Codes Beyond SCALE 5," Oak Ridge National Laboratory manuscript, March 1, 2005.

[36] "SCALE 6.1 released!" *SCALE Newsletter* (2011), No. 43, pp. 5.

[37] Oak Ridge National Laboratory. "NEWT: A New Transport Algorithm for Two-Dimensional Discrete Ordinates Analysis in Non-Othrogonal Geometries," ORNL/TM-2005/39, Version 5.1, Vols. II, Book 4, Sect. F21, November 2006.

[38] Oak Ridge National Laboratory. "SAMS: sensitivity analysis module in scale," ORNL/TM-2005/39, Version 5.1, Vols. II, Book 4, Sect. F22, November 2006.

[39] J. Horwedel. "Application of automatic differentiation to coupled SCALE modules using GRESS 90 – part I," *Proc. of ANS 2006 Winter Meeting 'Ensuring the Future in Times of Change: Nonproliferation and Security,* Albuquerque, NM, November 12–16, 2006.

[40] B. T. Rearden and J. E. Horwedel. "Automatic differentiation to couple SCALE modules using GRESS 90 –part II: application," *Proc. of ANS 2006 Winter Meeting 'Ensuring the Future in Times of Change: Nonproliferation and Security,* Albuquerque, NM, November 12–16, 2006.

[41] Oak Ridge National Laboratory. "CENTRM: a one-dimensional neutron transport code for computing pointwise energy spectra," ORNL/TM-2005/39, Version 5.1, Vols. II, Book 4, Sect. F18, November 2006.

[42] B. T. Rearden et al. "Advances in sensitivity analysis capabilities with SCALE 6.0 and 6.1*," *Joint International Conference on Supercomputing in Nuclear Applications and Monte Carlo 2010*, Tokyo, Japan, October 17-21, 2010.

[43] I. Kodeli. "Multidimensional deterministic nuclear data sensitivity and uncertainty code system: method and application," *Nuclear Science and Engineering*, Vol. 138, pp. 45-66, 2001.

[44] W. W. Engle, Jr. "A user's manual for ANISN, a one-dimensional discrete ordinates transport code with anisotropic scattering," K-1693, Oak Ridge National Laboratory, 1967.

[45] W. A. Rhoades and F. R. Mynatt., "The DOT-III two-dimensional discrete ordinates transport code," ORNL0TM-4280, Oak Ridge National Laboratory, 1973.

[46] R. E. Alcouffe et al. "DANTSYS 3.0—a diffusion-accelerated, neutral-particle transport code system," LA-12969-M, Los Alamos National Laboratory, June 1995.

[47] W. A. Rhoades and R. L. Childs. "TORT-DORT: two-and three-dimensional discrete ordinates transport, version 2.7.3," CCC-543, Radiation Safety Information Computation Center, Oak Ridge National Laboratory, 1993.

[48] G. Marleau. "DRAGON Theory Manual: Part 1: Collision Probability Calculations," Technical Report, IGE-236, Revision 1, École Polytechnique de Montreál, October 2001.

[49] B. Rearden. "SCALE TSUNAMI sensitivity and uncertainty analysis capabilities and data," Presentation. Pocatello, Idaho, September 22, 2009.

[50] W. Zwermann et al. "Uncertainty analysis with nuclear covariance data in reactor core calculations." *Journal of the Korean Physical Society*, Vol. 59, No. 2, August 2011, pp. 1256-1259.

[51] M. Klein, et al. "Influence of nuclear data covariance on reactor core calculations." *International Conference on Mathematics and Computational Methods Applied to Nuclear Science and Engineering (M&C 2011)*, Rio de Janeiro, Brazil, May 8-12, 2011.

[52] J. Rhodes, et al. "CASMO-5 development and applications." *ANS Topical Meeting on Reactor Physics (PHYSOR 2006),* Vancouver, Canada, September 14-16, 2006.

[53] M. Ball, et al. "The Effect on Super-Cell Calculations Due to Modeling CANDU Fuel Pin Clusters as Annuli." *ANS International Conference on Mathematics and Computational Methods Applied to Nuclear Science and Engineering (M&C 2011),* Rio de Janeiro, Brazil, 2011.

[54] A. C. Morreale at al. "The Effects of Actinide Based Fuels on Incremental Cross Sections in a CANDU Reactor." *ANS International Conference on Mathematics and Computational Methods Applied to Nuclear Science and Engineering (M&C 2011),* Rio de Janeiro, Brazil, 2011.

[55] H. Wolkowicz et al. *Handbook of Semidefinite Programming: Theory, Algorithms and Applications*, Norwell, Massachusetts: Kluwer Academic Publishers, 2000.

[56] A. Berman, N. Shaked-Monderer. *Completely Positive Matrices*, Singapore: World Scientific Publishing, 2003.

[57] Oak Ridge National Laboratory. "BONAMI: Resonance Self-Shielding by the Bondarenko Method," ORNL/TM-2005/39, Version 5.1, Vols. II, Book 1, Sect. F1, November 2006.

[58] Oak Ridge National Laboratory. "NITAWL: SCALE System Module for Performing Resonance Shielding and Working Library Production," ORNL/TM-2005/39, Version 5.1, Vols. II, Book 1, Sect. F2, November 2006.

[59] Oak Ridge National Laboratory. "SCALE 5.1 Cross-Section Covariance Libraries," ORNL/TM-2005/39, Version 5.1, Rev. 1, Vols. I, Book 3, Sect. M19, February 2008.

[60] A. Hébert. *Applied Reactor Physics.* Montréal: Presses Internationales Polytechnique, 2009.

[61] M. D. DeHart. "A deterministic study of the deficiency of the Wigner-Seitz approximation for Pu/MOX fuel pins," *Proc. of M&C'99-Madrid, Mathematics and Computations Meeting*, Madrid, Spain, Sept. 27–30, 1999.

[62] International Atomic Energy Agency. *WIMS-D library update : final report of a coordinated research project.* Vienna: IAEA, 2007.

[63] I. Kodeli. *Manual for ANGELO2 and LAMBDA codes*, NEA-1798 Package, 2008.

[64] A. Bouloré et al. "Modelling of the uncertainty of nuclear fuel thermal behaviour using the URANIE framework." *First Internation Conference on Advances in System Simulation,* pp. 50-55, 2009.

[65] W. Wullf, "Uncertainties in modeling and scaling in the prediction of fuel stored energy and thermal response," Brookhaven National Laboratory report, BNL-NUREG-40498, January 1987.

Appendix A

Cross-section uncertainties

This section contains 69-group relative covariance matrices of selected microscopic cross-sections from the *69GROUPV6REC* covariance library, ordered by nuclide atomic number.

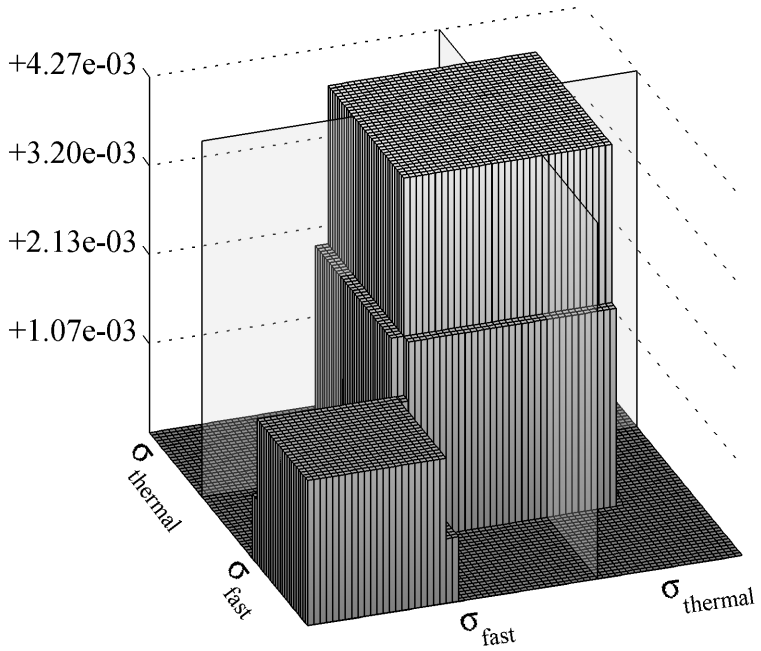

(a) relative covariance

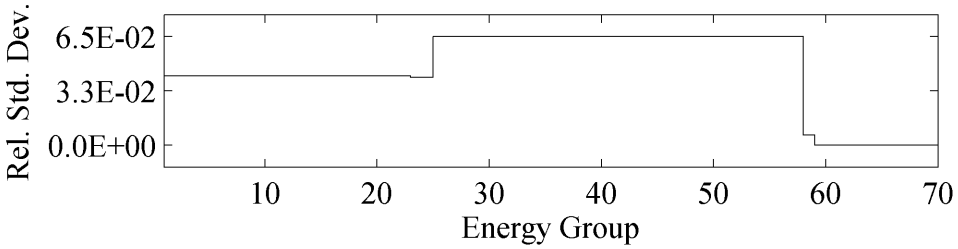

(b) relative standard deviation

Figure A.1: Xe^{135} (n, γ) 69-group uncertainty

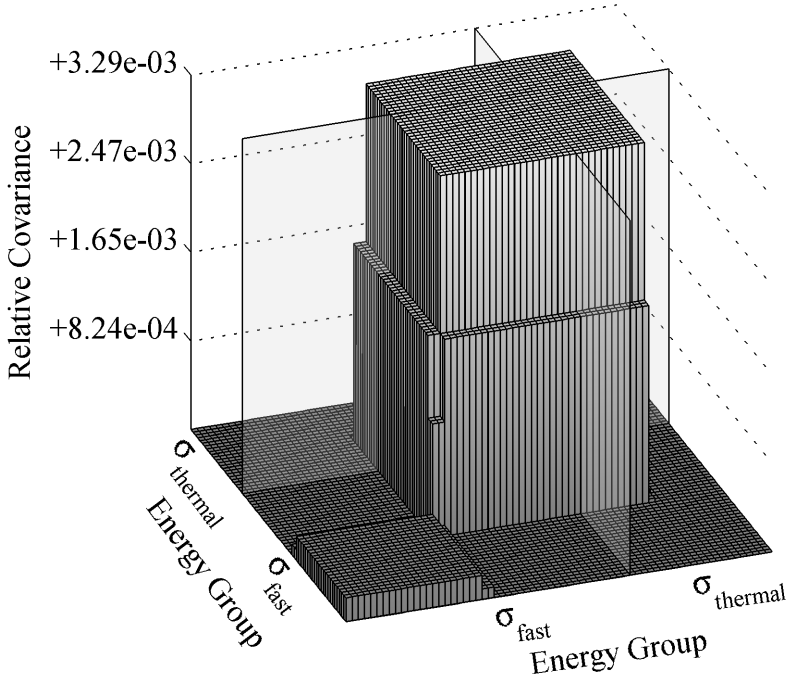

(a) relative covariance

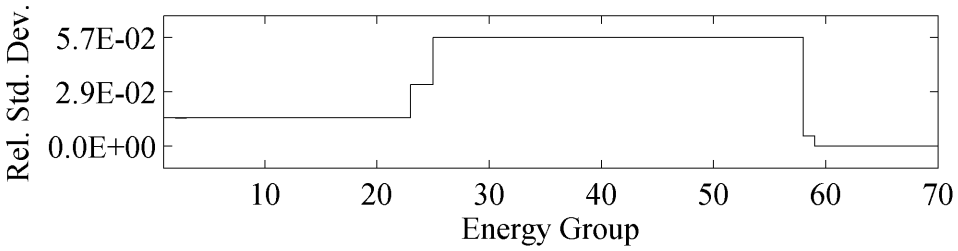

(b) relative standard deviation

Figure A.2: Sm^{149} (n, γ) 69-group uncertainty

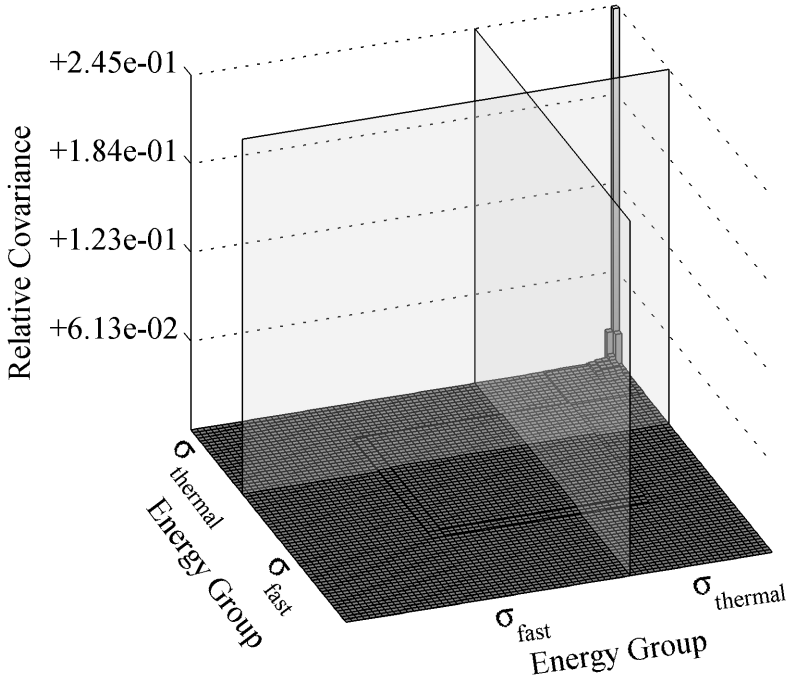

(a) relative covariance

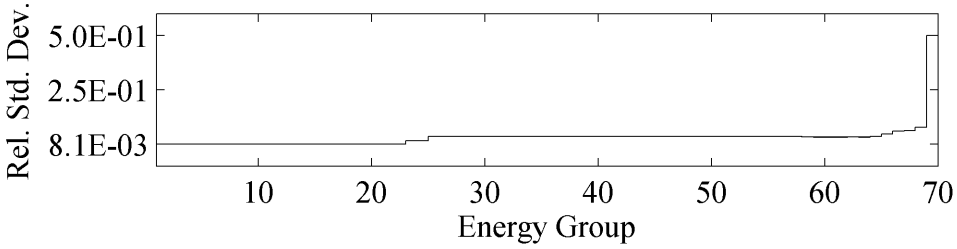

(b) relative standard deviation

Figure A.3: U^{235} (n, γ) 69-group uncertainty

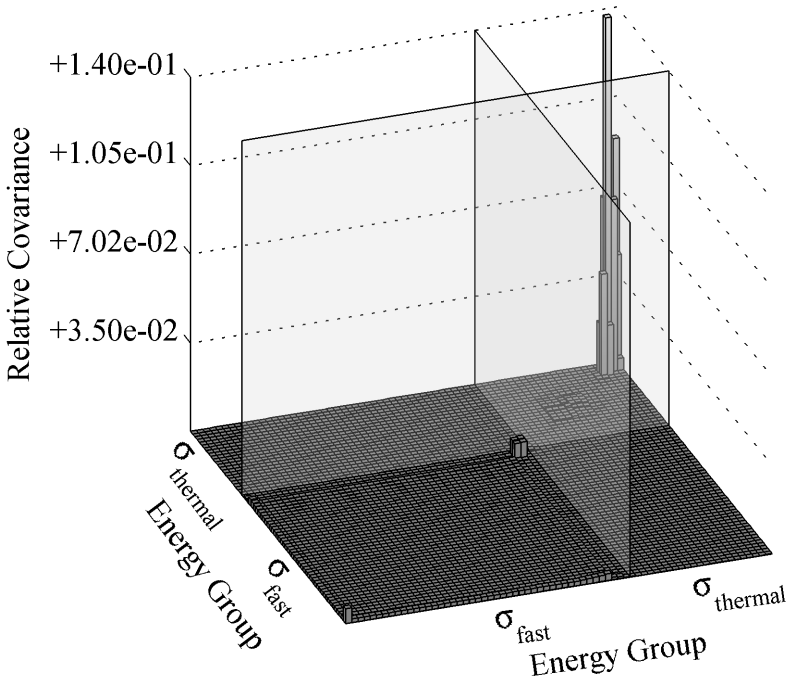

(a) relative covariance

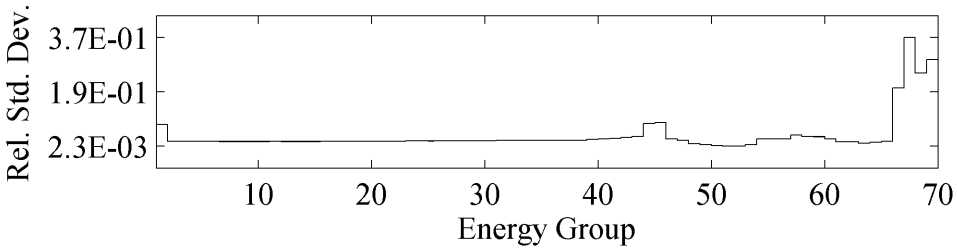

(b) relative standard deviation

Figure A.4: U^{238} (n, γ) 69-group uncertainty

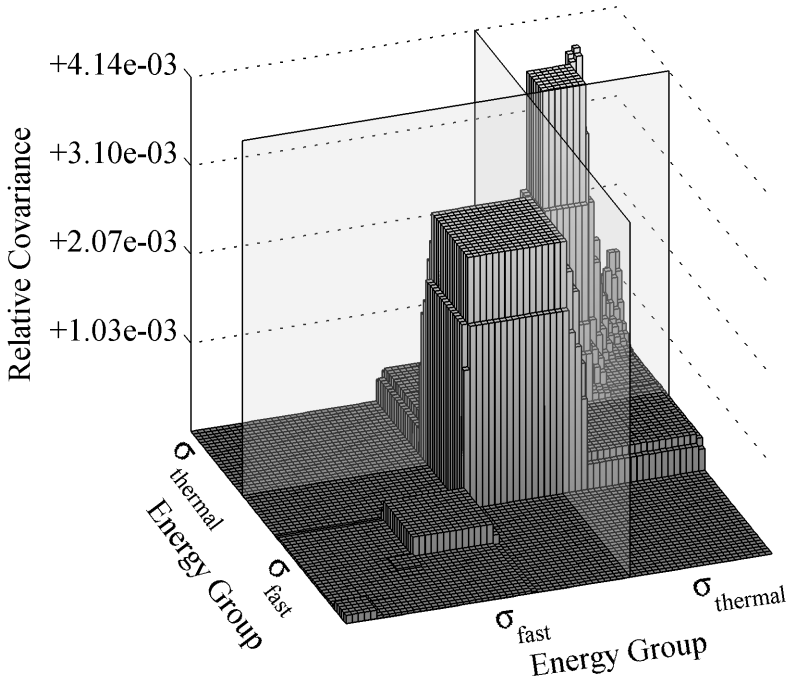

(a) relative covariance

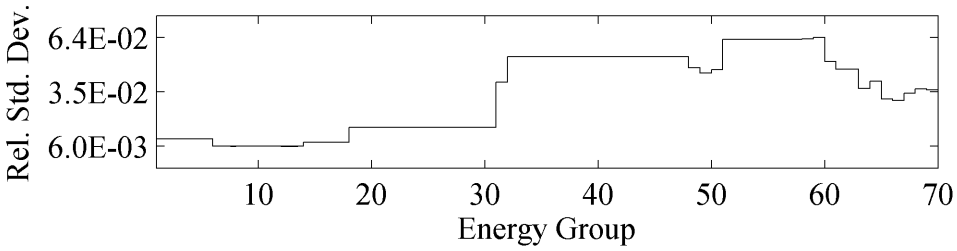

(b) relative standard deviation

Figure A.5: Pu^{239} (n, fission) 69-group uncertainty

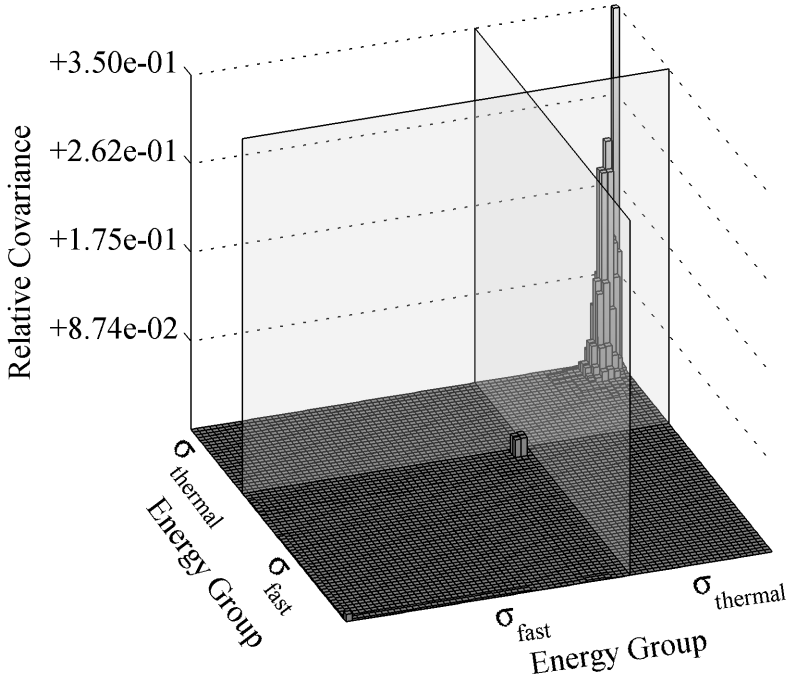

(a) relative covariance

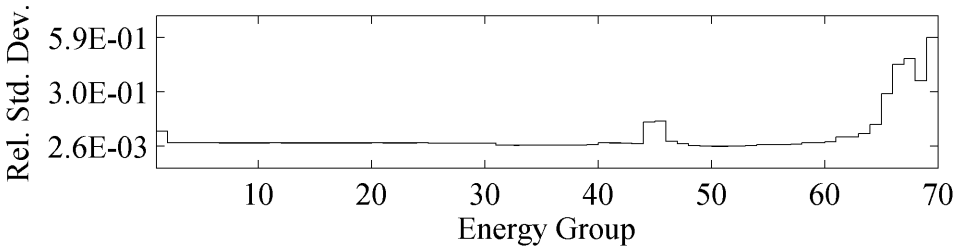

(b) relative standard deviation

Figure A.6: Pu^{240} (n, γ) 69-group uncertainty

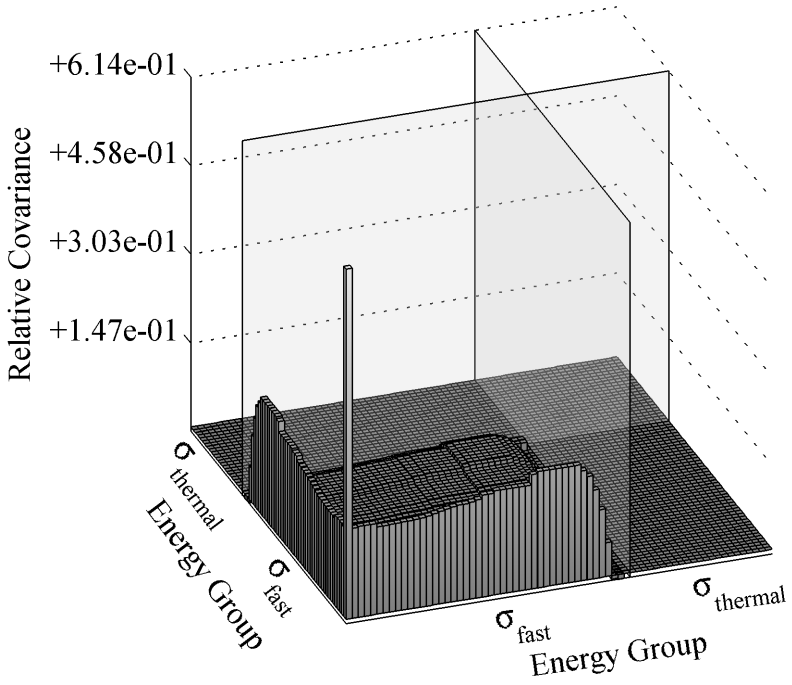

(a) relative covariance

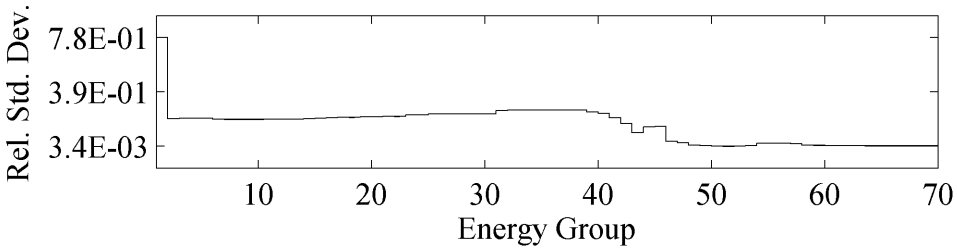

(b) relative standard deviation

Figure A.7: Pu^{240} (n, fission) 69-group uncertainty

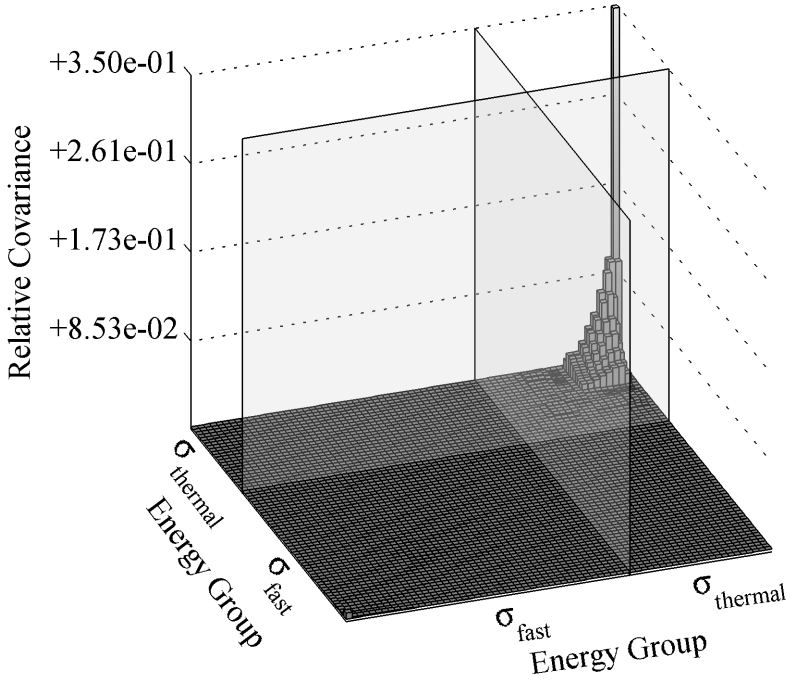

(a) relative covariance

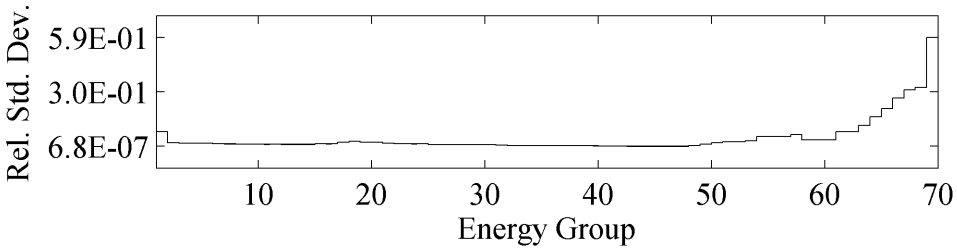

(b) relative standard deviation

Figure A.8: Pu^{241} (n, γ) 69-group uncertainty

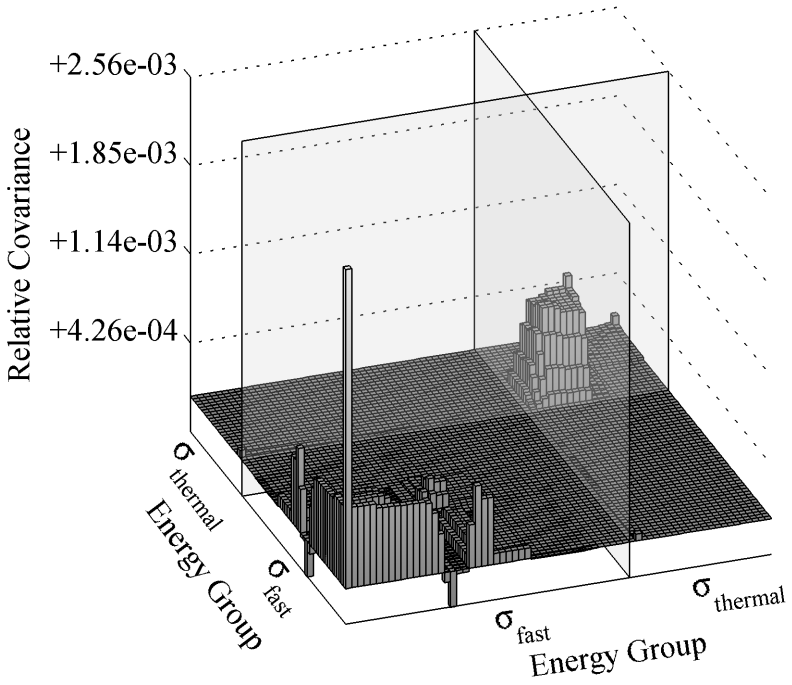

(a) relative covariance

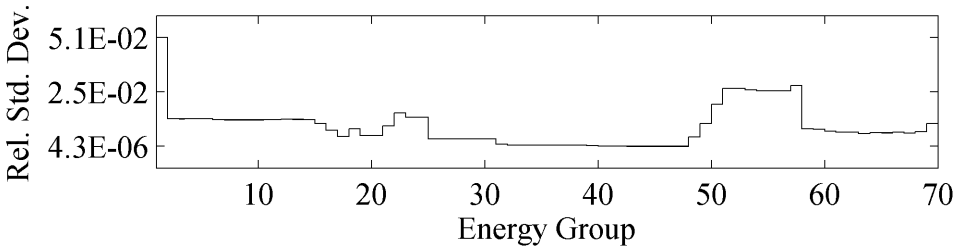

(b) relative standard deviation

Figure A.9: Pu^{241} (n, fission) 69-group uncertainty